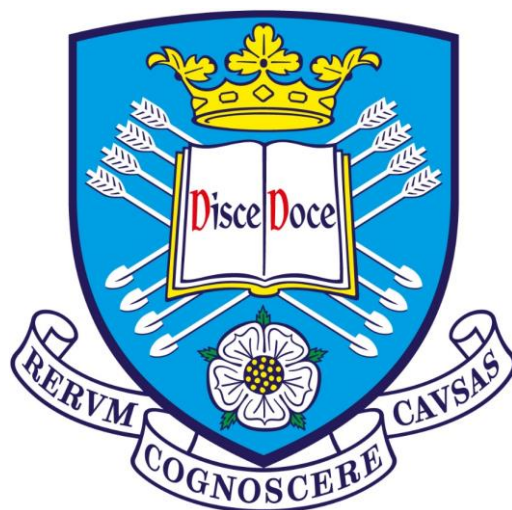


Ionic Encapsulation of Carbonylation Catalysts using Metal-Organic Framework and Polymer Supports

A thesis presented for the degree of
Doctor of Philosophy



Samuel Anton Ivko

Supervised by Dr A. Haynes

Department of Chemistry
The University of Sheffield

August 2020

For Mum

Summary

Chapter 1: Introduction

Chapter 1 provides an insight into chemical literature regarding the carbonylation of methanol as well as efforts to provide a heterogeneous alternative to the existing homogeneous processes. There is also discussion of metal-organic frameworks and their use in catalysis. The chapter concludes with a summary of the aims of the project.

Chapter 2: UiO MOFs with Linkers Containing Pyridine Moieties

Chapter 2 describes efforts to synthesise a cationic support via methylation of a range of pyridine-containing UiO-type metal-organic frameworks (UiO-67-bpy, UiO-67-bp/ppy and UiO-66-b/py). Reaction of these MOFs with MeI did not reach 100% conversion to the fully methylated forms. Reaction of the partially quaternised MOFs with $[\text{Rh}(\text{CO})_2\text{I}]_2$ resulted in a mixture of rhodium dicarbonyl species.

Chapter 3: UiO MOFs with Linkers Containing Imidazole Moieties

Chapter 3 describes the synthesis and postsynthetic modification of imidazole-functionalised UiO-66-type MOFs (UiO-66-imb and UiO-66-b/imb). The synthesised MOFs were postsynthetically modified by methylation of the pendant nitrogen site of the imidazole, converting it to imidazolium. Conversion of imidazole sites to *N*-methylimidazolium was 85% for the single-linker MOF (UiO-66-imb) and 97% for the mixed-linker MOF (UiO-66-b/imb). These cationic supports can be used to electrostatically immobilise *cis*- $[\text{Rh}(\text{CO})_2\text{I}]_2^-$. For the mixed-linker MOF, the catalyst was found to occupy the micropores of the MOF and the encapsulated complex underwent the

same organometallic processes as in solution. The supported complex was found to be active for the carbonylation of methanol to acetic acid, with lower activities than the homogeneous analogue. It demonstrated good recyclability and retained its crystallinity after catalysis.

Chapter 4: Dispersible Microporous Polymers with Pyridine Moieties

Chapter 4 describes the synthesis and postsynthetic modification of a novel dispersible microporous polymer containing a 4-vinylpyridine co-polymer. The material was postsynthetically modified via *N*-methylation of the pyridine moieties to form pyridinium cations. The cationic support was used to immobilise *cis*-[Rh(CO)₂I₂]⁻ and volumetric N₂ sorption studies revealed that the catalyst occupied the polymer's micropores. *In situ* IR reaction monitoring of the oxidative addition of MeI to the supported complex revealed that this step occurred faster than for the homogeneous analogue. The encapsulated catalyst was active for the carbonylation of methanol to form acetic acid, with activities slightly lower than the homogeneous analogue. The system demonstrated good recyclability in CHCl₃.

Chapter 5: Conclusions and Future Work

General conclusions and suggestions for further work are provided.

Chapter 6: Experimental

Full details of the instrumentation and experimental procedures used.

Chapter 7: Appendices

Supplementary data and spectra as well as details of calculations.

Acknowledgments

First and foremost, huge thanks go to my supervisor, Dr Tony Haynes, for his support and guidance throughout. Thanks also go to Dr Rob Dawson and Prof. Lee Brammer, for stimulating conversations and fruitful collaborations. I am also grateful to Sandra van Meurs, Craig Robertson and Heather Grievson. Some of this research was conducted with Masters students and so for this my thanks go to Anthony Griffiths and Tom Bailey.

I could not have completed my PhD without the support of the many friends I've made along the way. First, the "Burritrio" – Dave Griffin, for his sage advice and numerous alter-egos, and Liam Woodhead, for his sense of humour and slender fingers. I miss our daily crosswords and weekly burrito trips. Next, Alex James, a genuine "five-star man" if ever there was one. Thanks so much primarily for all the fun and nonsense, and secondarily for what turned out to be an extremely rewarding collaboration. Let's do it again sometime. To Jenna Spencer-Briggs – thanks for all the fun times drinking, chatting and baking (as well as moaning). A big thank you to the "Quaran-Tea Time" crew who managed to keep me sane while applying for jobs and finishing writing up amidst lockdown (no mean feat) – cheers Heather Carson and Eren Slate. A big thanks also to all attendees of tea and Friday pub over the years, especially Andy Sadler, Phil Reeve, Matt Dwyer, Jamie Wright, Stephen Dodsworth, Sally Morton and Tom Roseveare.

The last few years have been incredibly tough at times, and I am immensely indebted to both Lewis Thomas-Hargreaves and Charlie Ashworth for going above and beyond to help get me through it. Thank you both for being such outstanding friends.

I am extremely fortunate to have a supportive family who have patiently sympathised while I detailed my esoteric research challenges to them. I really don't know where I'd be without them, and so a huge thank you goes to Dad, Bernie, Dave, Katy, Davy, Ben, Mikaela, Sophie, Sadie, Jacob, Charlie and Samuel.

Finally to Fran, without whom I can say with complete confidence that what follows would not exist. Thank you for putting up with my nonsense over the past five years, here's to our next adventure.

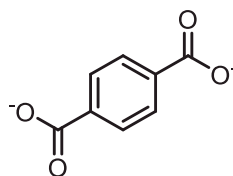
Abbreviations

Abbreviation	Technique
ATR	attenuated total reflectance
BET	Brunauer-Emmett-Teller
CIR	cylindrical internal reflectance
CP-MAS	cross polarisation magic angle spinning
FTIR	Fourier-transform infra-red
IR	infra-red
NMR	nuclear magnetic resonance
SAXS	small-angle X-ray scattering
SEM	scanning electron microscopy
TEM	transmission electron microscopy
TPPM	two-pulse phase modulation
UV-Vis	ultraviolet-visible

Abbreviation	General terms
MIL	Materials Institute Lavoisier
MOF	metal-organic framework
RCSR	Reticular Chemistry Structure Resource
SBU	secondary building unit
UiO	University of Oslo

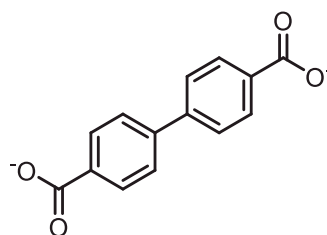
Abbreviation	Ligand / linker
--------------	-----------------

bdc



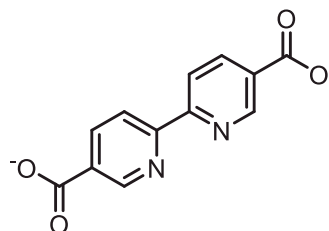
1,4-benzenedicarboxylate (or terephthalate)

bpdc



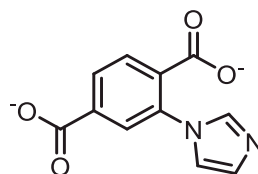
biphenyl-4,4'-dicarboxylate

bpydc



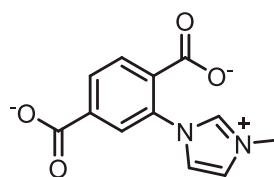
2,2'-bipyridine-5,5'-dicarboxylate

imbdc



2-(imidazol-1-yl)terephthalate

[imbdc-Me]⁺



2-(3-methyl-1*H*-imidazol-3-ium-1-yl)terephthalate

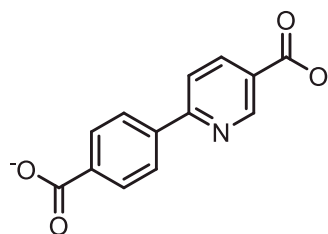
OAc



acetate

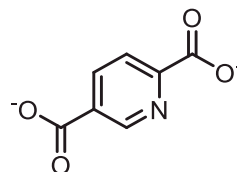
Abbreviation	Ligand / linker
--------------	-----------------

ppydc



2-phenylpyridine-5,4'-dicarboxylate

pydc



pyridine-2,5-dicarboxylate

Abbreviation	MOF composition (estimated)
--------------	-----------------------------

UiO-66	$[\text{Zr}_6\text{O}_4(\text{OH})_4(\text{bdc})_6]$
UiO-66-b/imb	$[\text{Zr}_6\text{O}_4(\text{OH})_4(\text{bdc})_{4.8}(\text{imbdc})_{1.1}(\text{OAc})_{0.1}]$
UiO-66-b/py	$[\text{Zr}_6\text{O}_4(\text{OH})_4(\text{bdc})_{4.6}(\text{pydc})_{0.9}(\text{OAc})_{0.9}]$
UiO-66-imb	$[\text{Zr}_6\text{O}_4(\text{OH})_4(\text{imbdc})_6]$
UiO-67-bpy	$[\text{Zr}_6\text{O}_4(\text{OH})_4(\text{bpydc})_6]$
UiO-67-bp/ppy	$[\text{Zr}_6\text{O}_4(\text{OH})_4(\text{bpdc})_{4.75}(\text{ppydc})_{1.25}]$

Abbreviation	Polymer composition (estimated)
--------------	---------------------------------

1	PEG ₁₁₃ - <i>b</i> -DVB ₃₀₀ - <i>co</i> -VP ₆₃
2	PEG ₁₁₃ - <i>b</i> -DVB ₃₀₀ - <i>co</i> -VP ₁₃ - <i>co</i> -[VP ⁺ I] ₅₀
3	PEG ₁₁₃ - <i>b</i> -DVB ₃₀₀ - <i>co</i> -VP ₁₃ - <i>co</i> -[VP ⁺ I] ₈ - <i>co</i> -[VP ⁺ Rh] ₄₂

Abbreviation	Chemical
bpy	2,2'-bipyridyl
BTC	benzene-1,3,5-tricarboxylate
Bu	butyl
COD	cyclooctadiene
Cy	cyclohexyl
[C ₆ mim]	1-hexyl-3-methylimidazolium
[C ₈ 4mpy]	1-octyl-4-methylpyridinium
D	deuterium
DMF	dimethylformamide
dppe	1,2-bisdiphenylphosphinoethane
DVB	1,4-divinylbenzene
Et	ethyl
Me	methyl
PEG	polyethylene glycol
PET	polyethylene terephthalate
Ph	phenyl
PVA	polyvinyl acetate
py	pyridine
THF	tetrahydrofuran
TPPTS	triphenylphosphine- <i>m</i> -trisulfonic acid
VP	4-vinylpyridine

Contents

Chapter 1	Introduction.....	1
1.1.	Catalysis.....	2
1.1.1.	Acetic acid production via methanol carbonylation	4
1.1.2.	Heterogenising the carbonylation of methanol.....	8
1.2.	Metal-organic frameworks.....	13
1.2.1.	The UiO series of metal-organic frameworks.....	15
1.2.2.	Applications of metal-organic frameworks	21
1.2.3.	Metal-organic frameworks and catalysis	23
1.3.	Project aims.....	30
1.4.	References.....	32
Chapter 2	UiO MOFs with Linkers Containing Pyridine Moieties	41
2.1.	Introduction.....	42
2.2.	UiO-67-bpy	45
2.2.1.	Synthesis and characterisation of UiO-67-bpy	45
2.2.2.	Quaternisation of UiO-67-bpy	46
2.2.3.	Reaction between UiO-67-bpy-Me _{87%} and [Rh(CO) ₂ I] ₂	53
2.2.4.	Reaction between UiO-67-bpy and [Rh(CO) ₂ I] ₂	54
2.2.5.	Reaction of MeI with UiO-67-bpy-Rh.....	57
2.3.	UiO-67-bp/ppy.....	60
2.3.1.	Synthesis and characterisation of UiO-67-bp/ppy	60
2.3.2.	Quaternisation of UiO-67-bp/ppy	63
2.3.3.	Reaction of UiO-67-bp/ppy-Me samples with [Rh(CO) ₂ I] ₂	66
2.4.	UiO-66-b/py.....	69
2.4.1.	Synthesis and characterisation of UiO-66-b/py	69
2.4.2.	Quaternisation of UiO-66-b/py	70
2.4.3.	Reaction of UiO-66-b/py-Me _{79%} with [Rh(CO) ₂ I] ₂	72
2.5.	Summary	74
2.6.	References.....	75
Chapter 3	UiO MOFs with Linkers Containing Imidazole Moieties	77
3.1.	Introduction.....	78
3.2.	UiO-66-imb.....	80
3.2.1.	Synthesis and postsynthetic modification of UiO-66-imb.....	80
3.2.2.	Attempted direct synthesis of UiO-66-imb-Me	86
3.3.	UiO-66-b/imb.....	90
3.3.1.	Synthesis and postsynthetic modification of UiO-66-b/imb.....	90

3.3.2.	Reaction of encapsulated <i>cis</i> -[Rh(CO) ₂ I ₂] ⁻ with MeI.....	98
3.3.3.	Catalytic carbonylation of MeOH with encapsulated <i>cis</i> -[Rh(CO) ₂ I ₂] ⁻ ..	99
3.4.	Attempted single crystal growth	103
3.5.	Discussion of pyridine- and imidazole-containing MOFs	105
3.6.	Summary	106
3.7.	References	107
Chapter 4	Dispersible Microporous Polymers with Pyridine Moieties	109
4.1.	Introduction	110
4.1.1.	Polymers as supports for methanol carbonylation	110
4.1.2.	Microporous organic polymers	112
4.2.	Synthesis and postsynthetic modification of dispersible microporous polymer nanoparticles	118
4.3.	Reaction of supported <i>cis</i> -[Rh(CO) ₂ I ₂] ⁻ with MeI.....	128
4.4.	Catalytic carbonylation of MeOH with supported <i>cis</i> -[Rh(CO) ₂ I ₂] ⁻	137
4.4.1.	In MeOH	137
4.4.2.	In CHCl ₃	140
4.5.	Summary	143
4.6.	References	144
Chapter 5	Conclusions and Future Work	149
5.1.	Conclusions	150
5.2.	Future Work	152
5.2.1.	Different catalysts	152
5.2.2.	Different supports.....	153
5.3.	References	154
Chapter 6	Experimental.....	155
6.1.	Solvents and reagents	156
6.2.	Instrumentation.....	157
6.2.1.	Infra-red spectra	157
6.2.2.	Nuclear magnetic resonance spectroscopy.....	157
6.2.3.	Powder X-ray diffraction	158
6.2.4.	Small angle X-ray scattering.....	159
6.2.5.	Volumetric N ₂ gas sorption.....	159
6.2.6.	Elemental analysis.....	159
6.2.7.	Electron microscopy.....	160
6.3.	Synthesis of rhodium precursors	162
6.3.1.	[Rh(CO) ₂ Cl] ₂	162

6.3.2.	[Rh(CO) ₂ I] ₂	162
6.4.	Synthesis of linkers.....	163
6.4.1.	2,2'-bipyridyl-5,5'-dicarboxylic acid (H₂bpydc).....	163
6.4.2.	2-phenylpyridine-5,4'-dicarboxylic acid (H₂ppydc).....	164
6.4.3.	2-(imidazole-1-yl)terephthalic acid (H₂imbdc).....	165
6.4.4.	Quaternisation of H₂imbdc	166
6.5.	Synthesis and postsynthetic modification of MOFs	167
6.5.1.	UiO-67-bpy	167
6.5.2.	UiO-67-bp/ppy.....	171
6.5.3.	UiO-66-b/py.....	176
6.5.4.	UiO-66	178
6.5.5.	UiO-66-imb.....	179
6.5.6.	UiO-66-imb-Me (attempted direct synthesis).....	182
6.5.7.	UiO-66-b/imb.....	183
6.5.8.	UiO-66-b/imb (attempted single crystal synthesis)	187
6.5.9.	UiO-66-b/imb-Me (attempted single crystal synthesis).....	188
6.6.	Synthesis of dispersible microporous polymer nanoparticles.....	189
6.6.1.	Synthesis of PEG ₁₁₃ -Br.....	189
6.6.2.	Synthesis of PEG-based macro-chain transfer agent (CTA)	189
6.6.3.	Synthesis of PEG ₁₁₃ - <i>b</i> -DVB ₃₀₀ - <i>co</i> -VP ₆₃ (1)	190
6.6.4.	<i>N</i> -methylation of 1 to give PEG ₁₁₃ - <i>b</i> -DVB ₃₀₀ - <i>co</i> -VP ₁₃ - <i>co</i> -[VP ⁺ I] ₅₀ (2) 191	
6.6.5.	Reaction of 2 with [Rh(CO) ₂ I] ₂ to give 3	191
6.7.	Kinetic measurements.....	193
6.8.	Catalytic reaction procedure	194
6.9.	References.....	196
Chapter 7	Appendices.....	199
7.1.	¹ H- ¹ H COSY NMR spectrum to distinguish mixture of products from reaction of UiO-67-bpy with MeI	200
7.2.	Determination of TOF value for MOF-supported catalyst in CHCl ₃	201
7.3.	Pawley phase fits	202
7.4.	SAXS fitting	204
7.5.	Decay graphs of IR absorption at 1987 cm ⁻¹ with double exponential curve fits during reaction of polymer-supported catalyst with MeI in CH ₂ Cl ₂ (298 K).....	205
7.6.	Determination of TOF value for polymer-supported catalyst in MeOH	208
7.7.	Determination of TOF value for polymer-supported catalyst in CHCl ₃	209
7.8.	References.....	210

Chapter 1 Introduction

1.1. Catalysis

A catalyst is a substance that speeds up a chemical process without itself being used up. It achieves this by lowering the Gibbs activation energy, ΔG^\ddagger , of a reaction by providing an alternative reaction pathway. This is often achieved by forming intermediates in a cyclical process that eventually regenerates the catalyst. This process is shown diagrammatically in Figure 1.1.

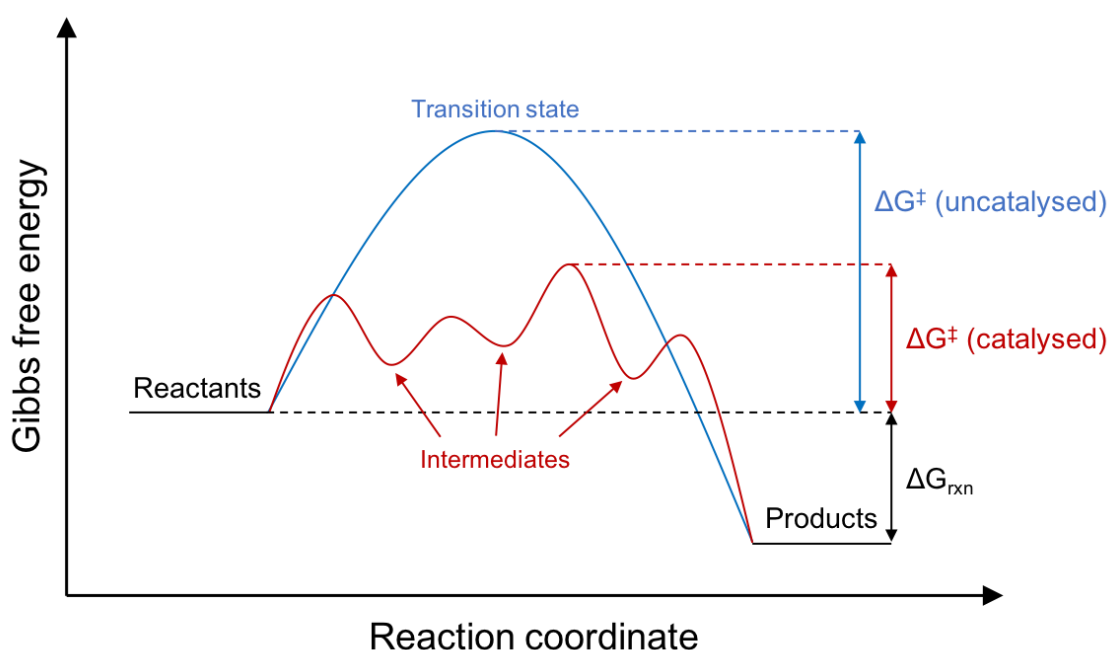


Figure 1.1. Gibbs free energy profile showing the effect of a catalyst on the Gibbs energy of activation.

Catalysts are ubiquitous – from digestive enzymes for breaking down food, to catalytic converters in cars for the oxidation of toxic carbon monoxide and other exhaust gases. It is estimated that around 90% of all materials and chemicals involve use of a catalyst at some point in their manufacture.¹

Catalytic reactions are classed as either homogeneous or heterogeneous. Homogeneous processes pertain to reactions in which all reactants and catalysts are in the same phase (often in solution), whereas heterogeneous processes represent reactions where the catalyst is in a different phase to the reactants (usually catalysts on solid supports with gaseous reactants passed over the surface).

Many homogeneous catalysts are comprised of well-defined molecular transition metal complexes that are soluble in common organic solvents. This allows for a detailed characterisation of reaction intermediates and products via spectroscopic and kinetic analyses, which help to elucidate the full catalytic mechanism. Another useful tool that is commonplace in this field of study is the use of computational models to study these mechanisms. The ability to scrutinise the mechanism in this manner allows for a great deal of tuning of the catalyst, for example by varying a catalyst's steric and electronic properties via careful ligand design. This can help enhance important factors such as selectivity and turnover frequency.

Thanks to these advantages, homogeneous catalysts are often responsible for high yields and selectivity, require reasonably mild reaction conditions, and have the potential for every catalyst molecule to be active. The downside of this method of catalysis is the requirement to separate the catalyst from the products at the end of the reaction in order to reuse it. Some examples of major homogeneous catalytic processes are alkene hydroformylation and methanol carbonylation, the specifics of which will form the subject of Section 1.1.1.

Heterogeneous catalysts, however, are generally solids, which are easily separated from reactants and products that are in solution or, more often, the gas phase. They are more chemically robust than their homogeneous analogues and are tolerant of more extreme

reaction conditions. However, they are often far less chemically sophisticated materials than homogeneous catalysts, and are thus less reactive and selective. Furthermore, the reaction mechanism is more challenging to study in the bulk solid state than it is for discrete molecules in solution. Because of this, vital pieces of information regarding the active site and the mechanism of reaction are much more difficult to ascertain, and thus tuning of heterogeneous catalysts is much more challenging. Some major examples of heterogeneous catalysis are the Haber process of fixing nitrogen and the Fischer-Tropsch process, which forms long-chain hydrocarbons from carbon monoxide and hydrogen gas.

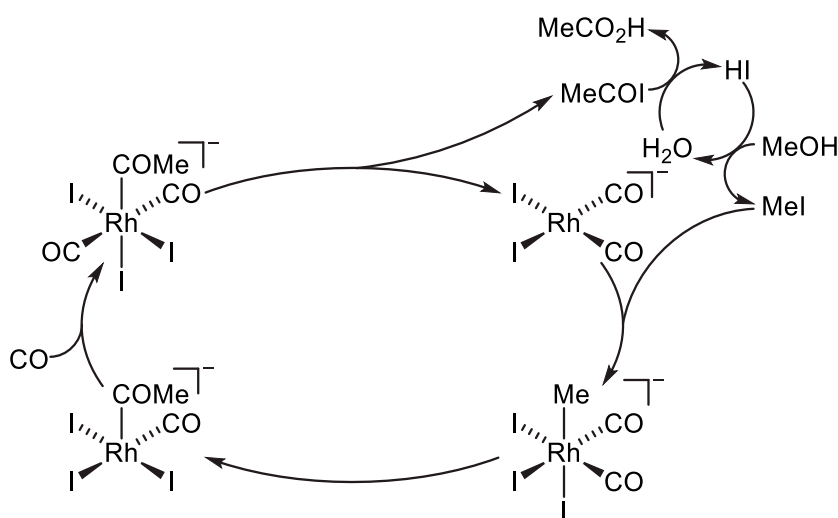
A lot of effort has been invested into designing new hybrid materials that capitalise on the advantages of both homogeneous and heterogeneous catalysis. One route that has generated significant interest is the immobilisation of a homogeneous transition metal catalyst onto a solid-state support - a process known as heterogenisation. This technique preserves the highly tuned molecular catalyst derived from detailed homogeneous studies and enables facile separation from the reaction mixture. Some further advantages of this method are (i) protection from some common homogeneous catalyst deactivation routes such as aggregation; (ii) better control of the catalyst's immediate chemical environment which can improve performance; (iii) the use of solvents that would otherwise not be accessible due to poor catalyst solubility. Some solid-state supports that have been studied include activated carbon, inorganic oxides, zeolites, insoluble polymers, and, more recently, metal-organic frameworks.²⁻⁶

1.1.1. Acetic acid production via methanol carbonylation

It was discovered in 1913 that methanol could be carbonylated to produce acetic acid,⁷ although methanol was not available in commercial quantities until after 1920. BASF

opened a plant in 1960 in which carbon monoxide was reacted with methanol in the presence of CO_2 at high pressures and temperatures to form acetic acid.⁸

Monsanto discovered in 1966 that a rhodium catalyst used in conjunction with an iodide co-catalyst could be used to facilitate the production of acetic acid via methanol carbonylation under milder conditions and with higher specificity.⁹



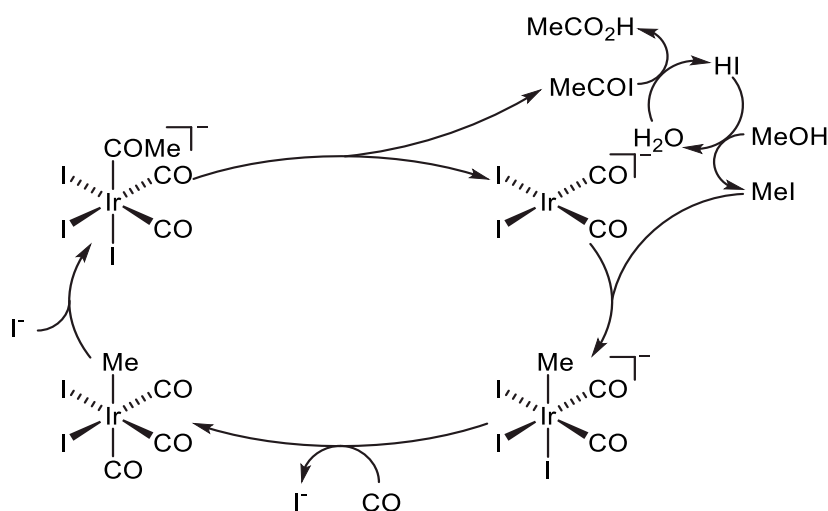
Scheme 1.1. Simplified representation of the Monsanto process.

As shown in Scheme 1.1, the hydrogen iodide co-catalyst reacts with methanol to form water and methyl iodide. The methyl iodide undergoes an $\text{S}_{\text{N}}2$ -type oxidative addition to the square planar rhodium(I) complex, and then the methyl group spontaneously migrates, causing a carbonyl insertion. Carbon monoxide associates, after which acetyl iodide is reductively eliminated. This reacts with the water formed previously to regenerate the hydrogen iodide co-catalyst and form the product, acetic acid. The catalytic reaction has been shown to be first order with respect to the catalyst and methyl iodide, and thus the oxidative addition step is considered to be rate-determining.

A relatively high water concentration (~10% wt.) is employed in the Monsanto process, to maintain high catalytic activity. At lower water concentrations, an inactive Rh(III)

species, $[\text{Rh}(\text{CO})_2\text{I}_4]^-$ can accumulate, as an intermediate in a competing water-gas shift reaction. This species can dissociate CO and lead to precipitation of RhI_3 in parts of the plant that have lower CO partial pressure (volatiles are mostly vaporised in a "flash-tank" to enable catalyst recycling). A disadvantage of the high water concentration is that it increases the costs of product purification, by distillation, to give dry acetic acid. Variations of the Monsanto process have been introduced that can operate at lower water concentration. For example, the Celanese Acid Optimization (AO Plus) technology employs a lithium iodide promoter that stabilises the Rh catalyst and achieves carbonylation rates that are comparable with those in the conventional Monsanto process – but at significantly lower water concentrations. Related processes for carbonylation of methyl acetate to acetic anhydride under anhydrous conditions use lithium iodide (Eastman) or quaternary ammonium iodide salts (BP) as additives.¹⁰

In 1996 BP Chemicals introduced the Cativa™ process for methanol carbonylation using an iridium catalyst, iodide co-catalyst and a ruthenium promoter.^{11,12} This gives higher selectivity, makes use of a cheaper catalyst, and operates at a lower water concentration (reducing product purification costs) compared with the Monsanto process.



Scheme 1.2. Simplified representation of the Cativa™ process.

The cycle in Scheme 1.2 is very similar to that of Scheme 1.1, but with a few key differences. In this process the octahedral complex formed after the oxidative addition of methyl iodide to the metal centre is more stable and so a ligand exchange (carbon monoxide for iodide) must occur before the methyl group migrates, which then allows for the carbonyl insertion and the re-association of iodide. In this process, the oxidative addition step is much faster than for the process shown in Scheme 1.1, and the ligand exchange is the rate-limiting step and promoted by iodide acceptors such as ruthenium iodocarbonyl complexes.¹³

The operating conditions of the three industrial methods of methanol carbonylation are compared in Table 1.1. All three require an iodide co-catalyst that acts to generate methyl iodide from methanol.

Table 1.1. Operating conditions of methanol carbonylation methods.^{8–12,14}

Method	Catalyst	Commercialised	Operating temperature / °C	Operating pressure / atm
BASF	$[\text{Co}(\text{CO})_4]^-$	1960	210	700
Monsanto	$[\text{Rh}(\text{CO})_2\text{I}_2]^-$	1966	180	30
Cativa	$[\text{Ir}(\text{CO})_2\text{I}_3(\text{Me})]^-$	1996	190	20

Due to the more forcing conditions required to reach commercially acceptable reaction rates in the BASF method as compared with the Monsanto and CativaTM processes, these latter two have largely supplanted the former industrially.¹⁴ Worldwide production for acetic acid was estimated at 20 million metric tons per annum in 2018.¹⁵

The main use of acetic acid is in the production of vinyl acetate,¹⁶ which is an important monomer for various copolymers as well as in the production of polyvinyl acetate (PVA). A growing use, however, is as solvent in the synthesis of ultrapure terephthalic acid,

which is used to make polyethylene terephthalate (PET). Thanks to these two major uses for acetic acid, worldwide demand is expected to grow by ~12% over the next five years.¹⁵

Since the introduction of the Cativa™ process, efforts have largely turned to alternative ways of improving the carbonylation of methanol, and one obvious route is in conversion to a heterogeneous process. Research undertaken into such a process forms the subject of Section 1.1.2, but it is worth noting that two heterogeneous routes for acetic acid formation have been adopted on an industrial scale; the Chiyoda/UOP Acetica™ process (which is discussed in detail in Section 1.1.2.2);¹⁷ and BP's SaaBre™ process, which uses syngas as its feedstock as opposed to methanol, and proceeds via carbonylation of dimethyl ether.¹⁶

1.1.2. Heterogenising the carbonylation of methanol

A range of solid supports have been used to heterogenise rhodium catalysts for methanol carbonylation, including activated carbon,⁵ clays,¹⁸ graphitic carbon nitride,¹⁹ covalent triazine frameworks,²⁰ inorganic oxides,^{21–24} zeolites,^{25–28} and various polymeric materials.^{29–34} A major limitation discovered with several of these systems was the leaching of catalyst from the solid supports, which prevented commercial implementation.⁶

1.1.2.1. Using zeolites

Zeolites are microporous aluminosilicate materials that accommodate loosely held cations such as Mg^{2+} and Na^+ in their pores (Figure 1.2). There are 232 synthetic and 67 naturally occurring zeolites known.³⁵

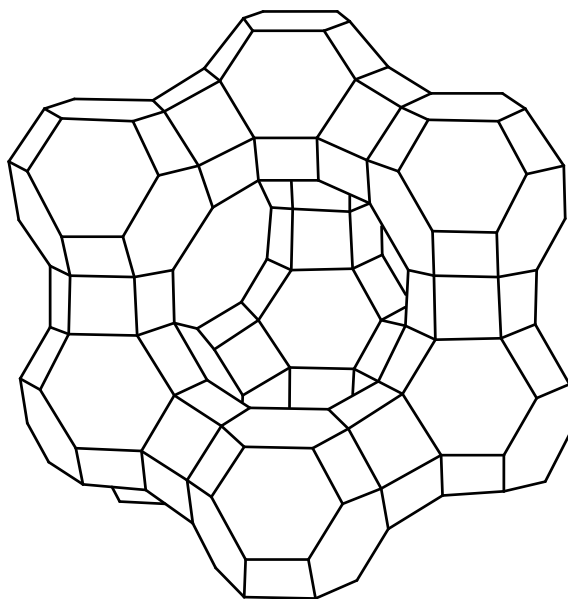


Figure 1.2. Schematic of zeolite Linde 13X highlighting its central pore.

The cations held within the pores can be exchanged for transition metal cations via ion exchange. The advantages of this method are that a high dispersal is often achieved when compared with silica gel, alumina, or other comparable solid supports. Furthermore, the high thermal stability of zeolites allows for harsher catalytic conditions to be employed when compared with solid supports such as organic polymers. Transition metal cations exchanged into zeolites tend to display similar catalytic activities to the same species in solution.^{28,36}

In a study by Lars *et al.*, the zeolite Linde 13X (Figure 1.2) was impregnated using a solution of $[\text{Rh}(\text{CO})\text{H}(\text{PPh}_3)_3]$ in CHCl_3 , followed by removal of solvent under reduced pressure.²⁷ The phosphine ligands were too large to enter the cavities of the zeolite, and the catalytic species was therefore expected to be confined to the outer surface of the zeolite particles. The same zeolite was also impregnated with $[\text{Rh}(\text{NH}_3)_5\text{Cl}]^{2+}$ by an ion-exchange procedure. This impregnation was more homogeneous in nature, with the catalytic species dispersed evenly throughout both the interior and the exterior of the zeolite particles.

Addition of methanol at 170 °C under carbon monoxide at 1 atm to these impregnated zeolites formed methyl acetate with dimethyl ether as a by-product. The formation of the by-product was lower for the catalytic species confined to the exterior of the zeolite than for the more homogeneously dispersed species. It was suggested that this was as a result of the occupation of active acidic sites for the by-product formation on the exterior of the zeolite by $[\text{Rh}(\text{CO})\text{H}(\text{PPh}_3)_3]$.

1.1.2.2. Using polymers

Polymers are large molecules made up of repeating units of smaller molecules, known as monomers. They can range from artificial synthetic polymers such as polystyrene to naturally occurring biological polymers such as DNA. Many long-chain polymers have low solubility, and they are thus attractive potential media for solid supports.

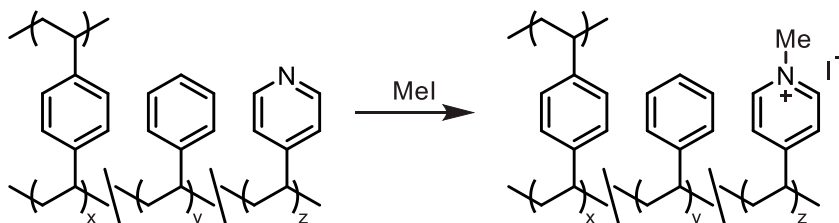
In 1980 Drago *et al.* demonstrated for the first time the ionic attachment of *cis*- $[\text{Rh}(\text{CO})_2\text{I}_2]^-$ on a solid support. The support used was a copolymer of styrene and 4-vinylpyridine and was methylated by treatment with MeI to form a cationic methylpyridinium-functionalised polymer with iodide counter-ions. Reaction of this material with $[\text{Rh}(\text{CO})_2\text{I}]_2$ resulted in generation of the desired species *in situ*. The supported species was found to be equal in catalytic activity with the homogeneous complex, and leaching could be minimised by appropriate solvent selection and altering the ratio of support to rhodium.

In 1998 the Chiyoda/UOP Acetica™ process was developed,¹⁷ which was the first commercially viable example of a heterogenised methanol carbonylation process.³⁷ The process involves use of a cross-linked poly-vinylpyridine resin which is tolerant of elevated temperatures and pressures, and a rhodium catalyst. Under the reaction conditions, the rhodium is converted into the catalytically active anionic square planar

complex, $cis\text{-}[\text{Rh}(\text{CO})_2\text{I}_2]^-$, and the resin pyridine groups become positively charged due to quaternisation with methyl iodide.

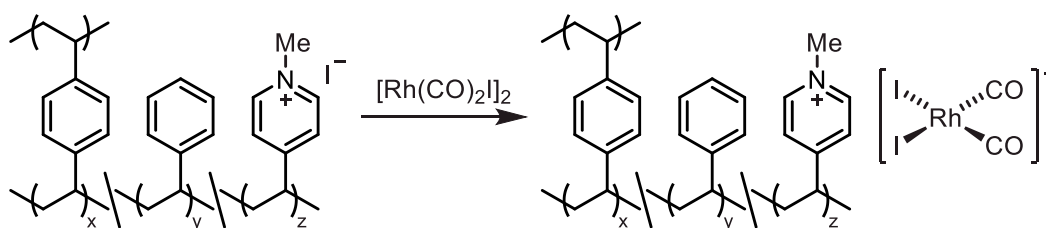
The process has carbonylation rates comparable with the homogeneous analogue but produces fewer by-products by virtue of the lower water concentrations used. Furthermore, higher catalyst loading can be achieved due to the removal of the solubility constraints in the homogeneous system. The Acetica™ process has since been implemented commercially in a plant in Brazil producing 200 kilotonnes of acetic acid per annum.³⁸

The mechanism of the polymer-supported carbonylation process was investigated by Haynes *et al.* using thin-films of poly(4-vinylpyridine-*co*-styrene-*co*-divinylbenzene) suitable for *in situ* IR spectroscopic study.³⁹ As shown in Scheme 1.3, the pyridyl groups were quaternised with methyl iodide, generating a cationic support with charge-balancing iodide anions.



Scheme 1.3. Reaction of polymer pyridyl groups with methyl iodide to generate a cationic support.

The rhodium complex was loaded onto the cationic polymer using the reaction between the catalytic precursor ($[\text{Rh}(\text{CO})_2\text{I}_2]$) dissolved in *n*-hexane and the support's iodide counter-ions, to form the square planar anionic catalyst as shown in Scheme 1.4.



Scheme 1.4. Reaction between quaternised polymer and rhodium precursor to form ionically encapsulated anionic rhodium square planar complex.

IR spectroscopy indicated the formation of the square planar anionic rhodium complex shown in Scheme 1.4, the $\nu(\text{CO})$ signals of which were close to the equivalent complex in solution.

The reaction of the supported $\text{cis-}[\text{Rh}(\text{CO})_2\text{I}_2]^-$ complex with methyl iodide was monitored *in situ* via IR spectroscopy, which demonstrated that the same basic steps of the cycle shown in Scheme 1.1 also occur in this heterogeneous analogue, while kinetic measurements showed rates similar to those in solution.

1.2. Metal-organic frameworks

Metal-organic frameworks (MOFs) are a class of coordination polymers constructed from metal-containing secondary building units (SBUs) that act as nodes and polytopic organic linkers (also known as struts). They first appeared in the literature in the early 1990s⁴⁰ and since then an estimated 70,000 MOF structures have been reported and studied.^{41,42}

Figure 1.3 shows how interest in MOFs has grown exponentially over recent years. In 2019, there were nearly 25 publications released on average every day concerning metal-organic frameworks.

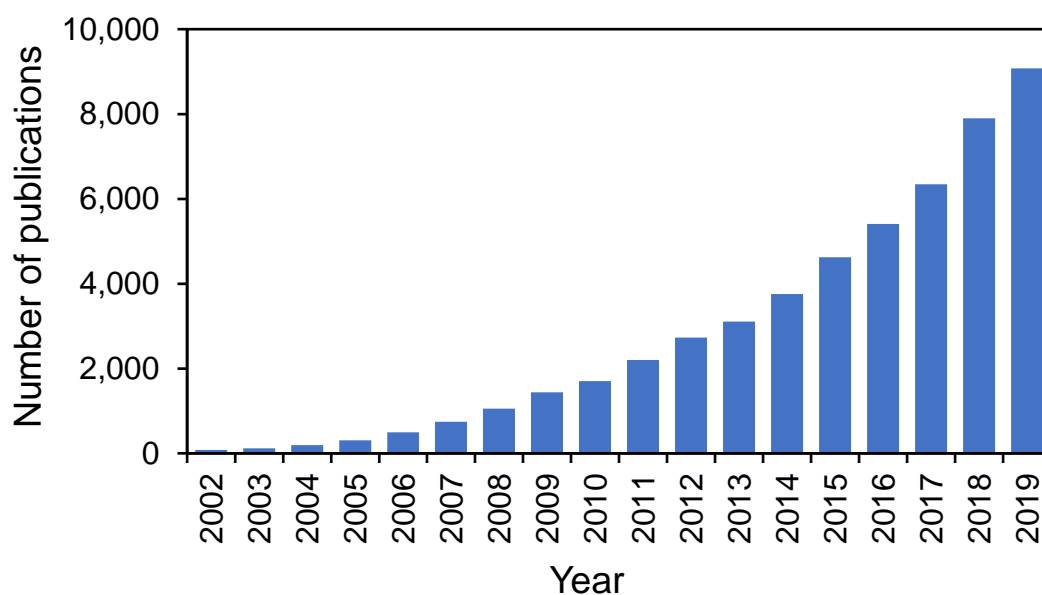


Figure 1.3. The number of publications per year in the area of metal-organic frameworks according to Web of Science.

Common SBUs consist chiefly of metal clusters, as demonstrated in Figure 1.4. Another way of considering these SBUs is as nodes with various coordination geometries – these are demonstrated above the SBUs shown in Figure 1.4.

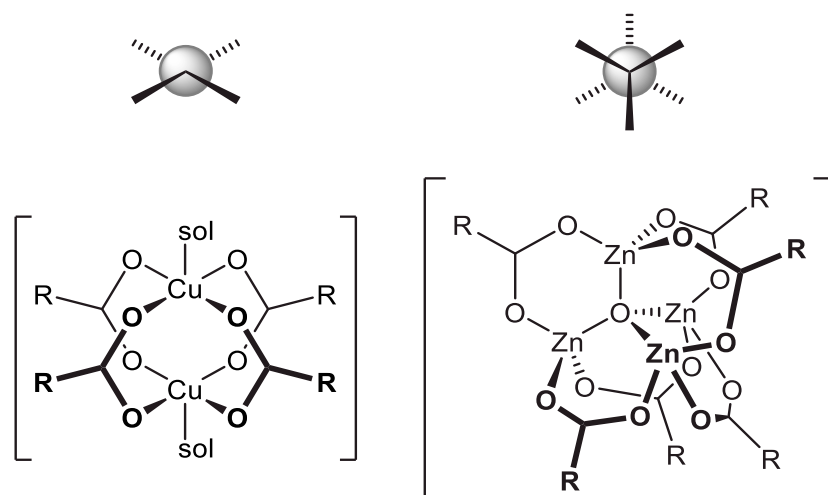


Figure 1.4. Examples of common types of SBUs found in MOFs.^{43,44}

Organic linkers are ditopic or polytopic Lewis bases of different geometries such as those shown in Figure 1.5, with their respective simplified geometries shown above.

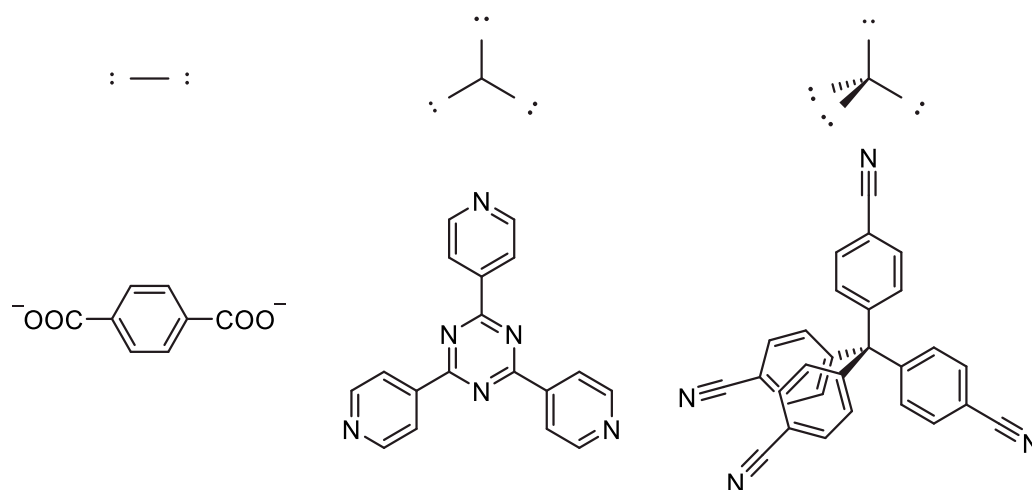


Figure 1.5. Examples of different geometries of commonly employed organic struts.⁴⁵

The appeal of MOFs is in the ability to tune their properties by careful selection of SBU and strut combinations, thus making them attractive designer media for a variety of applications, as discussed in Section 1.2.2.

1.2.1. The UiO series of metal-organic frameworks

Zirconium-based MOFs have attracted much attention due to their high stability and ease of synthesis. Lack of hydrolytic and chemical stability has hindered the performance of many MOFs, yet some zirconium MOFs are stable in water or even acidic conditions. This is largely due to the hard Lewis acid Zr^{4+} cations interacting very strongly with the hard Lewis base carboxylate ligands acting as linkers between the clusters. Most reported Zr-based MOFs possess the Zr_6 clusters shown in Figure 1.6 as their SBUs. This structure is robust and symmetric, which enables relatively simple prediction of the resulting MOF structure. Each zirconium ion in Figure 1.6 is coordinated by two O^{2-} ions and two $(OH)^-$ ions, which are themselves each shared between three zirconium ions. Each metal cation is also coordinated by four carboxylate anions that form a bridge with each adjacent cation; only one such carboxylate anion is displayed in Figure 1.6 for clarity.

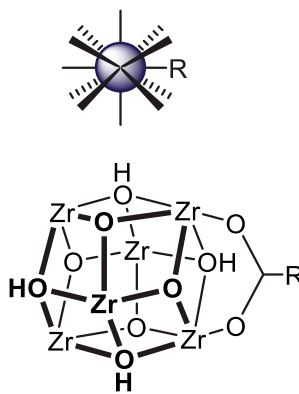


Figure 1.6. Structure and connectivity of $[Zr_6(\mu_3-O)_4(\mu_3-OH)_4]^{12+}$ clusters and their mode of binding with carboxylates. Only one bound carboxylate is shown for clarity. These clusters are hereafter identified using the purple sphere shown above the structure.

One of the most widely studied families of MOFs in recent years is the zirconium-based UiO-66 and its isorecticular (same topology) derivatives.⁴⁶ This series of MOFs is of

interest due to their high porosity, ease of synthesis, low cost and their high thermal, chemical and mechanical stability,^{47–49} although their long-term stability in ambient conditions is less convincing.⁵⁰

UiO-66 consists of the zirconium clusters shown in Figure 1.6 coordinated with 12 1,4-benzenedicarboxylate linkers. The adjacent carboxylate oxygen atoms on each linker are each coordinated to a different zirconium ion within the same cluster, thus forming a *syn-syn* bidentate bridge with the cluster while the ditopic nature of the linker enables two distinct clusters to be connected, as shown in Figure 1.7.

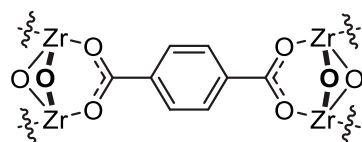


Figure 1.7. The *syn-syn* bidentate bridge mode of binding between a 1,4-benzenedicarboxylate strut and two of the $[\text{Zr}_6(\mu_3\text{-O})_4(\mu_3\text{-OH})_4]^{12+}$ SBUs shown in Figure 1.6.

The 1,4-benzenedicarboxylate struts of UiO-66 can be replaced with linear biphenyl dicarboxylate struts (giving UiO-67) or linear terphenyl dicarboxylate struts (giving UiO-68) – these have been shown to adopt the same basic structure as UiO-66 but with an increased surface area and pore window size (Table 1.2).^{46,51} These are thus isorecticular derivatives of UiO-66. It is noted that even in the case of the smallest MOF in the series (UiO-66), a molecule the size of hexamethylbenzene may pass through the triangular pore windows.⁴⁶ In the full structure, each SBU is linked to 12 others via the dicarboxylate bridges to give a face-centred cubic close-packed arrangement with both octahedral and tetrahedral pores, as demonstrated in Figure 1.8. This represents an **fcu** topology using the Reticular Chemistry Structural Resource (RCSR) net nomenclature.^{52,53}

Table 1.2. BET surface areas, and pore window sizes of UiO-type MOFs.^{46,51}

MOF	S_{BET} / $\text{m}^2 \text{g}^{-1}$	Window size / Å
UiO-66	1187	6
UiO-67	3000	8
UiO-68	4170	10

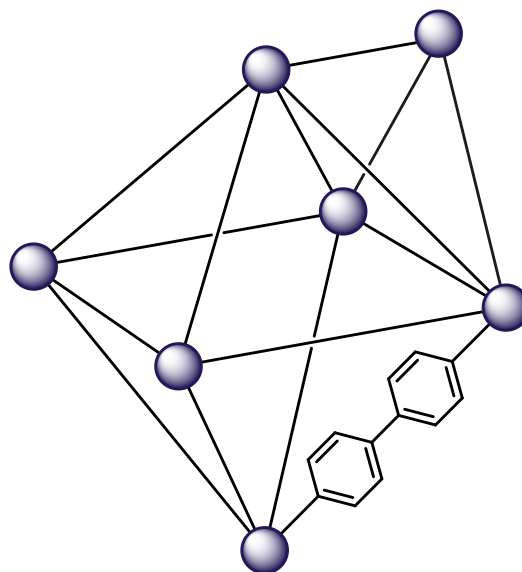


Figure 1.8. Schematic drawing of UiO-67 highlighting how biphenyl dicarboxylate struts link with the SBUs shown in Figure 1.6 to form both octahedral- and tetrahedral-shaped pores.⁴⁶ The struts are represented as straight black lines and the zirconium clusters are represented as purple spheres.

The crystal structure of UiO-67 has been solved and is shown in Figure 1.9.⁵⁴ The structure highlights the high symmetry brought about by the combination of the icosahedral SBUs shown in Figure 1.6 and the linear dicarboxylate struts.

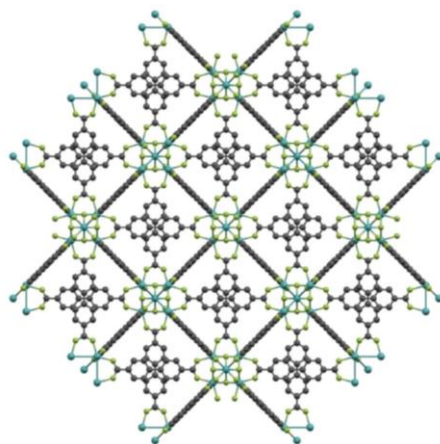


Figure 1.9. X-ray crystal structure of UiO-67.⁵⁴ Hydrogen atoms are omitted for clarity.

Much research has been undertaken into the defect chemistry of the UiO-series of MOFs due to its potential to improve the stability and porosity of synthesised MOFs.^{55,56} Two key defects have been identified – missing linker defects and missing cluster defects.⁵⁷

Different methods of synthesis favour different concentrations of defects, and indeed several different synthetic procedures exist for the synthesis of UiO MOFs.^{46,51,55,58–61} Each method has its own advantages for the properties of the MOF that is generated, for instance a higher defect concentration leading to greater porosity.

An acidic modulator is often used in the synthesis as this restricts nucleation, thereby leading to larger crystal formation. A range of acidic modulators have been reported, including acetic acid,⁶¹ hydrochloric acid,^{51,55} trifluoroacetic acid⁵⁷ and benzoic acid.⁶² An optimal benzoic acid to $ZrCl_4$ ratio of 30:1 has been suggested in the formation of UiO-67.⁵⁸ This modulator helps to increase crystallinity and leads to larger crystals growing by competing with the fast reaction between SBU and linker.

Previous work has indicated that the predominant defect present in the UiO-series of MOFs is missing cluster defects rather than missing linker defects.⁵⁷ Modulators with

greater acidity led to a higher concentration of defects in the MOF, to the extent that a different topology could be observed within the framework. The use of high acidity modulators led to what is described using the RCSR net nomenclature⁵² as **reo** phases appearing as opposed to the usual **fcu** topology of the pristine framework as shown in Figure 1.9. A tentative explanation for this observed trend is that modulators with a lower pK_a form stronger bonds with zirconium SBUs and are thus harder to displace by the ditopic strut, meaning that more defects begin to appear.

In place of simple benzene-based linkers, substituted struts are often used.^{54,59,60,62–66} A popular example is an analogue of UiO-67 which incorporates a bipyridyl motif, commonly known as UiO-67-bpy, shown in Figure 1.10. The bipyridyl motif is often used to chelate to transition metal complexes, as discussed in Section 1.2.3.1.

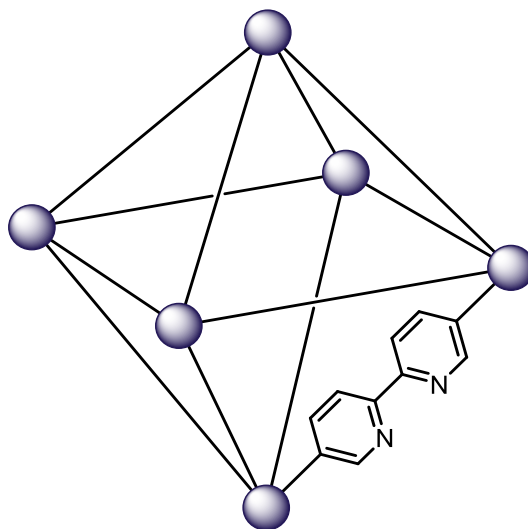
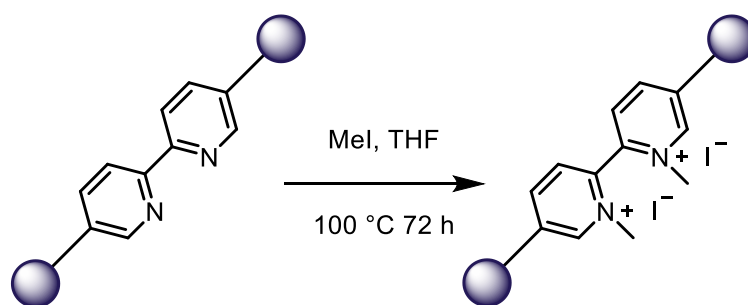


Figure 1.10. Schematic of the structure of UiO-67-bpy.

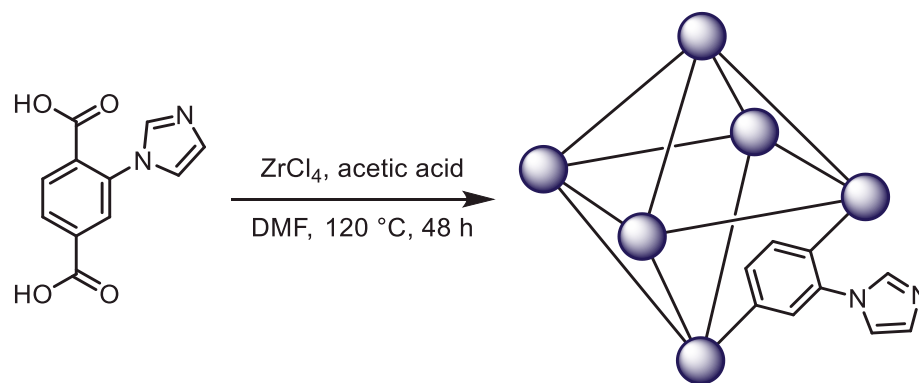
Compared with the number of anionic MOFs, the number of reported cationic MOFs is relatively low.^{67–69} In recent years, however, two cationic UiO-type MOFs have been reported that are prepared via postsynthetic modification of a UiO-type MOF containing a substituted linker.^{62,70}

In 2016, Xu *et al.* reported the quantitative quaternisation of the nitrogen sites in UiO-67-bpy with MeI to form a cationic support (UiO-67-bpy-Me) with iodide counter-ions in the pores (Scheme 1.5).⁶² After methylation, the BET surface area of the MOF dropped from 2306 m² g⁻¹ to 1104 m² g⁻¹, reflecting the increased congestion in the pores brought about by the newly introduced methyl groups and iodide counter-ions. The anionic dye methyl orange was taken up by ion exchange with the iodide counter-ions of the cationic framework. This postsynthetically modified MOF was shown to have increased light absorption and was used to catalyse methyl orange degradation under UV-Vis light irradiation.

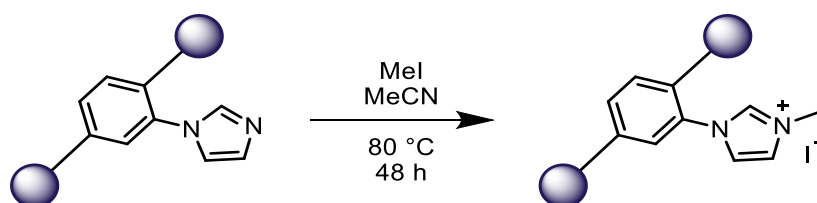


Scheme 1.5. Reported reaction of UiO-67-bpy with MeI.⁶²

In 2017, Liang *et al.* reported a novel UiO-66-type MOF (UiO-66-imb) composed of substituted linkers containing imidazole moieties, **H₂imbdc** (Scheme 1.6).⁷⁰ This MOF was postsynthetically modified with MeI to methylate 75% of the coordinatively unsaturated nitrogen sites on the imidazole moieties and generate a cationic MOF with iodide counter ions in the pores, UiO-66-imb-Me (Scheme 1.7). This material was shown to catalyse the cycloaddition of carbon dioxide with epoxides without a co-catalyst. An acid/base synergistic catalysis mechanism was proposed to explain this.



Scheme 1.6. Synthesis of UiO-66-imb from **H₂imbdc** and ZrCl_4 .⁷⁰



Scheme 1.7. Postsynthetic modification of UiO-66-imb to generate a cationic framework (UiO-66-imb-Me) via methylation of its pendant nitrogen sites.⁷⁰

1.2.2. Applications of metal-organic frameworks

Applications of MOFs are similar to those of other highly porous materials, such as activated carbon and zeolites. These include gas adsorption and separation, catalysis, and chemical purification.

The advantage of MOFs over other porous materials is their high tunability – careful selection of appropriate SBU and strut combinations generates MOFs with designer properties. This can result in a porous framework with the ideal pore size, window size and internal surface properties to preferentially adsorb specific gaseous molecules, or favour formation of one product of a chemical reaction over another, for example.

Selective gas adsorption in MOFs has been the subject of extensive review.^{71–75} In the interest of climate change prevention, CO₂ gas storage has attracted widespread interest

in recent years.^{71,72} MOFs are attractive media for the storage of CO₂ due to the ability to tune their properties to preferentially favour adsorption of these molecules over other atmospheric gases.

Storage of H₂ in MOFs has also been of widespread interest for similar environmental reasons⁷⁵ – hydrogen fuel is a promising candidate to replace dwindling fossil fuel reserves as it has a much higher energy density than traditional hydrocarbons and does not emit CO₂ upon burning.

Many MOFs are non-toxic and biodegradable, and this makes them attractive media to use in biomedicine.^{76,77} MOFs can exhibit therapeutic activity by direct incorporation of a bioactive molecule in their framework. Some MOFs can achieve very high loading capacities of therapeutic drugs compared with other carriers such as polymers or zeolites.⁷⁸

Heterogeneous catalysis was an early suggestion and example for an application of metal-organic frameworks.^{40,79} The large surface areas and uniform porosity of MOFs are also present in zeolites which are already ubiquitous in the field of heterogeneous catalysis.⁸⁰

It has been argued, however, that the comparisons with zeolites only serve to limit the potential of this burgeoning field of research.⁴ The possibility of incorporating multiple catalysts within a framework as well as designing environments that can determine a specific reactivity have led some to argue that catalytic MOFs could more closely resemble artificial enzymes, although the field of study has not yet reached this level of complexity. The use of metal-organic frameworks in catalysis is the subject of Section 1.2.3.

1.2.3. Metal-organic frameworks and catalysis

Metal-organic frameworks are particularly promising candidates for the heterogenisation of catalysts due to their crystallinity and porosity. The crystallinity of metal-organic frameworks is a desirable property as this allows for easier characterisation via crystallographic means, as well as a well-defined catalytic site for consistency and study. Porosity enables catalysts to be dispersed throughout the framework, rather than just on the surface, and allows for diffusion of reactants and products into and out of the framework. Metal-organic frameworks can also be tuned to enhance selectivity, for instance by designing pore and window sizes that will favour a certain product.

MOFs can incorporate catalytic behaviour in a number of ways; the as-synthesised MOF itself may be catalytic by virtue of its SBU or strut; it may be suitable for postsynthetic modification in order to incorporate a catalytic species via coordination to the strut; or the catalytic species may be encapsulated within the pores of a MOF. These latter two types of incorporation are discussed in Sections 1.2.3.1 and 1.2.3.2 respectively.

1.2.3.1. Covalent attachment

Three key methods have been employed to incorporate molecular catalysts into MOFs via covalent means; (i) direct solvothermal synthesis, in which a metalloligand such as those shown in Figure 1.11 is synthesised and used in the solvothermal synthesis of the MOF to incorporate a pre-coordinated metal complex; (ii) postsynthetic modification, in which a MOF with chelating sites is synthesised via the normal solvothermal procedure, and then reacted with a metal complex in solution which is incorporated into the framework via the coordination sites; and (iii) postsynthetic exchange, where an

unsubstituted MOF is synthesised, and then reacted with a metalloligand of the type shown in Figure 1.11 to exchange with its struts.

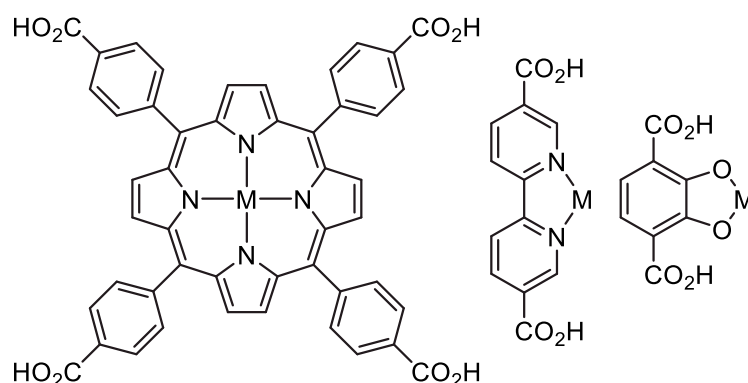


Figure 1.11. Examples of metalloligands commonly found in MOF literature.

The direct solvothermal synthesis method is desirable as a one-pot synthesis of catalytic MOFs, but the harsh conditions of the solvothermal process make this inappropriate for a number of more labile complexes that might not survive the procedure. Postsynthetic modification and postsynthetic exchange offer an alternative route that can avoid this problem by introducing the catalyst after the harsh solvothermal conditions that are necessary to synthesise the MOF.

UiO-67-bpy has been used as a solid support upon which to heterogenise transition metal catalysts. The bipyridyl moiety has been used extensively as a chelating coordination site to incorporate molecular catalysts, most notably by the groups of Cohen and Lin.^{54,59,63,64,66,81–97} Using this method, catalysts have been incorporated into the UiO-67-type framework that can be used for water oxidation, CO₂ reduction, and organic photocatalysis.

In an example relevant to this study, a flexible copper-based MOF was synthesised using the linker shown in Figure 1.12. The central sp³-hybridised carbon atom is highlighted to emphasise its hinged nature.⁹⁸

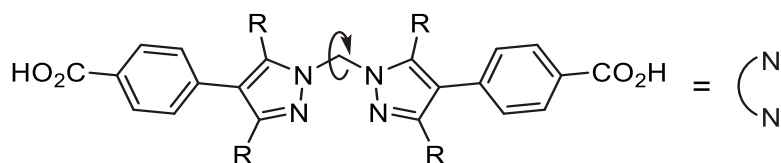
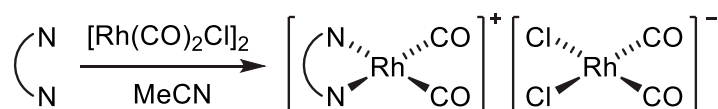


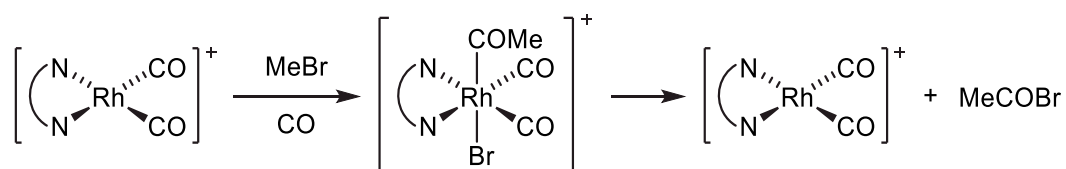
Figure 1.12. A hinged linker used to synthesise a structurally flexible MOF.⁹⁸ The linker is hereafter identified using the symbol on the left, emphasising the coordinatively unsaturated di-pyrazole nitrogen atoms.

The di-pyrazole nitrogen sites can act as soft electron pair donors, allowing them to be used as a chelating unit for postsynthetic metal binding.⁹⁹ This metalation step is quantitative, and the resultant MOF is often suitable for single crystal X-ray diffraction analysis. One such example is the reaction shown in Scheme 1.8 where a manganese(II)-based MOF containing the linker shown in Figure 1.12 was reacted with a rhodium carbonyl chloride dimer to form the ionic product shown.¹⁰⁰



Scheme 1.8. Reaction within the manganese(II) MOF between the di-pyrazole nitrogen sites and a rhodium precursor to form an ionic product.¹⁰⁰

The anionic rhodium complex was exchanged for a bromide anion, and the resultant MOF was found to be catalytically active for the carbonylation of methyl bromide. This was of significant interest as the carbonylation of methyl iodide is a key step in the production of acetic acid as discussed in Section 1.1.1. Upon reaction of this MOF with methyl iodide, the oxidative addition, methyl migration and carbon monoxide association steps from Scheme 1.1 were observed. The complex did not undergo reductive elimination, whereas the analogous reaction with methyl bromide underwent all the steps highlighted in Scheme 1.1, to give the reaction profile shown in Scheme 1.9.



Scheme 1.9. Reaction between rhodium-incorporated MOF, MeBr and CO. The MOF's bromide counter-ion is omitted for clarity.

1.2.3.2. Ionic encapsulation

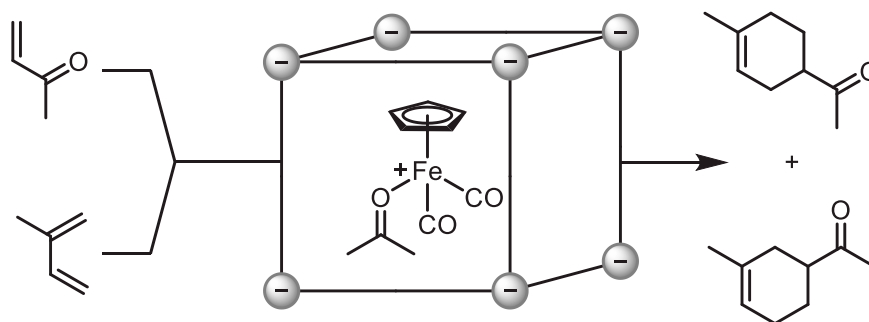
Covalent attachment of catalysts can require multiple synthetically challenging steps. Further, it fundamentally alters the chemical properties of the homogeneous catalyst that is being immobilised. This can affect the catalytic activity and selectivity compared to the solution phase. Because of this, simple encapsulation is increasingly being targeted as a means to heterogenise homogeneous catalysts, as this should, in principle, enable direct transfer of solution chemistry into the solid state.

Encapsulation as a strategy has its own inherent challenge however - a catalyst must be held firmly enough within the pores by non-covalent interactions not to leach into the reaction mixture upon turnover.

The first example of heterogenisation of ionic metal complexes within a metal-organic framework via electrostatic interactions was reported by Genna *et al.*¹⁰¹ A range of cationic complexes were exchanged for endogenous NH_2Me_2^+ in the pores of an anionic indium MOF, ZJU-28, or $[\text{H}_2\text{NMe}_2]_3[\text{In}_3(\text{BTC})_4]$ (where H_3BTC is benzene-1,3,5-tricarboxylic acid). In particular, MOF-supported $[\text{Rh}(\text{dppe})(\text{COD})]^+$ catalysed the hydrogenation of 1-octene to *n*-octane, with activity comparable with the homogeneous analogue and with retention of crystallinity of the MOF after catalysis.

Wang *et al.* reported another example shortly thereafter involving encapsulation of phosphotungstic acid anions ($[\text{PW}_{12}\text{O}_{40}]^{3-}$) in the mesopores of a chromium-based MOF decorated with amino groups (MIL-101-NH₂) via electrostatic interactions with the amino moieties.¹⁰² This system exhibited high catalytic activity in the extractive and catalytic oxidative desulfurisation system under mild conditions. It was also easy to recover and could be recycled several times without leaching or loss of activity.

Grigoropoulos *et al.* reported encapsulation of a cationic catalyst via direct exchange into an anionic indium MOF.¹⁰³ This catalyst was rigorously characterised and was shown to be active for the Diels-Alder reaction between isoprene and methyl vinyl ketone, as illustrated in Scheme 1.10.



Scheme 1.10. A cationic catalyst for the Diels-Alder reaction electrostatically immobilised in an anionic indium MOF.¹⁰³

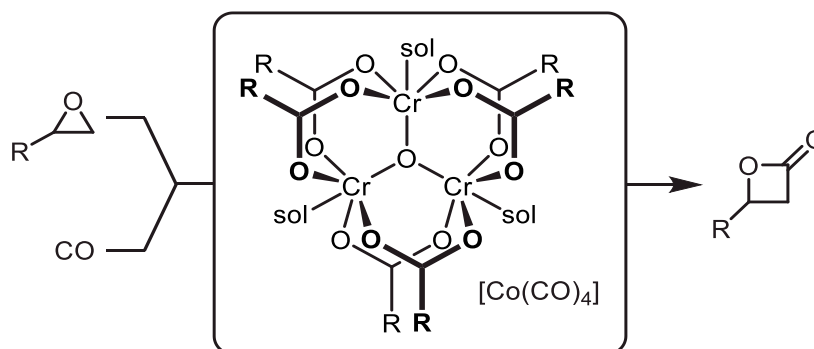
Grigoropoulos *et al.* later reported encapsulation of Crabtree's catalyst ($[\text{Ir}(\text{COD})(\text{PCy}_3)(\text{py})]^+$) in the pores of an anionic chromium-based MOF (MIL-101-SO₃) by cation exchange.¹⁰⁴ This supported complex was capable of hydrogenating non-functionalised alkenes under mild conditions, and it outperformed the homogeneous analogue, $[\text{Ir}(\text{COD})(\text{PCy}_3)(\text{py})][\text{BF}_4]$, in the hydrogenation of olefinic alcohols. Furthermore, encapsulation resulted in greater selectivity for hydrogenation by suppressing the competing isomerization reaction as a result of extended coordination

sphere interactions of the catalytic centre with the chemically functionalised internal surface of the MOF.

Another indium-based MOF (PCN-99) utilising an intentionally designed trigonal planar tritopic linker, 10,15-dihydro-5*H*-diindolo-[3,2-*a*:3',2'-*c*]carbazole-3,8,13-tricarboxylate (H₃DCTA), was used to immobilise the photocatalytic species [Ru(bpy)₃]²⁺ which was active for the aerobic hydroxylation of a range of arylboronic acids.¹⁰⁵

In 2016, Genna *et al.* reported a further study in the electrostatic immobilisation of catalysts within MOFs.¹⁰⁶ The authors once again used ZJU-28, a MOF with anionic nodes, and also a chromium based MOF with anionic linkers (MIL-101-SO₃). The two different types of MOFs, with anionic nodes and anionic linkers, could both be used to encapsulate cationic rhodium complexes, and both systems served as recyclable catalysts for hydrogenation of both terminal and internal alkenes, indicating either type of support could be used to encapsulate catalysts successfully.

The first example of the encapsulation of an anionic catalyst in the pores of a cationic MOF was reported by Leshkov *et al.* in which a chromium-based MOF (MIL-101) was treated with AlCl₃ in order to exchange the fluoride anions balancing the positive charge of the SBUs with more labile chloride anions.¹⁰⁷ This material was then treated with Na[Co(CO)₄] to exchange the chloride anions for [Co(CO)₄]⁻. This supported catalyst was active for the carbonylation of epoxides to form β -lactones (Scheme 1.11). Interestingly, the chromium ions in the framework had a synergistic effect on the catalysis by activating the epoxide, binding the oxygen via Lewis acidic interactions. This same system was later shown to be active for the subsequent carbonylation of β -lactones to form succinic anhydrides.¹⁰⁸



Scheme 1.11. MOF-supported catalytic epoxide carbonylation to form β -lactones.¹⁰⁷

More recently, Ma *et al.* have demonstrated the encapsulation of a trinuclear palladium complex into the pores of an anionic zinc-based MOF (bio-MOF 100) through postsynthetic cation exchange for NH_2Me_2^+ . This supported catalyst was active for the semihydrogenation of internal alkynes,¹⁰⁹ which could not be achieved with the heterogeneous analogue. This system demonstrated good recyclability.

Grela *et al.* also used the anionic chromium-based MOF, MIL-101- SO_3 , to immobilise a cationic olefin metathesis catalyst.¹¹⁰ A number of pharmaceutically relevant products were obtained in high yield and selectivity using this supported catalyst.

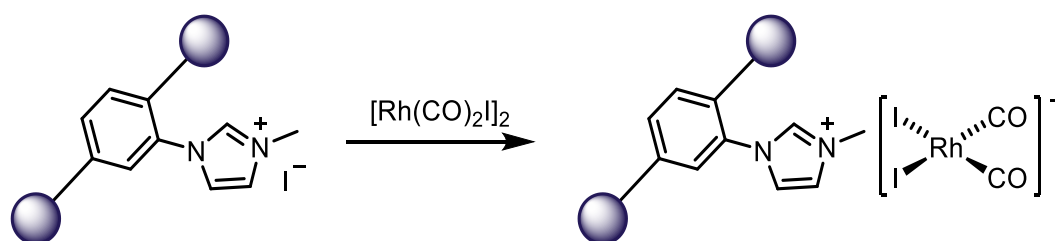
1.3. Project aims

As discussed in Section 1.1.2, heterogenisation of the carbonylation of methanol is desirable for a number of reasons including simplified catalyst recovery, higher catalyst loading capacity and formation of fewer by-products by virtue of the lower water content required.

Two key routes to heterogenisation of catalysts are covalent tethering and ionic immobilisation. Covalent tethering has often been found to lead to high levels of catalyst leaching due to the weak dative bonds employed, and this approach also necessitates alterations in the first coordination sphere of the catalyst. Ionic immobilisation, on the other hand, minimises leaching of the catalyst, and preserves its first coordination sphere, in principle leading to direct transfer of solution-phase chemistry into the solid state.

The overall aim of this thesis is to investigate the immobilisation of anionic carbonylation catalysts on cationic solid supports via Coulombic interactions.

The cationic UiO-type supports discussed in Section 1.2.1 will be used to incorporate the active catalyst in the Monsanto process for methanol carbonylation, $cis\text{-}[\text{Rh}(\text{CO})_2\text{I}_2]^-$, by reaction with a dimeric precursor, such as is shown in Scheme 1.12.



Scheme 1.12. Proposed incorporation of $cis\text{-}[\text{Rh}(\text{CO})_2\text{I}_2]^-$ on UiO-66-imb-Me.

Furthermore, a novel dispersible porous polymer system containing pyridine moieties (Figure 1.13) will be *N*-methylated to generate a cationic support. This will be used to support *cis*-[Rh(CO)₂I₂]⁻, as described previously.

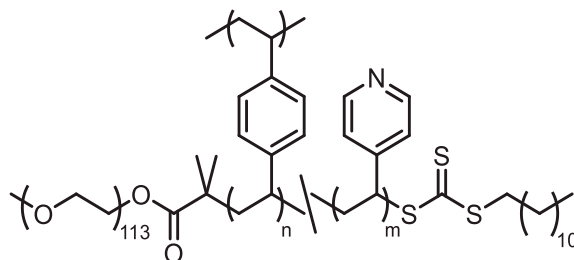


Figure 1.13. Pyridine-containing dispersible porous polymer system.

All of these systems will be extensively characterised, and the reactivity of the supported complexes investigated.

1.4. References

- 1 M. Bowker, *The Basis & Applications of Heterogeneous Catalysis*, Oxford University Press, Oxford, 1998.
- 2 A. E. C. Collis and I. T. Horváth, *Catal. Sci. Technol.*, 2011, **1**, 912–919.
- 3 S. C. Tang, T. E. Paxson and L. Kim, *J. Mol. Catal.*, 1980, **9**, 313–321.
- 4 J. Lee, O. K. Farha, J. Roberts, K. A. Scheidt, S. T. Nguyen and J. T. Hupp, *Chem. Soc. Rev.*, 2009, **38**, 1450–1459.
- 5 R. G. Schultz and P. D. Montgomery, *J. Catal.*, 1968, **13**, 105–106.
- 6 M. J. Howard, M. D. Jones, M. S. Roberts and S. A. Taylor, *Catal. Today*, 1993, **18**, 325–354.
- 7 R. P. Lowry and A. Aguilo, *Hydrocarb. Process.*, 1966, **53**, 103.
- 8 K. Weissermel and H.-J. Arpe, *Industrial Organic Chemistry*, Wiley-VCH, Weinheim, 5th edn., 2010.
- 9 F. E. Paulik and J. F. Roth, *Chem. Commun.*, 1968, **11**, 1578.
- 10 A. Haynes, *Adv. Catal.*, 2010, **53**, 1–45.
- 11 J. H. Jones, *Platin. Met. Rev.*, 2000, **44**, 94–105.
- 12 G. J. Sunley and D. J. Watson, *Catal. Today*, 2000, **58**, 293–307.
- 13 A. Haynes, B. E. Mann, G. E. Morris and P. M. Maitlis, *J. Am. Chem. Soc.*, 1993, **115**, 4093–4100.
- 14 B. Elvers, *Ullmann's Encyclopedia of Industrial Chemistry*, Wiley-VCH, Weinheim, 7th edn., 2011.
- 15 M. Asaro and P. Pavlechko, Acetic Acid by Chiyoda CT-ACETICA™ Process, <https://cdn.ihs.com/www/pdf/RW2018-01-toc.pdf>, accessed 15 May 2020.

-
- 16 A. W. Budiman, J. S. Nam, J. H. Park, R. I. Mukti, T. S. Chang, J. W. Bae and M. J. Choi, *Catal. Surv. from Asia*, 2016, **20**, 173–193.
- 17 N. Yoneda, T. Minami, J. Weiszmann and B. Spehlmann, *Stud. Surf. Sci. Catal.*, 1999, **121**, 93–98.
- 18 P. K. Saikia, P. P. Sarmah, B. J. Borah, L. Saikia and D. K. Dutta, *J. Mol. Catal. A Chem.*, 2016, **412**, 27–33.
- 19 J. S. Nam, A. Rong Kim, D. M. Kim, T. S. Chang, B. S. Kim and J. W. Bae, *Catal. Commun.*, 2017.
- 20 K. Park, S. Lim, J. H. Baik, H. Kim, K. D. Jung and S. Yoon, *Catal. Sci. Technol.*, 2018, **8**, 2894–2900.
- 21 A. Krzywicki and M. Marczewski, *J. Mol. Catal.*, 1979, **6**, 431–440.
- 22 G. A. Flores-Escamilla and J. C. Fierro-Gonzalez, *J. Mol. Catal. A Chem.*, 2012.
- 23 N. De Blasio, M. R. Wright, E. Tempesti, C. Mazzocchia and D. J. Cole-Hamilton, *J. Organomet. Chem.*, 1998, **551**, 229–234.
- 24 S. Bartsch, J. Falkowski and H. Hofmann, *Catal. Today*, 1989, **4**, 421–431.
- 25 L. D. Dingwall, A. F. Lee, J. M. Lynam, K. Wilson, L. Olivi, J. M. S. Deeley, S. Gaemers and G. J. Sunley, *ACS Catal.*, 2012, **2**, 1368–1376.
- 26 Y. Ni, L. Shi, H. Liu, W. Zhang, Y. Liu, W. Zhu and Z. Liu, *Catal. Sci. Technol.*, 2017, **7**, 4818–4822.
- 27 S. Lars, T. Andersson and M. S. Scurrall, *J. Mol. Catal.*, 1983, **18**, 375–380.
- 28 T. Yashima, Y. Orikasa, N. Takahashi and N. Hara, *J. Catal.*, 1979, **59**, 53–60.
- 29 S. Zhang, C. Guo, Q. Qian and G. Yuan, *Catal. Commun.*, 2008, **9**, 853–858.
- 30 N. De Blasio, E. Tempesti, A. Kaddouri, C. Mazzocchia and D. J. Cole-Hamilton, *J. Catal.*, 1998, **176**, 253–259.
- 31 Z. Ren, Y. Lyu, S. Feng, X. Song and Y. Ding, *Mol. Catal.*, 2017, **442**, 83–88.

- 32 F. Li, B. Chen, Z. Huang, T. Lu, Y. Yuan and G. Yuan, *Green Chem.*, 2013, **15**, 1600–1607.
- 33 R. J. Sowden, M. F. Sellin, N. De Blasio and D. J. Cole-Hamilton, *Chem. Commun*, 1999, 2511–2512.
- 34 M. S. Jarrell and B. C. Gates, *J. Catal.*, 1975, **40**, 255–267.
- 35 C. Baerlocher, L. B. McCusker and D. H. Olson, *Atlas of Zeolite Framework Types*, Elsevier Science Limited, New York, 6th edn., 2007.
- 36 T. Yashima, Y. Ushida, M. Ebisawa and N. Hara, *J. Catal.*, 1975, **36**, 320–326.
- 37 N. Yoneda, S. Kusano, M. Yasui, P. Pujado and S. Wilcher, *Appl. Catal. A Gen.*, 2001, **221**, 253–265.
- 38 Chiyoda Corporation, Chiyoda Licenses its Own Process Technology on Acetic Acid, https://www.chiyodacorp.com/media/file/pressrelease/2012/102301_e.pdf, accessed 8 March 2020.
- 39 A. Haynes, P. M. Maitlis, R. Quyoum, C. Pulling, H. Adams, S. E. Spey and R. W. Strange, *J. Chem. Soc., Dalton Trans.*, 2002, 2565–2572.
- 40 B. F. Hoskins and R. Robson, *J. Am. Chem. Soc.*, 1990, **112**, 1546–1554.
- 41 H. Furukawa, K. E. Cordova, M. O’Keeffe and O. M. Yaghi, *Science*, 2013, **341**, 974–987.
- 42 P. Z. Moghadam, A. Li, S. B. Wiggin, A. Tao, A. G. P. Maloney, P. A. Wood, S. C. Ward and D. Fairen-Jimenez, *Chem. Mater.*, 2017, **29**, 2618–2625.
- 43 N. L. Rosi, J. Eckert, M. Eddaoudi, D. T. Vodak, J. Kim, M. O’Keeffe and O. M. Yaghi, *Science*, 2003, **300**, 1127–1129.
- 44 S. S. Y. Chui, S. M. F. Lo, J. P. H. Charmant, A. G. Orpen and I. D. Williams, *Science*, 1999, **283**, 1148–1150.
- 45 J. R. Long and O. M. Yaghi, *Chem. Soc. Rev.*, 2009, **38**, 1213–1214.
- 46 J. H. Cavka, S. Jakobsen, U. Olsbye, N. Guillou, C. Lamberti, S. Bordiga, K. P.

-
- Lillerud, C. Lamberti, S. Bordiga and K. P. Lillerud, *J. Am. Chem. Soc.*, 2008, **130**, 13850–13851.
- 47 M. Kandiah, M. H. Nilsen, S. Usseglio, S. Jakobsen, U. Olsbye, M. Tilset, C. Larabi, E. A. Quadrelli, F. Bonino and K. P. Lillerud, *Chem. Mater.*, 2010, **22**, 6632–6640.
- 48 Y. Huang, W. Qin, Z. Li and Y. Li, *Dalton Trans.*, 2012, **41**, 9283–9285.
- 49 H. R. Abid, H. M. Ang and S. Wang, *Nanoscale*, 2012, **4**, 3089–3094.
- 50 M. C. Lawrence, C. Schneider and M. J. Katz, *Chem. Commun.*, 2016, **52**, 4971–4974.
- 51 M. J. Katz, Z. J. Brown, Y. J. Colón, P. W. Siu, K. a Scheidt, R. Q. Snurr, J. T. Hupp and O. K. Farha, *Chem. Commun.*, 2013, **49**, 9449–9451.
- 52 M. O’Keeffe, M. A. Peskov, S. J. Ramsden and O. M. Yaghi, *Accts. Chem. Res.*, 2008, **41**, 1782–1789.
- 53 S. R. Batten, N. R. Champness, X.-M. Chen, J. Garcia-Martinez, S. Kitagawa, L. Öhrström, M. O’Keeffe, M. Paik Suh and J. Reedijk, *Pure Appl. Chem.*, 2013, **85**, 1715–1724.
- 54 G. Nickerl, M. Leistner, S. Helten, V. Bon, I. Senkovska and S. Kaskel, *Inorg. Chem. Front.*, 2014, **1**, 325–440.
- 55 G. C. Shearer, S. Chavan, J. Ethiraj, J. G. Vitillo, S. Svelle, U. Olsbye, C. Lamberti, S. Bordiga and K. P. Lillerud, *Chem. Mater.*, 2014, **26**, 4068–4071.
- 56 Z. Hu, S. Faucher, Y. Zhuo, Y. Sun, S. Wang and D. Zhao, *Chem. - A Eur. J.*, 2015, **21**, 17246–17255.
- 57 G. C. Shearer, S. Chavan, S. Bordiga, S. Svelle, U. Olsbye and K. P. Lillerud, *Chem. Mater.*, 2016, **28**, 3749–3761.
- 58 A. Schaate, P. Roy, A. Godt, J. Lippke, F. Waltz, M. Wiebcke and P. Behrens, *Chem. - A Eur. J.*, 2011, **17**, 6643–6651.

- 59 H. Fei and S. M. Cohen, *Chem. Commun.*, 2014, **50**, 4810.
- 60 L. Li, S. Tang, C. Wang, X. Lv, M. Jiang, H. Wu and X. Zhao, *Chem. Commun.*, 2014, **50**, 2304–2307.
- 61 H. Wu, Y. S. Chua, V. Krungleviciute, M. Tyagi, P. Chen, T. Yildirim and W. Zhou, *J. Am. Chem. Soc.*, 2013, **135**, 10525–10532.
- 62 L. Xu, Y. Luo, L. Sun, S. Pu, M. Fang, R. Yuan and H. Du, *Dalton Trans.*, 2016, **45**, 8614–8621.
- 63 M. B. Chambers, X. Wang, N. Elgrishi, C. H. Hendon, A. Walsh, J. Bonnefoy, J. Canivet, E. A. Quadrelli, D. Farrusseng, C. Mellot-Draznieks and M. Fontecave, *ChemSusChem*, 2015, **8**, 603–608.
- 64 T. Toyao, M. Saito, S. Dohshi, K. Mochizuki, M. Iwata, H. Higashimura, Y. Horiuchi and M. Matsuoka, *Res. Chem. Intermed.*, 2016, **42**, 7679–7688.
- 65 Y. Yang, Q. Hu, Q. Zhang, K. Jiang, W. Lin, Y. Yang, Y. Cui and G. Qian, *Mol. Pharm.*, 2016, **13**, 2782–2786.
- 66 A. A. Barkhordarian and C. J. Kepert, *J. Mater. Chem. A*, 2017, **5**, 5612–5618.
- 67 S. R. Oliver, *Chem. Soc. Rev.*, 2009, **38**, 1868–1881.
- 68 C. Mao, R. A. Kudla, F. Zuo, X. Zhao, L. J. Mueller, X. Bu and P. Feng, *J. Am. Chem. Soc.*, 2014, **136**, 7579–7582.
- 69 X. Zhao, C. Mao, K. T. Luong, Q. Lin, Q. G. Zhai, P. Feng and X. Bu, *Angew. Chem. Int. Ed.*, 2016, **55**, 2768–2772.
- 70 J. Liang, R.-P. Chen, X.-Y. Wang, T.-T. Liu, X.-S. Wang, Y.-B. Huang and R. Cao, *Chem. Sci.*, 2017, **8**, 1570–1575.
- 71 K. Sumida, D. L. Rogow, J. A. Mason, T. M. McDonald, E. D. Bloch, Z. R. Herm, T. H. Bae, J. R. Long, Kenji Sumida, David L. Rogow, Jarad A. Mason, Thomas M. McDonald, Eric D. Bloch, Zoey R. Herm, Tae-Hyun Bae, Jeffrey R. Long, K. Sumida, D. L. Rogow, J. A. Mason, T. M. McDonald, E. D. Bloch, Z. R. Herm, T. H. Bae and J. R. Long, *Chem. Rev.*, 2012, **112**, 724–781.

-
- 72 S. D. Kenarsari, D. Yang, G. Jiang, S. Zhang, J. Wang, A. G. Russell, Q. Wei and M. Fan, *RSC Adv.*, 2013, **3**, 22739–22773.
- 73 J.-R. Li, R. J. Kuppler and H.-C. Zhou, *Chem. Soc. Rev.*, 2009, **38**, 1477–1504.
- 74 J.-R. Li, J. Sculley and H.-C. Zhou, *Chem. Rev.*, 2012, **112**, 869–932.
- 75 Myunghyun Paik Suh, Hye Jeong Park, Thazhe Kootteri Prasad, Dae-Woon Lim, M. P. Suh, H. J. Park, T. K. Prasad, D.-W. Lim, Myunghyun Paik Suh, Hye Jeong Park, Thazhe Kootteri Prasad and Dae-Woon Lim, *Chem. Rev.*, 2012, **112**, 782–835.
- 76 R. C. Huxford, J. Della Rocca and W. Lin, *Curr. Opin. Chem. Biol.*, 2010, **14**, 262–268.
- 77 P. Horcajada, C. Serre, G. Maurin, N. A. Ramsahye, F. Balas, M. Sebban, F. Taulelle, M. Vallet-Regi and G. Férey, *J. Am. Chem. Soc.*, 2008, **130**, 6774–6780.
- 78 P. Horcajada, C. Serre, M. Vallet-Regí, M. Sebban, F. Taulelle and G. Férey, *Angew. Chem. Int. Ed.*, 2006, **45**, 5974–5978.
- 79 M. Fujita, Y. J. Kwon, S. Washizu and K. Ogura, *J. Am. Chem. Soc.*, 1994, **116**, 1151–1152.
- 80 M. E. Davis, *Acc. Chem. Res.*, 1993, **26**, 111–115.
- 81 S. Diring, A. Carné-Sánchez, J. C. Zhang, S. Ikemura, C. Kim, H. Inaba, S. Kitagawa and S. Furukawa, *Chem. Sci.*, 2017, **8**, 2381–2386.
- 82 X. Li, R. Van Zeeland, R. V. Maligal-Ganesh, Y. Pei, G. Power, L. Stanley and W. Huang, *ACS Catal.*, 2016, **6**, 6324–6328.
- 83 K. Manna, T. Zhang, F. X. Greene and W. Lin, *J. Am. Chem. Soc.*, 2015, **137**, 2665–2673.
- 84 T. Zhang, K. Manna and W. Lin, *J. Am. Chem. Soc.*, 2016, **138**, 3241–3249.
- 85 W. A. Maza, A. J. Haring, S. R. Ahrenholtz, C. C. Epley, S. Y. Lin and A. J. Morris, *Chem. Sci.*, 2016, **7**, 719–727.

- 86 N. N. Yang, J. J. Fang, Q. Sui and E.-Q. Gao, *ACS Appl. Mater. Interfaces*, 2018, **10**, 2735–2744.
- 87 M. I. Gonzalez, E. D. Bloch, J. A. Mason, S. J. Teat and J. R. Long, *Inorg. Chem.*, 2015, **54**, 2995–3005.
- 88 M. I. Gonzalez, J. Oktawiec and J. R. Long, *Faraday Discuss.*, 2017, **201**, 351–367.
- 89 T. Kajiwara, M. Fujii, M. Tsujimoto, K. Kobayashi, M. Higuchi, K. Tanaka and S. Kitagawa, *Angew. Chem. Int. Ed.*, 2016, **55**, 2697–2700.
- 90 R. Van Zeeland, X. Li, W. Huang and L. M. Stanley, *RSC Adv.*, 2016, **6**, 56330–56334.
- 91 H. Fei, M. D. Sampson, Y. Lee, C. P. Kubiak and S. M. Cohen, *Inorg. Chem.*, 2015, **54**, 6821–6828.
- 92 K. Manna, T. Zhang and W. Lin, *J. Am. Chem. Soc.*, 2014, **136**, 6566–6569.
- 93 S. Øien, G. Agostini, S. Svelle, E. Borfecchia, K. A. Lomachenko, L. Mino, E. Gallo, S. Bordiga, U. Olsbye, K. P. Lillerud and C. Lamberti, *Chem. Mater.*, 2015, **27**, 1042–1056.
- 94 Y. Hong, J. Peng, Z. Sun, Z. Yu, A. Wang, Y. Wang, Y.-Y. Liu, F. Xu and L.-X. Sun, *Materials*, 2020, **13**, 829.
- 95 S. Demir, S. Usta, H. Tamar and M. Ulusoy, *Microporous Mesoporous Mater.*, 2017, **244**, 251–257.
- 96 P. Neves, A. C. Gomes, T. R. Amarante, F. A. A. Paz, M. Pillinger, I. S. Gonçalves and A. A. Valente, *Microporous Mesoporous Mater.*, 2015, **202**, 106–114.
- 97 B. An, L. Zeng, M. Jia, Z. Li, Z. Lin, Y. Song, Y. Zhou, J. Cheng, C. Wang and W. Lin, *J. Am. Chem. Soc.*, 2017, **139**, 17747–17750.
- 98 W. M. Bloch, C. J. Doonan and C. J. Sumby, *CrystEngComm*, 2013, **15**, 9663.
- 99 W. M. Bloch, A. Burgun, C. J. Coghlan, R. Lee, M. L. Coote, C. J. Doonan and C.

-
- J. Sumby, *Nat. Chem.*, 2014, **6**, 906–12.
- 100 A. Burgun, C. J. Coghlan, D. M. Huang, W. Chen, S. Horike, S. Kitagawa, J. F. Alvino, G. F. Metha, C. J. Sumby and C. J. Doonan, *Angew. Chem. Int. Ed.*, 2017, **56**, 8412–8416.
- 101 D. T. Genna, A. G. Wong-Foy, A. J. Matzger and M. S. Sanford, *J. Am. Chem. Soc.*, 2013, **135**, 10586–10589.
- 102 X. S. Wang, Y. B. Huang, Z. J. Lin and R. Cao, *Dalton Trans.*, 2014, **43**, 11950–11958.
- 103 A. Grigoropoulos, G. F. S. Whitehead, N. Perret, A. P. Katsoulidis, M. Chadwick, R. Davies, A. Haynes, L. Brammer, A. Weller, J. Xiao and M. J. Rosseinsky, *Chem. Sci.*, 2016, **7**, 2037–2050.
- 104 A. Grigoropoulos, A. I. McKay, A. P. Katsoulidis, R. P. Davies, A. Haynes, L. Brammer, J. Xiao, A. S. Weller and M. J. Rosseinsky, *Angew. Chem. Int. Ed.*, 2018, **130**, 4622–4627.
- 105 X. Wang, W. Lu, Z.-Y. Gu, Z. Wei and H.-C. Zhou, *Chem. Commun.*, 2016, **52**, 1926–1929.
- 106 D. T. Genna, L. Y. Pfund, D. C. Samblanet, A. G. Wong-Foy, A. J. Matzger and M. S. Sanford, *ACS Catal.*, 2016, **6**, 3569–3574.
- 107 H. D. Park, M. Dincă and Y. Román-Leshkov, *ACS Cent. Sci.*, 2017, **3**, 444–448.
- 108 H. D. Park, M. Dincă and Y. Román-Leshkov, *J. Am. Chem. Soc.*, 2018, **140**, 10669–10672.
- 109 J. Ren, P. C. Lan, M. Chen, W. Zhang and S. Ma, *Organometallics*, 2019, **38**, 3460–3465.
- 110 A. Chołuj, P. Krzesiński, A. Ruszczyńska, E. Bulska, A. Kajetanowicz and K. Grela, *Organometallics*, 2019, **38**, 3397–3405.

Chapter 2 UiO MOFs with Linkers Containing Pyridine Moieties

2.1. Introduction

As discussed in Chapter 1, a range of linear ditopic linkers can be employed in the synthesis of the UiO family of MOFs. These can differ in both length and functionality. One linker that has been extensively utilized in these systems is 2,2'-bipyridyl-5,5'-dicarboxylic acid (**H₂bpydc**).¹⁻⁷ The UiO-type MOF containing this linker, [Zr₆O₄(OH)₄(**bpydc**)₆] (known as UiO-67-bpy, shown in Figure 2.1), has received much attention in the literature due to the chelating ability of the bipyridyl motif, which has been employed to incorporate transition metals for applications in catalysis.

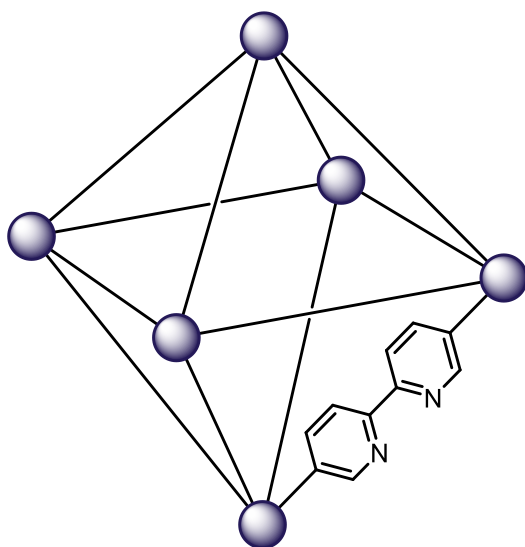


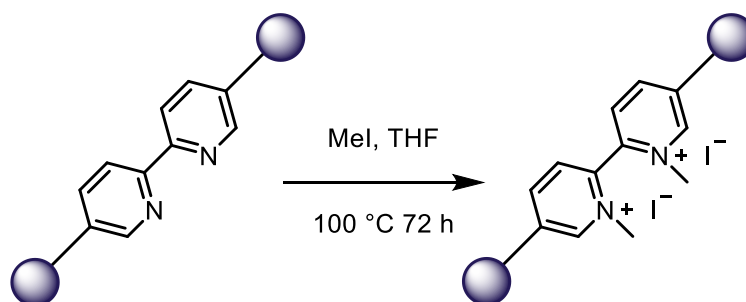
Figure 2.1. Schematic representation of UiO-67-bpy. The purple spheres represent [Zr₆(μ₃-O)₄(μ₃-OH)₄]¹²⁺ SBUs as shown in Figure 1.6.

UiO-67-bpy can also be postsynthetically modified via quaternisation of its nitrogen sites to form a cationic MOF. Several attempts to quaternise the nitrogen sites in UiO-67-bpy have been made.⁸⁻¹¹ Extent of quaternisation is usually quantified via the solution-phase ¹H NMR spectrum of the digested MOF. One study reported that stirring the neutral MOF with methyl trifluoromethanesulfonate (MeOTf) in CHCl₃ for 24 h resulted in 57% conversion of the neutral MOF to the cationic form.⁹ A further study found that extending

this reaction time to 48 h further increased the extent of quaternisation to > 70%.⁸ These approaches resulted in a mixture of neutral, mono-methylated, and di-methylated bipyridyl sites in the MOF.

Gao *et al.* employed a bifunctional quaternisation agent (ethylene ditrifluoromethanesulfonate) which proceeds via *N,N'*-dicycloalkylation to form the di-quaternised product. Reaction of UiO-67-bpy with ethylene ditrifluoromethanesulfonate in CHCl_3 for five hours resulted in 65% conversion of neutral sites into di-quaternised.^{10,11}

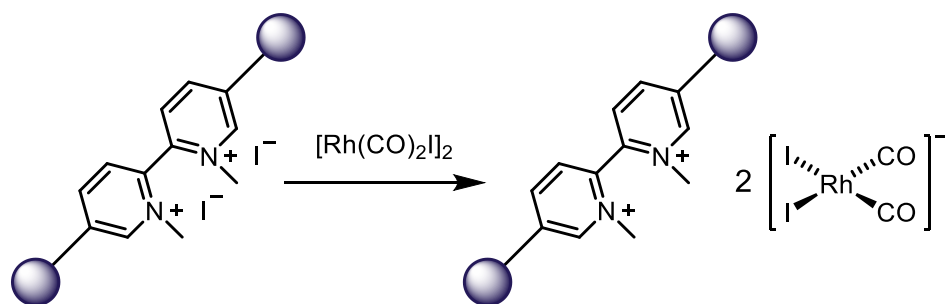
Du *et al.* reported full quaternisation of all nitrogen sites in UiO-67-bpy after reaction with MeI in THF for 72 h (Scheme 2.1).⁴ This was evidenced by ^1H NMR spectroscopy after digestion using HF.



Scheme 2.1. Reported reaction of UiO-67-bpy with methyl iodide.⁴

This work went on to demonstrate the versatility of the cationic MOF by performing a simple anion exchange of the iodide counterion for the dye methyl orange. This work provided an exciting prospect as compared with the number of anionic and neutral MOFs, very few cationic frameworks are known.

It was envisaged that the iodide counter ions in this framework could cleave a dimeric rhodium precursor and generate *cis*- $[\text{Rh}(\text{CO})_2\text{I}_2]^-$ *in situ*, as shown in Scheme 2.2.



Scheme 2.2. Proposed incorporation of Monsanto catalyst into cationic framework.

This chapter describes the synthesis of a range of pyridine-containing MOFs using the linkers shown in Figure 2.2, subsequent efforts to postsynthetically *N*-alkylate these moieties to generate a cationic MOF, and finally the attempted ionic encapsulation of *cis*- $[\text{Rh}(\text{CO})_2\text{I}]^-$ in their pores.

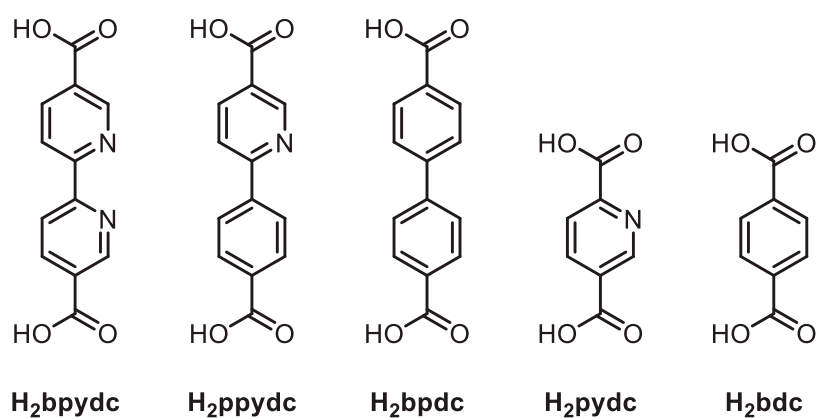


Figure 2.2. Range of dicarboxylic acids used in this chapter, and their abbreviations.

2.2. UiO-67-bpy

2.2.1. Synthesis and characterisation of UiO-67-bpy

The linker, 2,2'-bipyridyl-5,5'-dicarboxylic acid (**H₂bpydc**) was synthesised according to a literature procedure,¹² and its identity confirmed by ¹H NMR spectroscopy, mass spectrometry and elemental analysis.

[Zr₆O₄(OH)₄(**bpydc**)₆] (UiO-67-bpy) was synthesised via a modulated approach using 30 equivalents of benzoic acid to **H₂bpydc** to maximise crystallinity, in line with a reported procedure.¹³ The material was washed with methanol to remove unreacted starting materials and residual DMF from the pores, and the final MOF was activated from methanol by drying *in vacuo*, as reported previously.²

Successful synthesis of the crystalline framework was confirmed by powder X-ray diffraction, which showed good agreement with the simulated pattern based on the crystal structure of UiO-67 (Figure 2.3).¹ Further confirmation that UiO-67-bpy had been synthesised was provided via elemental and ICP-MS analyses. Confirmation of incorporation of **bpydc** linker into the framework was provided by digestion of the MOF in a solution of NaOD in D₂O, followed by characterisation using solution-phase ¹H NMR spectroscopy (Figure 2.4). There was no evidence of benzoic acid in the ¹H NMR spectrum, suggesting a low defect concentration in the final product.

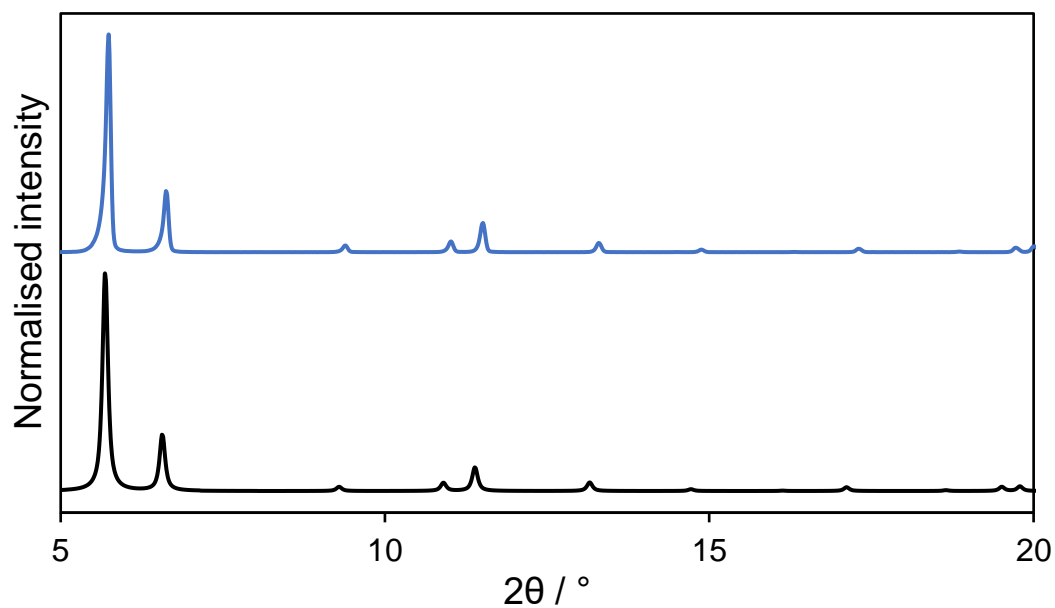


Figure 2.3. X-ray powder patterns of synthesised UiO-67-bpy (blue) and the simulated pattern based on the crystal structure of UiO-67 at 298 K (black).¹

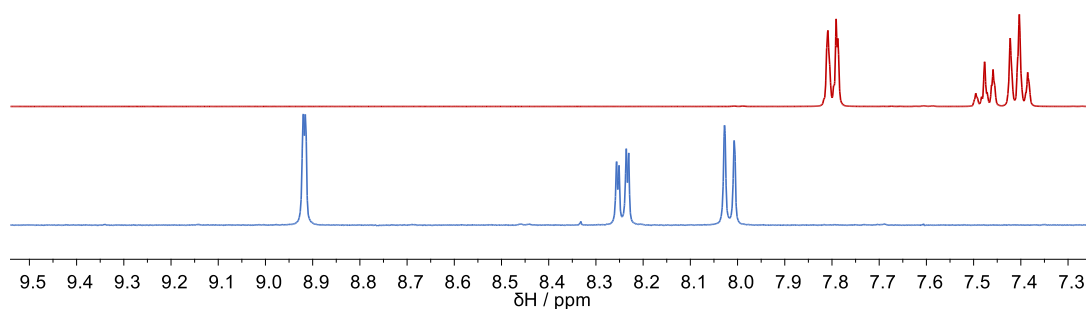


Figure 2.4. ¹H NMR spectra (aromatic region) of UiO-67-bpy digested in NaOD/D₂O (blue) and benzoic acid in NaOD/D₂O (red).

2.2.2. Quaternisation of UiO-67-bpy

2.2.2.1. Using methyl iodide

UiO-67-bpy was postsynthetically quaternised by incubation in a solvothermal vessel with a mixture of THF and MeI at 100 °C for 96 h. The extent of reaction was determined

by digestion using NaOD in D₂O, followed by measurement of a solution-phase ¹H NMR spectrum (Figure 2.5).

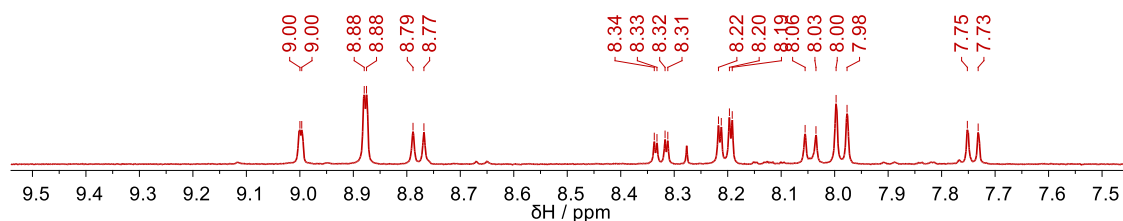


Figure 2.5. ¹H NMR spectrum (aromatic region) of product of reaction between UiO-67-bpy and MeI after 96 h (digested in NaOD/D₂O).

If the reaction had reached completion, three resonances would be observed in the aromatic region of the spectrum, with a singlet of triple their intensity at higher field representing the methyl groups. The spectrum shown in Figure 2.5 contains more resonances than can be accounted for purely by the di-methylated product, thus suggesting a mixture of products are present.

The possible products of the reaction between UiO-67-bpy and MeI are shown in Figure 2.6, namely; unreacted starting material (**A**); mono-quaternised product (**B**); and the desired di-quaternised product (**C**).

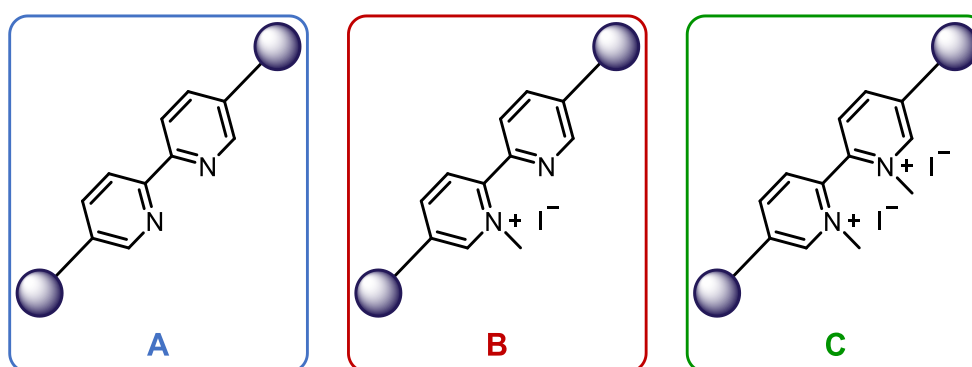


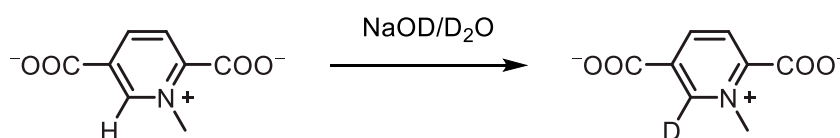
Figure 2.6. Possible products of the reaction of UiO-67-bpy with MeI.

Products **A** and **C** should each cause three resonances in the aromatic region of a ^1H NMR spectrum, whereas product **B** should cause six due to the asymmetry introduced by mono-methylation of the bipyridyl moiety.

In the spectra of the digested quaternisation products, resonances due to **A** can be identified by comparison with the starting material, UiO-67-bpy. The resonances due to **A** were identified as those at 7.99, 8.20 and 8.88 ppm in Figure 2.5 in this manner.

Resonances due to **B** and **C** can be differentiated using a ^1H - ^1H COSY NMR spectrum (Appendix 7.1) to identify which resonances in a mixture of products belong to the same species. The number of resonances correlated would indicate whether they were due to **B** or **C**. Five resonances were found to correspond to one another at 7.74, 8.05, 8.33, 8.78 and 9.00 ppm – these were assigned to product **B**.

When UiO-66-py (the mono-pyridine analogue to this system) is methylated, it has been found that the proximal hydrogen to the nitrogen readily exchanges with deuterium upon digestion in NaOD and D_2O (Scheme 2.3).⁷



Scheme 2.3. The exchange of an acidic proton for deuterium upon digestion of methylated UiO-66-py in NaOD/ D_2O .

An analogous reaction would explain the absence of a sixth resonance for product **B**, and indeed further experiments did show a sixth related resonance of varying intensity downfield from the other resonances (at 9.12 ppm), suggesting presence of a more acidic proton. The intensity of this resonance is presumed to be dependent on the length of time spent in solution before analysis.

There was no conclusive evidence of formation of product **C** from this reaction. Thus, all of the resonances observed in the ^1H NMR spectrum can be assigned (Figure 2.7).

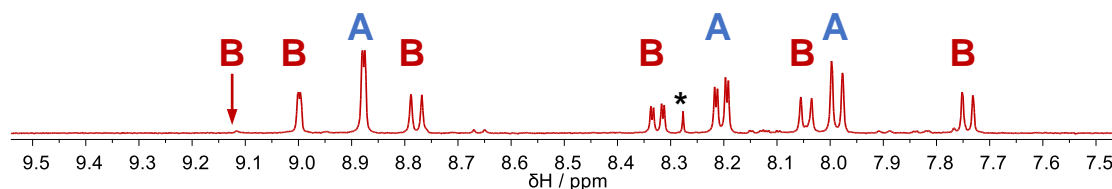


Figure 2.7. Assigned ^1H NMR spectrum (aromatic region) of product of reaction between UiO-67-bpy and MeI after 96 h (digested in NaOD/D₂O). The resonance marked with an asterisk is thought to be formic acid.

A sample of UiO-67-bpy was incubated with MeI, the ^1H NMR spectrum of the product in NaOD/D₂O was analysed, and then the remainder of the product was further incubated. In this way, the data in Table 2.1 were collected, which in turn was used to produce Figure 2.8, demonstrating the change in product composition over time.

Table 2.1. Relative intensities of ^1H NMR resonances at 8.88 ppm and 9.00 ppm over time, corresponding to products **A** and **B** respectively.

Incubation length / d	∫ at 8.88 ppm	∫ at 9.00 ppm
0	1.00	N/A
4	1.86	1.00
8	0.51	1.00
10	0.35	1.00
15	0.21	1.00

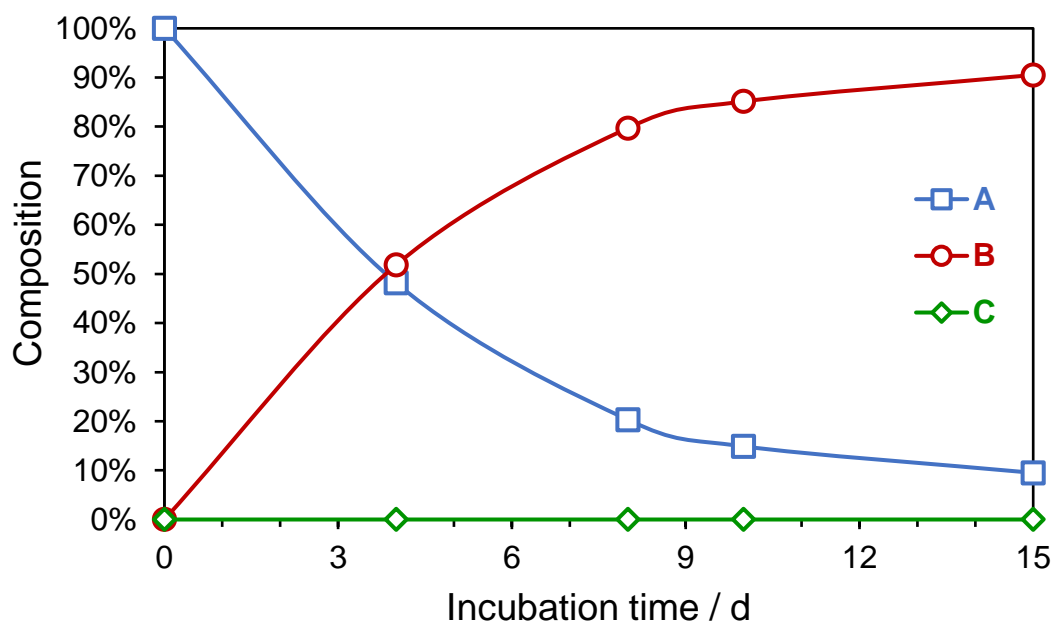


Figure 2.8. Relative amounts of products **A-C** after varying periods of incubation (after digestion in NaOD/D₂O).

Figure 2.8 shows how even after 15 days of incubation, some starting material (**A**) is still detectable, and there is no evidence for any formation of product **C**. Instead, the predominant component is **B**. This contrasts with the reported procedure, which indicated full conversion to product **C** after three days of incubation.⁴

It is possible that the method of digestion used could cause de-methylation to occur, and so in order to determine whether the procedure gave an accurate determination of the extent of quaternisation, a quaternised sample was digested using three different methods; NaOD in D₂O; D₃PO₄ in (CD₃)₂SO; and DCl in D₂O. The solution-phase ¹H NMR spectra of these mixtures were recorded, and the final product ratios calculated are shown in Figure 2.9. None of the ¹H NMR spectra showed any evidence for formation of product **C**, and all three are consistent in the ratio of products **A** and **B** that they indicate. The consistency between the three digestion methods suggests that the digestion conditions do not cause de-methylation.

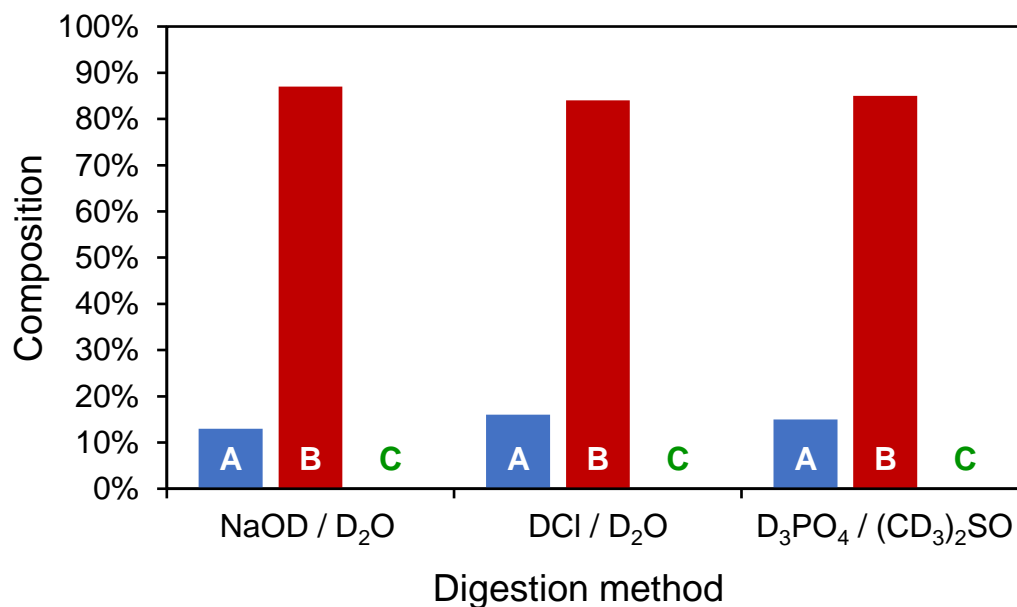


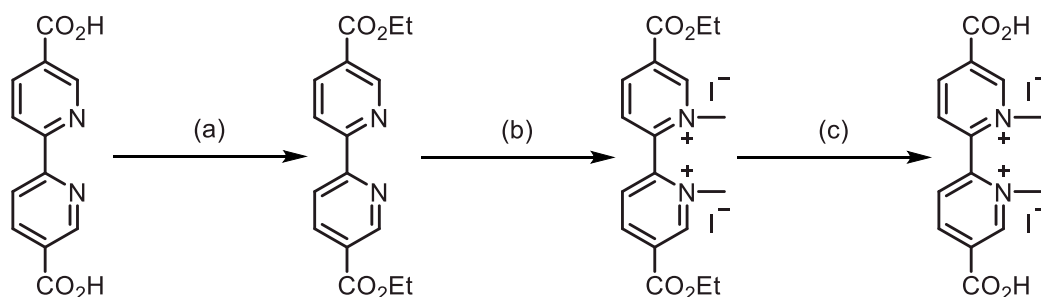
Figure 2.9. Relative amounts of products **A-C** (after 10 days of reaction) according to three different digestion methods.

Efforts were also made to quaternise the free linker, **H₂bpydc**, to determine whether this could be incorporated into the framework pre-quaternised. Several different methods were attempted, and these are listed in Table 2.2. Each method resulted in a similar ¹H NMR spectrum in (CD₃)₂SO, which indicated return of the starting material based on the lack of a resonance for any *N*-bound methyl groups.

Table 2.2. Methods employed to quaternise **H₂bpydc**.

Solvent	Method	Reaction time / h	Temperature / °C
Neat MeI	Reflux	16	45
EtOH / MeI	Reflux	16	70
Neat MeI	Solvothermal	100	120
THF / MeI	Solvothermal	100	120
MeCN / MeI	Solvothermal	60	100
MeCN / MeI	Microwave	0.5	140

Following a literature procedure for quaternisation of a similar linker,¹⁴ the acid groups on **H2bpydc** were protected via esterification prior to attempted quaternisation, and then re-acidified, as shown in Scheme 2.4.



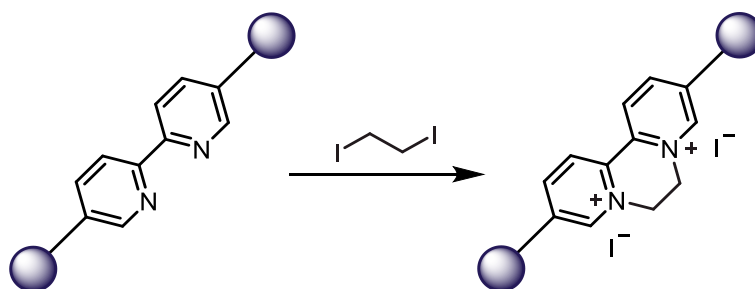
Scheme 2.4. Proposed quaternisation of **H2bpydc** via protection of carboxylic acid groups. (a) EtOH and DMF, SOCl₂ added dropwise, reflux 72 h, (b) MeCN and MeI reflux 24 h, (c) 6 M HCl reflux 16 h.

The product of the reaction shown in Scheme 2.4 was analysed via ¹H NMR spectroscopy in (CD₃)₂SO and mass spectrometry. This indicated a mixture of starting material with some (~40%) mono-quaternised product formed. None of the desired di-quaternised product was detected. Due to the lengthy nature of this method, further quaternisation via this route was ruled out.

2.2.2.2. Using 1,2-diiodoethane

In an effort to increase conversion to the fully quaternised form, 1,2-diiodoethane was proposed as an alternative quaternisation agent. Once one nitrogen site on the **bpydc** linker is quaternised there will be a high effective molarity on the remaining unquaternised nitrogen site, which should further favour formation of the diquaternised species. This approach has precedent in the literature, where ethylene ditrifluoromethanesulfonate has been used to quaternise UiO-67-bpy (albeit not to

complete conversion) as described in Section 2.1.¹¹ The proposed reaction is shown in Scheme 2.5.



Scheme 2.5. Proposed reaction between UiO-67-bpy and 1,2-diiodoethane.

The postsynthetic modification of UiO-67-bpy using 1,2-diiodoethane was attempted in MeCN using a solvothermal method involving incubation at 100 °C for 60 h. The product was digested using a solution of NaOD in D₂O and its ¹H NMR spectrum was recorded. The spectrum did not contain a resonance of double the intensity of the aromatic protons at higher field for a C₂H₄ moiety, which indicated that only starting material was returned.

2.2.3. Reaction between UiO-67-bpy-Me_{87%} and [Rh(CO)₂I]₂

A sample of partially (87%) mono-quaternised UiO-67-bpy was reacted with [Rh(CO)₂I]₂ in hexane for 24 h. The ATR-IR spectrum of the product contained two very weak $\nu(\text{CO})$ bands at 2066 cm⁻¹ and 1996 cm⁻¹ (Figure 2.10).

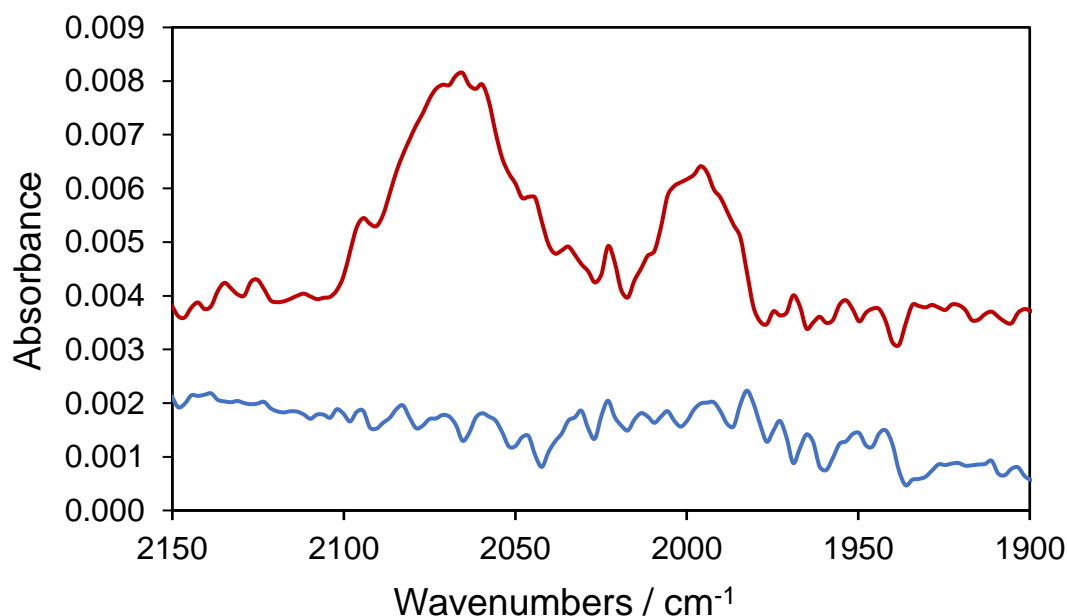
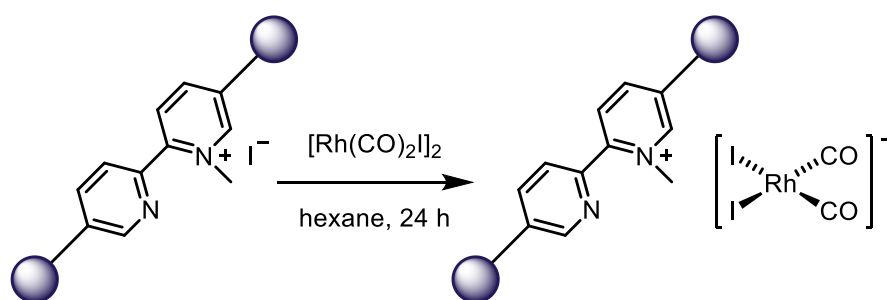


Figure 2.10. ATR-IR spectra of UiO-67-bpy-Me_{87%} (blue) and the product of the reaction of UiO-67-bpy-Me_{87%} with [Rh(CO)₂I]₂ in *n*-hexane for 24 h (red).

These two $\nu(\text{CO})$ absorptions are at a similar frequency to those for *cis*-[Rh(CO)₂I]₂⁻ in solution,¹⁵ which suggests that this species has been successfully encapsulated, presumably via the reaction shown in Scheme 2.6. The weak intensity of these bands, however, suggests minimal uptake of the complex into the framework.

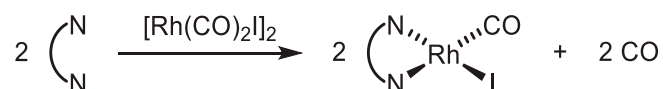


Scheme 2.6. Proposed reaction between UiO-67-bpy-Me_{87%} and [Rh(CO)₂I]₂.

2.2.4. Reaction between UiO-67-bpy and [Rh(CO)₂I]₂

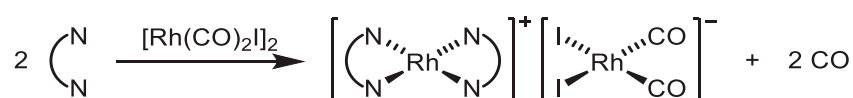
Given the presence of a potentially chelating moiety in the **bpydc** linkers in UiO-67-bpy, the reaction of neutral UiO-67-bpy with [Rh(CO)₂I]₂ was investigated.

Much research has been undertaken to investigate the effects of varying ligands on the active catalyst of the Monsanto process, including coordination to bipyridyl moieties as well as other diimine complexes – Scheme 2.7 shows a generalised reaction.^{16–18}



Scheme 2.7. General reaction for synthesising diimine-coordinated rhodium carbonyl complexes.

Some reactions, however, formed a cationic bis-chelated rhodium centre with *cis*-[Rh(CO)₂I₂][−] providing charge balance, as shown in Scheme 2.8.



Scheme 2.8. Route to ionic by-product formation.

As discussed in Section 1.2.3.1, this reactivity has been observed in a structurally flexible copper MOF, which employed the hinged diimine linker shown in Figure 2.11.¹⁹

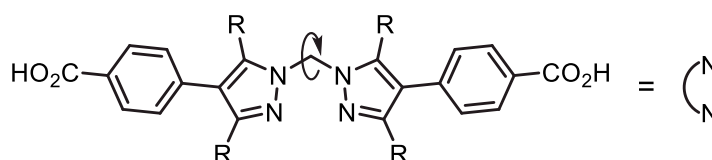
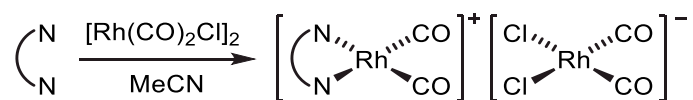


Figure 2.11. A hinged diimine-containing linker used to synthesise a structurally flexible MOF.¹⁹

This MOF was reacted with [Rh(CO)₂Cl]₂ which produced the ionic product shown in Scheme 2.9.²⁰



Scheme 2.9. Reaction between MOF containing diimine sites and $[\text{Rh}(\text{CO})_2\text{Cl}]_2$ to form ionic product.²⁰

The reaction of UiO-67-bpy with $[\text{Rh}(\text{CO})_2\text{I}]_2$ was carried out in hexane. The reaction reached completion after two hours. The ATR-IR spectrum of the product showed four $\nu(\text{CO})$ absorptions at 1998 cm^{-1} , 2036 cm^{-1} , 2063 cm^{-1} , and 2090 cm^{-1} (Figure 2.12).

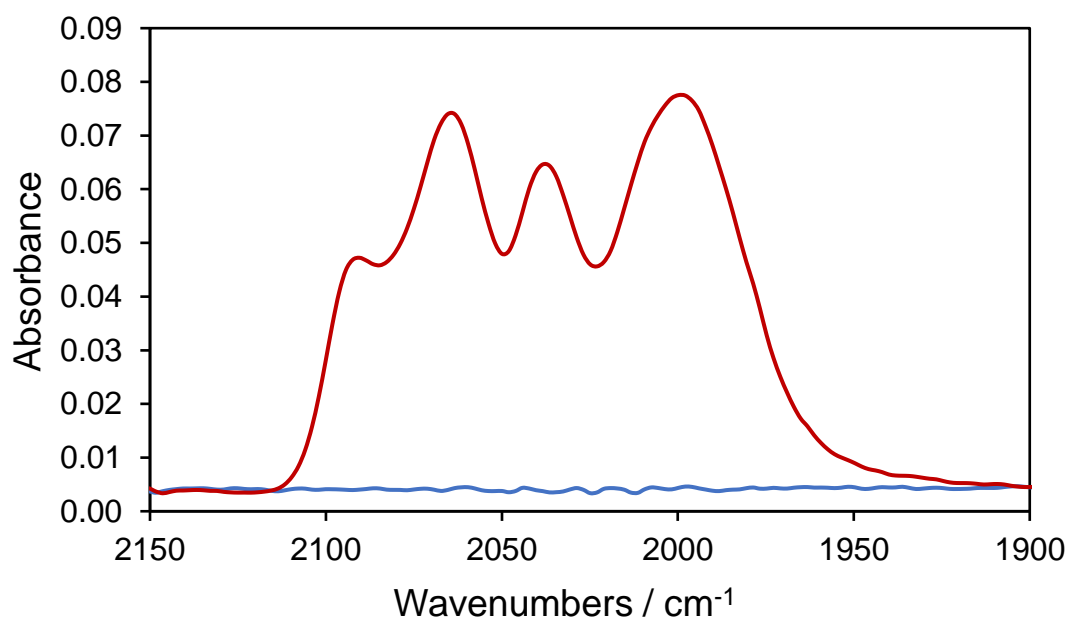
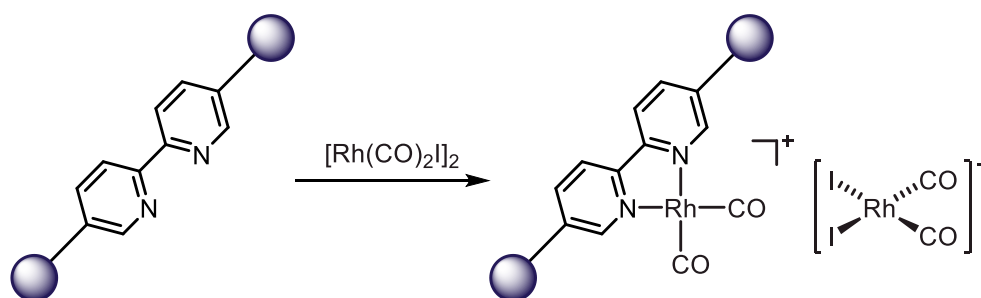


Figure 2.12. ATR-IR spectra ($\nu(\text{CO})$ region) of pristine UiO-67-bpy (blue) and the product of the reaction between UiO-67-bpy and $[\text{Rh}(\text{CO})_2\text{I}]_2$ after 2 hours (red).

The spectrum shown in Figure 2.12 shows four $\nu(\text{CO})$ absorptions and these can be interpreted as due to cationic and anionic Rh(I) dicarbonyl species, as shown in Scheme 2.10. The absorptions at 2090 cm^{-1} and 2036 cm^{-1} are assigned to the cationic species, as these are at a higher frequency due to weaker back-bonding from a less electron-rich metal centre. The absorptions at 2063 cm^{-1} and 1998 cm^{-1} are hence assigned to the

anionic complex, and these are similar to the same species in solution (and to the values reported in Section 2.2.3).¹⁵



Scheme 2.10. Proposed reaction between UiO-67-bpy and $[\text{Rh}(\text{CO})_2\text{I}]_2$.²⁰

The free ligand, **H**2**bpydc**, was reacted with $[\text{Rh}(\text{CO})_2\text{I}]_2$ in an analogous manner. The reaction was stopped after two hours and an ATR-IR spectrum of the product was recorded. This spectrum indicated minimal change from the starting material, and hence the complex was left to react for a further four days before another ATR-IR spectrum was recorded. This spectrum resembled that shown in Figure 2.12.

The slower reaction of **H**2**bpydc** with $[\text{Rh}(\text{CO})_2\text{I}]_2$ is surprising considering the diffusion limitations in the MOF. This observation is in accordance with the lack of reactivity of the free ligand towards methyl iodide discussed in Section 2.2.2.1.

2.2.5. Reaction of MeI with UiO-67-bpy-Rh

If the structure shown in Scheme 2.10 is correct, this would indicate presence of an electrostatically-bound *cis*- $[\text{Rh}(\text{CO})_2\text{I}]_2^-$ species in this MOF. Thus, the MOF was soaked in MeI, dried, and an ATR-IR spectrum was recorded (Figure 2.13).

There is significant overlap between the multiple absorptions present, but after soaking in MeI, the $\nu(\text{CO})$ band at 2065 cm^{-1} increases in intensity, whereas the band at 1998 cm^{-1} diminishes. The other bands at 2090 cm^{-1} and 2038 cm^{-1} merge with the larger absorption

at 2065 cm^{-1} . Furthermore, there is growth of an absorption at 1714 cm^{-1} which suggests formation of an acetyl ligand, and has good agreement with the acetyl $\nu(\text{CO})$ absorption of $[\text{Rh}(\text{CO})(\text{COMe})\text{I}_3]^-$ in solution.¹⁵

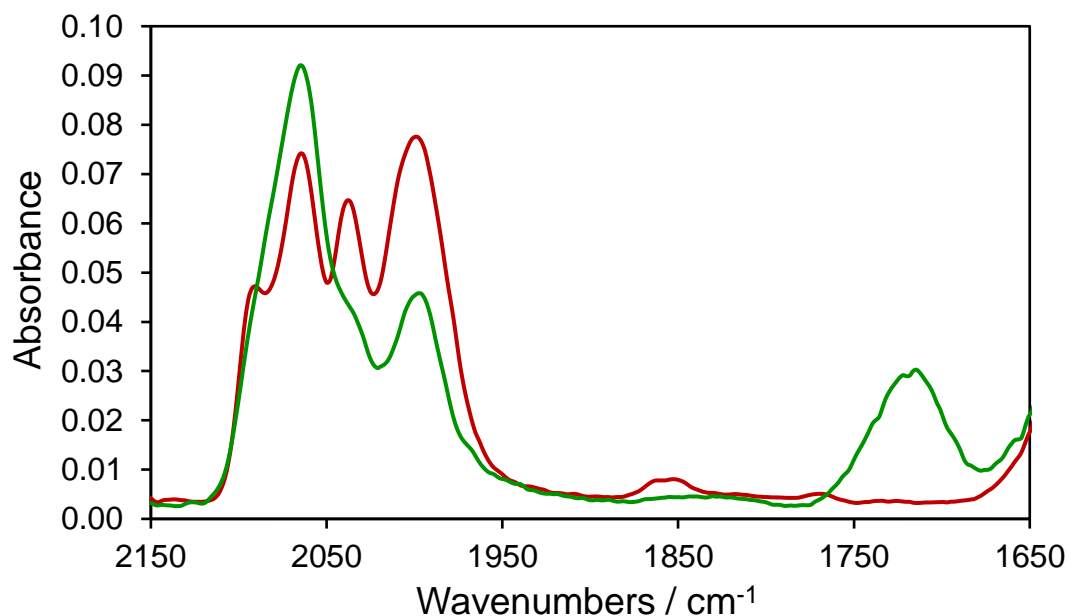
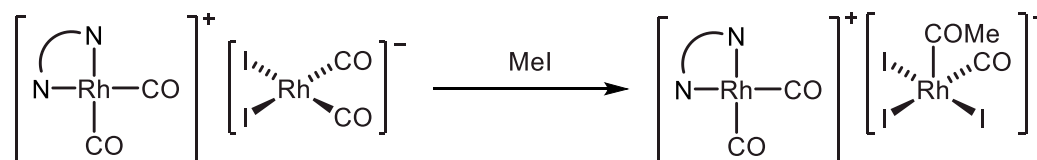


Figure 2.13. ATR-IR spectra ($\nu(\text{CO})$ region) of product of reaction between UiO-67-bpy and $[\text{Rh}(\text{CO})_2\text{I}]_2$ (red) and after this product was soaked in MeI for 6 d (green).

These observations suggest that the anionic species is undergoing oxidative addition and subsequent methyl migration as shown in Scheme 2.11.



Scheme 2.11. Proposed reaction between UiO-67-bpy-Rh and MeI.

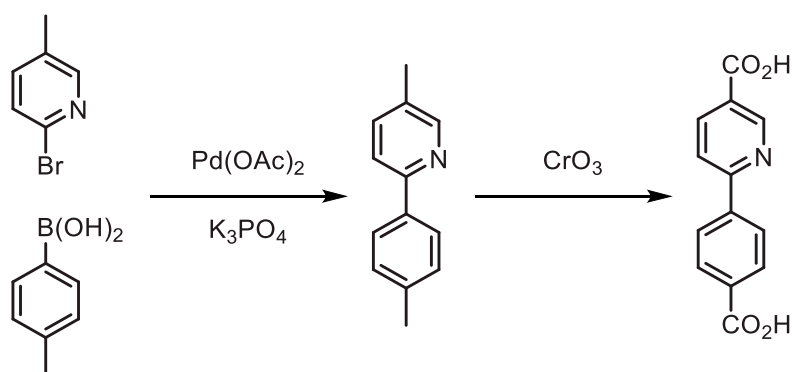
The higher reactivity of the anionic species is what would be expected if the oxidative addition of MeI were to follow the previously postulated $\text{S}_{\text{N}}2$ -type mechanism.²¹

The IR spectrum for the product of the reaction between neutral UiO-67-bpy and $[\text{Rh}(\text{CO})_2\text{I}]_2$ (Figure 2.12) highlights the need for all nitrogen sites in the **bpydc** linker to have been methylated, otherwise the reaction shown in Scheme 2.10 will also occur on exposure to $[\text{Rh}(\text{CO})_2\text{I}]_2$. The presence of cationic chelated $\text{Rh}(\text{CO})_2$ species partially obscures the IR absorptions of the electrostatically bound anionic complexes.

2.3. UiO-67-bp/ppy

2.3.1. Synthesis and characterisation of UiO-67-bp/ppy

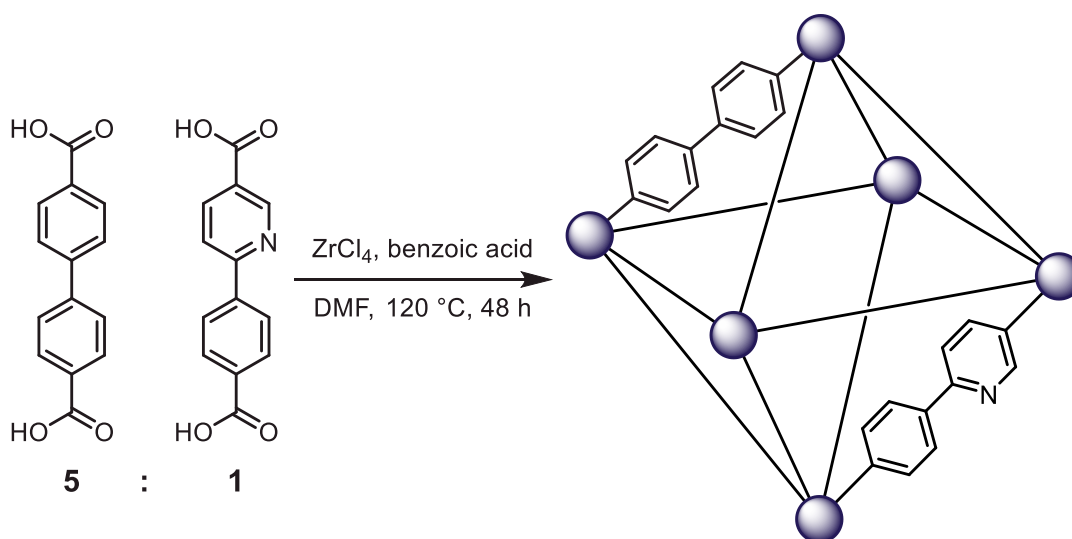
Due to the difficulty in achieving full quaternisation of the **ppydc** moiety in UiO-67-bpy, it was decided that a linker with a single nitrogen site should be investigated. A search of the literature found a preparative procedure for 2-phenylpyridine-5,4'-dicarboxylic acid (**H₂ppydc**), as shown in Scheme 2.12.²² A coupling reaction was performed between 2-bromo-5-methylpyridine and *p*-tolylboronic acid to form 5,4'-dimethyl-2-phenylpyridine. This was then oxidised using CrO₃ to form the dicarboxylic acid product, **H₂ppydc**. The obtained product was analysed by ¹H NMR spectroscopy, mass spectrometry and elemental analysis. This linker can directly substitute for **H₂ppydc** in the synthesis reported in Section 2.2.1 to form an isorecticular MOF with a single nitrogen site per linker.²³



Scheme 2.12. Synthetic route toward 2-phenylpyridine-5,4'-dicarboxylic acid (**H₂ppydc**).

It was decided that a mixed-linker approach would be taken, which would minimise steric hindrance in the pores upon quaternisation, thus potentially leading to a higher extent of conversion to the cationic form. A 1:5 ratio of **H₂ppydc** to biphenyl-4,4'-dicarboxylic

acid (**H₂bpdc**) was employed as this ratio would lead to one **ppydc** linker per zirconium cluster on average (Scheme 2.13).



Scheme 2.13. Synthesis of mixed-linker UiO-67-bp/ppy.

Successful synthesis of crystalline UiO-67-type MOF was confirmed via powder X-ray diffraction (Figure 2.14), which agreed with the simulated pattern of UiO-67.¹

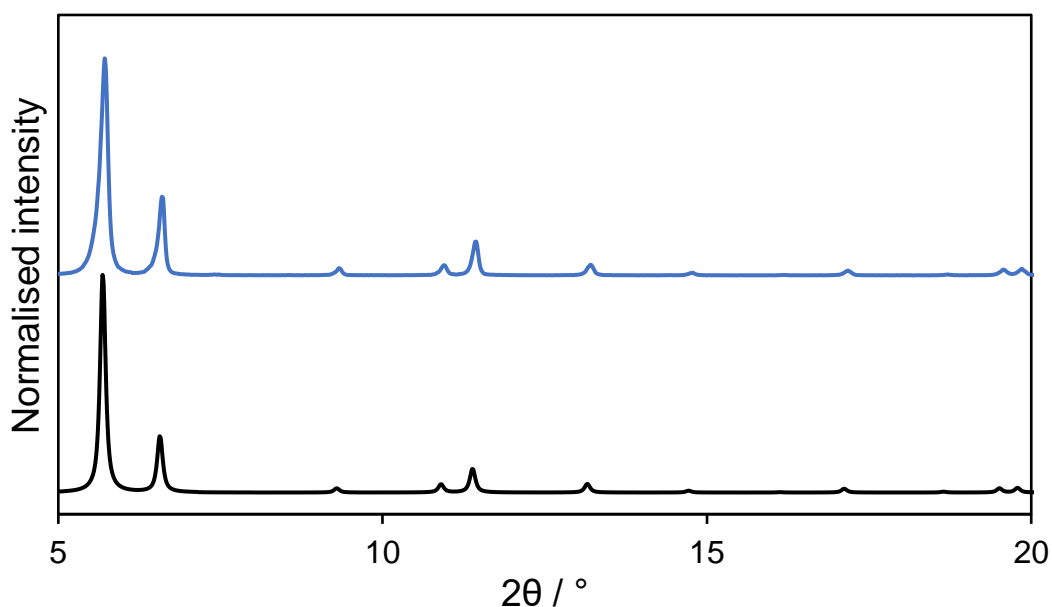


Figure 2.14. X-ray powder patterns of synthesised UiO-67-bp/ppy (blue) and the simulated pattern based on the crystal structure of UiO-67 at 298 K (black).¹

The sample was digested in a solution of NaOD in D₂O and a solution-phase ¹H NMR spectrum was recorded, which was used to determine the final linker ratios. The linker **bpdc** displays resonances at 7.60 and 7.81 ppm in this solvent mixture (corresponding to four aromatic protons each), whereas **ppydc** contains resonances at 8.16 and 8.85 ppm (corresponding to one aromatic proton each), and an overlapping multiplet at 7.80 ppm corresponding to the remaining five aromatic protons. The relative intensities for the resonances at 8.16 ppm and 7.60 ppm were 1.00 and 15.20 respectively. This indicated the relative abundance of **ppydc** to **bpdc** in the MOF as 1:3.8, giving the final formula as [Zr₆O₄(OH)₄(**bpdc**)_{4.75}(**ppydc**)_{1.25}] (UiO-67-bp/ppy). As observed for UiO-67-bpy in Section 2.2.1, there was no evidence of residual benzoic acid in the ¹H NMR spectrum.

The deviation of these values from the 1:5 ratio used in the reaction mixture is likely due to differing p*K*_a values between **H₂ppydc** and **H₂bpdc** affecting their relative rates of reaction. An alternate explanation is that these linkers have differing solubility, and so the effective concentration in solution could be different from that added to the reaction vessel.

The elemental analysis values for this MOF vary quite significantly from those expected, with a much lower carbon content than suggested by the formula (37.4% vs. 46.8%). This could be due to protonation of the nitrogen site on **ppydc** under the acidic synthesis conditions leading to incorporation of heavy counter-ions such as chloride (from ZrCl₄). In any case, the proposed formula for UiO-67-bp/ppy should be treated with some caution.

2.3.2. Quaternisation of UiO-67-bp/ppy

2.3.2.1. Reflux method with methyl iodide

The mixed-linker UiO-67-bp/ppy MOF was refluxed with MeI in CHCl_3 to methylate the nitrogen sites present in the MOF in a manner analogous to that discussed in Section 2.2.2.1. The extent of quaternisation was determined by digestion in a mixture of D_3PO_4 and $(\text{CD}_3)_2\text{SO}$, followed by recording the ^1H NMR spectrum of the solution. In the ^1H NMR spectrum of the digested product, the aromatic resonances due to the neutral and quaternised linkers were overlapping. Therefore in order to calculate extent of quaternisation, one of the combined aromatic resonances (at 8.85 ppm) was compared with the *N*-methyl resonance (at 4.09 ppm). After three days of reaction, analysis of the ^1H NMR spectrum indicated that only 51% of nitrogen sites had been quaternised. The reaction time was extended to see what effect this would have on the quaternisation extent and the results are shown in Table 2.3.

Table 2.3. Calculated extent of quaternisation for different reaction times.

Reaction time / d	\int at 8.85 ppm	\int at 4.09 ppm	Extent of quaternisation
3	1.00	1.54	51%
7	1.00	1.83	61%
14	1.00	2.20	73%

These data show that extent of quaternisation increases with reaction time, but with diminishing returns. These long reaction times indicate that reaching 100% quaternisation may be impracticable via this method. Lengthening the reaction time also seems to have an adverse effect on the crystallinity of the samples, as the powder patterns show a decrease in the intensity of the reflections on increasing the reaction time (Figure 2.15).

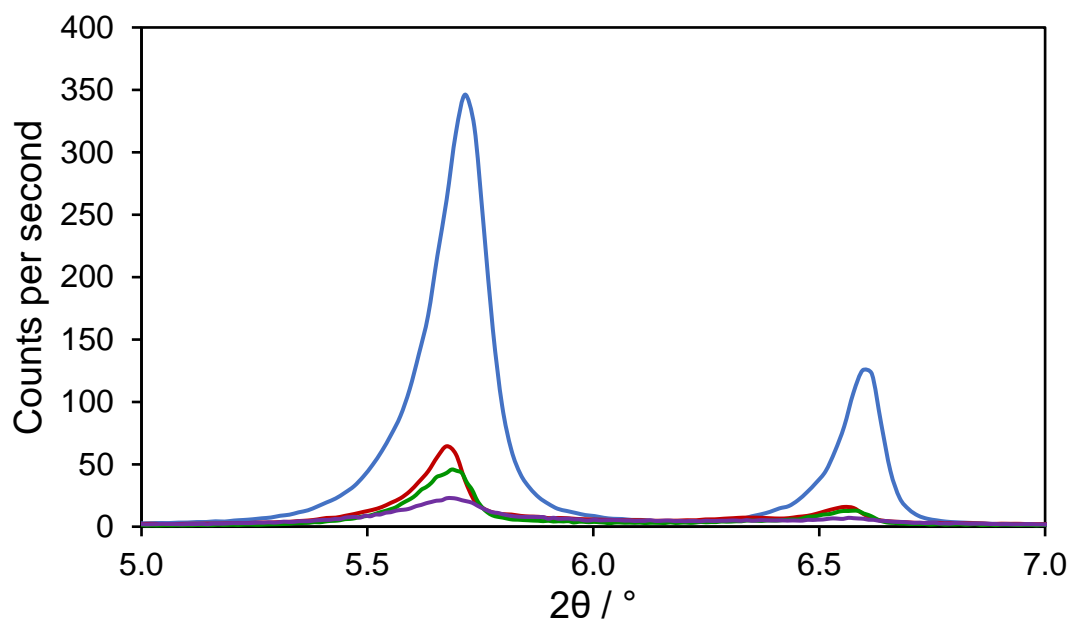


Figure 2.15. X-ray powder patterns of UiO-67-bp/ppy after varying lengths of reaction; starting material (blue); 3 days' (red); 7 days' (green); and after 14 days' reaction (purple).

2.3.2.2. Microwave method with methyl iodide

Microwave heating has been used previously to achieve high levels of quaternisation in a fraction of the time required by conventional heating methods.²⁴ Neutral UiO-67-bp/ppy was placed in a microwave tube and dry MeCN and MeI were added. This was heated in a microwave reactor at 120 °C for one hour, generating a pressure of 6 bar during reaction.

The product was digested in a mixture of D_3PO_4 and $(CD_3)_2SO$ and analysed via solution-phase 1H NMR spectroscopy which revealed a quaternisation extent of 60%. This highlights the utility of microwave heating for quaternisation reactions, as this extent of quaternisation took 7 days to attain via conventional heating (see Section 2.3.2.1).

The powder X-ray diffraction pattern of the product of this reaction is shown in Figure 2.16. This pattern suggested loss of crystallinity of the sample during the harsh reaction conditions employed.

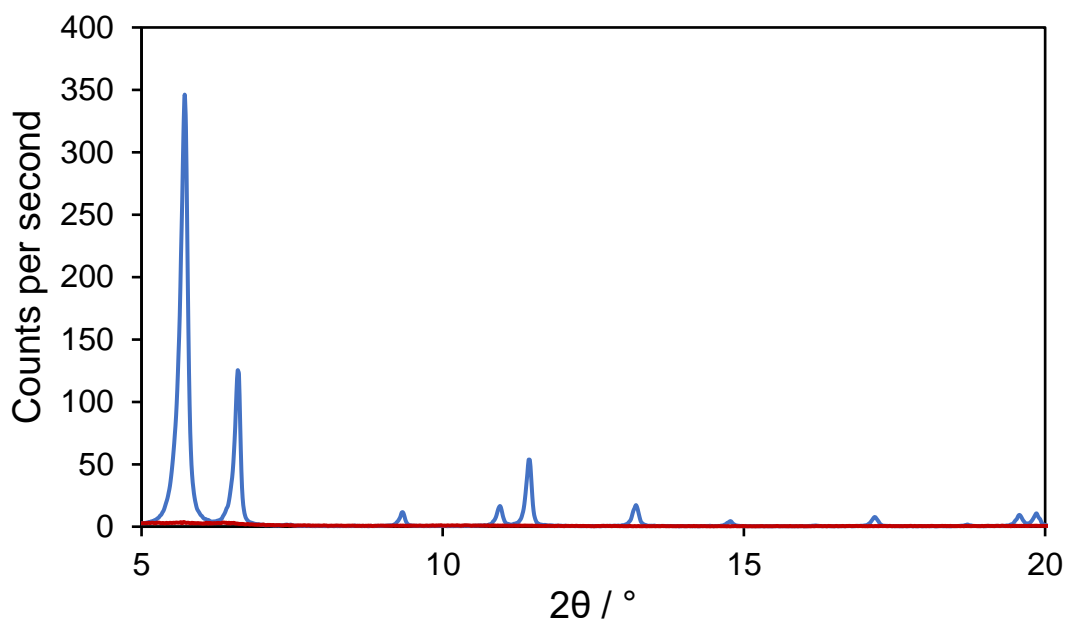


Figure 2.16. X-ray powder patterns of neutral UiO-67-bp/ppy (blue) and product of microwave quaternisation reaction (red).

2.3.2.3. Reflux method using trimethyloxonium tetrafluoroborate

In an effort to reach a higher extent of quaternisation, a stronger methylating agent was employed. In previous attempts, methyl iodide had been used, but this was replaced with $[\text{Me}_3\text{O}][\text{BF}_4]$ for this synthesis.

The mixture of neutral UiO-67-bp/ppy and $[\text{Me}_3\text{O}][\text{BF}_4]$ in dry CHCl_3 was heated to reflux for three days and the product of this reaction was digested in a mixture of D_3PO_4 and $(\text{CD}_3)_2\text{SO}$ and analysed via ^1H NMR spectroscopy. This analysis revealed a quaternisation extent of 85%, which compared favourably with the MeI quaternisation (51%) over the same period.

The X-ray powder pattern of the product was recorded and is shown in Figure 2.17. This indicated degradation of the crystalline framework, and the new powder pattern more closely resembled that of the linker, **H₂ppydc**.

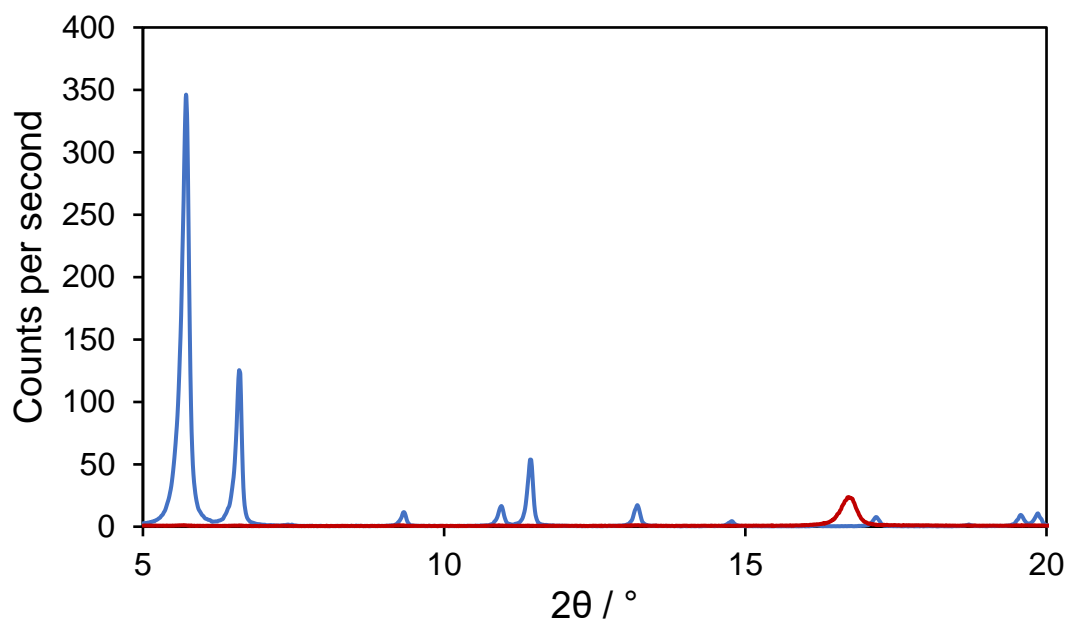


Figure 2.17. X-ray powder patterns of neutral UiO-67-bp/ppy (blue) and product of reaction with $[\text{Me}_3\text{O}][\text{BF}_4]$ (red).

2.3.3. Reaction of UiO-67-bp/ppy-Me samples with $[\text{Rh}(\text{CO})_2\text{I}]_2$

It was judged that the systems partially quaternised via conventional heating with MeI would be good candidates for reaction with $[\text{Rh}(\text{CO})_2\text{I}]_2$ as they did not contain the chelating unit present in the **bpdc** moiety explored in Section 2.2.4. The neutral MOF as well as the three quaternised MOFs were reacted with $[\text{Rh}(\text{CO})_2\text{I}]_2$ in dry hexane, followed by washing in more dry hexane, and finally drying. The ATR-IR spectra of the products were recorded, and the resultant $\nu(\text{CO})$ absorptions are reported in Table 2.4.

Table 2.4. The $\nu(\text{CO})$ absorptions in the ATR-IR spectra of various samples upon reaction with $[\text{Rh}(\text{CO})_2\text{I}]_2$, as well as the literature $\nu(\text{CO})$ values for $\text{cis-}[\text{Rh}(\text{CO})_2\text{I}_2]^-$ in MeOH.¹⁵

Sample	Asymmetric $\nu(\text{CO}) / \text{cm}^{-1}$	Symmetric $\nu(\text{CO}) / \text{cm}^{-1}$
$\text{cis-}[\text{Rh}(\text{CO})_2\text{I}_2]^-$	1990	2060
UiO-67-bp/ppy	2000	2077
UiO-67-bp/ppy-Me _{51%}	1998	2076
UiO-67-bp/ppy-Me _{61%}	1994	2070
UiO-67-bp/ppy-Me _{73%}	N/A	N/A

All of the samples investigated indicate formation of *cis*-dicarbonyl species. The $\nu(\text{CO})$ bands of the product of the reaction between UiO-67-bp/ppy and $[\text{Rh}(\text{CO})_2\text{I}]_2$ come at higher wavenumber than those for $\text{cis-}[\text{Rh}(\text{CO})_2\text{I}_2]^-$ in solution.¹⁵ This could indicate a neutral rhodium dicarbonyl species (Figure 2.18).

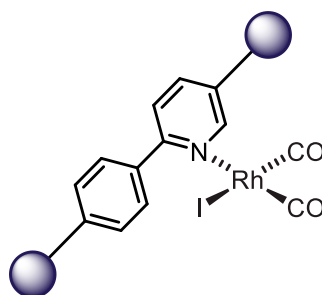


Figure 2.18. Proposed covalently tethered neutral rhodium dicarbonyl species.

The reaction of the 51% and 61% quaternised samples produced $\nu(\text{CO})$ absorptions that came between those for $\text{cis-}[\text{Rh}(\text{CO})_2\text{I}_2]^-$ in solution and the product of the reaction between neutral UiO-67-bp/ppy and $[\text{Rh}(\text{CO})_2\text{I}]_2$. This could be due to a mixture of covalently bound and electrostatically incorporated species being present. The $\nu(\text{CO})$ bands of the product of UiO-67-bp/ppy-Me_{61%} come at lower wavenumber than those for

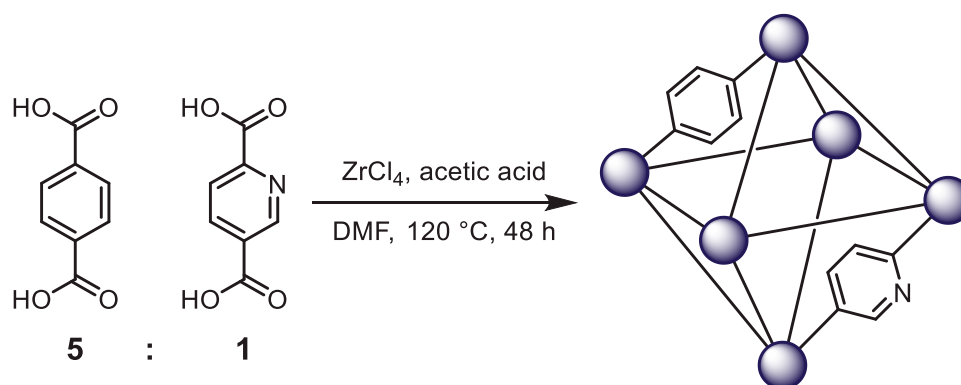
UiO-67-bp/ppy-Me_{51%}, which would be expected if a mixture of species is present in both cases.

The product of the reaction of the 73% quaternised MOF failed to display any discernible $\nu(\text{CO})$ bands in its ATR-IR spectrum.

2.4. UiO-66-b/py

2.4.1. Synthesis and characterisation of UiO-66-b/py

A mixed-linker approach was used to synthesise UiO-66-b/py which employed a 1:5 ratio of 2,5-pyridinedicarboxylic acid (**H₂pydc**) to terephthalic acid (**H₂bdc**). This ratio would lead to one **pydc** linker per zirconium cluster on average (Scheme 2.14).



Scheme 2.14. Synthesis of mixed-linker UiO-66-b/py.

Powder X-ray diffraction analysis of the product of this reaction revealed a crystalline material which showed good agreement with the simulated diffraction pattern based on the crystal structure of UiO-66 (Figure 2.19).²⁵

The final linker ratios were determined by digesting the MOF sample in a solution of NaOD in D₂O, followed by recording the solution-phase ¹H NMR spectrum. Terephthalic acid displays a single proton resonance at 7.75 ppm in this solvent mixture, which represents all four of its aromatic protons. The other linker, **pydc**, generates three resonances at 7.82, 8.17 and 8.82 ppm, each representing an aromatic proton. The resonance at 7.75 ppm for **bdc** was overlapping with the resonance at 7.82 for **pydc**, so these were combined together and the relative intensity at 8.82 ppm for **pydc** was subtracted to give the intensity of the resonance for **bdc**. The calculated relative intensities

for the resonances at 8.82 ppm and 7.75 ppm were 1.00 and 20.09 respectively. The spectrum also indicated the presence of acetic acid (**OAc**) in the product due to a resonance at 2.10 ppm representing three protons with a relative intensity of 1.50. This indicated a final ratio of **pydc** : **bdc** : acetic acid in the product of 2 : 10 : 1, giving the formula as $[\text{Zr}_6\text{O}_4(\text{OH})_4(\text{bdc})_{4.6}(\text{pydc})_{0.9}(\text{OAc})_{0.9}]$ (UiO-66-b/py). Elemental analysis of the MOF returned values that differed slightly from those expected for the above formula, and so the suggested formula of UiO-66-b/py should be treated with caution.

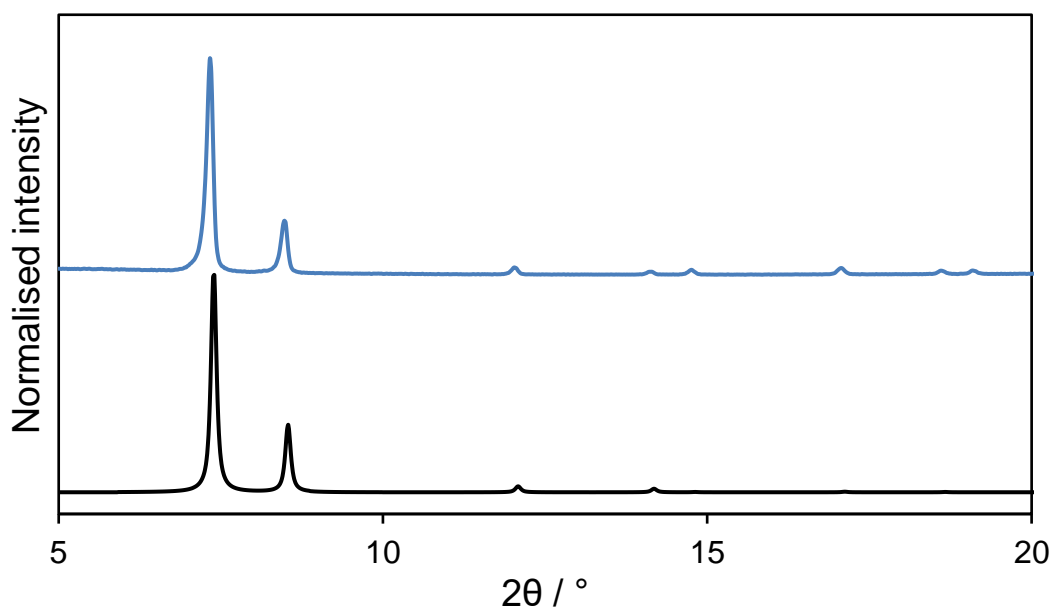


Figure 2.19. X-ray powder patterns of synthesised mixed-linker UiO-66-b/py (blue) and the simulated pattern based on the crystal structure of UiO-66 at 298 K (black).

2.4.2. Quaternisation of UiO-66-b/py

Neutral UiO-66-b/py was quaternised using a mixture of MeI in dry CHCl_3 which was heated to reflux for three days. The product of this reaction was digested in a mixture of D_3PO_4 in $(\text{CD}_3)_2\text{SO}$ and its solution-phase ^1H NMR spectrum was recorded.

In the ^1H NMR spectrum of the digested product, the aromatic resonances of the neutral and quaternised linkers were overlapping. Therefore, in order to calculate the extent of quaternisation, the combined aromatic resonance at 8.85 ppm was compared with the *N*-methyl resonance at 4.34 ppm. This indicated a quaternisation extent of 79%, suggesting the shorter linker **pydc** more readily undergoes quaternisation than its longer analogue, **ppydc**.

An X-ray powder pattern was recorded for the resultant postsynthetically modified MOF, which indicated retention of crystallinity over the course of the reaction (Figure 2.20), with a smaller loss of reflection intensity than that shown in Figure 2.15. This suggested that the MOF composed of the shorter linker, **pydc**, was more chemically robust than the larger MOF containing **ppydc**, which is in line with a previous report concerning the stability of UiO-66 vs. UiO-67-type MOFs.²⁶

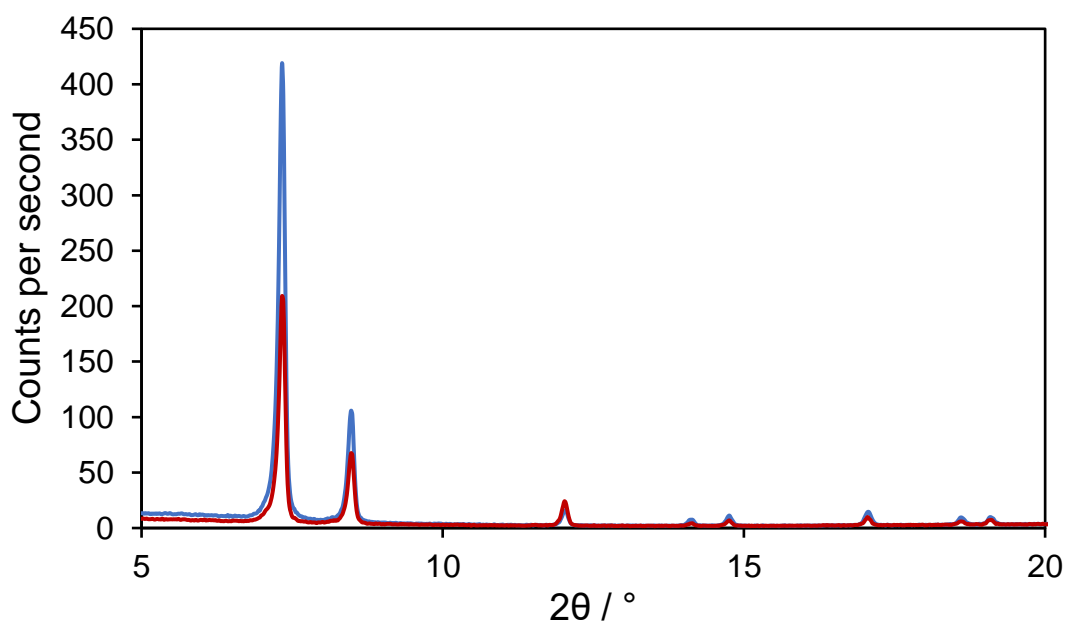


Figure 2.20. X-ray powder patterns of neutral UiO-66-b/py (blue) and after reaction with MeI for three days (red).

2.4.3. Reaction of UiO-66-b/py-Me_{79%} with [Rh(CO)₂I]₂

The quaternised MOF, UiO-66-b/py-Me_{79%}, was reacted with [Rh(CO)₂I]₂ in a manner analogous to that described in Section 2.3.2.1. A sample of neutral UiO-66-b/py was similarly reacted with [Rh(CO)₂I]₂ for comparison, and the $\nu(\text{CO})$ bands from the ATR-IR spectra of the two products are shown in Table 2.5.

Table 2.5. The $\nu(\text{CO})$ absorptions in the ATR-IR spectra of various samples upon reaction with [Rh(CO)₂I]₂, as well as the literature $\nu(\text{CO})$ values for *cis*-[Rh(CO)₂I]₂⁻ in solution.¹⁵

Sample	Asymmetric $\nu(\text{CO}) / \text{cm}^{-1}$	Symmetric $\nu(\text{CO}) / \text{cm}^{-1}$
<i>cis</i> -[Rh(CO) ₂ I] ₂ ⁻	1990	2060
UiO-66-b/py	2002	2072
UiO-66-b/py-Me _{79%}	2002	2075

Again, the $\nu(\text{CO})$ absorptions for the product of the reaction between neutral UiO-66-b/py and [Rh(CO)₂I]₂ come at a higher wavenumber than those for *cis*-[Rh(CO)₂I]₂⁻ in solution. This suggests a neutrally incorporated complex, potentially of the type shown in Figure 2.21.

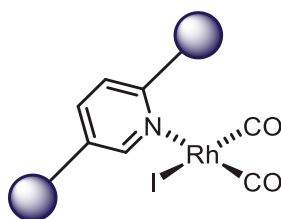


Figure 2.21. Proposed covalently tethered neutral rhodium dicarbonyl species.

The $\nu(\text{CO})$ absorptions for the product of the reaction between the quaternised MOF, UiO-66-b/py-Me_{79%}, and [Rh(CO)₂I]₂ are at similar frequency to those for the neutral

MOF reaction, indicating that the rhodium is bound by the 21% of neutral linkers in the MOF, as opposed to the quaternised linkers. This could again be due to increased steric hindrance in the pores that contain a quaternised linker.

2.5. Summary

Crystalline UiO-type MOFs incorporating a range of pyridine-containing linkers have been synthesised; UiO-67-bpy; UiO-67-bp/ppy; and UiO-66-b/py.

The literature procedure for the quaternisation of UiO-67-bpy did not produce a 100% quaternised MOF as previously reported,⁴ and increasing reaction time by a factor of five still did not achieve conversion to the fully quaternised form. This represented a problem, as any remaining neutral linker in the framework is potentially a chelating moiety that can bind covalently to rhodium. This was confirmed by reaction of neutral UiO-67-bpy with $[\text{Rh}(\text{CO})_2\text{I}]_2$, which seemed to result in a cationic rhodium dicarbonyl chelate species, charge balanced by *cis*- $[\text{Rh}(\text{CO})_2\text{I}_2]^-$.

The MOFs UiO-67-bp/ppy and UiO-66-b/py were synthesised via a mixed-linker method with their respective unsubstituted linkers. Quaternisation of UiO-67-bp/ppy was attempted via a range of methods, but ultimately conventional heating with MeI proved most effective. Increased reaction time led to higher extents of quaternisation, although even after two weeks, this had still not reached 100%, and increasing reaction length had an adverse effect on crystallinity. The UiO-66-b/py system was more amenable to quaternisation and appeared to be more robust than its extended-linker counterpart. This system, however, also failed to reach 100% quaternisation.

Reaction of these partially-quaternised systems with the rhodium precursor, $[\text{Rh}(\text{CO})_2\text{I}]_2$, appeared to show incorporation of a neutral rhodium dicarbonyl species, based on their ATR-IR spectra, presumably coordinating to the nitrogen sites on the remaining neutral linkers. This preference for covalent binding may be due to increased steric hindrance in pores containing linkers that have been quaternised.

2.6. References

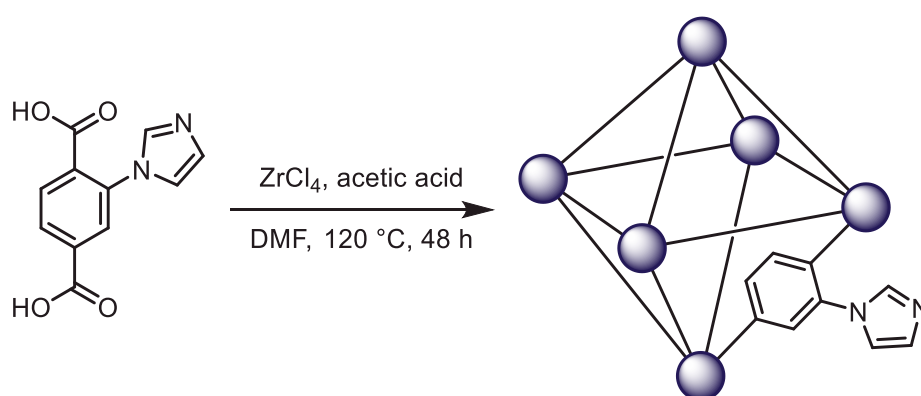
- 1 G. Nickerl, M. Leistner, S. Helten, V. Bon, I. Senkovska and S. Kaskel, *Inorg. Chem. Front.*, 2014, **1**, 325–440.
- 2 H. Fei and S. M. Cohen, *Chem. Commun.*, 2014, **50**, 4810.
- 3 L. Li, S. Tang, C. Wang, X. Lv, M. Jiang, H. Wu and X. Zhao, *Chem. Commun.*, 2014, **50**, 2304–2307.
- 4 L. Xu, Y. Luo, L. Sun, S. Pu, M. Fang, R. Yuan and H. Du, *Dalton Trans.*, 2016, **45**, 8614–8621.
- 5 M. B. Chambers, X. Wang, N. Elgrishi, C. H. Hendon, A. Walsh, J. Bonnefoy, J. Canivet, E. A. Quadrelli, D. Farrusseng, C. Mellot-Draznieks and M. Fontecave, *ChemSusChem*, 2015, **8**, 603–608.
- 6 T. Toyao, M. Saito, S. Dohshi, K. Mochizuki, M. Iwata, H. Higashimura, Y. Horiuchi and M. Matsuoka, *Res. Chem. Intermed.*, 2016, **42**, 7679–7688.
- 7 A. A. Barkhordarian and C. J. Kepert, *J. Mater. Chem. A*, 2017, **5**, 5612–5618.
- 8 Q. Zhang, J. Yu, J. Cai, L. Zhang, Y. Cui, Y. Yang, B. Chen and G. Qian, *Chem. Commun.*, 2015, **51**, 14732–14734.
- 9 Y. Yang, Q. Hu, Q. Zhang, K. Jiang, W. Lin, Y. Yang, Y. Cui and G. Qian, *Mol. Pharm.*, 2016, **13**, 2782–2786.
- 10 N. Yang, L. Zhou, P. Li, Q. Sui and E.-Q. Gao, *Chem. Sci.*, 2019, **10**, 3307–3314.
- 11 N. N. Yang, J. J. Fang, Q. Sui and E.-Q. Gao, *ACS Appl. Mater. Interfaces*, 2018, **10**, 2735–2744.
- 12 N. J. Hales and J. F. Beattie, *J. Med. Chem.*, 1993, 3853–3858.
- 13 A. Schaate, P. Roy, A. Godt, J. Lippke, F. Waltz, M. Wiebcke and P. Behrens, *Chem. - A Eur. J.*, 2011, **17**, 6643–6651.
- 14 J. Liang, Y.-Q. Xie, X.-S. Wang, Q. Wang, T.-T. Liu, Y.-B. Huang and R. Cao,

- Chem. Commun.*, 2017, **54**, 342–345.
- 15 A. Fulford, C. E. Hickey and P. M. Maitlis, *J. Organomet. Chem.*, 1990, **398**, 311–323.
- 16 J. A. Gaunt, PhD Thesis, University of Sheffield, 2003.
- 17 C. M. Conifer, D. J. Law, G. J. Sunley, A. Haynes, J. R. Wells, A. J. P. White and G. J. P. Britovsek, *Eur. J. Inorg. Chem.*, 2011, **2011**, 3511–3522.
- 18 L. Gonsalvi, J. A. Gaunt, H. Adams, A. Castro, G. J. Sunley and A. Haynes, *Organometallics*, 2003, **22**, 1047–1054.
- 19 W. M. Bloch, C. J. Doonan and C. J. Sumby, *CrystEngComm*, 2013, **15**, 9663.
- 20 A. Burgun, C. J. Coghlan, D. M. Huang, W. Chen, S. Horike, S. Kitagawa, J. F. Alvino, G. F. Metha, C. J. Sumby and C. J. Doonan, *Angew. Chem. Int. Ed.*, 2017, **56**, 8412–8416.
- 21 A. Haynes, B. E. Mann, G. E. Morris and P. M. Maitlis, *J. Am. Chem. Soc.*, 1993, **115**, 4093–4100.
- 22 T. Liu, D.-Q. Li, S.-Y. Wang, Y.-Z. Hu, X.-W. Dong, X.-Y. Liu and C.-M. Che, *Chem. Commun.*, 2014, **50**, 13261–13264.
- 23 P. V Dau, M. Kim, S. J. Garibay, H. L. Mu, C. E. Moore and S. M. Cohen, *Inorg. Chem.*, 2012, **51**, 5671–5676.
- 24 M. Topuzogullari, *J. Polym. Res.*, 2018, **25**, 1–7.
- 25 J. H. Cavka, S. Jakobsen, U. Olsbye, N. Guillou, C. Lamberti, S. Bordiga, K. P. Lillerud, C. Lamberti, S. Bordiga and K. P. Lillerud, *J. Am. Chem. Soc.*, 2008, **130**, 13850–13851.
- 26 J. B. Decoste, G. W. Peterson, H. Jasuja, T. G. Glover, Y. G. Huang and K. S. Walton, *J. Mater. Chem. A*, 2013, **1**, 5642–5650.

Chapter 3 UiO MOFs with Linkers Containing Imidazole Moieties

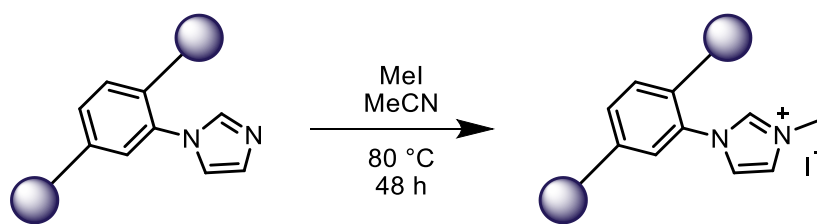
3.1. Introduction

Liang *et al.* recently reported the preparation of a cationic support via postsynthetic modification of a UiO-66-type MOF with imidazole groups attached to the **bdc** linkers as shown in Scheme 3.1.¹ The neutral MOF, UiO-66-imb, had a reported surface area of 538 m² g⁻¹ (compared with 1187 m² g⁻¹ for unsubstituted UiO-66).² The lower surface area is presumably due to increased pore occupancy from the pendant imidazole groups.



Scheme 3.1. Synthesis of UiO-66-imb. $[\text{Zr}_6(\mu_3\text{-O})_4(\mu_3\text{-OH})_4]^{12+}$ SBUs are represented using purple spheres.

The pendant imidazole group was quaternised with methyl iodide (MeI) to generate a cationic framework with iodide counter-ions present in the pores (Scheme 3.2). Following 48 h reflux in MeI and MeCN, the extent of conversion of imidazole groups to *N*-methylimidazolium was calculated as 75% from the solution-phase ¹H NMR spectrum of the sample digested in HF/(CD₃)₂SO. After the quaternisation reaction, the surface area of the postsynthetically modified MOF had dropped to 328 m² g⁻¹. This is expected to be due to increased pore congestion from the *N*-bound methyl groups and the iodide counter-ions.



Scheme 3.2. Postsynthetic modification of UiO-66-imb to generate a cationic framework via methylation of its pendant nitrogen sites.¹

This chapter describes the use of this cationic MOF to heterogenise the anionic carbonylation catalyst, *cis*-[Rh(CO)₂I₂]⁻, via ionic encapsulation, and investigations into its activity.

The linkers discussed in this chapter are shown in Figure 3.1 along with their abbreviations.

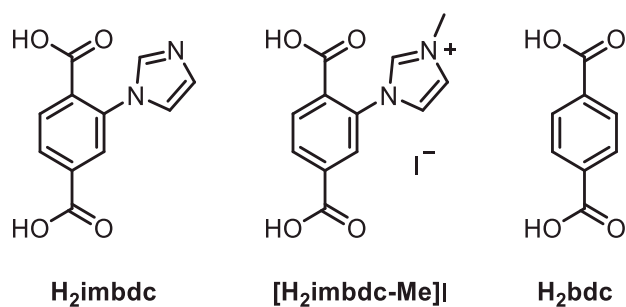
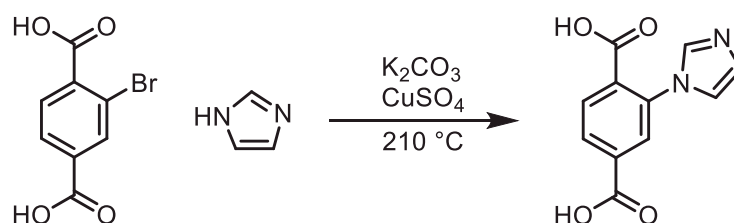


Figure 3.1. Range of dicarboxylic acids used in this chapter, and their abbreviations.

3.2. UiO-66-imb

3.2.1. Synthesis and postsynthetic modification of UiO-66-imb

2-(imidazol-1-yl)terephthalic acid (**H₂imbdc**) was synthesised and purified according to a reported procedure (Scheme 3.3).¹ This linker was used to synthesise highly crystalline [Zr₆O₄(OH)₄(**imbdc**)₆] (UiO-66-imb) in a high yield (63%) according to the reported procedure.¹



Scheme 3.3. Synthesis of 2-(imidazol-1-yl)terephthalic acid (**H₂imbdc**).¹

Successful synthesis of the crystalline framework was confirmed by powder X-ray diffraction, which showed good agreement with the simulated pattern based on the crystal structure of UiO-66 (Figure 3.2).² Elemental analysis of the product of the reaction indicated presence of chlorine – this is presumed to be in the form of chloride (originating from ZrCl₄) which is charge balancing the pendant nitrogen site in **imbdc** that has been protonated in the acidic reaction conditions. The elemental analysis value for chlorine is about a third of that calculated for [Zr₆O₄(OH)₄(**imbdc**•HCl)₆], which suggests a mixture of anions may be present (including e.g. formate), or that not all nitrogen sites are protonated.

Confirmation of incorporation of **imbdc** linker into the framework was provided by digestion of the MOF in a mixture of D₃PO₄ in D₂O, followed by characterisation via

solution-phase ^1H NMR spectroscopy. No acetic acid was detected in the ^1H NMR spectrum of the digested MOF, suggesting a low defect concentration.

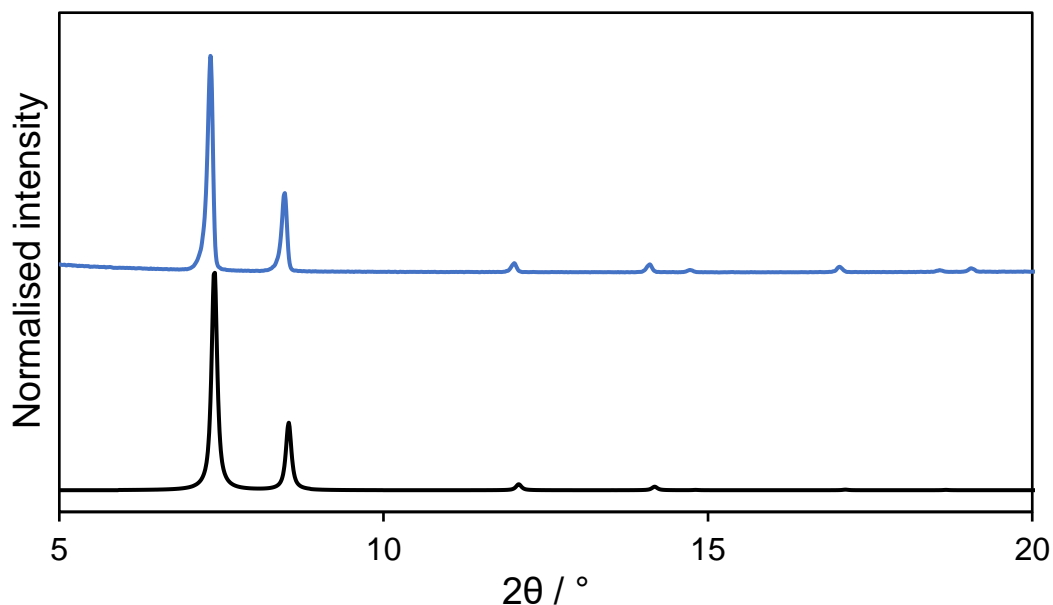


Figure 3.2. X-ray powder patterns of synthesised UiO-66-imb (blue) and the simulated pattern based on the crystal structure of UiO-66 at 298 K (black).²

Furthermore, the solid-state CP-MAS $^{13}\text{C}\{^1\text{H}\}$ NMR spectrum contains broad signals in the expected regions based on the solution-phase $^{13}\text{C}\{^1\text{H}\}$ NMR spectrum of **H₂imbdc** in $(\text{CD}_3)_2\text{SO}$, as well as weak resonances at 20.4 ppm and 29.9 ppm thought to be due to residual acetic acid and silicone grease respectively (Figure 3.3).

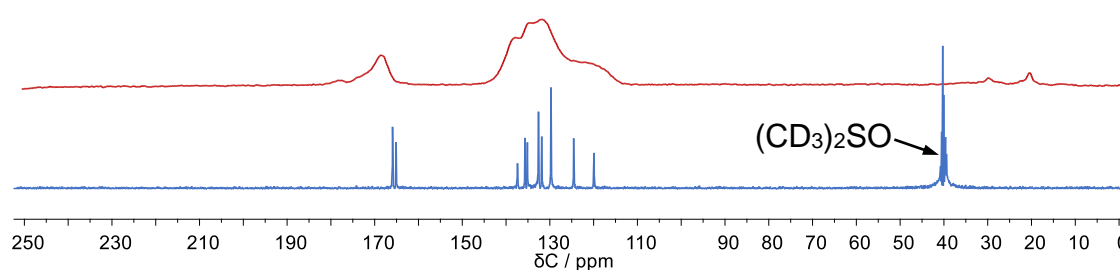


Figure 3.3. Solution-phase $^{13}\text{C}\{^1\text{H}\}$ NMR spectrum of **H₂imbdc** (blue, in $(\text{CD}_3)_2\text{SO}$) and solid-state CP-MAS $^{13}\text{C}\{^1\text{H}\}$ NMR spectrum of UiO-66-imb (red).

The presence of acetic acid in the solid-state spectrum is thought to be due to residual acetic acid in the pores from the solvothermal MOF synthesis arising from incomplete activation, as opposed to defects in the MOF. This would explain why acetic acid was not observed in the solution-phase ^1H NMR spectrum in $\text{D}_3\text{PO}_4/\text{D}_2\text{O}$, as this spectrum was recorded following volumetric gas sorption analysis which involved degassing at lower pressures and elevated temperatures than the standard post-synthetic activation procedure.

In order to generate a cationic support, the MOF was refluxed in a mixture of MeI and MeCN for 72 h, as shown in Scheme 3.2.¹ The product was digested in $\text{D}_3\text{PO}_4/(\text{CD}_3)_2\text{SO}$ for analysis by ^1H NMR spectroscopy. In the solution-phase ^1H NMR spectrum of the digested product, the aromatic resonances due to the neutral and quaternised linkers overlap one another (Figure 3.4). Therefore, in order to calculate extent of quaternisation, the intensity of one of the combined aromatic resonances (at 9.42 ppm) is compared with the *N*-methyl resonance (at 3.92 ppm). The relative integrals of these resonances are 1.00 and 1.45 respectively. If the reaction had reached 100% conversion, the *N*-methyl resonance would have an integration value of 3.00. The reaction is therefore calculated to have reached 48% conversion of imidazole to *N*-methylimidazolium groups, giving a formula of $[\text{Zr}_6\text{O}_4(\text{OH})_4(\text{imbdc})_{3.1}(\text{imbdc-Me})_{2.9}]\text{I}_{2.9}$ (UiO-66-imb-Me_{48%}).

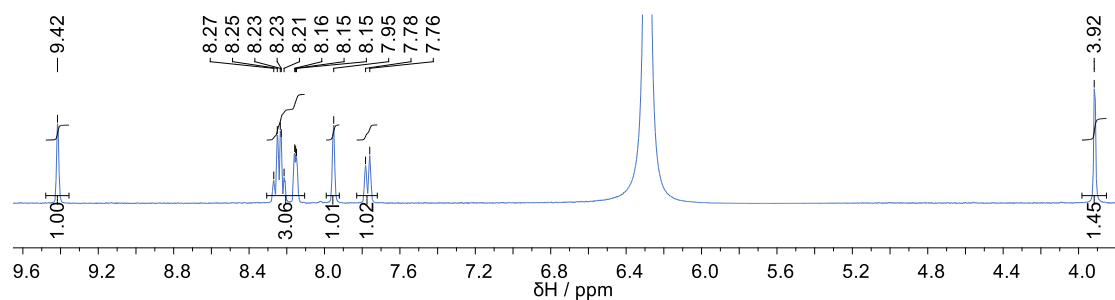
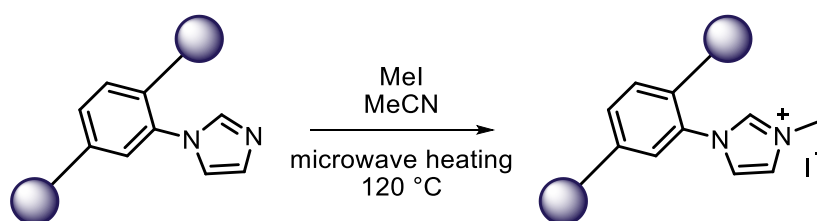


Figure 3.4. ^1H NMR spectrum of UiO-66-imb-Me_{48%} digested in $\text{D}_3\text{PO}_4/\text{D}_2\text{O}$. Resonance at ~6.3 ppm is caused by residual H_2O .

In order to increase this conversion and reduce reaction time a microwave reactor was utilised for this procedure (Scheme 3.4). Microwave heating has been used previously to achieve high levels of quaternisation in a fraction of the time required by conventional heating methods.³ Samples of UiO-66-imb were added to solutions of MeI (3.2 – 8.0 M) in MeCN and heated at 120 °C for the periods shown in Table 2.3. The recovered samples were washed and digested in a mixture of D₃PO₄ and (CD₃)₂SO and their ¹H NMR spectra analysed to determine their extent of conversion in the manner described previously (Table 2.3).



Scheme 3.4. Microwave quaternisation of UiO-66-imb.

Table 3.1. Calculated extent of quaternisation of UiO-66-imb for different incubation times (microwave heating at 120 °C) and MeI concentrations.

Incubation time / h	[MeI] / mol dm ⁻³	∫ at 9.42 ppm	∫ at 3.92 ppm	Extent of quaternisation
1	3.2	1.00	2.34	78%
1	4.0	1.00	2.56	85%
1	8.0	1.00	2.17	72%
2	4.0	1.00	2.54	85%

The maximum extent of conversion is reached after one hour of incubation at 120 °C in a 4 M solution of MeI in MeCN, which results in 85% conversion of imidazole to *N*-methylimidazolium groups. This represents a notable improvement on the literature procedure, which achieved 75% conversion after three days of reflux in MeI and MeCN.

Solid-state CP-MAS $^{13}\text{C}\{^1\text{H}\}$ NMR spectroscopy confirmed the successful quaternisation of imidazole groups in the MOF, with an extra resonance at 37 ppm consistent with that for the *N*-methyl carbon atom in the solution-phase $^{13}\text{C}\{^1\text{H}\}$ NMR spectrum of **[H₂imbdc-Me]I** in $(\text{CD}_3)_2\text{SO}$ (Figure 3.5).

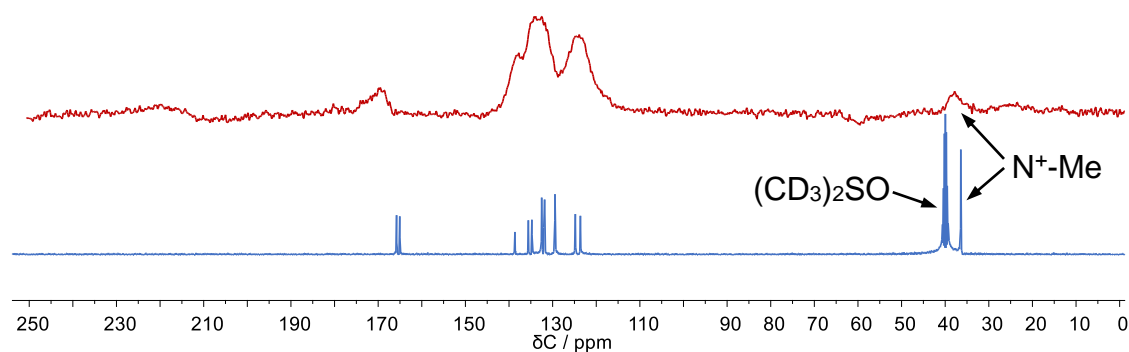


Figure 3.5. Solution-phase $^{13}\text{C}\{^1\text{H}\}$ NMR spectrum of **[H₂imbdc-Me]I** (blue, in $(\text{CD}_3)_2\text{SO}$) and solid-state CP-MAS $^{13}\text{C}\{^1\text{H}\}$ NMR spectrum of UiO-66-imb-Me_{85%} (red).

The powder X-ray diffraction pattern of the product revealed retention of crystallinity, albeit with some loss of intensity (Figure 3.6).

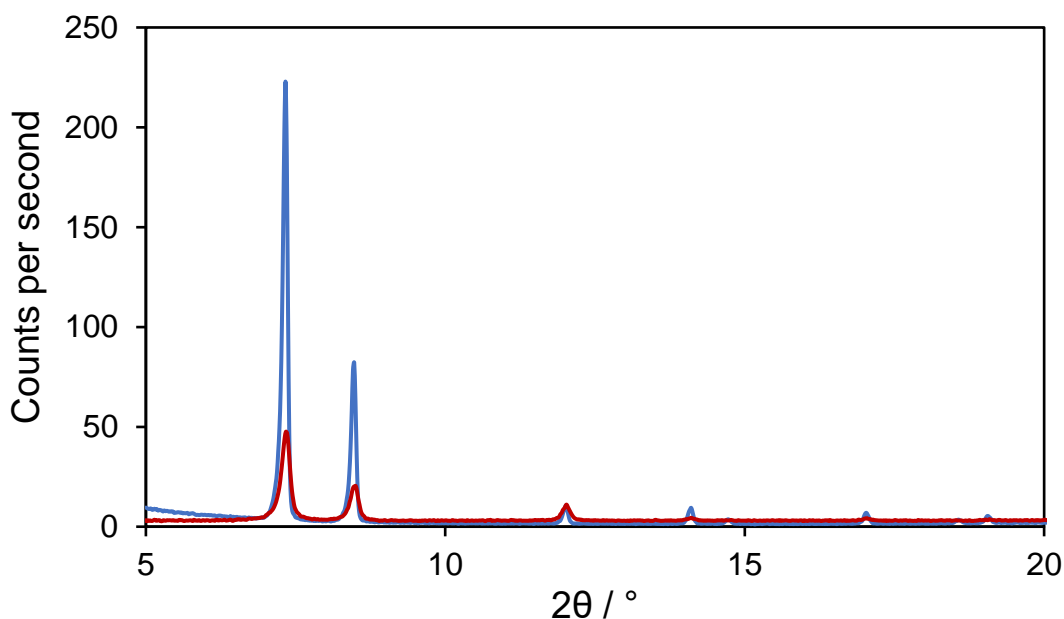
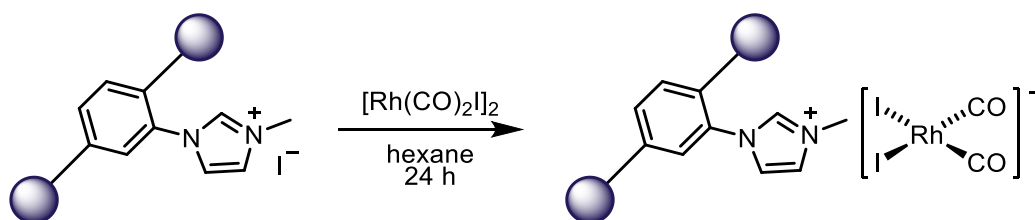


Figure 3.6. X-ray powder patterns of neutral UiO-66-imb (blue) and product of microwave quaternisation reaction (red).

The quaternised product, UiO-66-imb-Me_{85%}, was reacted with $[\text{Rh}(\text{CO})_2\text{I}]_2$ in hexane (Scheme 3.5).



Scheme 3.5. Reaction between UiO-66-imb-Me_{85%} and $[\text{Rh}(\text{CO})_2\text{I}]_2$.

The IR spectrum of the product of this reaction is shown in Figure 3.7. It contains $\nu(\text{CO})$ absorptions at 2064 cm^{-1} and 1994 cm^{-1} , indicative of a *cis*-dicarbonyl species. These frequencies are similar to those for $[n\text{-Bu}_4\text{N}][\text{Rh}(\text{CO})_2\text{I}_2]$ in MeOH (2060 cm^{-1} and 1990 cm^{-1}).⁴ This suggests generation of *cis*- $[\text{Rh}(\text{CO})_2\text{I}]^-$ via cleavage of the dimeric precursor by the iodide counter-ions in the framework. There is a degree of asymmetry in the bands shown in Figure 3.7, with high-frequency shoulders on both bands. This is consistent with the presence of neutral $\text{Rh}(\text{CO})_2$ moieties arising from covalent

attachment of rhodium complex to the 15% of imidazole sites that remain unquaternised (illustrated in Figure 3.8).

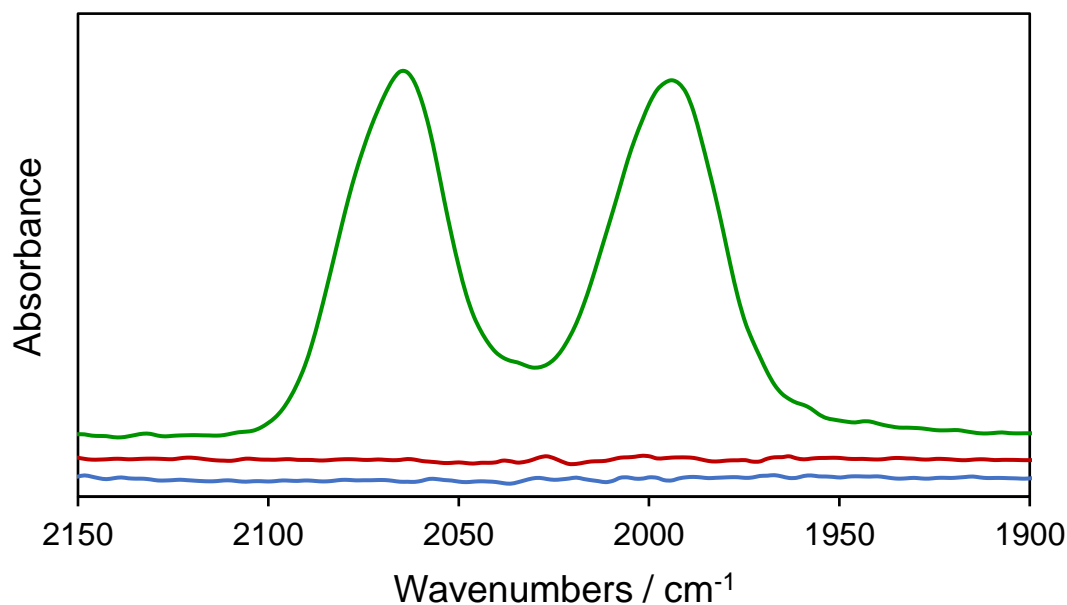


Figure 3.7. ATR-IR spectra ($\nu(\text{CO})$ region) of UiO-66-imb (blue), UiO-66-imb-Me_{85%} (red) and the MOF-encapsulated catalyst (green).

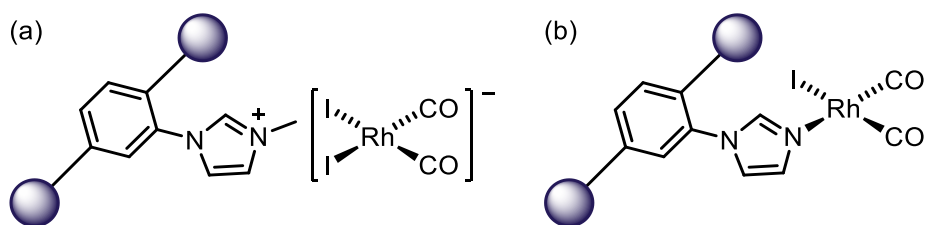
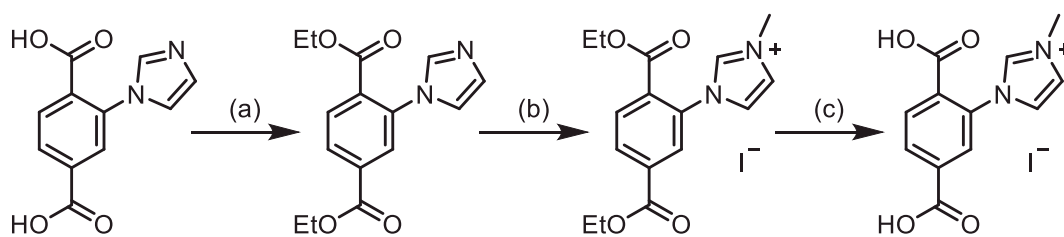


Figure 3.8. (a) Ionic and (b) covalent incorporation of rhodium complex.

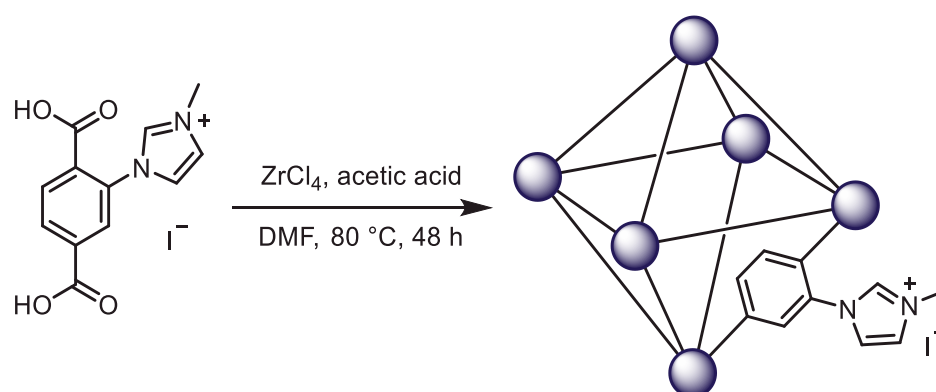
3.2.2. Attempted direct synthesis of UiO-66-imb-Me

The pendant imidazole group in **H₂imbdc** can be methylated to form [**H₂imbdc-Me**]I via protection of the carboxylic acid groups according to a literature procedure (Scheme 3.6).⁵



Scheme 3.6. Methylation of **H₂imbdc** to form **[H₂imbdc-Me]I**.⁵ (a) EtOH and DMF, SOCl₂ added dropwise, reflux 72 h, (b) MeCN and MeI reflux 24 h, (c) 6 M HCl reflux 16 h.

Several attempts were made to directly incorporate **[H₂imbdc-Me]I** into a UiO-66-type MOF via direct solvothermal synthesis (Scheme 3.7). Direct synthesis using both Teflon-lined stainless-steel autoclaves and glass vials resulted in no precipitate forming. Surprisingly, subsequent incubation of the recovered reaction mixture from the glass vials in stainless-steel autoclaves did result in formation of a small amount of precipitate (~18% yield based on Zr).



Scheme 3.7. Attempted direct synthesis of UiO-66-imb-Me using **[H₂imbdc-Me]I**.

The solution-phase ¹H NMR spectrum of the product digested in D₃PO₄/(CD₃)₂SO revealed that all (100%) of the imidazolium sites remained quaternised after incubation. This analysis also indicated presence of substantial residual MeOH, acetic acid and DMF.

Elemental analysis of the product indicated a mixture of iodide and chloride counter-ions were present, either due to the HCl used in the linker re-acidification step (Scheme 3.6), or the chloride ions present in the zirconium salt used in the MOF synthesis (Scheme 3.7).

Powder X-ray diffraction analysis of the product (Figure 3.9) showed some agreement with the simulated pattern based on the crystal structure of UiO-66,² although Pawley fitting of the powder pattern indicated that the sample was not phase pure (Figure 3.10).

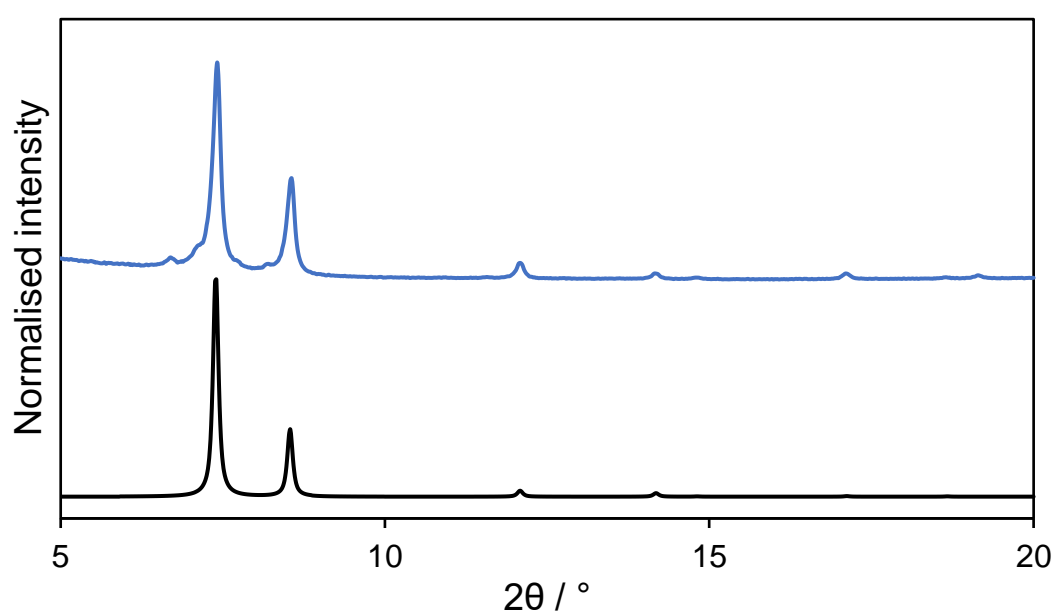


Figure 3.9. X-ray powder patterns of directly synthesised UiO-66-imb-Me (blue) and the simulated pattern based on the crystal structure of UiO-66 at 298 K (black).²

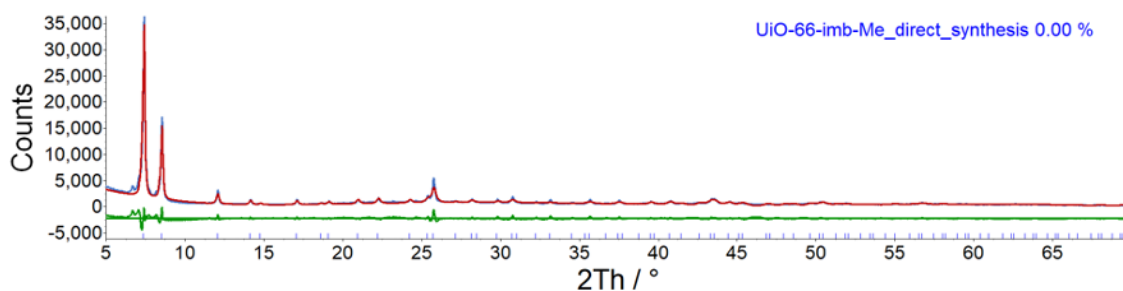


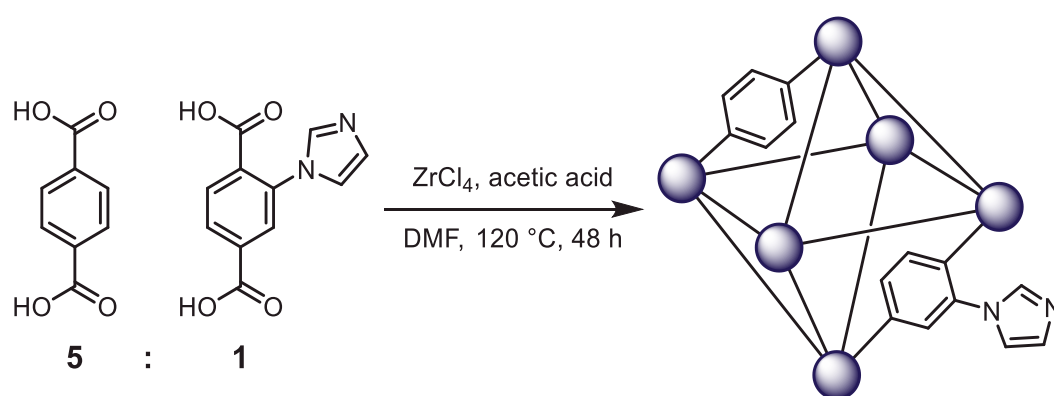
Figure 3.10. Pawley fit of the powder X-ray diffraction pattern for directly synthesised UiO-66-imb-Me showing the observed pattern (blue), the fit (red), and the difference between the two (green).

Further work was not pursued with this preparative method as the synthesis was not replicable in one step in either glass vials or Teflon-lined stainless-steel autoclaves, and it resulted in poor quality product and low yields.

3.3. UiO-66-b/imb

3.3.1. Synthesis and postsynthetic modification of UiO-66-b/imb

A mixed-linker approach was taken in order to minimise steric hindrance within the pores upon quaternisation, thus potentially leading to a higher extent of conversion to the cationic form. A 1:5 mixture of **H₂imbdc** and **H₂bdc** was used to synthesise a mixed-linker MOF with an average of one **imbdc** linker per SBU (Scheme 3.8).



Scheme 3.8. Synthesis of mixed-linker UiO-66-b/imb.

Successful synthesis of crystalline UiO-66-type MOF was confirmed via powder X-ray diffraction (Figure 3.11), which showed agreement with the simulated pattern of UiO-66.²

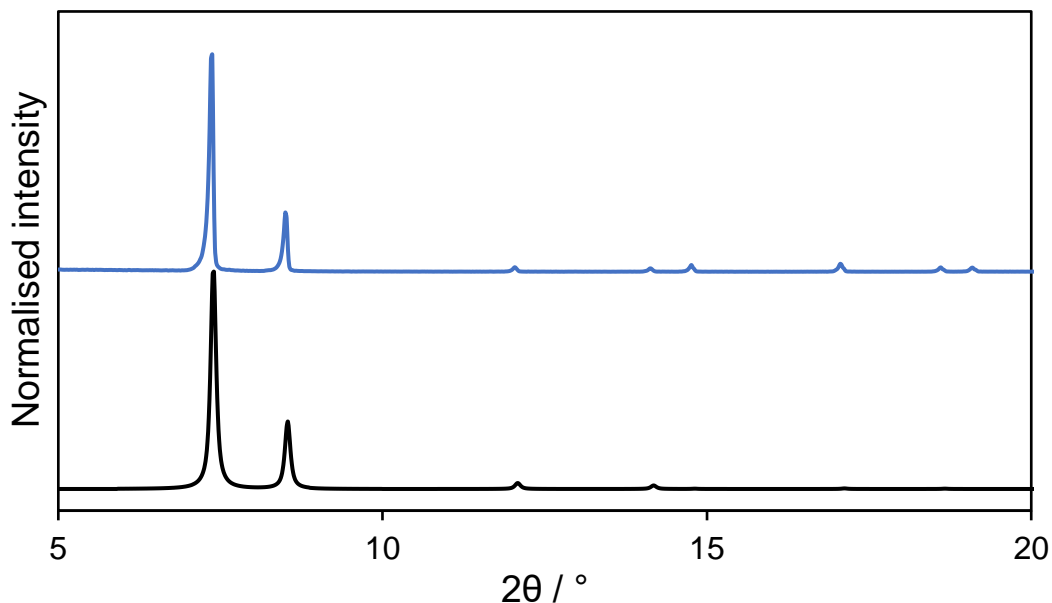


Figure 3.11. X-ray powder patterns of synthesised UiO-66-b/imb (blue) and the simulated pattern based on the crystal structure of UiO-66 at 298 K (black).²

UiO-66-b/imb was digested in a solution of NaOD in D₂O and a solution-phase ¹H NMR spectrum was recorded (Figure 3.12), which was used to determine the final linker ratios.

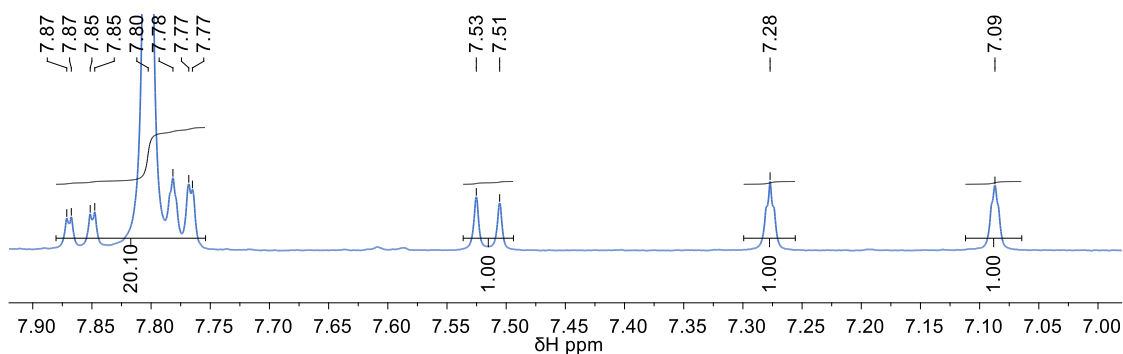
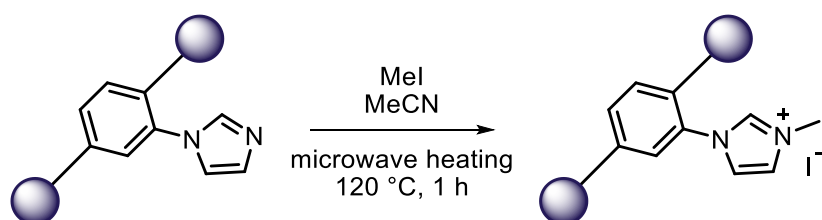


Figure 3.12. ¹H NMR spectrum of UiO-66-b/imb digested in NaOD/D₂O.

The linker **bdc** displays one resonance at 7.80 ppm in this solvent mixture (corresponding to four aromatic protons), whereas **imbdc** displays resonances at 7.09, 7.28, 7.52, 7.77 and 7.86 ppm (all corresponding to one aromatic proton, apart from the resonance at 7.86 ppm which corresponds to two). The resonance for **bdc** overlaps with the resonances at 7.77 and 7.86 ppm for **imbdc** in the spectrum of the digested product. These combined

resonances give a relative intensity 20.10 times larger than the resonance at 7.09 ppm for **imbdc**. This intensity includes contribution from three protons in **imbdc** from the resonances at 7.77 and 7.86 ppm, meaning that the relative intensity due to **bdc** is actually 17.10. Acetic acid (**OAc**) is also detectable in the spectrum (2.12 ppm) with a relative intensity of 0.30. This gives a final ratio for **bdc** : **imbdc** : **OAc** of 4.3:1:0.1, giving the final formula of the MOF as $[\text{Zr}_6\text{O}_4(\text{OH})_4(\mathbf{bdc})_{4.8}(\mathbf{imbdc})_{1.1}(\mathbf{OAc})_{0.1}]$. Elemental analysis of the product found a lower carbon content than expected – this is assumed to be due to the presence of a mixture of counter-ions charge-balancing a protonated nitrogen site on **imbdc**.

As described in Section 3.2.1, microwave heating was employed to maximise the extent of quaternisation of imidazole sites in UiO-66-b/imb (Scheme 3.9).



Scheme 3.9. Quaternisation of mixed-linker UiO-66-b/imb using microwave heating.

The product was digested in a solution of D_3PO_4 in $(\text{CD}_3)_2\text{SO}$ and its ^1H NMR spectrum was recorded to determine the extent of quaternisation of imidazole sites. The resonances due to imidazole and *N*-methylimidazolium overlap in the spectrum, and so the extent of quaternisation is determined by comparing the relative intensities of one of these combined resonances (at 9.40 ppm) with the *N*-methyl resonance (at 3.92 ppm). The resonance at 3.92 ppm had an intensity 2.90 times larger than the resonance at 9.40 ppm, indicating conversion of 97% of imidazole sites to *N*-methylimidazolium, giving a formula of $[\text{Zr}_6\text{O}_4(\text{OH})_4(\mathbf{bdc})_{4.8}(\mathbf{imbdc}\text{-Me})_{1.1}(\mathbf{OAc})_{0.1}]\text{I}_{1.1}$ (UiO-66-b/imb-Me_{97%}). This

suggests that the mixed-linker approach was indeed successful at enabling a higher extent of quaternisation under these conditions as compared with the single-linker analogue (which achieved 85% quaternisation after the same reaction).

The postsynthetically modified MOF, UiO-66-b/imb-Me_{97%}, was found to have retained its crystallinity via PXRD (Figure 3.13), and the loss of intensity of reflections was less pronounced than that observed in the single-linker analogue (Figure 3.6).

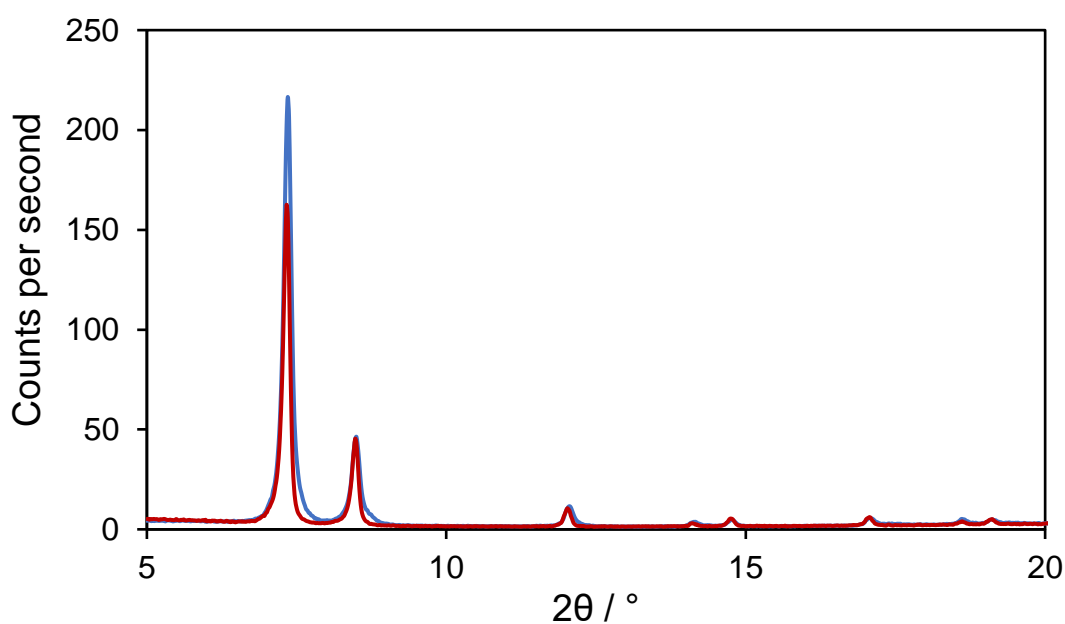


Figure 3.13. X-ray powder patterns of neutral UiO-66-b/imb (blue) and product of microwave quaternisation (red).

The postsynthetically modified MOF, UiO-66-b/imb-Me_{97%}, was reacted with [Rh(CO)₂I]₂ in hexane. The IR spectrum of the product is shown in Figure 3.14.

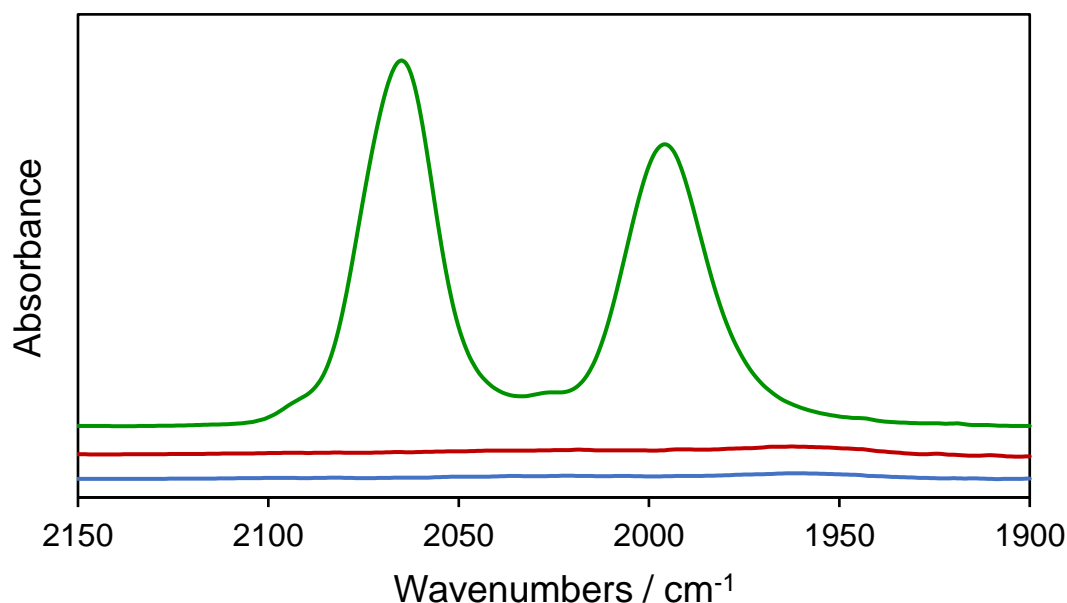
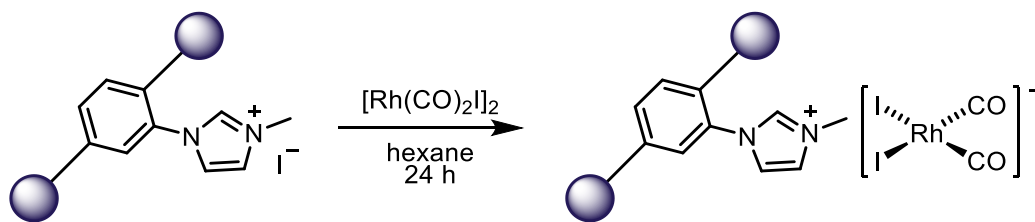


Figure 3.14. Infrared spectra (KBr disc, $\nu(\text{CO})$ region) of UiO-66-b/imb (blue), UiO-66-b/imb-Me_{97%} (red) and the MOF-encapsulated catalyst (green).

The IR spectrum of the product of the reaction between UiO-66-b/imb-Me_{97%} and $[\text{Rh}(\text{CO})_2\text{I}]_2$ displays two $\nu(\text{CO})$ absorptions at 2060 cm^{-1} and 1986 cm^{-1} (Figure 3.14). These $\nu(\text{CO})$ values are consistent with those for $[\text{n-Bu}_4\text{N}][\text{Rh}(\text{CO})_2\text{I}_2]$ in MeOH (2060 cm^{-1} and 1990 cm^{-1}),⁴ which suggests that the iodide counter-ions in the pores of UiO-66-b/imb-Me_{97%} cleave the dimeric precursor to generate the catalytic species $\text{cis-}[\text{Rh}(\text{CO})_2\text{I}_2]^-$ *in situ* (Scheme 3.10). The absorptions are narrower and more symmetrical than those found for the single-linker MOF (Figure 3.7), suggesting the absence of significant neutral, covalently attached complex (illustrated in Figure 3.8). ICP-MS analysis confirmed the presence of rhodium in the product (5% by mass), which corresponds to stoichiometric uptake of Rh to $[\text{imbdc-Me}]^+$, giving a formula of $[\text{Zr}_6\text{O}_4(\text{OH})_4(\text{bdc})_{4.8}(\text{imbdc-Me})_{1.1}(\text{OAc})_{0.1}][\text{Rh}(\text{CO})_2\text{I}_2]_{1.1}$ (Rh@UiO-66-b/imb-Me_{97%}).



Scheme 3.10. Proposed reaction between UiO-66-b/imb-Me_{97%} and $[\text{Rh}(\text{CO})_2\text{I}]_2$.

Reaction of neutral UiO-66-b/imb with $[\text{Rh}(\text{CO})_2\text{I}]_2$ gave a product with $\nu(\text{CO})$ absorptions at 2075 cm^{-1} and 2007 cm^{-1} , indicating presence of a neutral rhodium dicarbonyl species, presumably coordinated to the imidazole-functionalised linker.

The powder X-ray diffraction pattern of the product of this reaction indicated retention of the crystalline framework, although the intensities of the reflections were altered (Figure 3.15). This is thought to be due to the inclusion of the heavy elements rhodium and iodine in the framework.

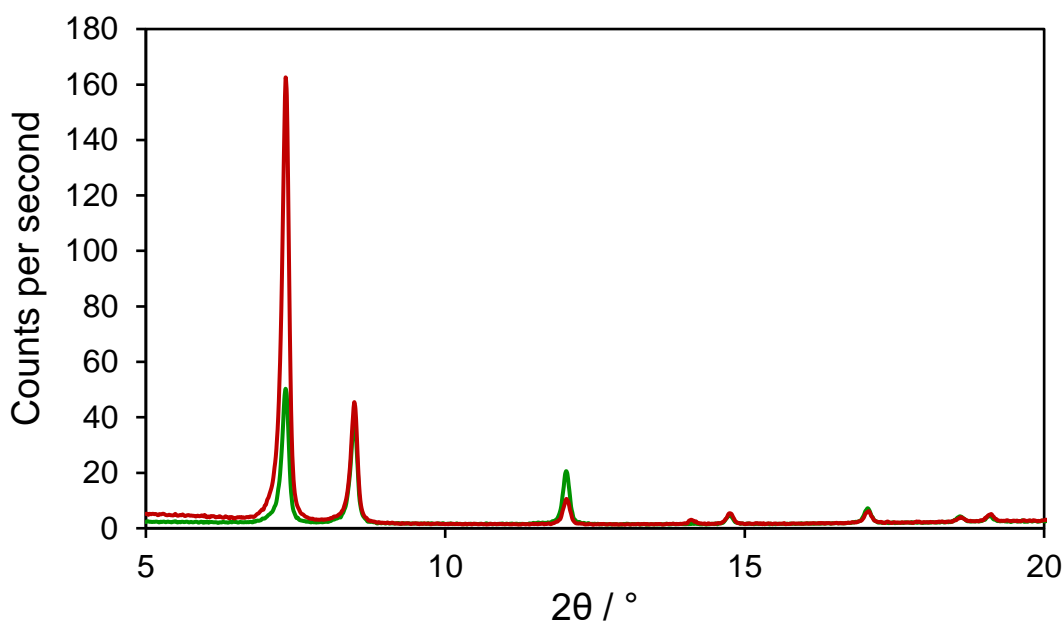


Figure 3.15. X-ray powder patterns of UiO-66-b/imb-Me_{97%} (red) and product of reaction with $[\text{Rh}(\text{CO})_2\text{I}]_2$ (green).

Volumetric N₂ gas sorption studies at 77 K were performed on unsubstituted UiO-66 (synthesised via an analogous reaction to UiO-66-b/imb), UiO-66-b/imb, UiO-66-b/imb-Me_{97%} and the catalyst-incorporated MOF (Figure 3.16). The calculated surface area of the synthesised UiO-66 was higher than the literature example (1238 m² g⁻¹ vs. 1187 m² g⁻¹) which is likely a result of the different synthesis method used, potentially altering the defect concentration in the resultant MOF.² In the low relative pressure region (< 0.1 p/p_0), there is uptake of N₂ across all samples, with uptake decreasing with increasing substitution. The total pore volume of UiO-66 is significantly higher than for UiO-66-b/imb (Table 3.2), suggesting that the substituted linkers are distributed throughout the framework and not solely on the surface. The micropore (pores with diameters < 2 nm) volume of UiO-66-b/imb reduces upon methylation to UiO-66-b/imb-Me_{97%}. This suggests that the iodide counter-ions occupy the micropores of the MOF, in addition to increased steric congestion from the newly-introduced *N*-bound methyl groups. Furthermore, when *cis*-[Rh(CO)₂I₂]⁻ is incorporated into the cationic framework, the micropore volume drops further, suggesting micropore occupancy of the catalyst. Given that the ratio of micropore volume to total pore volume decreases upon each subsequent postsynthetic modification, it appears that substitution (i.e. methylation or catalyst encapsulation) is predominantly occurring in the micropores of the MOF.

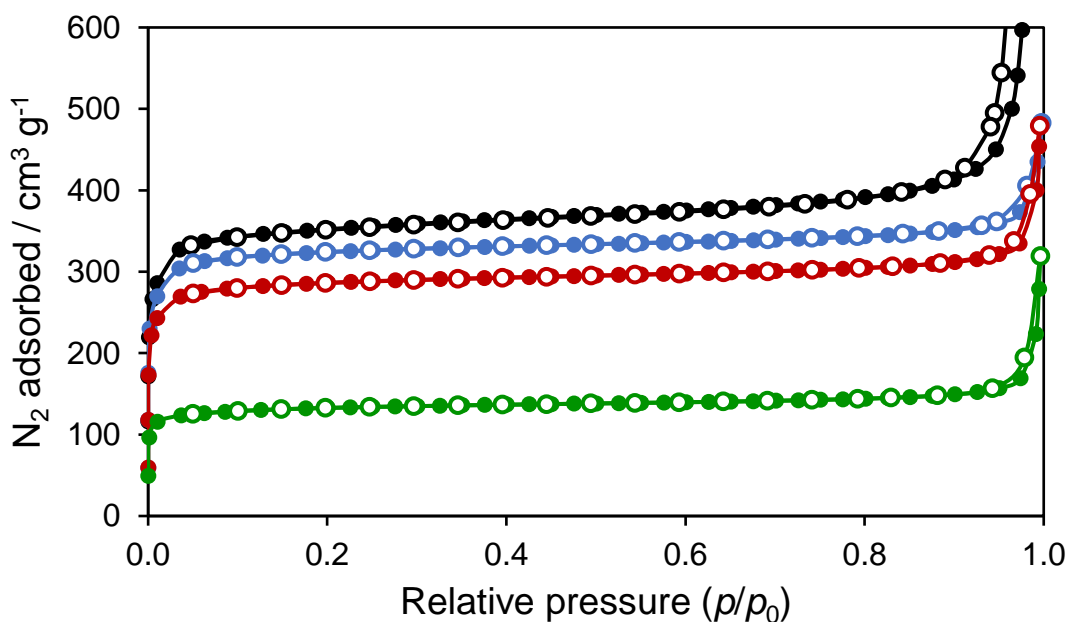


Figure 3.16. Nitrogen adsorption (filled) and desorption (open) isotherms at 77 K for UiO-66 (black), UiO-66-b/imb (blue), UiO-66-b/imb-Me_{97%} (red) and the MOF-encapsulated catalyst (green).

Table 3.2. Surface areas and pore volumes of UiO-66-type MOF samples.

Sample	$S_{\text{ABET}}^{\text{a}}$ / $\text{m}^2 \text{g}^{-1}$	$V_{\text{tot}}^{\text{b}}$ / $\text{cm}^3 \text{g}^{-1}$	$V_{0.1}^{\text{c}}$ / $\text{cm}^3 \text{g}^{-1}$	$(V_{0.1}/V_{\text{tot}})$
UiO-66	1238	0.71	0.53	0.75
UiO-66-b/imb	1139	0.55	0.49	0.89
UiO-66-b/imb-Me _{97%}	1031	0.50	0.43	0.86
Rh@UiO-66-b/imb-Me _{97%}	477	0.24	0.20	0.83

The surface area of synthesised UiO-66-b/imb is much higher than that reported for UiO-66-imb ($1139 \text{ m}^2 \text{ g}^{-1}$ vs. $538 \text{ m}^2 \text{ g}^{-1}$), and the surface area of synthesised UiO-66-b/imb-Me_{97%} is similarly higher than the literature value for UiO-66-imb-Me_{75%} ($1031 \text{ m}^2 \text{ g}^{-1}$ vs. $328 \text{ m}^2 \text{ g}^{-1}$).¹ This is likely due to the presence of fewer imidazole groups occupying

^a Calculated over the pressure range 0.01-0.15 p/p_0 .

^b Calculated at 0.99 p/p_0 .

^c Calculated at 0.1 p/p_0 .

space in the pores. This suggests further that the mixed-linker approach was indeed successful in reducing pore congestion, allowing for a higher extent of quaternisation.

3.3.2. Reaction of encapsulated *cis*-[Rh(CO)₂I₂]⁻ with MeI

A sample of Rh@UiO-66-b/imb-Me_{97%} was soaked in MeI under N₂ overnight and the ATR-IR spectrum of the product contained only one terminal $\nu(\text{CO})$ band at 2060 cm⁻¹, as well as a broad band at around 1735 cm⁻¹ (Figure 3.17). This indicates that oxidative addition of MeI takes place, followed by methyl migration to generate an acetyl ligand, as observed for the homogeneous analogue (Scheme 3.11). Upon exposure of this product to CO gas (1 atm), the IR spectrum gradually converts to a product with absorptions at 2088 cm⁻¹ and 1694 cm⁻¹ (Figure 3.17), which is consistent with formation of the *trans*-dicarbonyl complex *trans*-[Rh(CO)₂(COMe)I₃]⁻ found in solution studies (Scheme 3.11).⁶ Thus, the key organometallic steps seen in solution for the Monsanto catalytic cycle also occur for the supported complex, as observed previously in polymer supported systems.⁷

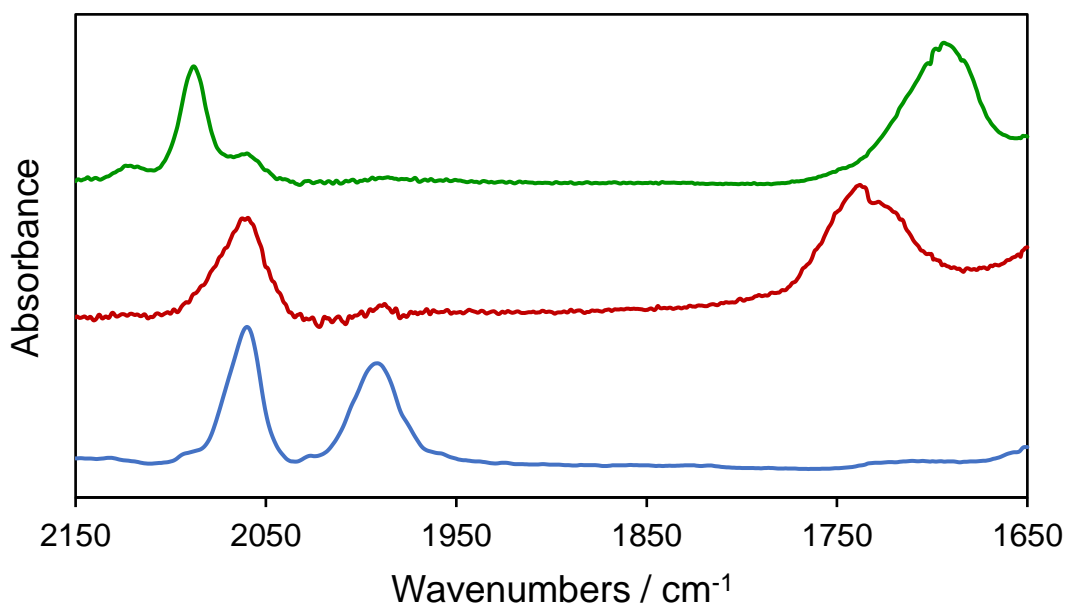
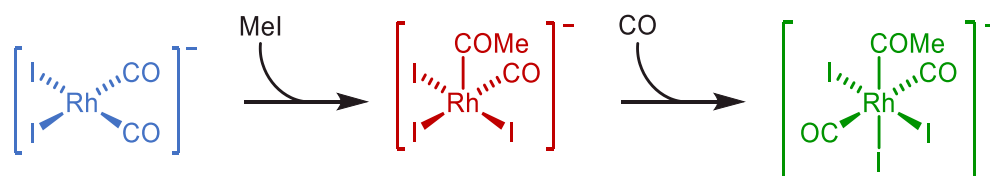


Figure 3.17. IR spectra (ATR-IR, $\nu(\text{CO})$ region) of Rh@UiO-66-b/imb-Me_{97%} (blue), after soaking in MeI overnight (red), and after exposure to CO atmosphere for 10 d (green).



Scheme 3.11. Reaction of encapsulated $\text{cis}[\text{Rh}(\text{CO})_2\text{I}_2]^-$ with MeI and CO.

3.3.3. Catalytic carbonylation of MeOH with encapsulated $\text{cis}[\text{Rh}(\text{CO})_2\text{I}_2]^-$

The carbonylation of methanol catalysed by Rh@UiO-66-b/imb-Me_{97%} was probed by *in situ* high-pressure IR spectroscopy. In a typical experiment, UiO-66-b/imb-Me_{97%} was stirred in a solution of $[\text{Rh}(\text{CO})_2\text{I}_2]$ in CHCl_3 under CO overnight and then added to the cell. A mixture of MeOH and MeI in CHCl_3 was added to give final concentrations of 0.8 M MeI and 2.5 M MeOH in CHCl_3 . The cell was pressurised with CO (10 bar) and stirred.

The IR spectrum of the solution phase at 120 °C was collected every five minutes over the course of four hours.

During the course of the reaction, growth of an absorption at 1741 cm^{-1} is observed which corresponds to the acetyl $\nu(\text{CO})$ band of methyl acetate in CHCl_3 (Figure 3.18). Methyl acetate is formed when the carbonylation product, acetic acid, esterifies in the presence of an excess of MeOH (Scheme 3.12). The homogeneous catalytic reaction using an equivalent amount of $[\textit{n}\text{-Bu}_4\text{N}][\text{Rh}(\text{CO})_2\text{I}_2]$ was also monitored under identical conditions (Figure 3.18).

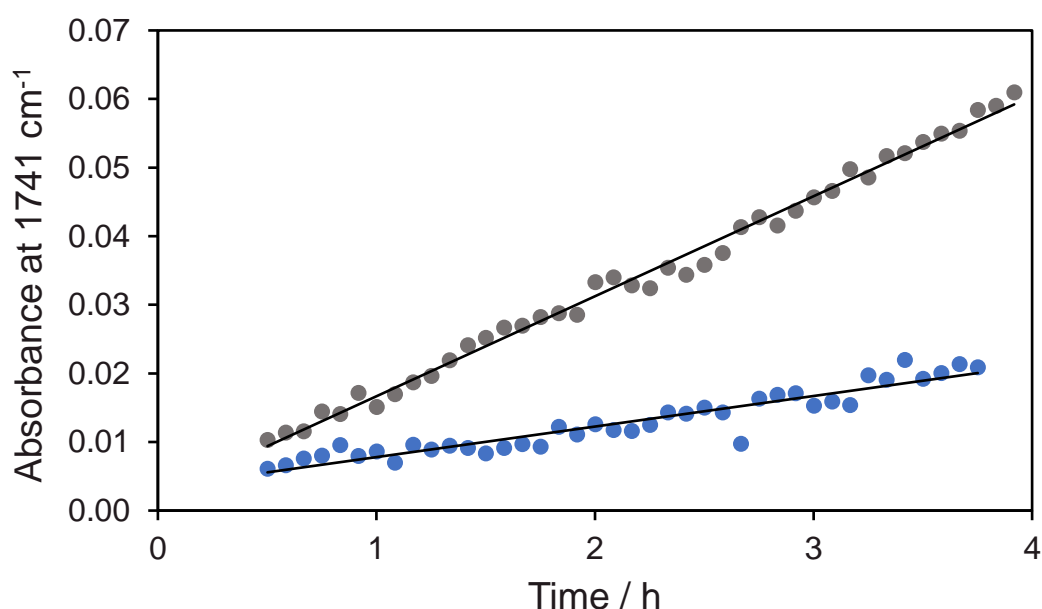
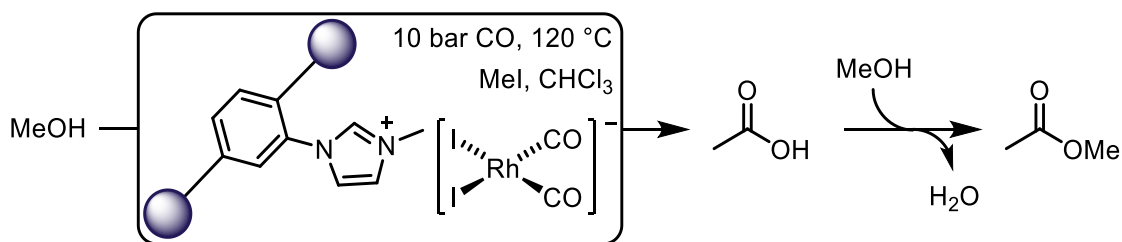


Figure 3.18. Plot of absorbance vs. time for $\nu(\text{CO})$ band of methyl acetate during methanol carbonylation catalysed by $\text{Rh@UiO-66-b/imb-Me}_{97\%}$ (blue) and $[\textit{n}\text{-Bu}_4\text{N}][\text{Rh}(\text{CO})_2\text{I}_2]$ (grey) in CHCl_3 at 120 °C (10 bar CO, 0.8 M MeI, 2.5 M MeOH).

The TOF values for heterogeneous and homogeneous catalysts are 6.5 h^{-1} and 21.8 h^{-1} , respectively (based on Rh content, Appendix 7.2). The lower TOF value for the MOF-supported catalyst is consistent with limitations in diffusion in the microporous support.



Scheme 3.12. Reaction between methanol and carbon monoxide catalysed by MOF-encapsulated cis -[Rh(CO)₂I₂]⁻ to form acetic acid, followed by esterification with excess methanol to form methyl acetate.

The powder X-ray diffraction pattern of the recovered material following catalysis indicated crystallinity and phase purity of the MOF is retained (Figure 3.19).

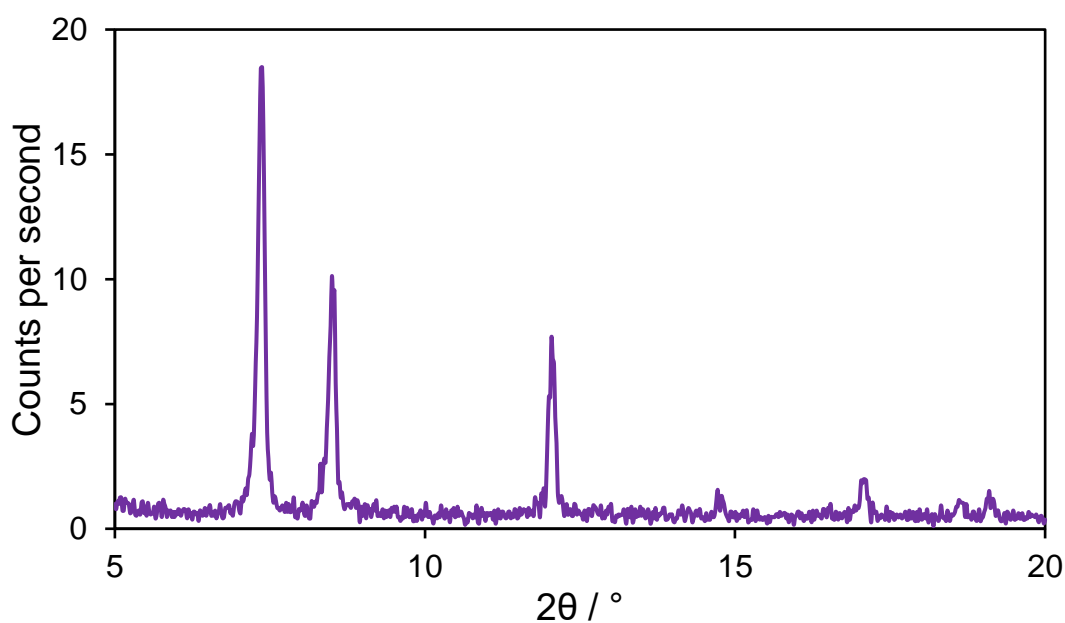


Figure 3.19. PXRD pattern of recovered MOF-supported catalyst.

Subsequent testing of the recovered material shows that it retains activity comparable with the first experiment (Figure 3.20).

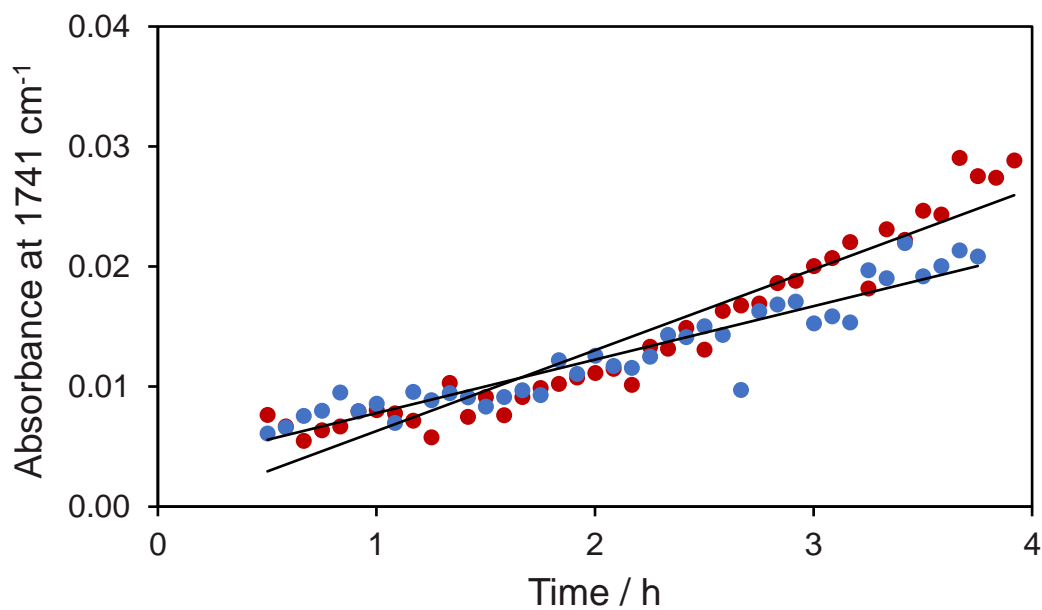


Figure 3.20. Absorbance vs. time plots for the $\nu(\text{CO})$ band of methyl acetate during methanol carbonylation catalysed by Rh@UiO-66-b/imb-Me_{97%} (blue) and a subsequent experiment with the recovered material (red) in CHCl₃ at 120 °C (10 bar CO, 0.8 M MeI, 2.5 M MeOH).

3.4. Attempted single crystal growth

It was attempted to grow crystals of UiO-66-b/imb and UiO-66-b/imb-Me of suitable quality for single crystal X-ray diffraction analysis at Diamond Light Source Beamline I24. The method used was based on a modified procedure reported by Øien *et al.* for the preparation of single crystals of UiO-66.⁸

Two mixed-linker syntheses were attempted; one using a 1:5 mixture of **H₂imbdc** and **H₂bdc** and the other a 1:5 mixture of [**H₂imbdc-Me**]I and **H₂bdc**. Scanning electron microscope (SEM) imaging of these samples (Figure 3.21) indicated crystals of about 1 μm and smaller in size. Unfortunately, the minimum size required for single crystal X-ray diffraction analysis at Diamond Light Source Beamline I24 is 5 μm .

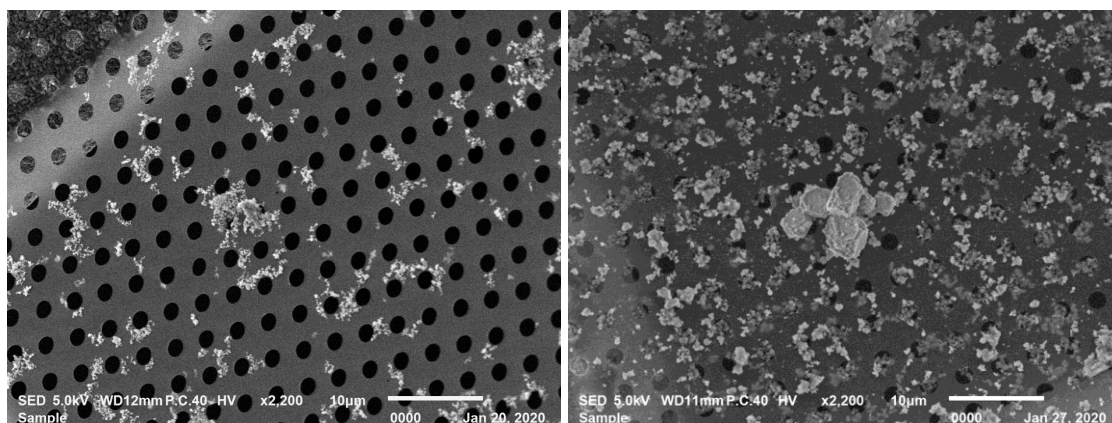


Figure 3.21. SEM images of samples of UiO-66-b/imb (L) and UiO-66-b/imb-Me (R) (from attempted synthesis for single crystal diffraction).

Furthermore, this method of synthesis appeared to result in unidentifiable phases appearing in the powder X-ray diffraction pattern of the product (Figure 3.22). It was therefore not possible to collect any single crystal diffraction data for these imidazole-functionalised systems.

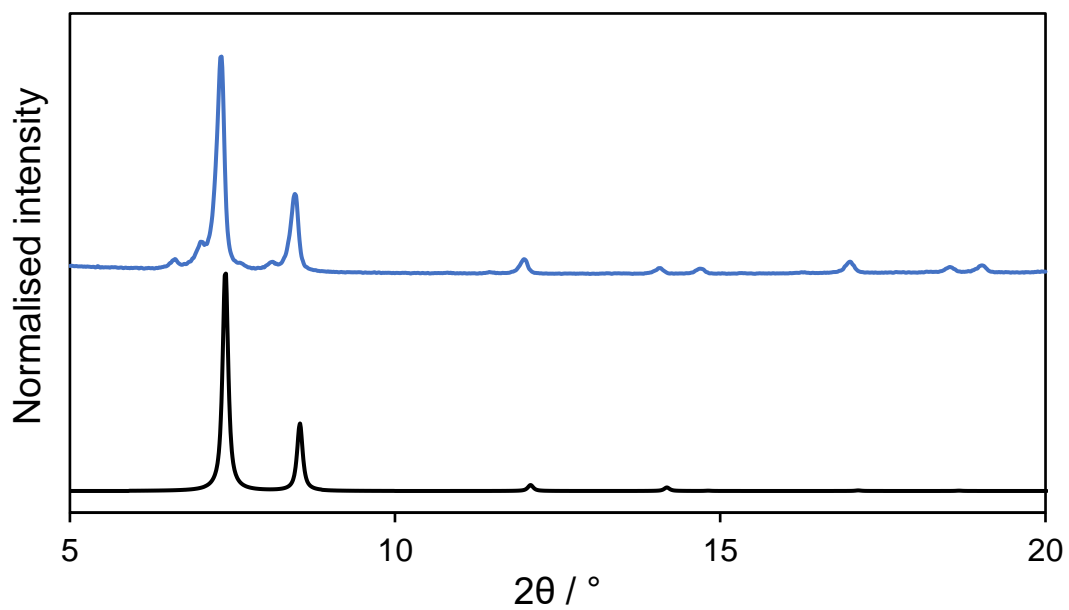


Figure 3.22. X-ray powder pattern of UiO-66-b/imb-Me (blue) (from attempted synthesis for single crystal diffraction) and the simulated pattern based on the crystal structure of UiO-66 at 298 K (black).²

3.5. Discussion of pyridine- and imidazole-containing MOFs

Chapter 2 detailed the investigation of a range of pyridine-containing MOFs for the heterogenisation of *cis*-[Rh(CO)₂I₂]⁻. None of the systems investigated could be fully quaternised, and this resulted in a mixture of covalently and ionically incorporated rhodium dicarbonyl species being present upon reaction with [Rh(CO)₂I]₂, thus complicating the IR spectra. It was also found that UiO-66-py was more stable to the harsh quaternisation conditions than the longer linker UiO-67-type MOFs investigated.

This chapter has described how imidazole-containing UiO-66-type MOFs are both stable to harsh quaternisation conditions and undergo quaternisation more readily than their pyridine-containing counterparts. A mixed-linker approach was found to maximise conversion to cationic form, and the optimised MOF (UiO-66-b/imb) achieved a near quantitative (97%) conversion to the desired quaternised system.

Reaction of this cationic support with [Rh(CO)₂I]₂ resulted in an IR spectrum with narrow, symmetrical ν(CO) absorptions, implying ionically supported *cis*-[Rh(CO)₂I₂]⁻ was the major product, as desired. This is in contrast with the pyridine-containing MOFs that were studied, all of which gave evidence for a mixture of covalently and ionically incorporated rhodium dicarbonyl species.

3.6. Summary

Imidazole-functionalised UiO-66-type MOFs have been synthesised using both single-linker and mixed-linker synthetic strategies. The MOFs were postsynthetically modified by methylation of the pendant imidazole moiety to form *N*-methylimidazolium cations. In the case of the single-linker MOF (UiO-66-imb), this resulted in 85% conversion of imidazole to *N*-methylimidazolium sites, whereas in the mixed-linker MOF (UiO-66-b/imb) this resulted in 97% conversion, presumably by virtue of the lower steric congestion in the pores.

The postsynthetically modified mixed-linker MOF, UiO-66-b/imb-Me_{97%}, was used to immobilise the active catalyst for the Monsanto process for the carbonylation of methanol to form acetic acid, *cis*-[Rh(CO)₂I₂]⁻, via Coulombic interactions. Volumetric N₂ gas sorption analysis indicated catalyst micropore occupancy. The supported complex was found to undergo the same organometallic reaction sequence with MeI and CO as found in solution.⁶

The MOF-supported catalyst was found to catalyse the carbonylation of methanol, with somewhat lower activity than the homogeneous analogue. The recovered supported catalyst showed similar activity in a repeat experiment, indicating good recyclability, and X-ray powder diffraction indicated that the MOF catalyst had retained its crystallinity.

3.7. References

- 1 J. Liang, R.-P. Chen, X.-Y. Wang, T.-T. Liu, X.-S. Wang, Y.-B. Huang and R. Cao, *Chem. Sci.*, 2017, **8**, 1570–1575.
- 2 J. H. Cavka, S. Jakobsen, U. Olsbye, N. Guillou, C. Lamberti, S. Bordiga, K. P. Lillerud, C. Lamberti, S. Bordiga and K. P. Lillerud, *J. Am. Chem. Soc.*, 2008, **130**, 13850–13851.
- 3 M. Topuzogullari, *J. Polym. Res.*, 2018, **25**, 1–7.
- 4 A. Fulford, C. E. Hickey and P. M. Maitlis, *J. Organomet. Chem.*, 1990, **398**, 311–323.
- 5 J. Liang, Y.-Q. Xie, X.-S. Wang, Q. Wang, T.-T. Liu, Y.-B. Huang and R. Cao, *Chem. Commun.*, 2017, **54**, 342–345.
- 6 H. Adams, N. A. Bailey, B. E. Mann, A. G. Kent, C. P. Manuel and C. M. Spencer, *J. Chem. Soc., Dalton Trans.*, 1988, 2–9.
- 7 A. Haynes, P. M. Maitlis, R. Quyoun, C. Pulling, H. Adams, S. E. Spey and R. W. Strange, *J. Chem. Soc., Dalton Trans.*, 2002, 2565–2572.
- 8 S. Øien, D. Wragg, H. Reinsch, S. Svelle, S. Bordiga, C. Lamberti and K. P. Lillerud, *Cryst. Growth Des.*, 2014, **14**, 5370–5372.

Chapter 4 Dispersible Microporous Polymers with Pyridine Moieties

4.1. Introduction

4.1.1. Polymers as supports for methanol carbonylation

Ionic attachment of metal complexes to polymeric supports has been employed for a range of catalytic processes including hydroformylation,¹⁻⁹ hydrogenation,⁹⁻¹⁴ and, pertinently, methanol carbonylation.¹⁵⁻²³ In 1980 Drago *et al.* described the effective immobilisation of *cis*-[Rh(CO)₂I₂]⁻ on polymer supports based on methylated polyvinylpyridines.²³ The carbonylation activity was equal to the homogeneous system at 120 °C with minimal leaching of the supported catalyst.

Following this, Chiyoda and UOP developed the AceticaTM process which employs a polyvinylpyridine resin capable of tolerating high temperatures and pressures.¹⁶ Under the reaction conditions, the pyridyl nitrogen sites become positively charged via methylation, and the anionic catalyst, *cis*-[Rh(CO)₂I₂]⁻, is bound electrostatically to the support. The supported catalyst showed no deactivation after continuous operation for 7,000 hours and its activity is competitive with the homogeneous process, with decreased by-product formation due to the lower water concentration employed.

The mechanism of the polymer-supported process was investigated by Haynes *et al.* using thin films of cross-linked poly(4-vinylpyridine-*co*-styrene-*co*-divinylbenzene)²³ suitable for *in situ* transmission IR spectroscopy. These were postsynthetically *N*-methylated to form a cationic support with iodide counter-ions in the pores. Subsequent reaction with [Rh(CO)₂I]₂ generated the catalyst, *cis*-[Rh(CO)₂I₂]⁻, *in situ*. Mechanistic studies of this material suggested that it undergoes the same organometallic processes as the catalyst in solution, with kinetics of MeI oxidative addition comparable to the solution phase.

Use of porous polymers as supports for rhodium-catalysed methanol carbonylation has continued in recent years.

Crosslinked “spherules” were synthesised by Yuan and co-workers by suspension polymerisation between 2-vinylpyridine and ethylene glycol diacrylate to give a porous material with a surface area of $\sim 75 \text{ m}^2 \text{ g}^{-1}$.²⁴ The authors reported that reaction of this material with $[\text{Rh}(\text{CO})_2\text{Cl}]_2$ resulted in a rhodium dicarbonyl species covalently attached to the polymer via coordination to a pyridyl nitrogen. The surface area of the material dropped to $60 \text{ m}^2 \text{ g}^{-1}$ upon incorporation of the rhodium species. This supported complex was found to catalyse the carbonylation of methanol to acetic acid with high selectivity, and furthermore, the water-gas shift reaction was barely observed for this system.

Yuan and co-workers later reported another crosslinked support synthesised via suspension polymerisation between 2-vinylpyridine, methyl acrylate, and 1,4-divinylbenzene.²⁵ In this work, the material was then reacted with MeI, which resulted in methylation of an estimated 30% of pyridine groups (from fitting of XPS data). Reaction of this cationic support with $(\text{NH}_4)_2[\text{RhCl}_5]$ and reduction with NaBH_4 resulted in monodispersed rhodium nanoparticles. The supported catalyst was found to be active in MeI-free carbonylation of MeOH to form methyl acetate. The catalyst showed reasonable recyclability; over a five-run test, there was a loss of about 25% of activity attributed to leaching of iodide promoters which was mitigated by regeneration with HI. After the second such regeneration, the catalyst activity was found to be about 80% of the fresh catalyst, presumably due to irreversible leaching of rhodium from the support.

Ding and co-workers reacted a previously reported phosphine-containing polymeric support²⁶ with $[\text{Rh}(\text{CO})_2\text{Cl}]_2$ in CH_2Cl_2 which the authors claimed generated a rhodium mono-carbonyl mono-chloride complex stabilised by Lewis basic interactions from

phosphorus sites in the support.²⁷ The supported catalyst slightly outperformed the homogeneous system for methanol carbonylation with a TOF of 1553 h⁻¹ (as compared with 1470 h⁻¹ for the homogeneous system) at 195 °C under 2.5 MPa CO.

Ding and co-workers later synthesised a similar phosphine-containing crosslinked support by pre-treating the monomer with MeI to generate a quaternised phosphine monomer with charge-balancing iodide anions.¹⁷ This monomer was polymerised via solvothermal polymerisation to generate a cationic support, which was treated with [Rh(CO)₂Cl]₂. The authors claimed this resulted in generation of [Rh(CO)I₃]²⁻ in the pores, although no spectroscopic evidence was given to support this assignment. Nonetheless, the system had a reported TOF for the carbonylation of methanol of 3500 h⁻¹ at 195 °C under 3.5 MPa of CO. This represented a marked improvement on the homogeneous process, which had a TOF of 1474 h⁻¹ under similar conditions (190 °C, 4 MPa CO).

A further study by the group of Ding reported a crosslinked polymer synthesised via solvothermal polymerisation using 6,6'-divinyl-2,2'-bipyridine which was reacted with [Rh(CO)₂Cl]₂.²⁸ The IR spectrum of the product of this reaction contained a single ν(CO) absorption at 2065 cm⁻¹ which was rather improbably assigned to [Rh(CO)I₃]²⁻ coordinated to a bipyridyl moiety. This system achieved a TOF for the carbonylation of methanol of 1400 h⁻¹ at 195 °C under 2.5 MPa CO.

4.1.2. Microporous organic polymers

Microporous organic polymers (MOPs) are materials of growing interest due to their high surface area, good chemical and thermal stability, and their ease of functionalisation.²⁹

These attractive properties have led to considerable interest in applications including gas storage and separation,^{30–34} chemosensing^{35–38} and catalysis.^{39,40}

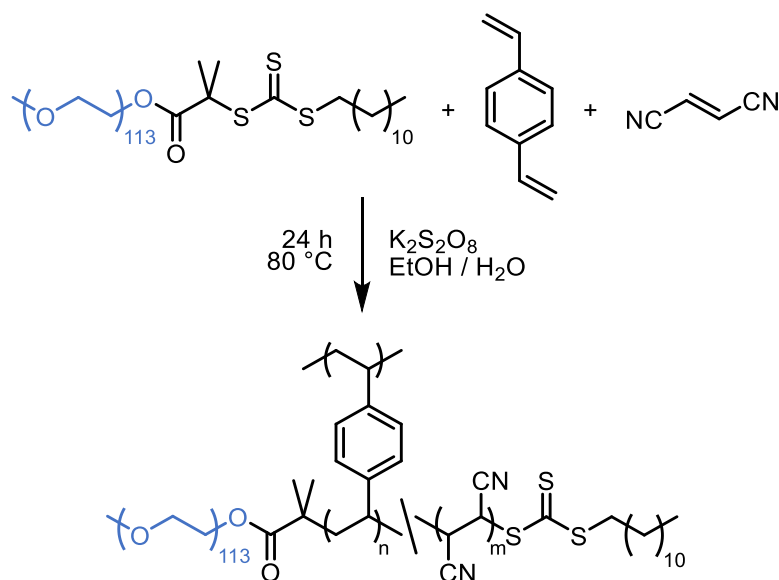
One key disadvantage to most MOPs is their complete insolubility in all solvents, arising from their highly crosslinked structure. Numerous attempts have been made at making these materials processable in solution, such as introduction of solubilising side chains on the monomers^{41,42} and hypercrosslinking at high dilution,⁴³ with mixed success.

Matyjaszewski *et al.* found more success with a three-step process involving the synthesis of vinylbenzyl chloride particles via emulsion polymerisation, followed by crosslinking with stoichiometric quantities of FeCl₃.⁴⁴ Solubilising polymer chains could be added to the unreacted end groups via atom transfer radical polymerisation (ATRP) which resulted in a core-shell structure with a high surface area (562 m² g⁻¹).

Li *et al.* reported the synthesis of hypercrosslinked polymers from the widely available precursors 1,4-divinylbenzene and fumaronitrile.⁴⁵ The bifunctionality of the 1,4-divinylbenzene comonomer led to the crosslinking in the polymer and hence avoided the necessity of stoichiometric quantities of FeCl₃. The synthesised material was found to be microporous with a high surface area (805 m² g⁻¹), but it was completely insoluble in common organic solvents, as with most reported MOPs.

Recently a new class of MOPs have been reported by the Dawson group in Sheffield, which are synthesised using reversible addition-fragmentation chain transfer-mediated polymerisation-induced self-assembly (RAFT-mediated PISA).⁴⁶ The polymerisation of 1,4-divinylbenzene and fumaronitrile was mediated using a polyethylene glycol (PEG) based macro-chain transfer agent (CTA) in an anti-solvent for the growing polymer chain. This resulted in the formation of polymer nanoparticles with a core-shell morphology. The nanoparticle core is crosslinked due to the bifunctional nature of 1,4-divinylbenzene,

and this renders it microporous. The nanoparticles are dispersed in solution due to the covalently bound macro-CTA which forms the shell of the nanoparticles (Scheme 4.1, Figure 4.1).



Scheme 4.1. Synthetic route towards dispersible microporous polymeric nanoparticles highlighting the dispersion-stabilising polyethylene glycol (PEG) chains in blue.

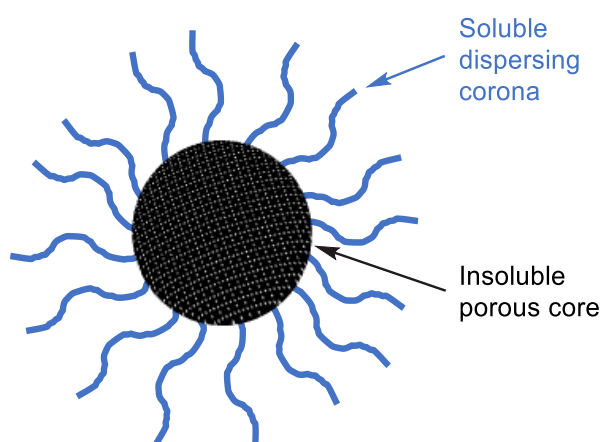


Figure 4.1. Schematic of polymer nanoparticles highlighting the core-shell morphology.

The initial report of these materials demonstrated their utility in sensing applications, but the dispersibility of these nanoparticles makes them attractive candidates for a wide range of applications due to their efficient mixing with solution but also their trivial recovery via centrifugation or addition of antisolvent.

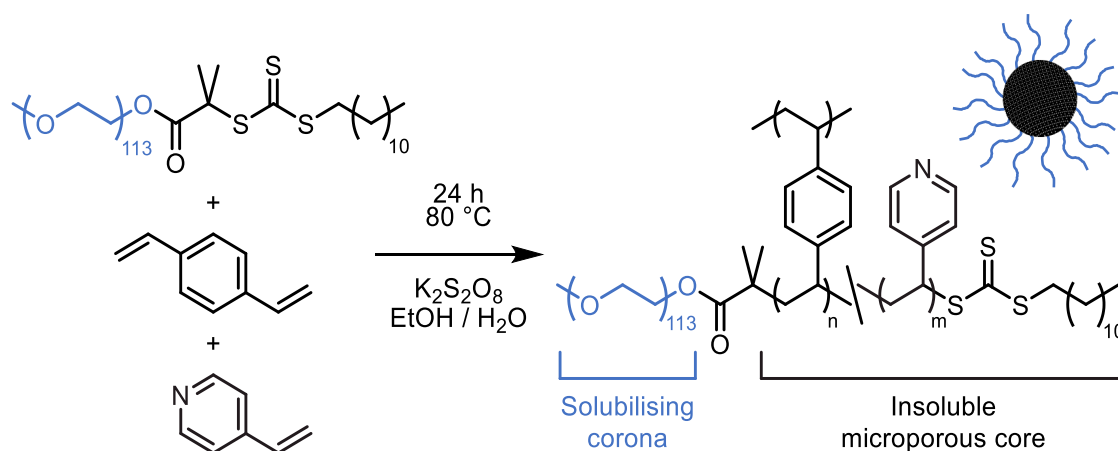
These materials represent ideal supports for catalysis due to their inexpensive synthesis, high surface area, microporosity, dispersibility, and robust chemical and thermal stability.

Recently, nanoparticles of this type were synthesised which incorporated the photocatalytic crosslinker 4,7-bis(4-vinylphenyl)benzo[*c*][1,2,5]thiadiazole, as well as 1,4-divinylbenzene and fumaronitrile.⁴⁷ This material was found to be active for a range of photocatalytic reactions and was dispersible in a variety of solvents, enabling selection of the ideal solvent for any given reaction.

In a further demonstration of the versatility of this novel class of materials, James *et al.* synthesised materials of the type illustrated in Scheme 4.1, substituting acrylic acid for fumaronitrile.⁴⁸ Postsynthetic modification of the acrylic acid functionality in this material with 9-anthracenemethanol via esterification produced a blue-emitting porous polymer. This functionalised porous polymer was used to encapsulate the yellow-emitting fluorophore rhodamine B, resulting in a white-light emitting dispersion.

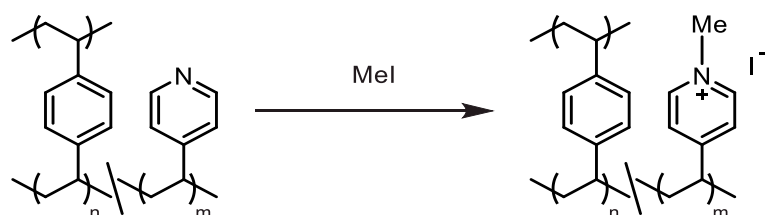
Dispersible microporous polymer nanoparticles containing 4-vinylpyridine (VP) and 1,4-divinylbenzene (DVB) monomers and a polyethylene glycol (PEG) based macro-chain transfer agent (CTA) were synthesised in Sheffield by A. M. James (with whom this work was carried out in collaboration, Scheme 4.2). The PEG-based macro-CTA both mediated the copolymerisation and facilitated the dispersibility of the resulting nanoparticles in a wide range of common organic solvents. The bifunctional nature of

1,4-divinylbenzene led to a hypercrosslinked microporous core, with a BET surface area exceeding $350 \text{ m}^2 \text{ g}^{-1}$.

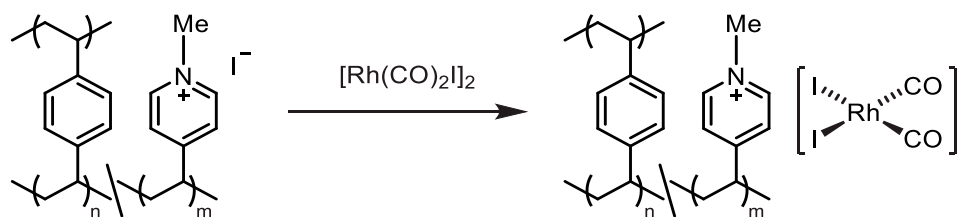


Scheme 4.2. Synthesis of pyridine-containing dispersible microporous polymer nanoparticles.

The use of the 4-vinylpyridine co-monomer in this material presented an opportunity for postsynthetic modification via *N*-methylation using methyl iodide, to form a cationic support, as shown in Scheme 4.3. This cationic material could then be used to heterogenise the Monsanto catalyst, *cis*- $[\text{Rh}(\text{CO})_2\text{I}_2]^-$ (Scheme 4.4).



Scheme 4.3. Proposed postsynthetic modification of polymer nanoparticles via *N*-methylation of the pyridine moiety.



Scheme 4.4. Proposed loading of *cis*-[Rh(CO)₂I]₂⁻ on cationic support.

This chapter describes the synthesis and characterisation of this polymer system, its postsynthetic N-quaternisation, and incorporation and behaviour of the supported rhodium catalyst.

4.2. Synthesis and postsynthetic modification of dispersible microporous polymer nanoparticles

Dispersible microporous polymer nanoparticles were synthesised by James according to a modified reported procedure⁴⁶ using 1,4-divinylbenzene and 4-vinylpyridine monomers and a PEG-based macro-CTA as shown in Scheme 4.2. Elemental analysis of the product revealed lower nitrogen content than would be expected if all of the reactants been incorporated quantitatively. Based on the data, a formula of PEG₁₁₃-*b*-DVB₃₀₀-*co*-VP₆₃ (**1**) was estimated. The low 4-vinylpyridine content is reflected in the low yield calculated for the reaction (~30%).

The material was suspended in CH₂Cl₂ and the UV-Vis spectrum of the dispersion was recorded over 72 h (Figure 4.2). This experiment suggested that over 80% of **1** remained in suspension after 72 h. In contrast, the insoluble analogue to this system (synthesised via simple radical polymerisation between 1,4-divinylbenzene and 4-vinylpyridine) could not be suspended for a single UV-Vis spectrum to be recorded.

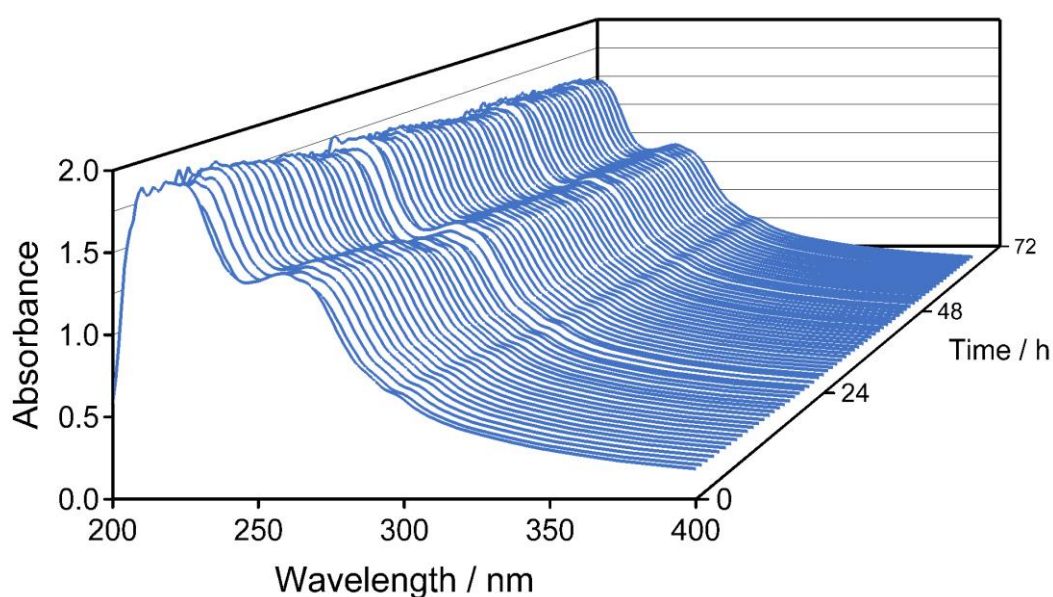
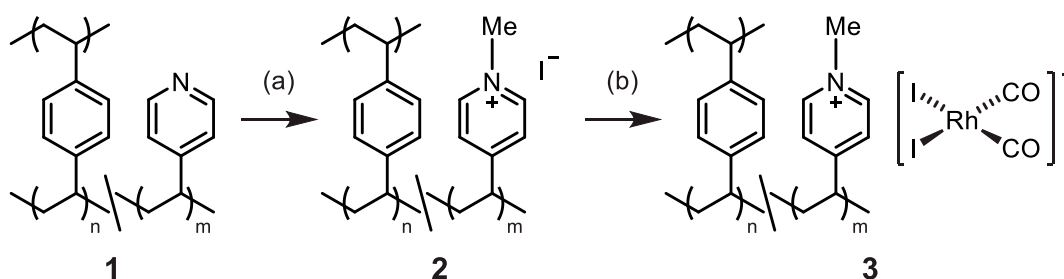


Figure 4.2. Series of UV-Vis spectra of a suspension of **1** in CH₂Cl₂ over 72 h.

This result demonstrates the long-term stability of dispersions of **1** by virtue of the incorporation of the PEG-based hydrophilic coronae.

The neutral polymeric material was reacted with MeI as shown in Scheme 4.5. The product turned from white to yellow after this treatment, as reported in the reactions of analogous crosslinked vinylpyridine copolymers with MeI.²³ Elemental analysis of the product suggests conversion of ~80% of pyridine sites to *N*-methylpyridinium as shown in Table 4.1.



Scheme 4.5. Generation of cationic support (**2**) and subsequent incorporation of *cis*-[Rh(CO)₂I]₂⁻ (**3**); (a) MeI and CHCl₃, 70 °C 72 h; (b) [Rh(CO)₂I]₂ in CHCl₃, RT 16 h.

Table 4.1. Calculated elemental analysis values for neutral polymer, fully quaternised polymer, and ~80% quaternised polymer, along with measured values for **2**.

Composition	% C	% H	% N	% I
PEG ₁₁₃ - <i>b</i> -DVB ₃₀₀ - <i>co</i> -VP ₆₃	86.7	7.8	1.7	0.0
PEG ₁₁₃ - <i>b</i> -DVB ₃₀₀ - <i>co</i> -[VP ⁺ I] ₆₃	75.1	6.9	1.5	13.3
PEG ₁₁₃ - <i>b</i> -DVB ₃₀₀ - <i>co</i> -VP ₁₃ - <i>co</i> -[VP ⁺ I] ₅₀	77.2	7.1	1.5	10.9
2 (experimental)	76.9	6.9	1.7	10.5

These data are consistent with the reactivity shown in Scheme 4.5, indicating generation of a partially cationic support with iodide counter-ions, PEG₁₁₃-*b*-DVB₃₀₀-*co*-VP₁₃-*co*-

[VP⁺I⁻]₅₀ (**2**). This cationic support was treated with a solution of [Rh(CO)₂I]₂ in CHCl₃ to form *cis*-[Rh(CO)₂I]₂⁻ *in situ* as shown in Scheme 4.5. While the initial solution of [Rh(CO)₂I]₂ in CHCl₃ was yellow in colour, over the course of the reaction the supernatant phase gradually became colourless.

There are two potential modes of incorporation of rhodium into the material (Figure 4.3). These are: (i) ionic attachment, where [Rh(CO)₂I]₂ is cleaved by iodide counterions to generate *cis*-[Rh(CO)₂I]₂⁻ *in situ* (denoted as [VP⁺Rh⁻]); (ii) covalent attachment, where a neutral rhodium(I) *cis*-dicarbonyl species is coordinated to an unquaternised pyridyl moiety, [Rh(CO)₂I(pyridyl)] (denoted as (VP-Rh)).

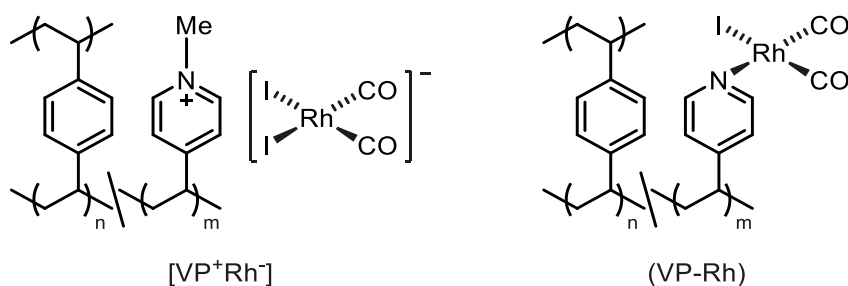


Figure 4.3. Modes of incorporation of Rh into polymer support: ionic attachment (denoted as [VP⁺Rh⁻]) and covalent attachment (denoted as (VP-Rh)).

ICP-MS analysis of **3** indicated a rhodium content of 4.5% by mass. The elemental analysis data of **3** is presented in Table 4.2. Also shown in Table 4.2 are calculated values for quantitative incorporation of rhodium, as well as the values for a composition with 4.5% incorporation of rhodium (in the generic form [Rh(CO)₂I]).

Table 4.2. Calculated elemental analysis values for rhodium-incorporated **2**, along with measured values for **3**.

Composition	% C	% H	% N	% I
PEG ₁₁₃ - <i>b</i> -DVB ₃₀₀ - <i>co</i> -VP ₁₃ - <i>co</i> -[VP ⁺ I] ₅₀ + 4.5% Rh	68.6	6.2	1.3	15.1
PEG ₁₁₃ - <i>b</i> -DVB ₃₀₀ - <i>co</i> -VP ₁₃ - <i>co</i> -[VP ⁺ I] ₅₀ + [Rh(CO) ₂ I] ₄₂	65.4	5.9	1.3	16.7
3 (experimental)	59.0	5.1	1.9	22.0

The recorded ICP-MS and elemental analysis data are inconsistent with one another. The recorded elemental analysis data suggests that [Rh(CO)₂I] was incorporated quantitatively into the polymer, although even then there is significant deviation from the experimental values (Table 4.2). Quantitative incorporation of [Rh(CO)₂I] would lead to a rhodium content of 6.2% by mass, which is at least in the region of the recorded ICP-MS value (4.5%). Quantitative incorporation is supported by the observation of loss of colour in the supernatant phase over the course of the incorporation reaction.

It should be noted that elemental analysis values of these systems are notoriously imprecise due to a range of factors such as incomplete polymerisation and impurities trapped in pores, and so the proposed compositions of samples **1-3** should be treated with some caution.

Successful formation of a majority of *cis*-[Rh(CO)₂I]⁻ in **3** was confirmed via IR spectroscopy (Figure 4.4) which revealed $\nu(\text{CO})$ absorptions at 2059 cm⁻¹ and 1987 cm⁻¹, consistent with the same species in MeOH.⁴⁹ Conversely, reaction of the neutral polymer, **1**, with [Rh(CO)₂I]₂ produced a product with $\nu(\text{CO})$ absorptions at 2080 cm⁻¹ and 2010 cm⁻¹, indicative of a neutral rhodium(I) *cis*-dicarbonyl species, coordinated to a pyridyl moiety (shown as (VP-Rh) in Figure 4.3). This allows an estimate for the composition of **3** as PEG₁₁₃-*b*-DVB₃₀₀-*co*-VP₁₃-*co*-[VP⁺I]₈-*co*-[VP⁺Rh]₄₂.

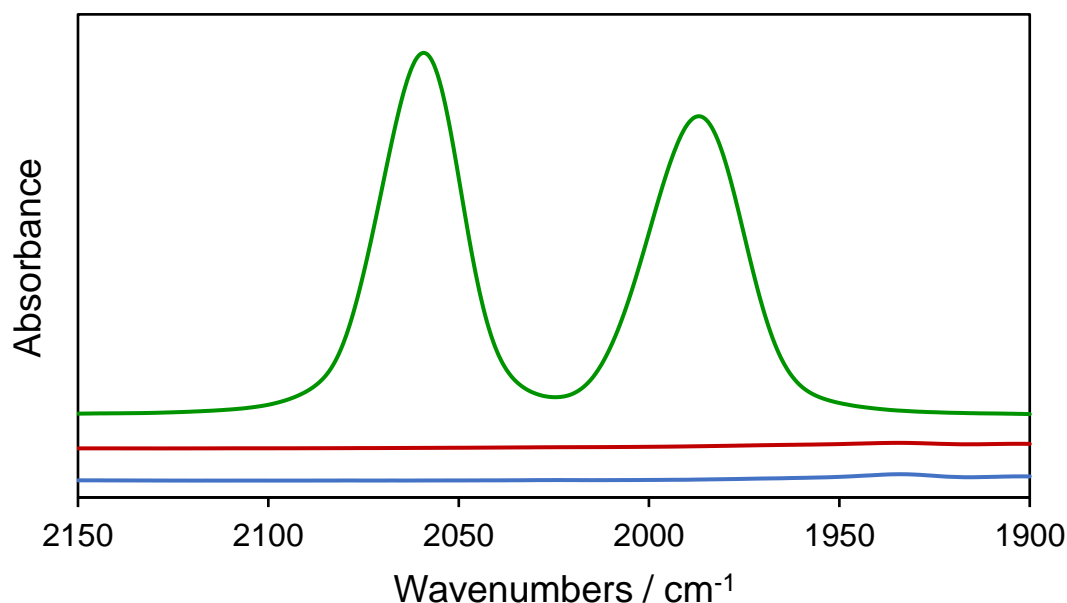


Figure 4.4. Infrared spectra (KBr disc, $\nu(\text{CO})$ region) of **1** (blue), **2** (red), and **3** (green).

Volumetric gas sorption studies were performed using N_2 at 77 K on samples **1-3** (Figure 4.5). In the low relative pressure region ($< 0.1 p/p_0$), there is uptake of N_2 across all samples, with uptake decreasing upon further modification from **1-3**. In the medium relative pressure region ($0.1 - 0.8 p/p_0$) sample **1** adsorbs more gas than samples **2** and **3**, and hysteresis is observed for **1** between the adsorption and desorption cycles. In the high relative pressure region ($> 0.8 p/p_0$), there is large uptake of N_2 for all three samples indicating surface condensation of N_2 .

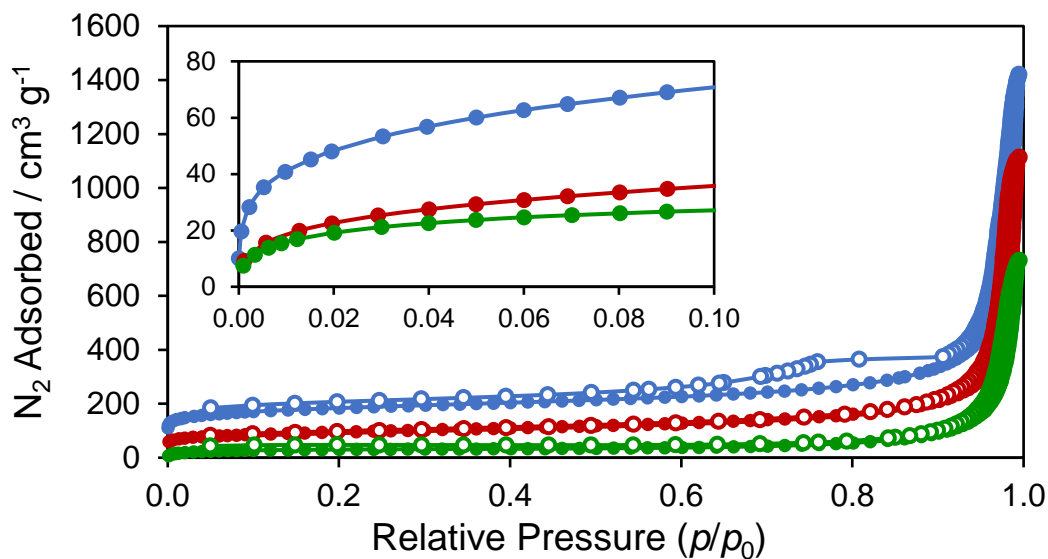


Figure 4.5. Nitrogen adsorption (filled) and desorption (open) isotherms at 77 K for **1** (blue), **2** (red), and **3** (green). Isotherms are offset successively by $50 \text{ cm}^3 \text{ g}^{-1}$. Inset shows the low relative pressure region.

Uptake in the low relative pressure region is caused by filling of micropores (pores with diameters $< 2 \text{ nm}$), and so the lower uptake in samples **2** and **3** is consistent with occupation of these pores by iodide and rhodium complex respectively reducing their accessibility. Uptake in the medium relative pressure region is indicative of filling of mesopores ($2 - 50 \text{ nm}$) due to multilayer adsorption, and this is further evidenced in sample **1** with the hysteresis loop observed between adsorption and desorption cycles, indicative of capillary condensation within the mesopores. The lack of hysteresis in samples **2** and **3** suggests that mesopores present in **1** are being partially occupied by the guests introduced through postsynthetic modification. The large gas uptake in the high partial pressure region is thought to be due to condensation of N_2 between spherical particles, and as such is not an artefact of the pores themselves.

Table 3.2 gives the calculated surface areas, total pore volumes, micropore volumes, and micropore ratios of samples **1-3**. These data show that the initial porous polymer had a

surface area of $366 \text{ m}^2 \text{ g}^{-1}$, but this reduced significantly to $166 \text{ m}^2 \text{ g}^{-1}$ upon quaternisation with MeI to **2**. This change is ascribed to the newly introduced methyl groups and iodide counter-ions occupying the pores of the sample, thereby lowering the available surface area. It is also noted that sample **1** possesses a combination of both micro- and mesopores, as evidenced by the pore size distribution (Figure 4.6), yet after postsynthetic modification the micropore volume is lost and instead the sample contains only mesopores. Indeed, the micropore volume drops significantly from $0.15 \text{ cm}^3 \text{ g}^{-1}$ to $0.04 \text{ cm}^3 \text{ g}^{-1}$ upon incorporation of the rhodium complex in **2** to form **3**. This shows that the methylation and subsequent rhodium incorporation primarily affects the micropores of the sample, though there is also some loss of the smaller mesopores ($< 10 \text{ nm}$). That there is no observable hysteresis in the isotherms of samples **2** and **3** evidences the filling of the mesopores and the lower uptake over the low partial pressure region also suggests significant reduction of micropore volume. These observations suggest that methylation occurs in the pores of the material causing the reduction in surface area. Incorporation of the anionic rhodium complex further lowers the surface area of the material.

Table 4.3. Surface areas and pore volumes of polymer samples **1-3**.

Sample	S_{ABET}^4 / $\text{m}^2 \text{ g}^{-1}$	V_{tot}^5 / $\text{cm}^3 \text{ g}^{-1}$	$V_{0.1}^6$ / $\text{cm}^3 \text{ g}^{-1}$	$(V_{0.1}/V_{\text{tot}})$
1	366	0.53	0.15	0.28
2	166	0.37	0.06	0.16
3	114	0.25	0.04	0.16

⁴ Calculated over the pressure range 0.01-0.15 p/p_0 .

⁵ Calculated at 0.99 p/p_0 .

⁶ Calculated at 0.1 p/p_0 .

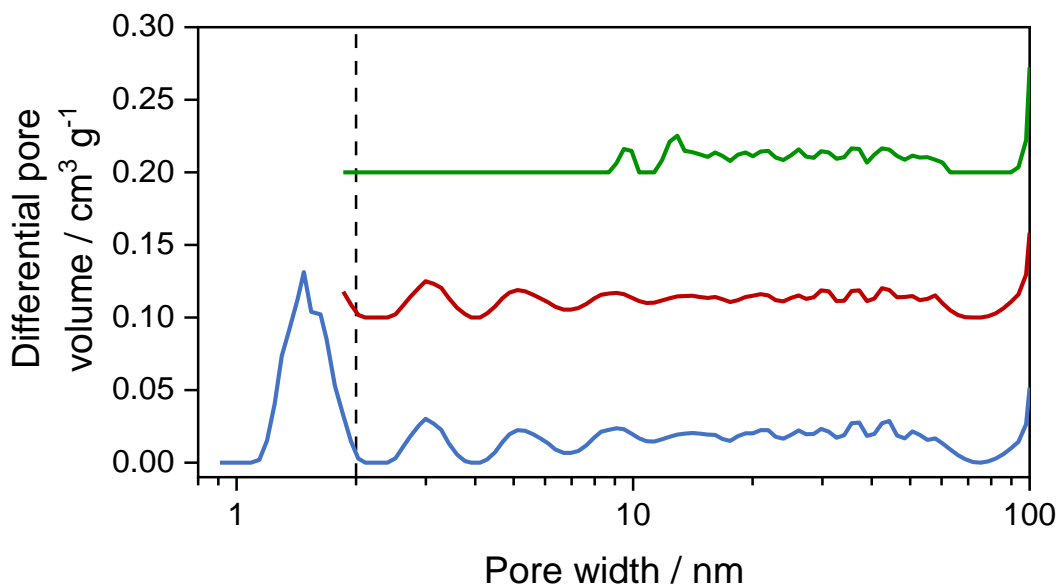


Figure 4.6. NL-DFT differential pore size distribution of **1** (blue), **2** (red), and **3** (green). Area to the left of dashed line represents micropore region. Pore size distributions are offset successively by 0.1 cm³ g⁻¹.

The solid-state CP-MAS ¹³C{¹H} NMR spectra of all three samples show a group of resonances at 110-160 ppm for the aromatic carbon atoms, a broad resonance for the alkyl backbone at ~40 ppm, and a weak resonance at ~70 ppm characteristic of the suspension-stabilising PEG groups (Figure 4.7).

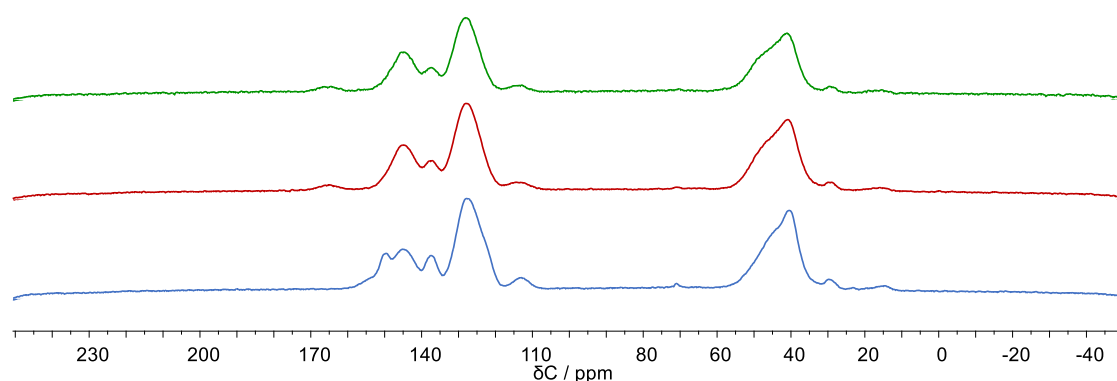


Figure 4.7. Solid-state CP-MAS ¹³C{¹H} NMR spectra of **1** (blue), **2** (red), and **3** (green).

Small angle X-ray scattering (SAXS) studies were performed on a 5% w/w dispersion of each sample in MeOH (Figure 4.8). The fitting of this data is detailed in Appendix 7.4. Fitting suggests an analogous morphology to the reported example;⁴⁶ aggregates of smaller assemblies linked together (illustrated in Figure 4.9), presumably due to crosslinking both within and between the particles as a result of the bifunctionality of the 1,4-divinylbenzene monomer used. Table 4.4 gives the calculated mean diameter of both the primary particles (D_1) and the aggregates (D_2).

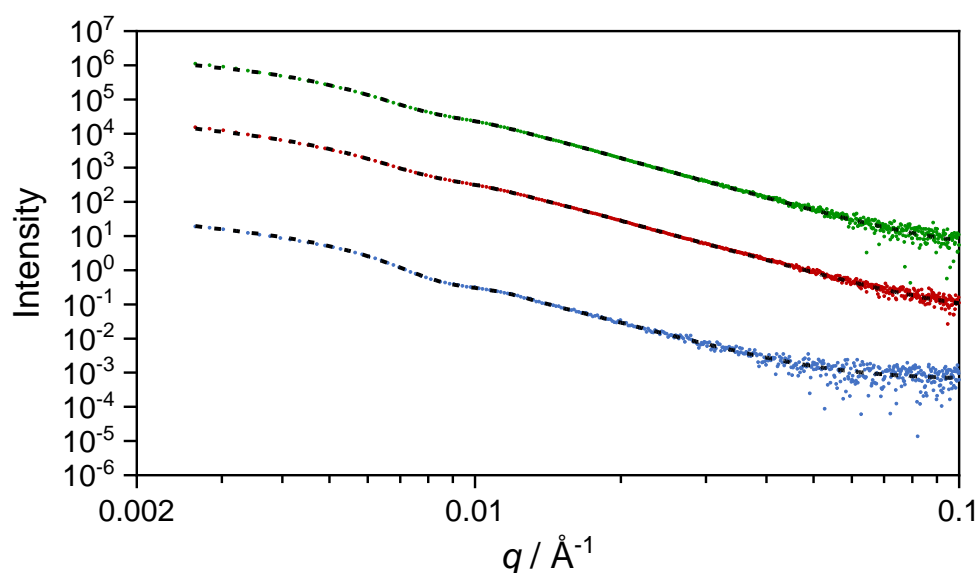


Figure 4.8. Small angle X-ray scattering of sample **1** (blue), **2** (red), and **3** (green) along with two-population fitting (dashed lines). Datasets are offset successively by a factor of 100.

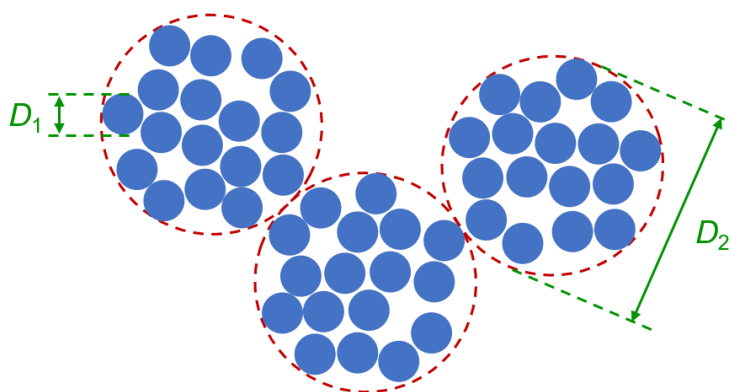


Figure 4.9. Schematic of particle aggregate morphology.

Table 4.4. SAXS particle analysis for samples **1-3** where D_1 is the mean diameter of the primary particles and D_2 is the mean diameter of the aggregates.

Sample	D_1 / nm	D_2 / nm
1	25.2 ± 27.1	101.3 ± 15.7
2	31.6 ± 19.8	103.1 ± 20.6
3	34.2 ± 20.3	104.8 ± 19.2

Transmission electron microscopy (Figure 4.10) confirmed that each sample consisted of aggregates of smaller assemblies, as predicted by SAXS. This result also supported the assertion that the N_2 uptake at high relative pressure seen in Figure 4.5 is a result of condensation between the spherical nanoparticles.

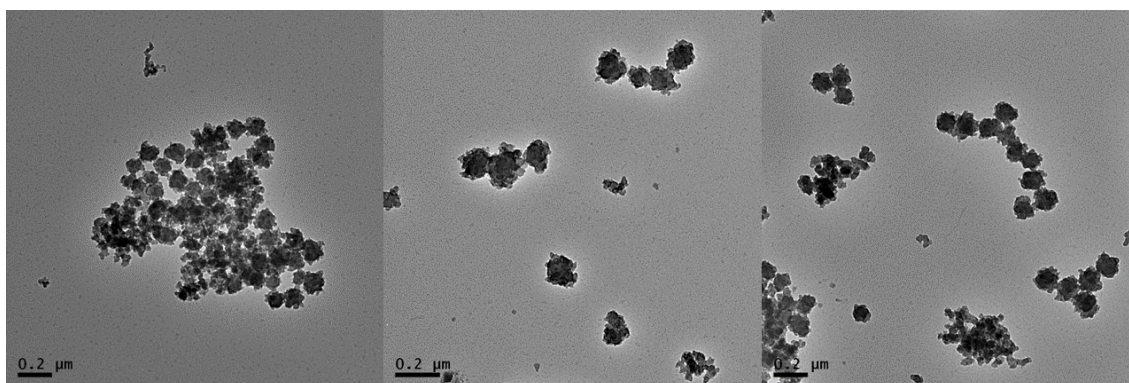


Figure 4.10. From left to right: transmission electron microscopy images of samples **1**, **2** and **3** respectively.

4.3. Reaction of supported cis - $[Rh(CO)_2I_2]^-$ with MeI

After soaking a sample of **3** in MeI overnight the IR spectrum of the product displayed one terminal metal carbonyl absorption at 2058 cm^{-1} , as well as a broad absorption in the acetyl region at around 1700 cm^{-1} (Figure 4.11). These data indicate that the supported complex undergoes oxidative addition of MeI, followed by methyl migration onto an adjacent carbonyl (Scheme 4.6), analogous to the solution chemistry. Upon exposure of this product to a CO atmosphere, the IR spectrum gradually evolved to resemble that of pristine **3** (Figure 4.11). By contrast, exposure of the oxidative addition product to an N_2 atmosphere resulted in no change in the IR spectrum, suggesting CO had associated and acetyl iodide was reductively eliminated to reform cis - $[Rh(CO)_2I_2]^-$. A shoulder at $\sim 2080\text{ cm}^{-1}$ could indicate either the intermediate $trans$ - $[Rh(CO)_2(COMe)I_3]^-$, found in solution studies prior to reductive elimination of MeCOI, or a by-product $trans$ - $[Rh(CO)_2I_4]^-$ from reaction of cis - $[Rh(CO)_2I_2]^-$ with I_2 , or $trans$ - $[Rh(CO)_2HI_3]^-$ from reaction with HI.

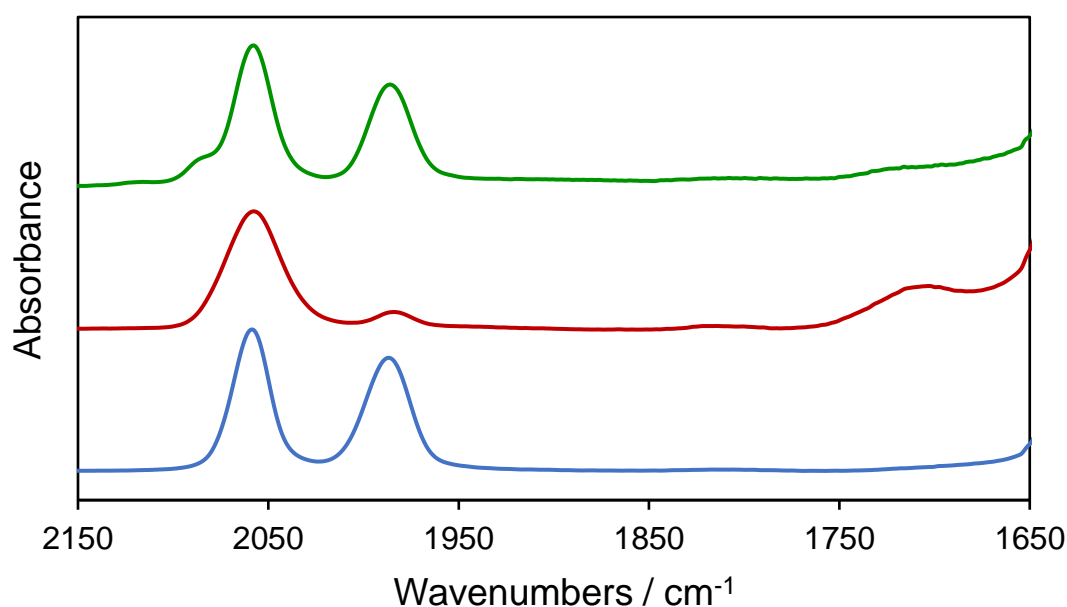
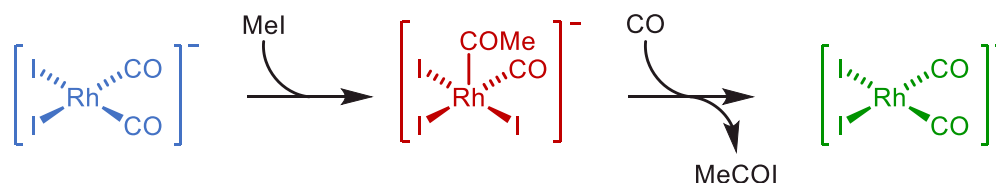


Figure 4.11. IR spectra (KBr disc, $\nu(CO)$ region) of pristine **3** (blue), after soaking in MeI (red), and after exposure to CO (green).



Scheme 4.6. Reaction of encapsulated $\text{cis-}[\text{Rh}(\text{CO})_2\text{I}_2]^-$ with MeI and CO.

Due to the stability of suspensions of these nanoparticles, the reaction between **3** and MeI could be monitored *in situ* using IR spectroscopy. The terminal $\nu(\text{CO})$ region of the IR spectra over the course of one of these experiments is shown in Figure 4.12.

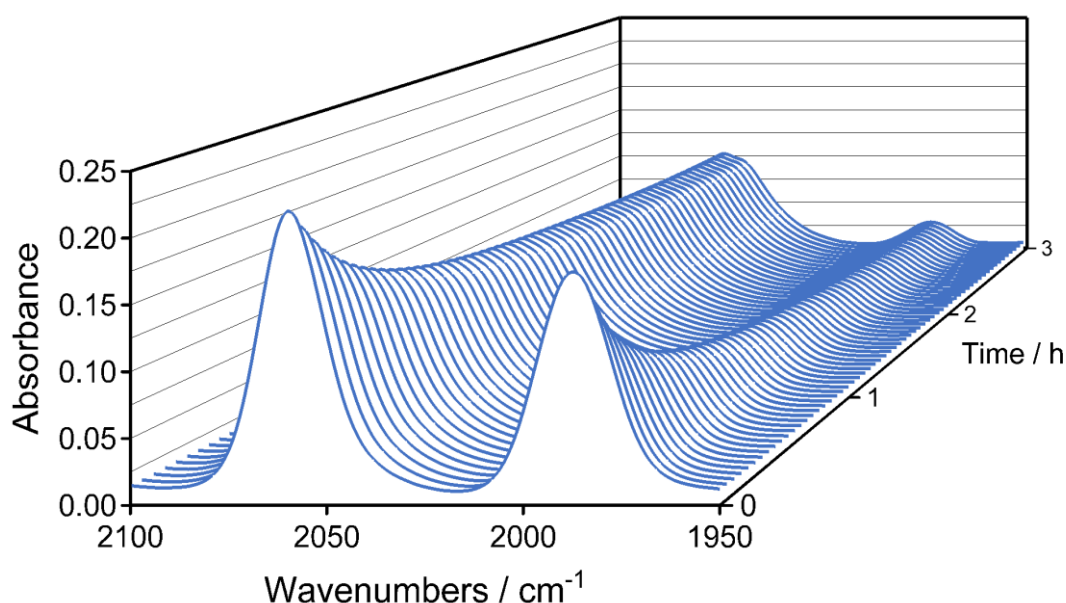


Figure 4.12. Series of IR spectra ($\nu(\text{CO})$ region) during reaction of **3** with 1 M MeI in CH_2Cl_2 (298 K).

The absorbance value of the anti-symmetric $\nu(\text{CO})$ band at 1987 cm^{-1} was recorded over time during the reaction. Pseudo first-order conditions were ensured by the use of an excess of MeI. If the rate is first order in Rh(I) complex, the intensity of this band would be expected to follow an exponential decay that could be fitted using Equation 4.1, where A_t is absorbance at a given time (t), A_∞ is the absorbance at infinite time, A_0 is the initial absorbance value and k_{obs} is the pseudo first-order rate constant. Figure 4.13 shows a

plot of the kinetic data for one of these experiments, with curve fitting using Equation 4.1.

$$A_t = A_\infty + (A_0 - A_\infty)e^{-k_{obs} \times t}$$

Equation 4.1.

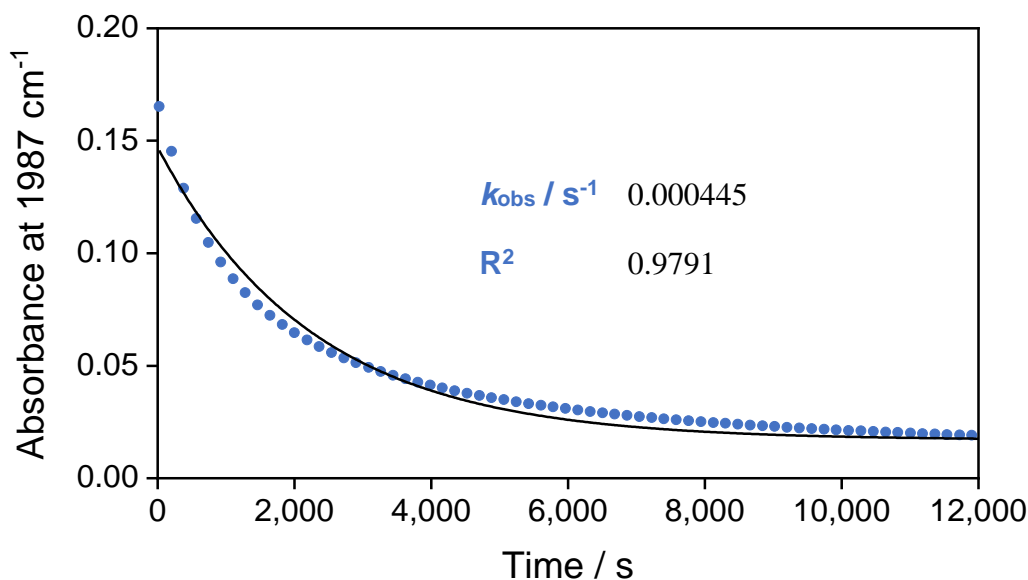


Figure 4.13. Decay of IR absorption at 1987 cm⁻¹ with exponential curve fit during reaction of **3** with 1 M MeI in CH₂Cl₂ (298 K).

It is clear that the exponential decay shown in Figure 4.13 does not describe the data perfectly. There appears an initial phase which is quicker than that accounted for by the fitting, and then a second phase which is slower.

It was therefore attempted to fit the data using a double exponential decay, Equation 4.2, where two separate pseudo first-order rate constants (k_{obs}^1 and k_{obs}^2) contribute to the decay. In Equation 4.2, A_1 and A_2 refer to separate starting absorbances for each decay. The double exponential decay fitting of one of these experiments is shown in Figure 4.14.

$$A_t = A_\infty + A_1 e^{-k_{obs}^1 \times t} + A_2 e^{-k_{obs}^2 \times t}$$

Equation 4.2.

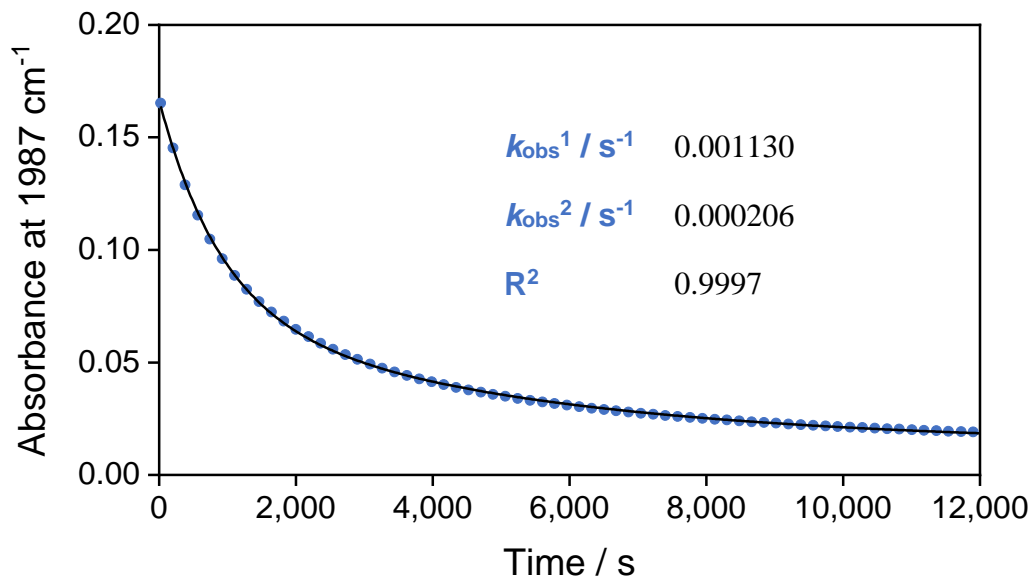


Figure 4.14. Decay of IR absorption at 1987 cm^{-1} with double exponential curve fit during reaction of **3** with 1 M MeI in CH_2Cl_2 (298 K).

Figure 4.14 shows that a double exponential decay fits the data much more closely than the single exponential fit shown in Figure 4.13, as reflected in its R^2 value. Experiments of this sort were repeated across a range of MeI concentrations and similar behaviour was observed in all cases, with a double exponential decay providing a better fit to the data. The derived pseudo first-order rate constants are collected in Table 4.5. All traces are given in Appendix 7.5.

Table 4.5. Pseudo first-order rate constants for single exponential decay fit (k_{obs} , Equation 4.1) and double exponential decay fit (k_{obs}^1 , k_{obs}^2 , Equation 4.2) and their R^2 values at a range of MeI concentrations in CH_2Cl_2 (298 K).

[MeI] / mol dm ⁻³	$10^4 \times k_{\text{obs}}$ / s ⁻¹	R^2	$10^4 \times k_{\text{obs}}^1$ / s ⁻¹	$10^4 \times k_{\text{obs}}^2$ / s ⁻¹	R^2
1.0	4.44	0.9791	11.30	2.06	0.9997
2.1	6.25	0.9822	13.34	3.44	0.9998
4.2	10.01	0.9890	17.46	5.15	0.9997
6.2	13.00	0.9862	29.02	5.05	1.0000
8.3	16.52	0.9953	28.88	6.09	1.0000

Figure 4.15 shows the derived k_{obs}^1 and k_{obs}^2 values plotted against the concentration of MeI. There is a linear dependence between the variables plotted, and the gradients can be equated to second order rate constants for the oxidative addition of MeI to **3** in CH_2Cl_2 , k_2^1 and k_2^2 .

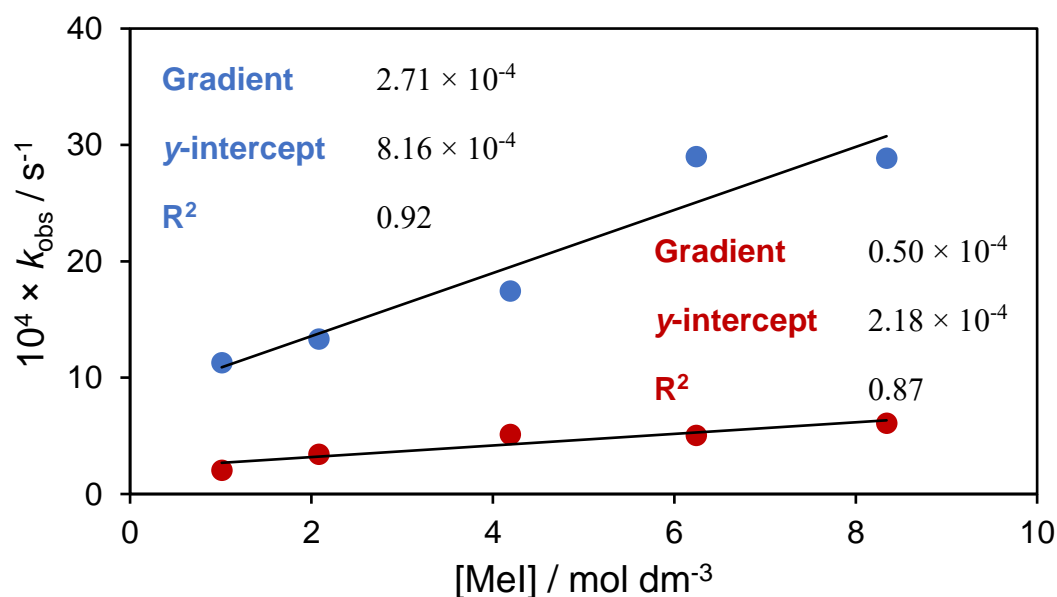


Figure 4.15. Plot of k_{obs}^1 (blue) and k_{obs}^2 (red) vs. MeI concentration for oxidative addition reaction of **3** in CH_2Cl_2 (298 K).

The k_2^1 value for this system was calculated as $27.1 \times 10^{-5} \text{ mol}^{-1} \text{ dm}^3 \text{ s}^{-1}$ and the k_2^2 value was $5.0 \times 10^{-5} \text{ mol}^{-1} \text{ dm}^3 \text{ s}^{-1}$ at 298 K in CH_2Cl_2 (Figure 4.15). The chemical significance of these two rate constants is not immediately clear, but it can be speculated that they may correlate to rates at different sites within the polymer (for instance, surface *vs.* bulk rates). It is unlikely that these rates correspond to the rates for $[\text{VP}^+\text{Rh}^-]$ and (VP-Rh) (Figure 4.3) as the anionic species has been found to undergo oxidative addition *ca.* 100 times faster than the neutral.⁵⁰ Interestingly, both of these rates are greater than the k_2 value for the homogeneous analogue, $[\textit{n}\text{-Bu}_4\text{N}][\text{Rh}(\text{CO})_2\text{I}_2]$ ($2.7 \times 10^{-5} \text{ mol}^{-1} \text{ dm}^3 \text{ s}^{-1}$ at 298 K in CH_2Cl_2).⁴⁹ They are also higher than that reported for the insoluble polymer system previously studied by Haynes *et al.* ($2.6 \times 10^{-5} \text{ mol}^{-1} \text{ dm}^3 \text{ s}^{-1}$),⁵⁰ suggesting that the dispersibility of the material in the present study contributes to the enhanced rate.

Surprisingly, the plots shown in Figure 4.15 have non-zero intercepts. The reason for this is again uncertain but it may be due to the inhomogeneous nature of these materials, which could alter the effective concentration of MeI in the pores of the material versus the bulk solution.

Variable temperature studies were also carried out in CH_2Cl_2 and an Eyring plot of the resulting data is shown in Figure 4.16, along with previously measured values for the homogeneous analogue, $[\textit{n}\text{-Bu}_4\text{N}][\text{Rh}(\text{CO})_2\text{I}_2]$.⁴⁹

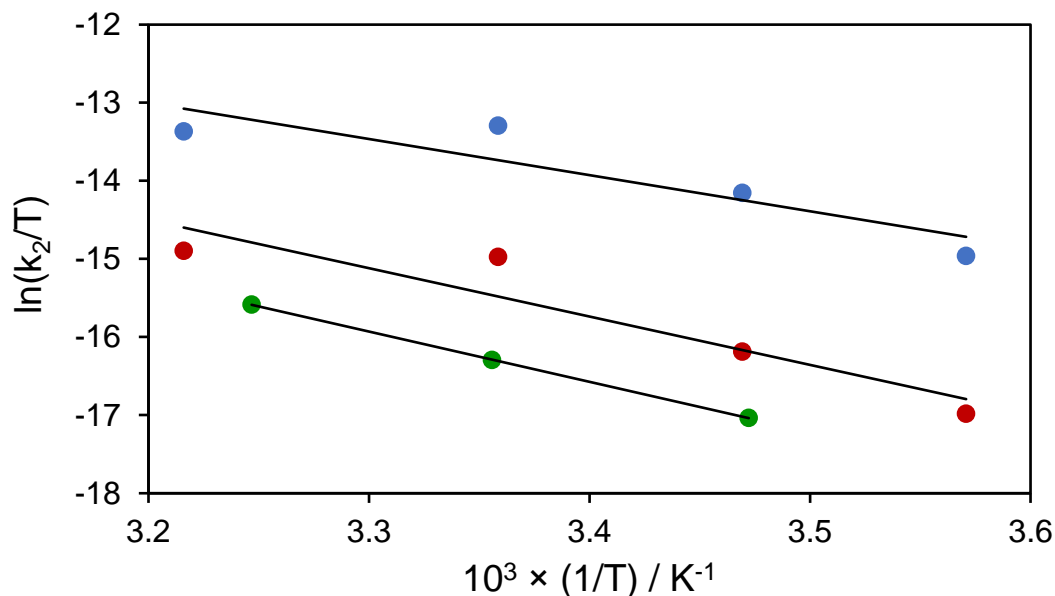


Figure 4.16. Eyring plot to determine activation parameters ΔH^\ddagger and ΔS^\ddagger for the oxidative addition of MeI to **3** (k_2^1 , blue; k_2^2 , red) and $[n\text{-Bu}_4\text{N}][\text{Rh}(\text{CO})_2\text{I}_2]$ (green) in CH_2Cl_2 .⁴⁹

The Eyring plots shown in Figure 4.16 show significant deviation from linearity and therefore lead to large uncertainties in the derived activation parameters; for k_2^1 , $\Delta H^\ddagger = 38 \pm 13 \text{ kJ mol}^{-1}$ and $\Delta S^\ddagger = -183 \pm 45 \text{ J K}^{-1} \text{ mol}^{-1}$; for k_2^2 , $\Delta H^\ddagger = 51 \pm 14 \text{ kJ mol}^{-1}$ and $\Delta S^\ddagger = -153 \pm 47 \text{ J K}^{-1} \text{ mol}^{-1}$. It is notable that the data points for **3** at highest temperature (308 K) are lower than expected by linear extrapolation from the points at lower temperature.

The activation parameters derived from these plots should therefore be treated with caution, and do not allow the rate difference between homogeneous and supported systems to be ascribed to an enthalpic or entropic effect. Nonetheless, the kinetic data clearly indicate a significant rate increase compared with $[n\text{-Bu}_4\text{N}][\text{Rh}(\text{CO})_2\text{I}_2]$ in CH_2Cl_2 .

Similar effects have been observed in the group when using related soluble linear polymers.⁵¹ That work used a soluble poly(4-vinylpyridine-*co*-styrene) polymer that had

been *N*-methylated using MeI as the counterion to *cis*-[Rh(CO)₂I₂]⁻. A k_2 value of $19.7 \times 10^{-5} \text{ mol}^{-1} \text{ dm}^3 \text{ s}^{-1}$ (CH₂Cl₂, 298 K) was measured.

Other work in the group has investigated the use of ionic liquid media as solvents for this process due to their negligible vapour pressure.^{52,53} Iodide-containing ionic liquids have been explored as promising media for this reaction as they have the potential to eliminate the necessity of a separate iodide promoter.⁵⁴⁻⁵⁶ The ionic liquids 1-hexyl-3-methylimidazolium iodide ([C₆mim]I)⁵² and 1-octyl-4-methylpyridinium iodide ([C₈4mpy]I)⁵³ (Figure 4.17) were investigated as solvents in the oxidative addition of MeI to *cis*-[Rh(CO)₂I₂]⁻ and yielded k_2 values of $33.9 \times 10^{-5} \text{ mol}^{-1} \text{ dm}^3 \text{ s}^{-1}$ and $18.3 \times 10^{-5} \text{ mol}^{-1} \text{ dm}^3 \text{ s}^{-1}$, respectively (298 K), both notably faster than the rate in CH₂Cl₂.

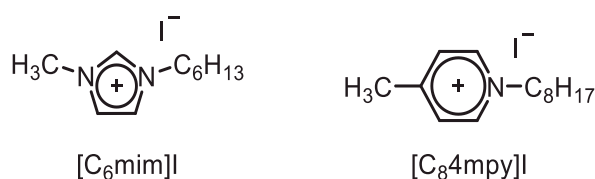
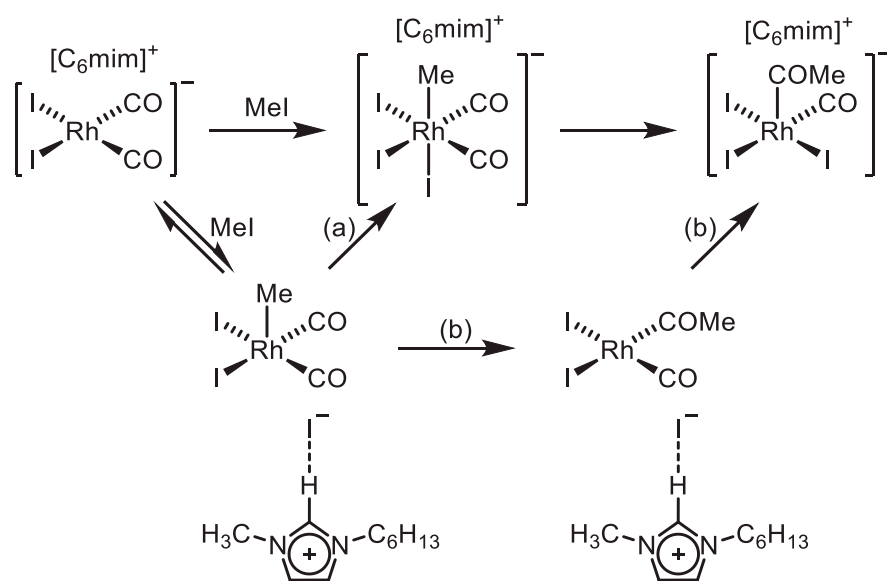


Figure 4.17. The structures of room-temperature ionic liquids [C₆mim]I and [C₈4mpy]I.

The k_2 values for these ionic liquid systems suggested a significant cation effect on the rate of reaction. It has been suggested that hydrogen bonding of the cation with the free iodide anion generated upon the S_N2-type oxidative addition step may reduce the energy of the transition state, thus increasing the rate (Scheme 4.7). This would be supported by the larger k_2 value in [C₆mim]I compared to [C₈4mpy]I, as the 4-methylpyridinium cation is expected to be a poorer hydrogen-bond donor than imidazolium.⁵⁷

Another possibility that has been proposed is an alternative pathway, in which methyl migration occurs on the neutral complex formed by S_N2 reaction of [Rh(CO)₂I₂]⁻ with MeI, before iodide association to complete the formal oxidative addition.⁵¹ Density

functional theory (DFT) calculations have indicated a lower activation energy for methyl migration in neutral $[\text{Rh}(\text{Me})(\text{CO})_2\text{I}_2]$ than in anionic $[\text{Rh}(\text{Me})(\text{CO})_2\text{I}_3]^-$, indicating that the migratory insertion could perhaps compete better with the potential reverse $\text{S}_{\text{N}}2$ reaction and increase the net forward rate.⁵⁸ It is possible that a similar effect could arise from ion-pairing interactions of the methylated pyridine moieties in the polymer-supported system.



Scheme 4.7. Proposed hydrogen-bond stabilisation of neutral intermediate in oxidative addition of MeI to $\text{cis}-[\text{Rh}(\text{CO})_2\text{I}_2]^-$ in $[\text{C}_6\text{mim}]\text{I}$. (a) is the typically observed $\text{S}_{\text{N}}2$ -type oxidative addition pathway; (b) is the postulated alternative route.

4.4. Catalytic carbonylation of MeOH with supported *cis*-[Rh(CO)₂I₂]⁻

4.4.1. In MeOH

The reaction between a suspension of **3**, methanol and carbon monoxide was probed by *in situ* high-pressure IR (HPIR) spectroscopy. Briefly, in a typical experiment, **3** was suspended in MeOH via sonication and added to the cell. A mixture of MeOH and MeI was added to give a final MeI concentration of 0.8 M in MeOH. The cell was pressurised with CO (10 bar) and stirred. The IR spectrum of the solution phase at 120 °C was collected every ten minutes over the course of twelve hours.

During the course of the reaction, there is growth of an absorption at 1736 cm⁻¹ (Figure 4.18) which represents the C=O stretch of methyl acetate in MeOH. Methyl acetate is formed when the carbonylation product, acetic acid, esterifies in the presence of an excess of MeOH, as shown in Scheme 4.8. The homogeneous process was also probed under these conditions, as shown in Figure 4.18. The turnover frequency (TOF) values calculated from the slopes of these plots over the first four hours of reaction were 38.9 h⁻¹ and 15.4 h⁻¹ for the polymer-supported catalyst and the homogeneous system respectively (Appendix 7.5).

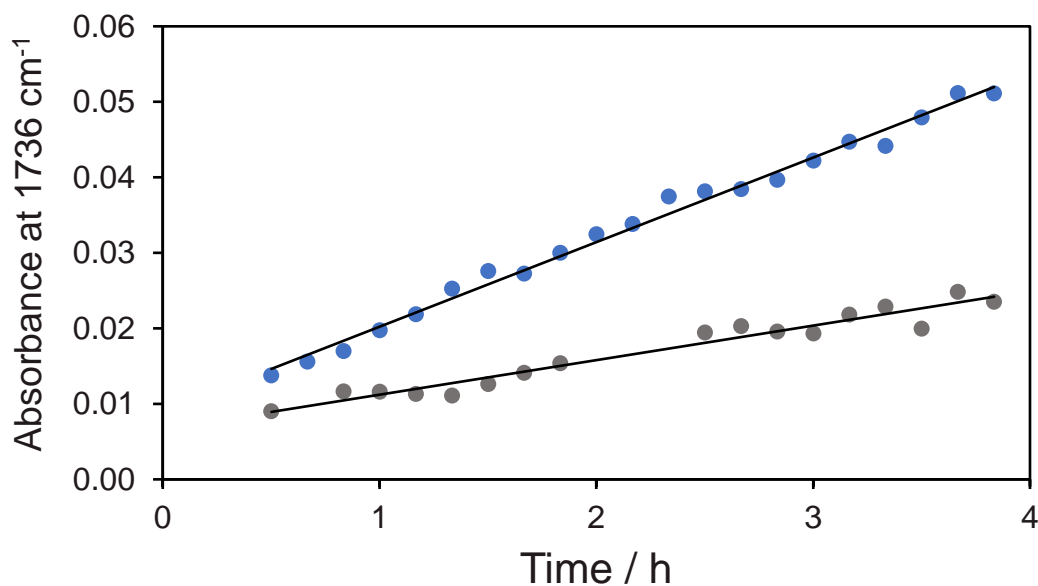
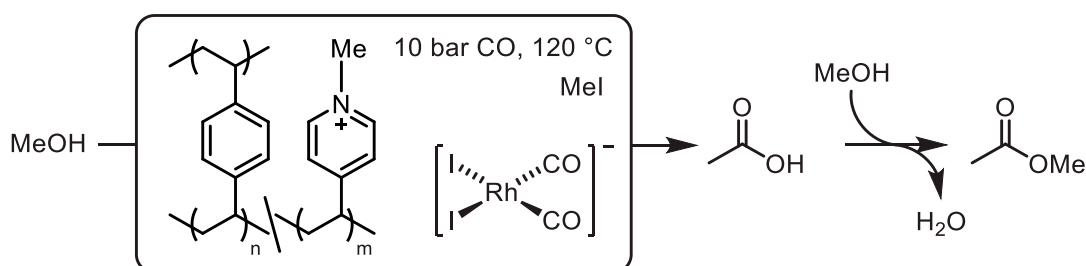


Figure 4.18. Plot of absorbance vs. time for $\nu(\text{CO})$ band of methyl acetate during methanol carbonylation catalysed by **3** (blue) and $[n\text{-Bu}_4\text{N}][\text{Rh}(\text{CO})_2\text{I}_2]$ (grey) in MeOH at 120 °C (10 bar CO, 0.8 M MeI).



Scheme 4.8. Reaction between methanol and carbon monoxide in presence of **3** to form acetic acid, followed by esterification with excess methanol to form methyl acetate.

It is important to note that the derived TOF value for **3** is calculated from the rhodium content of the supported catalyst measured by ICP-MS. As mentioned in Section 4.2, the rhodium content based on the estimated formula is slightly higher than that measured via ICP-MS, which leads to a TOF value of 28.0 h^{-1} . In either case, the TOF value for polymer-supported $\text{cis-}[\text{Rh}(\text{CO})_2\text{I}_2]^-$ is higher than that for the homogeneous system.

Although the initial rate of catalysis for **3** is significantly faster than for the homogeneous system, after ~4 h the rate of formation begins to decrease (Figure 4.19). After 24 h reaction time, the solid was recovered and ICP-MS analysis of the supernatant phase revealed that >95% of the rhodium had leached into solution over this period. Another catalytic reaction was attempted with the recovered solid, but formation of methyl acetate was not observed.

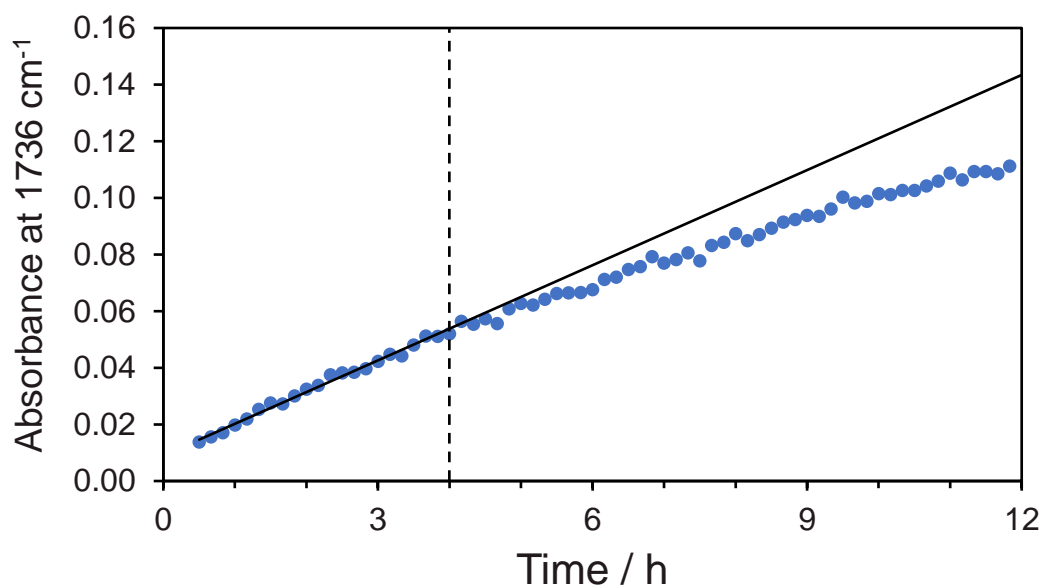
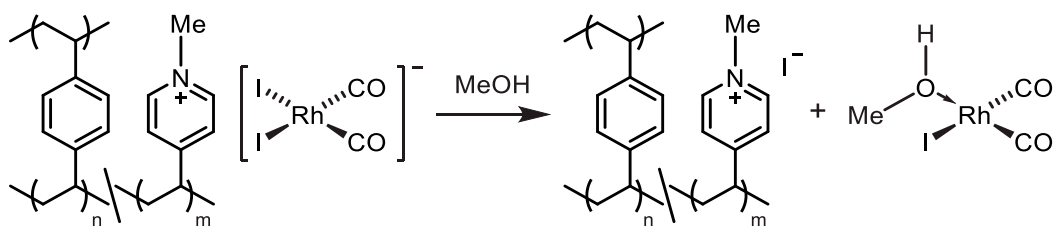


Figure 4.19. Plot of absorbance vs. time for $\nu(\text{CO})$ band of methyl acetate during methanol carbonylation catalysed by **3** in MeOH at 120 °C (10 bar CO, 0.8 M MeI) showing change in gradient over time.

The leaching of rhodium into solution from **3** may be due to displacement of an iodide ligand from $\text{cis-}[\text{Rh}(\text{CO})_2\text{I}_2]^-$ by MeOH (Scheme 4.9), resulting in a neutral complex which is no longer electrostatically attracted to the polymer, as reported for related systems.²³



Scheme 4.9. Leaching of rhodium species by ligand substitution.

4.4.2. In CHCl_3

In view of the leaching observed in MeOH, CHCl_3 was tested as the bulk solvent in the reaction. Due to the difficulties in ascertaining the amount of rhodium in the system discussed in Section 4.4.1, in a typical experiment, **2** was suspended in a solution of $[\text{Rh}(\text{CO})_2\text{I}]_2$ in CHCl_3 via sonication and added to the cell. A mixture of MeOH and MeI in CHCl_3 was added, to give a final mixture of 10% MeOH by volume. The cell was pressurised with CO (10 bar) and stirred. The IR spectrum of the solution phase at 120 °C was collected every five minutes over the course of four hours.

During the course of the reaction, an absorption grows at 1741 cm^{-1} (Figure 4.20) which represents the C=O stretch of methyl acetate in CHCl_3 . The homogeneous process was also probed under these conditions (Figure 4.20). The TOF values calculated from the slopes of these plots for the polymer-supported catalyst and the homogeneous system were 11.3 h^{-1} and 21.8 h^{-1} respectively (Appendix 7.7).

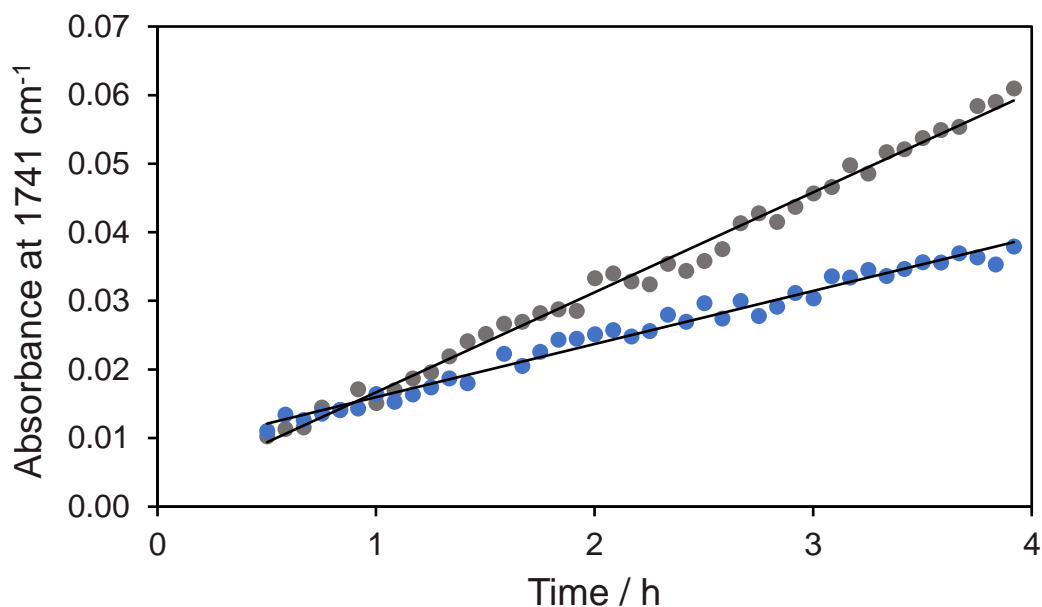


Figure 4.20. Plot of absorbance vs. time for $\nu(\text{CO})$ band of methyl acetate during methanol carbonylation catalysed by **3** (blue) and $[\textit{n}\text{-Bu}_4\text{N}][\text{Rh}(\text{CO})_2\text{I}_2]$ (grey) in CHCl_3 at 120 °C (10 bar CO, 0.8 M MeI, 2.5 M MeOH).

The lower TOF value for **3** was unexpected given the enhancement of the rate-limiting step described in Section 4.3. It is possible that under these conditions (120 °C, 10 bar) more of the catalyst is converting into its inactive form, $\textit{trans}\text{-}[\text{Rh}(\text{CO})_2\text{I}_4]^-$, leading to a lower active catalyst loading. The precise explanation is unclear, however.

Subsequent testing of the recovered material showed that it retained activity comparable with the first experiment (Figure 4.21) and ICP-MS analysis of the supernatant in these reactions revealed about 5% leaching of rhodium from the support in each case.

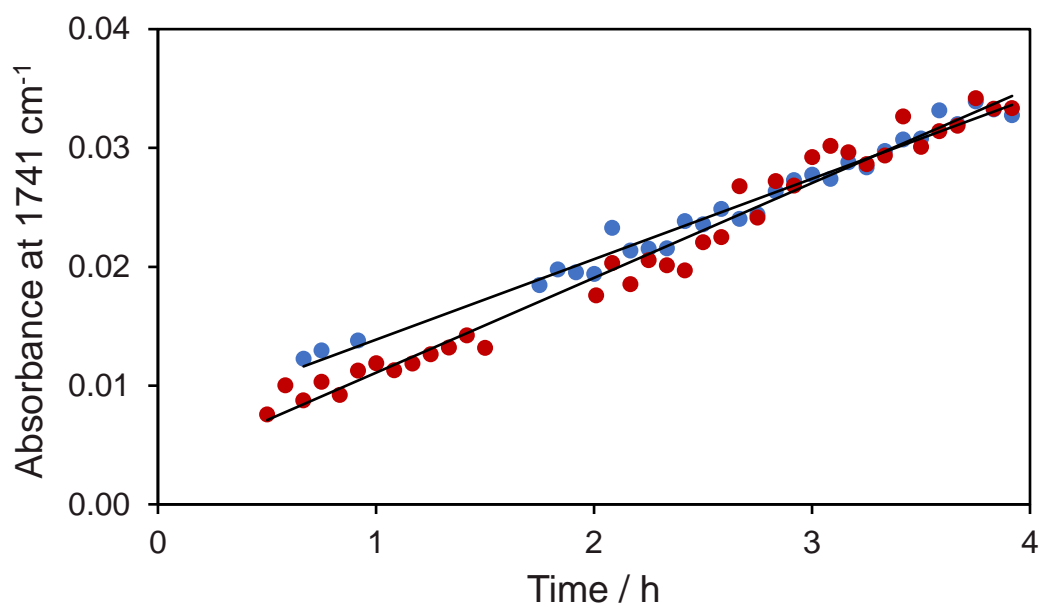


Figure 4.21. Plot of absorbance vs. time for $\nu(\text{CO})$ band of methyl acetate during methanol carbonylation catalysed by **3** (blue) and a subsequent experiment with the recovered catalyst (red) in CHCl_3 at 120 °C (10 bar CO , 0.8 M MeI , 2.5 M MeOH).

4.5. Summary

A novel dispersible microporous polymer material has been postsynthetically modified via *N*-methylation of its 4-vinylpyridine moieties using MeI to generate a cationic support containing iodide counter-ions in its pores. Reaction with $[\text{Rh}(\text{CO})_2\text{I}]_2$ generates the anionic carbonylation catalyst, $\text{cis-}[\text{Rh}(\text{CO})_2\text{I}_2]^-$, which is heterogenised in the micropores via electrostatic interactions. The oxidative addition of MeI to the square-planar Rh(I) complex (the rate limiting step in the Monsanto process for the catalytic carbonylation of methanol) was probed *in situ* using infrared spectroscopy. Kinetic studies revealed that the reaction of $\text{cis-}[\text{Rh}(\text{CO})_2\text{I}_2]^-$ with MeI required fitting using a double exponential decay. Interestingly, both derived k_2 values were larger than for the homogeneous analogue, $[\text{n-Bu}_4\text{N}][\text{Rh}(\text{CO})_2\text{I}_2]$, at 298 K in CH_2Cl_2 .²³ The polymer-supported catalyst was shown to be active for catalytic carbonylation of methanol. Initial activity was higher than the homogeneous analogue in methanol, but substantial leaching from the support was observed. In CHCl_3 , leaching was much reduced, but the catalytic activity was slightly lower than the homogeneous catalyst.

4.6. References

- 1 N. Yoneda, Y. Nakagawa and T. Mimami, *Catal. Today*, 1997, **36**, 357–364.
- 2 J. Balu e and J. C. Bay on, *J. Mol. Catal. A Chem.*, 1999, **137**, 193–203.
- 3 L. Alvila, T. A. Pakkanen, T. T. Pakkanen and O. Krause, *J. Mol. Catal.*, 1992, **71**, 281–290.
- 4 S. C. Tang, T. E. Paxson and L. Kim, *J. Mol. Catal.*, 1980, **9**, 313–321.
- 5 M. E. Ford and J. E. Premech, *J. Mol. Catal.*, 1983, **19**, 99–112.
- 6 I. Guo, B. E. Hanson, I. Toth and M. E. Davis, *J. Mol. Catal.*, 1991, **70**, 363–368.
- 7 I. Toth, B. E. Hanson, I. Guo and M. E. Davis, *Catal. Letters*, 1991, **8**, 209–214.
- 8 E. Schwab and S. Mecking, *Organometallics*, 2001, **20**, 5504–5506.
- 9 R. T. Smith, R. K. Ungar, L. J. Sanderson and M. C. Baird, *Organometallics*, 1983, **2**, 1138–1144.
- 10 Y. Chauvin, D. Commereuc and F. Dawans, *Prog. Polym. Sci.*, 1977, **5**, 95–226.
- 11 I. T oth and B. E. Hanson, *J. Mol. Catal.*, 1992, **71**, 365–371.
- 12 E. Renaud and M. C. Baird, *J. Chem. Soc., Dalton Trans.*, 1992, **0**, 2905–2906.
- 13 D. E. Bergbreiter, B. L. Case, Y. S. Liu and J. W. Caraway, *Macromolecules*, 1998, **31**, 6053–6062.
- 14 M. Kralik, M. Hronec, V. Jorik, S. Lora, G. Palma, M. Zecca, A. Biffis and B. Corain, *J. Mol. Catal. A Chem.*, 1995, **101**, 143–152.
- 15 N. De Blasio, E. Tempesti, A. Kaddouri, C. Mazzocchia and D. J. Cole-Hamilton, *J. Catal.*, 1998, **176**, 253–259.
- 16 N. Yoneda, T. Minami, J. Weiszmann and B. Spehlmann, *Stud. Surf. Sci. Catal.*, 1999, **121**, 93–98.

-
- 17 Z. Ren, Y. Lyu, X. Song, Y. Liu, Z. Jiang, R. Lin and Y. Ding, *Adv. Mater.*, 2019, **1904976**, 1–6.
- 18 R. S. Drago, E. D. Nyberg, A. El A'mma, A. Zombeck, A. El A'mma and A. Zombeck, *Inorg. Chem.*, 1981, **20**, 641–644.
- 19 US Pat., US Pat. 4,328,125, 1982.
- 20 D. Jiang, X. Li and E. Wang, *Macromol. Symp.*, 1996, **105**, 161–166.
- 21 N. De Blasio, M. R. Wright, E. Tempesti, C. Mazzocchia and D. J. Cole-Hamilton, *J. Organomet. Chem.*, 1998, **551**, 229–234.
- 22 N. Yoneda, S. Kusano, M. Yasui, P. Pujado and S. Wilcher, *Appl. Catal. A Gen.*, 2001, **221**, 253–265.
- 23 A. Haynes, P. M. Maitlis, R. Quyoum, C. Pulling, H. Adams, S. E. Spey and R. W. Strange, *J. Chem. Soc., Dalton Trans.*, 2002, 2565–2572.
- 24 S. Zhang, C. Guo, Q. Qian and G. Yuan, *Catal. Commun.*, 2008, **9**, 853–858.
- 25 F. Li, B. Chen, Z. Huang, T. Lu, Y. Yuan and G. Yuan, *Green Chem.*, 2013, **15**, 1600–1607.
- 26 Q. Sun, M. Jiang, Z. Shen, Y. Jin, S. Pan, L. Wang, X. Meng, W. Chen, Y. Ding, J. Li and F. S. Xiao, *Chem. Commun.*, 2014, **50**, 11844–11847.
- 27 Z. Ren, Y. Lyu, S. Feng, X. Song and Y. Ding, *Mol. Catal.*, 2017, **442**, 83–88.
- 28 Z. Ren, Y. Liu, Y. Lyu, X. Song, C. Zheng, S. Feng, Z. Jiang and Y. Ding, *J. Catal.*, 2019, **369**, 249–256.
- 29 N. Chaoui, M. Trunk, R. Dawson, J. Schmidt and A. Thomas, *Chem. Soc. Rev.*, 2017, **46**, 3302–3321.
- 30 R. Dawson, A. I. Cooper and D. J. Adams, *Polym. Int.*, 2013, **62**, 345–352.
- 31 D. M. D'Alessandro, B. Smit and J. R. Long, *Angew. Chem. Int. Ed.*, 2010, **49**, 6058–6082.

- 32 R. Dawson, E. Stöckel, J. R. Holst, D. J. Adams and A. I. Cooper, *Energy Environ. Sci.*, 2011, **4**, 4239–4245.
- 33 R. Dawson, T. Ratvijitvech, M. Corker, A. Laybourn, Y. Z. Khimyak, A. I. Cooper and D. J. Adams, *Polym. Chem.*, 2012, **3**, 2034–2038.
- 34 W. Wang, M. Zhou and D. Yuan, *J. Mater. Chem. A*, 2017, **5**, 1334–1347.
- 35 N. A. Rakow, M. S. Wendland, J. E. Trend, R. J. Poirier, D. M. Paolucci, S. P. Maki, C. S. Lyons and M. J. Swierczek, *Langmuir*, 2010, **26**, 3767–3770.
- 36 K. Jiang, D. Kuang, T. Fei and T. Zhang, *Sensors Actuators, B Chem.*, 2014, **203**, 752–758.
- 37 K. Jiang, T. Fei and T. Zhang, *Sensors Actuators, B Chem.*, 2014, **199**, 1–6.
- 38 S. Dalapati, S. Jin, J. Gao, Y. Xu, A. Nagai and D. Jiang, *J. Am. Chem. Soc.*, 2013, **135**, 17310–17313.
- 39 M. Rose, *ChemCatChem*, 2014, **6**, 1166–1182.
- 40 P. Kaur, J. T. Hupp and S. T. Nguyen, *ACS Catal.*, 2011, **1**, 819–835.
- 41 A. Deshmukh, S. Bandyopadhyay, A. James and A. Patra, *J. Mater. Chem. C*, 2016, **4**, 4427–4433.
- 42 G. Cheng, T. Hasell, A. Trewin, D. J. Adams and A. I. Cooper, *Angew. Chem. Int. Ed.*, 2012, **51**, 12727–12731.
- 43 Y. Yang, B. Tan and C. D. Wood, *J. Mater. Chem. A*, 2016, **4**, 15072–15080.
- 44 W. Mai, B. Sun, L. Chen, F. Xu, H. Liu, Y. Liang, R. Fu, D. Wu and K. Matyjaszewski, *J. Am. Chem. Soc.*, 2015, **137**, 13256–13259.
- 45 F. Xie, W. Hu, L. Ding, K. Tian, Z. Wu and L. Li, *Polym. Chem.*, 2017, **8**, 6106–6111.
- 46 A. M. James, M. J. Derry, J. S. Train and R. Dawson, *Polym. Chem.*, 2019, **10**, 3879–3886.

-
- 47 C. T. J. Ferguson, N. Huber, T. Kuckhoff, K. A. I. Zhang and K. Landfester, *J. Mater. Chem. A*, 2020, **8**, 1072–1076.
- 48 A. M. James and R. Dawson, *Macromol. Rapid Commun.*, 2020, **2000176**, 1–5.
- 49 A. Fulford, C. E. Hickey and P. M. Maitlis, *J. Organomet. Chem.*, 1990, **398**, 311–323.
- 50 A. Haynes, P. M. Maitlis, I. A. Stanbridge, S. Haak, J. M. Pearson, H. Adams and N. A. Bailey, *Inorganica Chim. Acta*, 2004, **357**, 3027–3037.
- 51 L. Nocera, MChem Thesis, University of Sheffield, 2002.
- 52 S. Bell, MChem Thesis, University of Sheffield, 2015.
- 53 S. Ivko, MChem Thesis, University of Sheffield, 2016.
- 54 US Pat., US Pat. 7,115,774 B2, 2003.
- 55 US Pat., US Pat. 7,582,792 B2, 2009.
- 56 A. Riisager, B. Jørgensen, P. Wasserscheid and R. Fehrmann, *Chem. Commun.*, 2006, 994–996.
- 57 P. L. Verma, S. S. Rao and S. P. Gejji, *J. Mol. Liq.*, 2015, **212**, 885–899.
- 58 M. Cheong, R. Schmid and T. Ziegler, *Organometallics*, 2000, **19**, 1973–1982.

Chapter 5 Conclusions and Future Work

5.1. Conclusions

The use of a range of solid supports to electrostatically incorporate an anionic carbonylation catalyst, *cis*-[Rh(CO)₂I₂]⁻, has been investigated. Postsynthetic *N*-methylation of nitrogen-functionalised neutral materials was used to generate cationic sites on the supports.

In the cases of pyridine-containing UiO-type MOFs, *N*-methylation was investigated using a range of linkers, heating methods and methylating agents. It was found that a MOF containing the shorter linker (UiO-66-b/py) was more stable to harsh methylation conditions than isorecticular analogues with longer linkers (UiO-67-bpy and UiO-67-bp/ppy). In all of these systems, however, it was not found to be possible to reach quantitative conversion of pyridyl to *N*-methylpyridinium sites. The presence of residual neutral nitrogen sites in these frameworks led to incorporation of covalently bound rhodium dicarbonyl species as well as the desired ionic encapsulation of *cis*-[Rh(CO)₂I₂]⁻.

For the imidazole-containing UiO-type MOFs, microwave heating was employed to achieve *N*-methylation. In the case of the single-linker MOF (UiO-66-imb), the maximum extent of conversion of imidazole to *N*-methylimidazolium sites was 85%. Incorporation of rhodium into this MOF yielded a mixture of *cis*-[Rh(CO)₂I₂]⁻ and a neutral rhodium dicarbonyl species, presumably coordinated to the remaining 15% of imidazole nitrogen sites ([Rh(CO)₂I(imidazolyl)]). In pursuit of maximising *N*-methylation, a mixed-linker approach using terephthalic acid was employed as this was expected to reduce pore congestion and thus aid conversion. Indeed, the mixed-linker MOF (UiO-66-b/imb) achieved near-quantitative conversion of imidazole to *N*-methylimidazolium (97%). Reaction of this MOF with [Rh(CO)₂I]₂ resulted in incorporation of *cis*-[Rh(CO)₂I₂]⁻. The supported complex was found to undergo the same key organometallic steps as observed

in the solution phase under ambient conditions. The material was active for the carbonylation of methanol, with slightly lower activity than the soluble analogue consistent with diffusion limitations in the framework. The material could be recycled without appreciable loss of activity, and the recovered material retained its crystallinity.

A novel dispersible microporous polymer material was synthesised from the controlled polymerisation of 1,4-divinylbenzene and 4-vinylpyridine, mediated via a PEG-based chain-transfer agent. The material was postsynthetically modified via *N*-methylation of the pyridine moiety to generate a support with cationic sites, which could be used to electrostatically incorporate cis -[Rh(CO)₂I₂]⁻. The supported complex underwent the key organometallic steps observed for the solution-phase Monsanto catalytic cycle under ambient conditions, although the octahedral $trans$ -[Rh(COMe)(CO)₂I₃]⁻ complex formed prior to reductive elimination of acetyl iodide was not clearly observed. The oxidative addition of MeI to the square planar catalyst (the rate limiting step in the Monsanto process for the carbonylation of methanol) could be probed *in situ* using infrared spectroscopy. Kinetic studies revealed the disappearance of the Rh(I) complex to follow a double-exponential decay where both derived k_2 values were larger than for the homogeneous analogue, [*n*-Bu₄N][Rh(CO)₂I₂], at 25 °C in CH₂Cl₂.¹ The polymer-supported catalyst was shown to be active for the catalytic carbonylation of methanol, with slightly lower activity than the homogeneous analogue. The supported catalyst demonstrated good recyclability in CHCl₃.

The carbonylation catalyst, cis -[Rh(CO)₂I₂]⁻, has hence been successfully encapsulated via electrostatic interactions on both MOF and organic polymer supports which have been thoroughly characterised and their reactivity extensively investigated.

5.2. Future Work

5.2.1. Different catalysts

The work presented herein can be viewed as a general approach towards non-covalent catalyst encapsulation and, in that sense, any anionic catalyst offers a promising candidate for incorporation in this manner.

The active species in the Cativa catalytic process (*fac*-[Ir(CO)₂I₃Me]⁻) is an obvious candidate in parallel with this work, as this complex is also active for the carbonylation of methanol to form acetic acid.²

Another candidate complex is [Co(CO)₄]⁻. This species has recently been supported in an analogous manner on Cr-MIL-101 and has been shown to be active for epoxide carbonylation to form β-lactones,³ and also β-lactone carbonylation to form succinic anhydrides.⁴

More broadly, any phosphine-containing catalyst could be encapsulated in this manner by substituting the phosphine ligand for a sulfonated analogue. Previously, a hydroformylation catalyst was prepared containing trisulfonated triphenylphosphine (TPPTS) ligands, [HRh(CO)(TPPTS)₃]⁹⁻ in place of the usual triphenylphosphine ligands.^{5,6} This resulted in an anionic catalyst that could be supported via electrostatic interactions in an ionic liquid,⁶ or onto cationic micelle surfaces.⁵ This anionic hydroformylation catalyst could be immobilised onto a solid support as described in this thesis, although the support used would presumably need to contain larger pores to accommodate the bulky phosphine ligands. Furthermore, the TPPTS ligand could be substituted onto other phosphine-containing transition metal catalysts to introduce a negative charge and allow for their ionic encapsulation.

5.2.2. Different supports

The pre-quaternised imidazole-containing linker, [**H₂imbdc-Me**]I, can also be incorporated into Cr-MIL-101 to generate a cationic framework,⁷ and this system represents an opportunity to encapsulate *cis*-[Rh(CO)₂I₂]⁻ and other anionic catalysts in an analogous manner to that explored in this thesis.

Furthermore, Cr-MIL-101 is cationic in its own right by virtue of its SBUs, and the tightly-bound fluoride counter-ions can be exchanged for more mobile chloride anions by treatment with AlCl₃.⁸ This approach has been utilised previously to encapsulate [Co(CO)₄]⁻ on Cr-MIL-101,^{3,4} a strategy that could be extended to immobilise a range of anionic catalysts as described in Section 5.2.1.

Cr-MIL-101 represents an attractive candidate for support in this manner due to its large pore sizes. If, as postulated in Chapter 3, diffusion limitations are responsible for the lower catalytic activity observed for the UiO-66-b/imb system, this system may potentially represent an improvement on the turnover frequency of the supported complex.

5.3. References

- 1 A. Haynes, P. M. Maitlis, R. Quyoum, C. Pulling, H. Adams, S. E. Spey and R. W. Strange, *J. Chem. Soc., Dalton Trans.*, 2002, 2565–2572.
- 2 G. J. Sunley and D. J. Watson, *Catal. Today*, 2000, **58**, 293–307.
- 3 H. D. Park, M. Dincă and Y. Román-Leshkov, *ACS Cent. Sci.*, 2017, **3**, 444–448.
- 4 H. D. Park, M. Dincă and Y. Román-Leshkov, *J. Am. Chem. Soc.*, 2018, **140**, 10669–10672.
- 5 A. Riisager and B. E. Hanson, *J. Mol. Catal. A Chem.*, 2002, **189**, 195–202.
- 6 H. N. T. Ha, D. T. Duc, T. V. Dao, M. T. Le, A. Riisager and R. Fehrmann, *Catal. Commun.*, 2012, **25**, 136–141.
- 7 J. Liang, Y.-Q. Xie, X.-S. Wang, Q. Wang, T.-T. Liu, Y.-B. Huang and R. Cao, *Chem. Commun.*, 2017, **54**, 342–345.
- 8 C. Mao, R. A. Kudla, F. Zuo, X. Zhao, L. J. Mueller, X. Bu and P. Feng, *J. Am. Chem. Soc.*, 2014, **136**, 7579–7582.

Chapter 6 Experimental

6.1. Solvents and reagents

Dry solvents (excluding MeOH) were obtained from a Grubbs solvent purification system in which the solvents were degassed prior to being passed through activated alumina and a supported copper catalyst to remove protic contaminants and trace oxygen respectively.¹ These solvents were stored under N₂. Solvents were used within 24 h of collection from the dry solvent system. Other solvents were purchased from either Fisher Scientific or Sigma Aldrich (HPLC grade unless otherwise stated) and were used without further purification. Standard Schlenk techniques and glassware were used for preparative reactions.

Rhodium trichloride hydrate was purchased from Precious Metals Online, Monash University LPO, Melbourne, Australia. Argon and carbon monoxide (99.9% CP grade) were supplied by BOC. All other reagents were purchased from either Fisher Scientific or Sigma Aldrich and used without further purification.

6.2. Instrumentation

6.2.1. Infra-red spectra

Infra-red spectra were collected using a Perkin-Elmer 100 FTIR spectrometer with ATR accessory. KBr disc samples were prepared by grinding with a 20-fold excess of pure KBr dried overnight in a vacuum oven at 80 °C. The samples were pelletized at high pressure (10 tons) and analysed as a thin transparent disc. Solution IR spectra were recorded using a transmission cell (CaF₂ windows, 0.5 mm pathlength).

6.2.2. Nuclear magnetic resonance spectroscopy

Solution-phase ¹H and ¹³C{¹H} NMR spectra were collected using a Bruker AC400 spectrometer fitted with an automatic sample changer using the solvent as the internal standard.

To digest in a mixture of NaOD/D₂O, samples were added to a capped sample vial to which D₂O (1 cm³) and NaOD (40% w/w in D₂O, 0.05 cm³) were added. The mixture was sonicated for 10 minutes and then filtered through cotton wool before analysing.

To digest in a mixture of D₃PO₄ with D₂O or (CD₃)₂SO, samples were added to a capped sample vial to which D₂O or (CD₃)₂SO (1 cm³) and D₃PO₄ (85% w/w in D₂O, 0.25 cm³) were added. The mixture was stirred overnight and then filtered through cotton wool before analysing.

To digest in a mixture of DCl/D₂O, samples were added to a capped sample vial to which D₂O (1 cm³) and DCl (35% w/w in D₂O, 0.25 cm³) were added. The mixture was stirred overnight and then filtered through cotton wool before analysing.

Solid-state NMR samples were packed into 4 mm zirconia rotors and transferred to a Bruker Avance III HD spectrometer. 1D ^1H - ^{13}C cross-polarisation magic angle spinning (CP/MAS) NMR experiments were measured at 125.76 MHz (500.13 MHz ^1H) at a MAS rate of 10.0 kHz. The ^1H $\pi/2$ pulse was 3.4 μs , and two-pulse phase modulation (TPPM) decoupling was used during the acquisition. The Hartmann-Hahn condition was set using hexamethylbenzene. The spectra were measured using a contact time of 2.0 ms. The relaxation delay, D1, for each sample was individually determined from the proton T1 measurement ($D1 = 5 \times T1$). Samples were collected until sufficient signal to noise ratio was observed, typically greater than 1094 scans. The values of the chemical shifts are referenced to that of TMS.

6.2.3. Powder X-ray diffraction

For powder X-ray diffraction pattern collection, samples were dried under high vacuum before being ground into a fine powder using a pestle and mortar. The microcrystalline samples were then analysed using a Bruker D8 Advance X-ray powder diffractometer equipped with a LynxEye Detector, a Cu $K\alpha$ sealed tube source (with wavelength, λ , of 1.5406 Å) and a variable motorised slit. Patterns were recorded in either Bragg-Brentano geometry (in which samples were placed in a zero-background Si sample holder rotated at 15 rpm) or Debye-Scherrer geometry (in a capillary stage with samples loaded in either 0.5 mm or 0.7 mm borosilicate capillaries and rotated at 30 rpm). Data were collected between 5° to 70° 2θ with data being recorded at 0.02° increments. Data were collected under ambient conditions. Indexing and Pawley refinements were carried out using TOPAS Academic version 4.1 (Appendix 7.3).²

6.2.4. Small angle X-ray scattering

SAXS studies were performed by M. J. Derry at Diamond Light Source Beamline I22 using monochromatic X-ray radiation (X-ray wavelength $\lambda = 0.999 \text{ \AA}$, with scattering vector q ranging from 0.0027 to 0.25 \AA^{-1} , where $q = 4\pi \sin \theta/\lambda$ and θ is one-half of the scattering angle) and a 2D Pilatus 2M pixel detector (Dectris, Switzerland). Scattering data were reduced and normalized with glassy carbon being used for the absolute intensity calibration utilising standard routines available at the beamline³ and further analysed (background subtraction and data modelling) using Irena SAS macros for Igor Pro.⁴

6.2.5. Volumetric N₂ gas sorption

Nitrogen gas sorption isotherms were collected at 77 K using approximately 100 mg of sample on an ASAP 2020 micromeritics volumetric adsorption analyser. Prior to analysis all samples except those with encapsulated *cis*-[Rh(CO)₂I₂]⁻ were degassed for at least 16 h at 120 °C under a vacuum of at least 10⁻⁵ bar. Samples containing rhodium were degassed under the same vacuum level but without heating due to issues relating to the stability of the complex. BET surface areas were calculated over a relative pressure range (p/p_0) of between 0.01 – 0.15. Pore size distributions and pore volumes were calculated from the adsorption isotherms and modelled using the nonlocal density functional theory model (NL-DFT) for N₂ on carbon slit pores found within the micromeritics ASAP software.

6.2.6. Elemental analysis

Carbon, hydrogen, nitrogen and sulfur elemental analysis was performed by the Departmental Microanalysis Service by burning a small amount of sample in a stream of pure oxygen. The sample was placed in a tin capsule and introduced into the combustion

tube of the Elementar Vario MICRO Cube CHN/S analyser via a stream of helium. Combustion products were analysed by first passing the sample through a copper tube to remove excess oxygen and reduce any NO_x to N₂. Gases were separated using a Thermal Programmed Desorption column and detected using a Thermal Conductivity Detector.

Iodide analysis was performed using the Schöninger flask combustion method in which an amount of sample is combusted in an oxygen-enriched environment, the resultant gases are absorbed, and a titration is conducted to determine the iodide concentration.

6.2.7. Electron microscopy

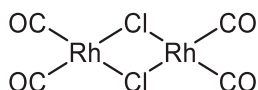
Transmission electron microscopy (TEM) images were collected using a Philips CM 100 instrument operating at 100 kV and equipped with a Gatan 1 k CCD camera. A diluted solution of the polymer material (0.10% w/w) was placed on carbon-coated copper grids, allowed to dry and then exposed to ruthenium(VIII) oxide vapor for 7 min at 20 °C prior to analysis. The ruthenium(VIII) oxide was prepared as follows: Ruthenium(IV) oxide (0.30 g) was added to water (50 g) to form a black slurry; addition of sodium periodate (2.0 g) with stirring produced a yellow solution of ruthenium(VIII) oxide within 1 min.⁵

Scanning electron microscopy (SEM) images were collected as follows: Cu 200 mesh TEM grids coated with Quantifoil R 2/2 carbon film were glow discharged before application of the sample. A small amount of the dried MOF sample was suspended in propan-2-ol (\approx 1 mL) and agitated. A 2 μ L aliquot of the MOF suspension was pipetted onto the Quantifoil side of the grid and allowed to dry. A custom-made copper shuttle was used to hold the TEM grids during these experiments. Grids were imaged using a JEOL JSM-IT100 Scanning Electron Microscope. An accelerating voltage of 5.0 kV, a

working distance of 12 mm and a probe current of 40 (arbitrary units) were used to image the grids.

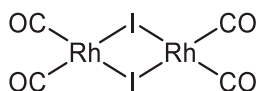
6.3. Synthesis of rhodium precursors

6.3.1. $[\text{Rh}(\text{CO})_2\text{Cl}]_2$



$[\text{Rh}(\text{CO})_2\text{Cl}]_2$ was synthesised according to an established literature procedure.⁶ $\text{RhCl}_3 \cdot x\text{H}_2\text{O}$ (~5 g) was placed in a glass sintered tube and heated to 100 °C. This was purged with a stream of CO gas that was pre-saturated with MeOH. After 1 h MeOH was removed. After another hour, the temperature was increased to 150 °C and heated for a further 3 h. Product was purified by vacuum sublimation (100 °C) to yield $[\text{Rh}(\text{CO})_2\text{Cl}]_2$ (1.55 g, 3.9 mmol) as red crystals, $\nu(\text{CO}) / \text{cm}^{-1}$ (solution cell, *n*-hexane) 2107 (s), 2092 (s), 2036 (s), 2001 (w).

6.3.2. $[\text{Rh}(\text{CO})_2\text{I}]_2$

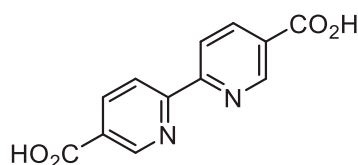


$[\text{Rh}(\text{CO})_2\text{I}]_2$ was synthesised according to an established literature procedure.⁷ Briefly, a solution of $[\text{Rh}(\text{CO})_2\text{Cl}]_2$ (747 mg, 1.9 mmol) in CO-saturated *n*-hexane (50 cm³) was stirred over dry KI (4.4 g, 26.5 mmol) under CO at RT for 24 h. The solution was filtered and the volume reduced *in vacuo* until precipitation began to form, when the mixture was sealed under CO and heated to dissolve the solid. This was left to crystallise at 0 °C before isolation by filtration to give $[\text{Rh}(\text{CO})_2\text{I}]_2$ (835 mg, 1.5 mmol, 76%) as red needles, $\nu(\text{CO}) / \text{cm}^{-1}$ (solution cell, *n*-hexane) 2091 (s), 2081 (s), 2027 (s).

6.4. Synthesis of linkers

2,5-pyridinedicarboxylic acid (**H₂pydc**) and terephthalic acid (**H₂bdc**) were supplied by Sigma-Aldrich Chemicals Ltd and used as supplied.

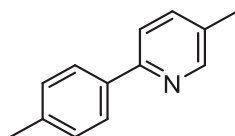
6.4.1. 2,2'-bipyridyl-5,5'-dicarboxylic acid (**H₂bpydc**)



In a typical experiment 5,5'-dimethyl-2,2'-bipyridyl (0.97 g, 5.3 mmol) was dissolved in sulfuric acid (25 cm³). Potassium dichromate (4.86 g, 16.5 mmol) was added over twenty minutes and the reaction mixture was cooled using an ice bath if the temperature exceeded 80 °C. After completion, the mixture was poured onto a slurry of ice and water (~200 cm³). The product was isolated by filtration and washed thoroughly with water until it lost its green colour. The product was then washed with acetone (20 cm³) and dried under vacuum overnight, giving 2,2'-bipyridine-5,5'-dicarboxylic acid (1.1 g, 4.5 mmol, 86%) as a white powder, δ_{H} (400 MHz; (CD₃)₂SO) 8.45 (dd, *J* = 8.5, 2.0 Hz, 2 H), 8.57 (d, *J* = 8.5 Hz, 2 H), 9.20 (d, *J* = 2.0 Hz, 2 H), 13.54 (br s, 2 H); ν_{max} /cm⁻¹ (ATR-IR) 2563 (w, O-H), 1679 (s, C=O), 1593 (s, *ar.* C=C), 1426 (m, C-O-H), 1306 (s, C-O).

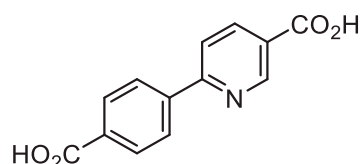
6.4.2. 2-phenylpyridine-5,4'-dicarboxylic acid (**H₂ppydc**)

6.4.2.1. Coupling



The synthesis was performed according to a literature procedure.⁸ 2-bromo-5-methylpyridine (3.440 g, 20 mmol) and *p*-tolylboronic acid (3.130 g, 23 mmol) were dissolved in water (80 cm³) and isopropanol (80 cm³). After stirring to dissolve the solids, Pd(OAc)₂ (0.112 g, 0.5 mmol) and K₃PO₄ (8.48 g, 40 mmol) were added, and the mixture was heated to reflux for four hours. The resulting mixture was filtered through Celite and brine solution (150 cm³) was added to the filtrate. This was extracted with ethyl acetate (3 × 150 cm³) and the organic phase was dried over MgSO₄ before removing the solvent *in vacuo* to give a yellow oil. This was purified using flash column chromatography (9:1 *n*-hexane to ethyl acetate) to give 5-methyl-2-(4-methylphenyl)pyridine (2.910 g, 15.9 mmol, 53%) as a white powder (Found: C, 84.9; H, 7.1; N, 7.5. C₁₃H₁₃N expected: C, 85.2; H, 7.2; N, 7.6%); δ_H (400 MHz; CDCl₃) 2.39 (s, 3 H), 2.43 (s, 3 H), 7.29 (d, *J* = 8.0 Hz, 1 H), 7.54 (dd, *J* = 8.0, 2.0 Hz, 1 H), 7.63 (d, *J* = 8.0 Hz, 1 H), 7.80 (d, *J* = 8.0 Hz, 2 H), 8.53 (d, *J* = 2.0 Hz, 1 H); *m/z* 184.1 (100%, M⁺).

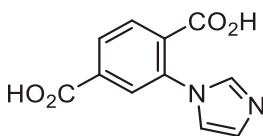
6.4.2.2. Oxidation



The synthesis was performed according to a literature procedure.⁸ 5-methyl-2-(4-methylphenyl)pyridine (0.3 g, 1.6 mmol) was dissolved in a mixture of acetic acid (8 cm³)

and hydrochloric acid (1 cm³). The solution was cooled to 0 °C, and CrO₃ (1.74 g, 17.4 mmol) was added slowly. Acetic anhydride (1 cm³) was added and the mixture was stirred under Ar for one hour at 0 °C, then for 16 h at room temperature. The resulting mixture was poured into ice and the green crude product was filtered off. This was dissolved in 4% aq. KOH, filtered through Celite and then acidified using 6 M HCl to obtain 2-phenyl-5,4'-dicarboxylic acid (0.26 g, 1.1 mmol, 65%) as a white solid (Found: C, 59.9; H, 3.7; N, 5.3. C₁₃H₉NO₄ expected: C, 64.2; H, 3.7; N, 5.8); δ_{H} (400 MHz; (CD₃)₂SO) 8.07 (d, J = 8.5 Hz, 2 H), 8.19 (d, J = 8.5 Hz, 1 H), 8.29 (d, J = 8.5 Hz, 2 H), 8.38 (dd, J = 8.5, 2.0 Hz, 1 H), 9.18 (d, J = 2.0 Hz 1 H), 13.28 (br. s, 2 H); m/z 242.1 (100%, M⁺).

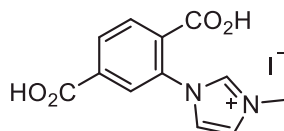
6.4.3. 2-(imidazole-1-yl)terephthalic acid (H₂imbdc)



The linker was synthesised according to a modified procedure from the literature.⁹ Imidazole (8.500 g, 125 mmol), 2-bromoterephthalic acid (6.125 g, 25 mmol), K₂CO₃ (9.674 g, 70 mmol) and CuSO₄ (0.250 g, 1 mmol) were ground together and added to a 125 cm³ solvothermal vessel which had been flushed with Ar. The mixture was sealed and incubated at 210 °C for 10 h before cooling to room temperature. The crude solid product was dissolved in H₂O (300 cm³) and filtered. The pH of the filtrate was adjusted to between 2 and 3 with 6 M HCl. The grey precipitate was isolated by filtration and recrystallised from 6 M HCl. The product was heated at 80 °C under vacuum for 16 h to yield 2-(imidazol-1-yl)terephthalic acid (3.182 g, 47%) as light brown crystals, (Found: C, 49.0; H, 3.4; N, 10.5; Cl, 13.4. C₁₁H₉N₂O₄Cl expected: C, 49.2; H, 3.4; N, 10.4; Cl, 13.2%); δ_{H} (400 MHz; D₂O and D₃PO₄) 6.81 (s, 1 H), 6.84 (s, 1 H), 7.35 (s, 1 H),

7.45 (br. m, 2 H), 8.13 (s, 1 H); δ_C (400 MHz; D₂O and D₃PO₄) 118.77, 123.00, 128.31, 129.84, 131.33, 131.82, 133.37, 134.19, 135.11, 165.83, 166.96; m/z 233 (100%, M⁺).

6.4.4. Quaternisation of H₂imbdc



This reaction was performed according to a modified procedure from the literature.¹⁰ 2-(imidazol-1-yl)terephthalic acid (5.166 g, 19.2 mmol) was dissolved in EtOH (64 cm³) and DMF (3 drops). SOCl₂ (7 cm³, 96.4 mmol) was added dropwise. The mixture was refluxed at 80 °C for 48 h, and then the solvent was removed under reduced pressure. The crude product was dissolved in H₂O (40 cm³) and the pH was adjusted to above 9 with 2M aq. KOH. The solution was extracted with EtOAc (4 × 70 cm³) and the organic layers were combined and dried over MgSO₄. The solvent was removed under reduced pressure. The white solid product was dissolved in MeCN (52 cm³) and MeI (13 cm³, 208.8 mmol) and refluxed at 80 °C for 72 h. Solvent was removed under reduced pressure and the solid product was dissolved in 6 M aq. HCl (32 cm³) and refluxed for 16 h. The mixture was allowed to cool, at which point the product crashed out of solution. This was collected by filtration and dried in a vacuum oven for 16 h to yield 1-(2,5-dicarboxyphenyl)-3-methyl-1H-imidazol-3-ium iodide (2.171 g, 30%) as a yellow powder, δ_H (400 MHz; D₂O and D₃PO₄) 3.20 (s, 3 H), 6.79 (s, 1 H), 6.83 (s, 1 H), 7.35 (s, 1 H), 7.46 (br. m, 2 H), 8.12 (s, 1 H); δ_C (400 MHz; D₂O and D₃PO₄) 35.45, 122.74, 123.44, 128.31, 129.85, 131.38, 131.86, 133.31, 134.24, 136.36, 165.85, 167.00; m/z 247 (100%, M⁺).

6.5. Synthesis and postsynthetic modification of MOFs

6.5.1. UiO-67-bpy

6.5.1.1. Synthesis

This MOF was prepared solvothermally using a modified method from the literature.¹¹ In a typical experiment ZrCl₄ (505 mg, 2.17 mmol), 2,2'-bipyridine-5,5'-dicarboxylic acid (530 mg, 2.17 mmol) and benzoic acid (7942 mg, 65.1 mmol) were placed in a round bottom flask with anhydrous DMF (85 cm³). The solids were dispersed with stirring for 15 minutes and then the suspension was placed within a Teflon-lined stainless steel autoclave and incubated at 80 °C for 48 hours. The vessel was then cooled at a rate of 0.1 °C min⁻¹ and the solids were then collected by centrifugation and the solvent decanted. The solids were washed with DMF (2 × 100 cm³) and then soaked in methanol for 72 hours, exchanging for fresh methanol (100 cm³) every 24 hours. The solids were collected by centrifugation and dried under vacuum overnight to give [Zr₆O₄(OH)₄(bpydc)₆] (485 mg, 0.228 mmol, 63%) as a white powder, (Found: C, 40.4; H, 2.6; N, 7.7. Expected: C, 40.6; H, 1.9; N, 7.9%); δ_H (400 MHz; D₂O and NaOD) 7.95 (d, *J* = 8.0 Hz, 2 H), 8.18 (dd, *J* = 8.2, 2.1 Hz, 2 H), 8.85 (d, *J* = 1.6 Hz, 2 H); ν_{max}/cm⁻¹ (ATR-IR) 1593 (m, *ar.* C=C), 1409 (s, C-O), 1365 (m, C-O). The powder pattern was fitted using TOPAS Academic version 4.1 as an *Fm* $\bar{3}$ *m* space group where *a* = 26.6062(4) Å (Figure 6.1, Appendix 7.3).²

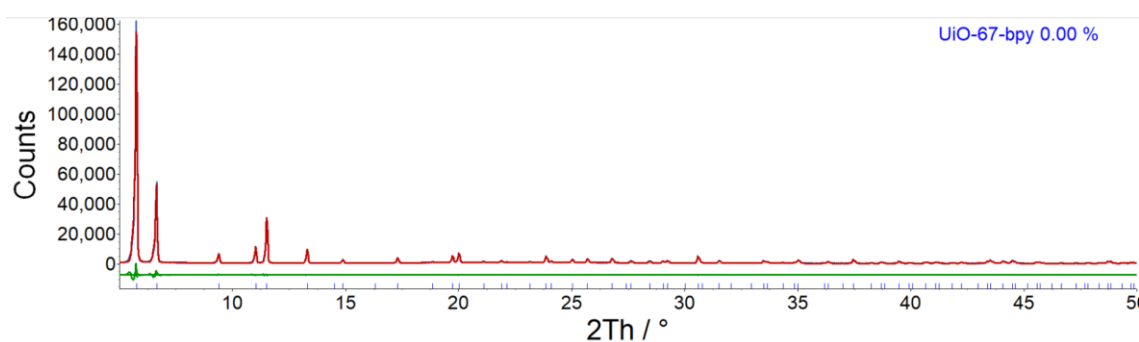


Figure 6.1. Pawley fit of UiO-67-bpy showing the observed pattern (blue), the fit (red), and the difference (green).

6.5.1.2. Reactions with MeI

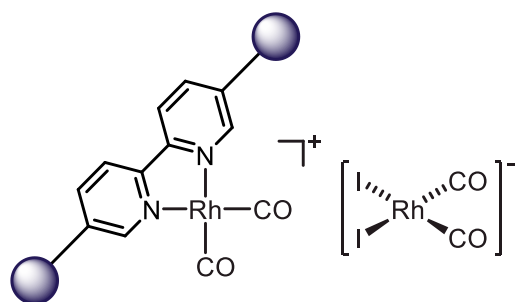
The quaternisation of UiO-67-bpy was attempted according to a modified literature method.¹² Dry UiO-67-bpy (200 mg, 0.09 mmol) was added to anhydrous THF (2 cm³) in a capped sample vial. MeI (2 cm³, 32 mmol) was added and the mixture was sonicated for 15 minutes to ensure full dispersion of the solid. The suspension was placed within a Teflon-lined stainless steel autoclave and incubated at 100 °C for 72 h. The vessel was cooled at a rate of 0.1 °C min⁻¹ and the solids were collected via centrifugation. The crude material was washed with DMF (3 × 10 cm³) and acetone (10 cm³) and dried under vacuum overnight to give a yellow powder. Analysis of the product by ¹H NMR spectroscopy after digesting in NaOD/D₂O indicated partial mono-quaternisation of the **bpydc** linkers, as discussed in Chapter 2. The procedure was repeated using incubation periods of up to 15 days in an attempt to increase the extent of quaternisation. A maximum of 87% mono-methylation was found as discussed in Chapter 2.

6.5.1.3. Reaction with 1,2-diiodoethane

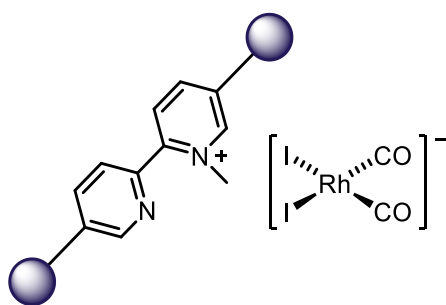
Dry UiO-67-bpy (50 mg, 0.02 mmol) was added to anhydrous MeCN (4 cm³) in a Teflon-lined stainless steel autoclave. 1,2-diiodoethane (419 mg, 1.5 mmol) was added, and the vessel was incubated at 100 °C for 60 h. The vessel was cooled naturally and the solids

were collected by filtration. The crude material was washed with DMF ($3 \times 10 \text{ cm}^3$) and acetone (10 cm^3) and dried under vacuum overnight to give a brown powder. The product was analysed by ^1H NMR spectroscopy after digesting in NaOD/D₂O and found to have returned starting material.

6.5.1.4. Reaction of UiO-67-bpy with $[\text{Rh}(\text{CO})_2\text{I}]_2$



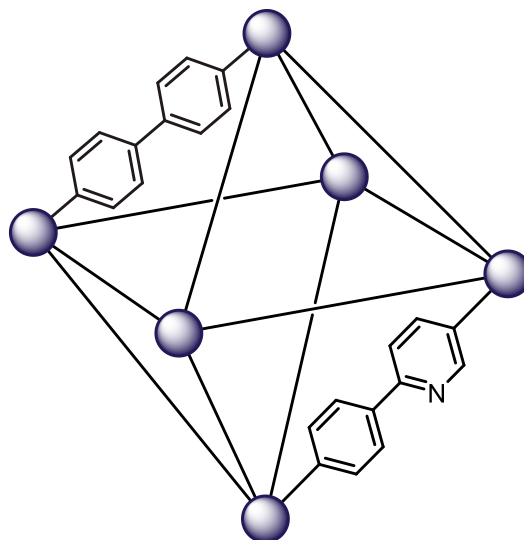
$[\text{Rh}(\text{CO})_2\text{I}]_2$ (62 mg, 0.1 mmol) in dry hexane (20 cm^3) was added to dry UiO-67-bpy (26 mg, 0.01 mmol) under Ar via cannula. Immediately upon addition of the dimer solution to the solid, the MOF changed colour from white to black. The reaction was monitored by measuring the concentration of rhodium dimer in the supernatant via IR spectroscopy and was deemed complete after two hours of stirring. The supernatant was removed via centrifugation and the solid was washed with dry hexane ($2 \times 20 \text{ cm}^3$) before drying under vacuum overnight to give UiO-67-bpy-Rh (12 mg) as a black powder, $\nu(\text{CO}) / \text{cm}^{-1}$ (ATR-IR) 2090 (m), 2064 (m), 2038 (m), 1999 (m).

6.5.1.5. Reaction of UiO-67-bpy-Me_{87%} with [Rh(CO)₂I]₂

[Rh(CO)₂I]₂ (34 mg, 0.06 mmol) in dry hexane (20 cm³) was added to dry UiO-67-bpy-Me_{87%} (56 mg, 0.02 mmol) under Ar via cannula. Immediately upon addition of the dimer solution to the solid, the MOF changed colour from yellow to brown. The mixture was stirred under Ar for 24 h. The supernatant was removed via centrifugation and the solid was washed with dry hexane (2 × 20 cm³) before drying under vacuum overnight to give Rh @ UiO-67-bpy-Me_{87%} (22 mg) as a light brown powder, $\nu(\text{CO}) / \text{cm}^{-1}$ (ATR-IR) 2066 (w), 1996 (w).

6.5.2. UiO-67-bp/ppy

6.5.2.1. Synthesis



The mixed-linker MOF was synthesised according to a modified literature procedure.⁸ Biphenyl-4,4'-dicarboxylic acid (445 mg, 1.8 mmol), 2-phenylpyridine-5,4'-dicarboxylic acid (88 mg, 0.4 mmol), ZrCl₄ (513 mg, 2.2 mmol) and benzoic acid (7.950 g, 65 mmol) were added into dry DMF (83 cm³) in a Teflon-lined stainless steel autoclave. This was incubated at 120 °C for 48 h, followed by slow cooling at 0.1 °C min⁻¹. The product was recovered by centrifugation and washed with DMF (2 × 30 cm³) and soaked in MeOH for 72 h, exchanging for fresh MeOH every 24 h (3 × 30 cm³). The product was isolated via centrifugation and dried under vacuum overnight to give [Zr₆O₄(OH)₄(**bpdc**)_{4.75}(**ppydc**)_{1.25}] (0.451 g, 59%) as a white powder, (Found: C, 37.4; H, 4.3; N, 0.7; Zr, 23.7. Expected: C, 46.8; H, 2.4; N, 0.8; Zr, 25.8%); δ_H (400 MHz; D₂O and NaOD) 7.65 (d, *J* = 8.5 Hz, 11 H), 7.83 (dd, *J* = 6.0, 4.5 Hz, 15 H), 8.17 (dd, *J* = 8.0, 2.0 Hz, 1 H), 8.31 (s, 1 H), 8.86 (d, *J* = 2.0 Hz, 1 H). The powder pattern was fitted using TOPAS Academic version 4.1 as an *Fm* $\bar{3}$ *m* space group where *a* = 26.890(2) Å (Figure 6.2, Appendix 7.3).²

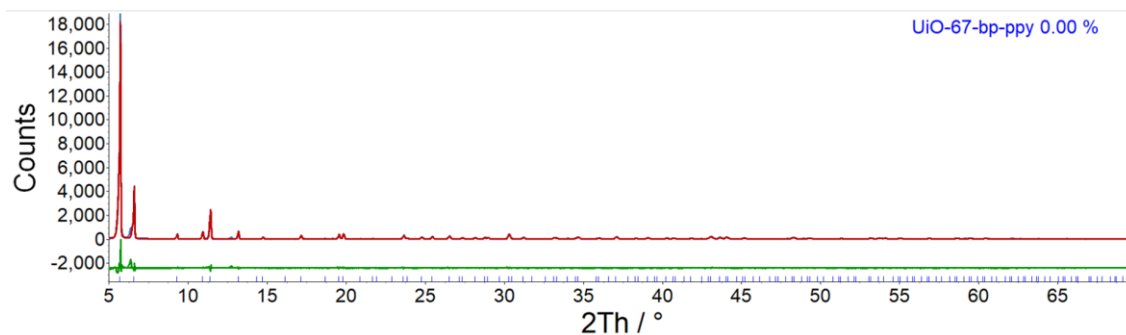
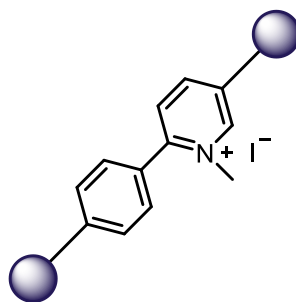


Figure 6.2. Pawley fit of UiO-67-bp/ppy showing the observed pattern (blue), the fit (red), and the difference (green).

6.5.2.2. Reaction with MeI (reflux)



UiO-67-bp/ppy (200 mg, 0.1 mmol), MeI (8 cm³, 129 mmol) and dry CHCl₃ (40 cm³) were refluxed together for 3 days, 1 week and 2 weeks separately. The solids from these reactions were recovered via centrifugation and washed with MeOH (2 × 20 cm³). The product was isolated via centrifugation and dried under vacuum to give UiO-67-bp/ppy-Me_X% as a yellow powder (where X = the calculated extent of quaternisation). The products were analysed by ¹H NMR spectroscopy after digesting in D₃PO₄/(CD₃)₂SO to determine the extent of quaternisation of the **ppydc** linkers as described in Chapter 2.

The three-day reaction reached a quaternisation extent of 51% (Found: C, 38.5; H, 3.3; N, 0.8. Expected: C, 45.3; H, 2.4; N, 0.8%); δ_H (400 MHz; (CD₃)₂SO and D₃PO₄) 4.09 (s, 1.5 H), 7.71 (d, *J* = 8.5 Hz, 1 H), 7.80 (d, *J* = 8.5 Hz, 1 H), 7.86 (d, *J* = 7.5 Hz, 1 H), 8.03 (m, 5 H), 8.85 (d, *J* = 9.5 Hz, 1 H). The powder pattern was fitted using TOPAS

Academic version 4.1 as an $Fm\bar{3}m$ space group where $a = 26.880(3)$ Å (Figure 6.3, Appendix 7.3).²

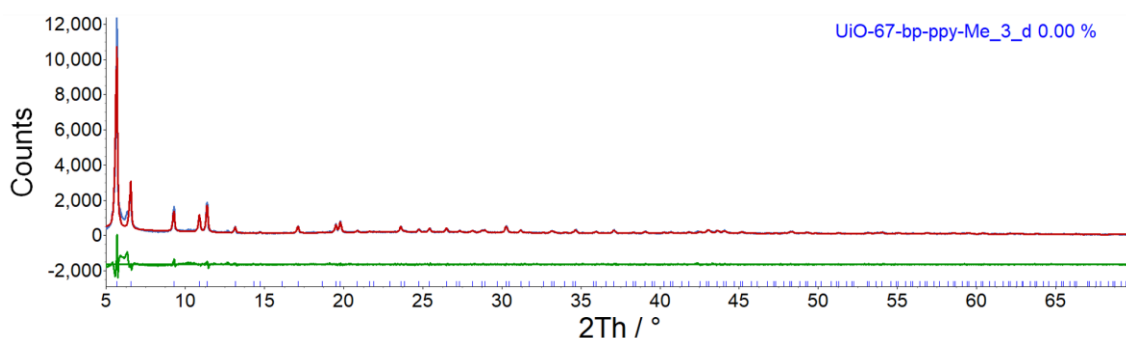


Figure 6.3. Pawley fit of the product of the reaction of UiO-67-bp/ppy with Mel after 3 days showing the observed pattern (blue), the fit (red), and the difference (green).

The one-week reaction reached a quaternisation extent of 61% (Found: C, 42.6; H, 3.1; N, 0.5. Expected: C, 45.0; H, 2.4; N, 0.8%); δ_{H} (400 MHz; $(\text{CD}_3)_2\text{SO}$ and D_3PO_4) 4.09 (s, 1.8 H), 7.72 (d, $J = 8.5$ Hz, 1 H), 7.80 (d, $J = 7.0$ Hz, 1 H), 7.86 (d, $J = 7.5$ Hz, 1 H), 8.03 (m, 5 H), 8.85 (d, $J = 9.0$ Hz, 1 H). The powder pattern was fitted using TOPAS Academic version 4.1 as an $Fm\bar{3}m$ space group where $a = 26.931(4)$ Å (Figure 6.4, Appendix 7.3).²

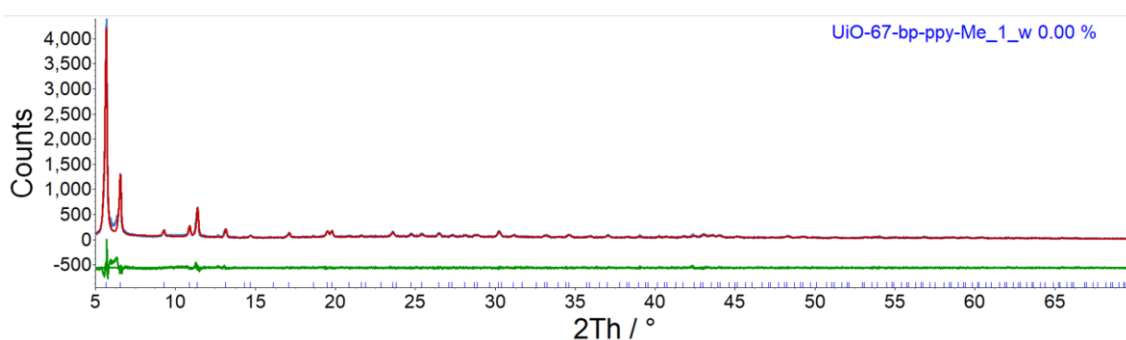


Figure 6.4. Pawley fit of the product of the reaction of UiO-67-bp/ppy with Mel after 1 week showing the observed pattern (blue), the fit (red), and the difference (green).

The two-week reaction reached a quaternisation extent of 73% (Found: C, 41.1; H, 3.3; N, 0.6. Expected: C, 44.6; H, 2.4; N, 0.8%); δ_{H} (400 MHz; $(\text{CD}_3)_2\text{SO}$ and D_3PO_4) 4.09 (s, 2.2 H), 7.71 (d, $J = 7.5$ Hz, 1 H), 7.79 (d, $J = 8.0$ Hz, 1 H), 7.85 (d, $J = 7.5$ Hz, 1 H), 8.03 (m, 5 H), 8.85 (d, $J = 8.5$ Hz, 1 H). The powder pattern was fitted using TOPAS Academic version 4.1 as an $Fm\bar{3}m$ space group where $a = 26.890(25)$ Å (Figure 6.5, Appendix 7.3).²

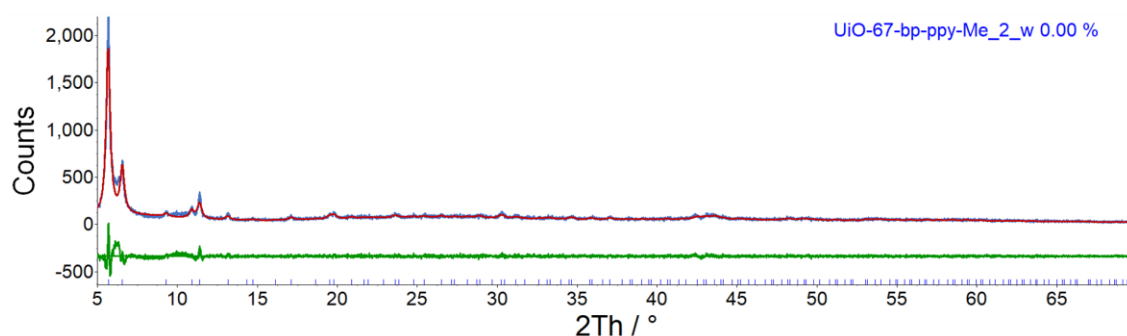
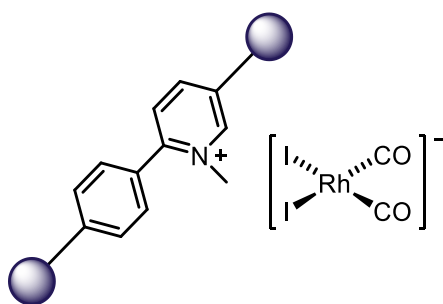


Figure 6.5. Pawley fit of the product of the reaction of UiO-67-bp/ppy with MeI after 2 w showing the observed pattern (blue), the fit (red), and the difference (green).

6.5.2.3. Reaction with $[\text{Rh}(\text{CO})_2\text{I}]_2$



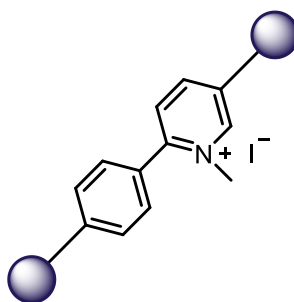
$[\text{Rh}(\text{CO})_2\text{I}]_2$ (27 mg, 0.06 mmol) in dry hexane (50 cm^3) was added to dry UiO-67-bp/ppy-Me_x% (100 mg) samples and stirred overnight under N_2 . The solids were recovered by centrifugation and washed with dry hexane ($2 \times 20 \text{ cm}^3$) before drying under vacuum and storing under a CO atmosphere at 5°C .

Product of reaction of UiO-67-bp/ppy-Me_{51%} with [Rh(CO)₂I]₂ was a grey powder (51 mg); $\nu(\text{CO}) / \text{cm}^{-1}$ (ATR-IR) 2076 (m), 1998 (m).

Product of reaction of UiO-67-bp/ppy-Me_{61%} with [Rh(CO)₂I]₂ was a grey powder (75 mg); $\nu(\text{CO}) / \text{cm}^{-1}$ (ATR-IR) 2070 (m), 1994 (m).

Product of reaction of UiO-67-bp/ppy-Me_{73%} with [Rh(CO)₂I]₂ was a grey powder (67 mg) and contained no discernible terminal metal carbonyl absorptions.

6.5.2.4. Reaction with MeI (microwave)



UiO-67-bp/ppy (100 mg, 0.05 mmol) was added to a 10 cm³ microwave tube with dry MeCN (3 cm³) and MeI (1 cm³, 16 mmol). The tube was heated to 120 °C in a microwave for 1 h, reaching a pressure of 6 bar, before drying under vacuum overnight to give the product (164 mg) as a yellow powder; δ_{H} (400 MHz; (CD₃)₂SO and D₃PO₄) 4.09 (s, 1.8 H), 7.22 (d, $J = 8.0$ Hz, 1 H), 7.80 (d, $J = 8.0$ Hz, 2 H), 8.00 (m, 3 H), 8.09 (d, $J = 8.0$ Hz, 2 H), 8.85 (d, $J = 8.0$ Hz, 1 H). Powder X-ray diffraction analysis of the product indicated loss of crystallinity in the sample.

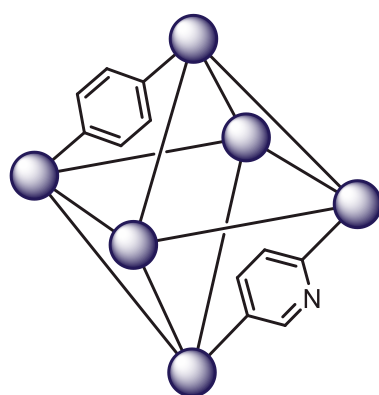
6.5.2.5. Reaction with [Me₃O][BF₄]

[Me₃O][BF₄] (148 mg, 1 mmol) was added to UiO-67-bp/ppy (250 mg, 0.1 mmol) under N₂. Dry CHCl₃ was added and the mixture was refluxed under N₂ for 3 days. The product was washed with MeOH (3 × 20 cm³) and the product was recovered by centrifugation.

The product was isolated as a powder (85 mg), δ_{H} (400 MHz; $(\text{CD}_3)_2\text{SO}$ and D_3PO_4) 3.72 (s, 2.6 H), 7.36 (s, 1 H), 7.43 (s, 1 H), 7.98 (d, $J = 8.0$ Hz, 2 H), 8.11 (m, 1 H), 8.65 (s, 1H). Powder X-ray diffraction analysis of the product indicated loss of crystallinity in the sample.

6.5.3. UiO-66-b/py

6.5.3.1. Synthesis



ZrCl_4 (679 mg, 2.9 mmol), terephthalic acid (398 mg, 2.4 mmol), pyridine-2,5-dicarboxylic acid (84 mg, 0.4 mmol), acetic acid (17 cm^3) and dry DMF (69 cm^3) were added into a 125 cm^3 Teflon-lined stainless steel autoclave. This was incubated at $120 \text{ }^\circ\text{C}$ for 48 h before cooling to room temperature at a rate of $0.1 \text{ }^\circ\text{C min}^{-1}$. The solids were recovered by centrifugation and washed with DMF ($2 \times 30 \text{ cm}^3$) followed by leaving to stand in MeOH for 72 h, exchanging for fresh solvent every 24 h. The product was isolated by centrifugation and dried under vacuum overnight to give $[\text{Zr}_6\text{O}_4(\text{OH})_4(\text{bdc})_{4.6}(\text{pydc})_{0.9}(\text{OAc})_{0.9}]$ (737 mg, 90%) as a white powder, (Found: C, 29.3; H, 3.3; N, 0.9. Expected: C, 32.9; H, 1.7; N, 0.8%); δ_{H} (400 MHz; D_2O and NaOD) 7.79 (s, 1 H), 7.81 (s, 1 H), 8.15 (dd, $J = 8.0, 2.0$ Hz, 1 H), 8.32 (s, 1 H), 8.80 (d, $J = 2.0$ Hz, 1 H). The powder pattern was fitted using TOPAS Academic version 4.1 as an $Fm\bar{3}m$ space group where $a = 20.7364(4) \text{ \AA}$ (Figure 6.6, Appendix 7.3).²

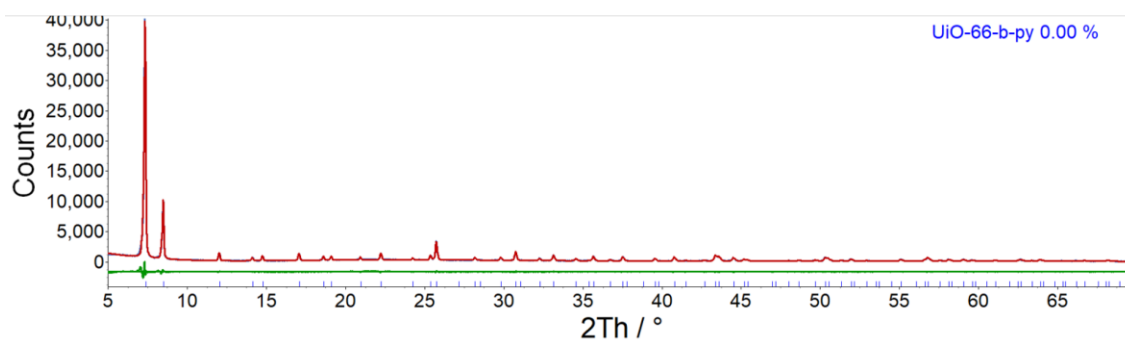
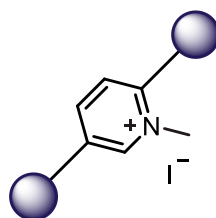


Figure 6.6. Pawley fit of UiO-66-b/py showing the observed pattern (blue), the fit (red), and the difference (green).

6.5.3.2. Reaction with MeI



UiO-66-b/py (200 mg, 0.1 mmol), MeI (8 cm³, 129 mmol) and dry CHCl₃ (40 cm³) were heated to reflux for 3 d. The product was isolated via centrifugation and dried under vacuum overnight to give UiO-66-b/py-Me_{79%} (211 mg) as a yellow powder (Found: C, 28.6; H, 3.6; N, 1.7. Expected: C, 31.4; H, 1.7; N, 0.7%); δ_{H} (400 MHz; (CD₃)₂SO and D₃PO₄) 4.34 (s, 2.4 H), 7.80 (s, 2 H), 7.96 (s, 31 H), 8.18 (dd, $J = 18.0, 8.5$ Hz, 2 H), 8.85 (d, $J = 9.5$ Hz, 1 H). The powder pattern was fitted using TOPAS Academic version 4.1 as an $Fm\bar{3}m$ space group where $a = 20.7548(7)$ Å (Figure 6.7, Appendix 7.3).²

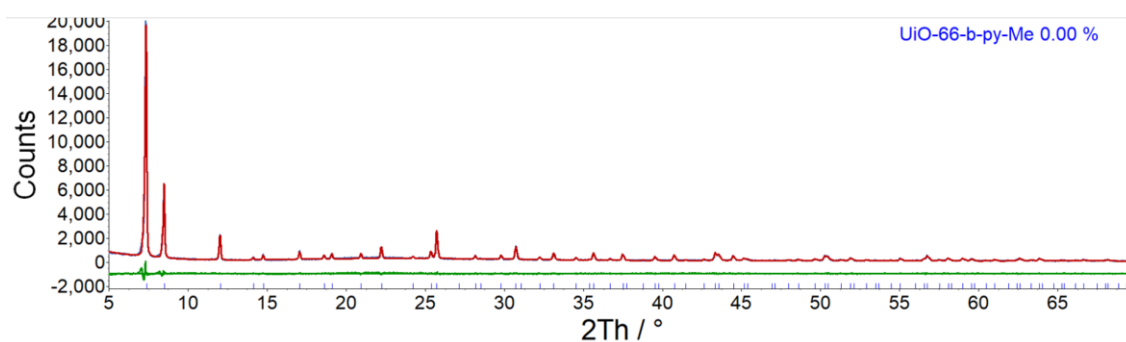
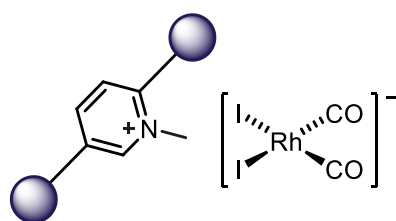


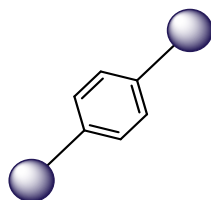
Figure 6.7. Pawley fit of the product of the reaction of UiO-66-b/py with MeI after 3 days showing the observed pattern (blue), the fit (red), and the difference (green).

6.5.3.3. Reaction of UiO-66-b/py-Me_{79%} with [Rh(CO)₂I]₂



[Rh(CO)₂I]₂ (21 mg, 0.05 mmol) in dry hexane (50 cm³) was added to UiO-66-b/py-Me_{79%} (50 mg) under N₂ and left to stir overnight. The solids were isolated via centrifugation and washed with dry hexane (2 × 20 cm³) to give Rh@UiO-66-b/py-Me_{79%} (10 mg) as a grey powder; $\nu(\text{CO}) / \text{cm}^{-1}$ (ATR-IR) 2075 (m), 2002 (m).

6.5.4. UiO-66



Unsubstituted UiO-66 was synthesised via an analogous procedure from the literature.⁹ Terephthalic acid (483 mg, 2.9 mmol) and ZrCl₄ (683 mg, 2.9 mmol) were dissolved in dry DMF (70 cm³). To this was added acetic acid (17 cm³). This mixture was left to stir

for 1 h before being added into a 125 cm³ Teflon-lined stainless steel autoclave. This was incubated at 120 °C for 48 h, with a ramping rate of 1 °C min⁻¹ and a cooling rate of 0.1 °C min⁻¹. Once cooled to room temperature, the product was collected via centrifugation and washed with DMF (2 × 70 cm³), followed by leaving to stand in MeOH for 72 h, exchanging for fresh solvent every 24 h. Finally, the product was dried under high vacuum for 16 h, to give [Zr₆O₄(OH)₄(bdc)₆] (0.594 g, 74% based on zirconium) as a white powder. The powder pattern was fitted using TOPAS Academic version 4.1 as an *Fm* $\bar{3}$ *m* space group where $a = 20.8054(5)$ Å (Figure 6.8, Appendix 7.3).²

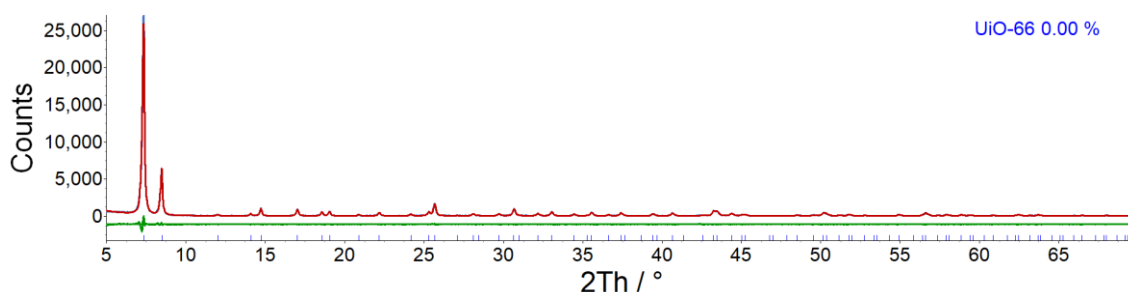
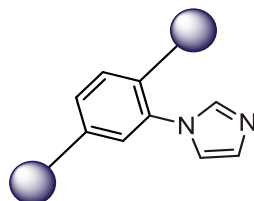


Figure 6.8. Pawley fit of UiO-66 showing the observed pattern (blue), the fit (red), and the difference (green).

6.5.5. UiO-66-imb

6.5.5.1. Synthesis



The MOF was synthesised according to a modified procedure from the literature.⁹ 2-(imidazol-1-yl)terephthalic acid (2.497 g, 8.7 mmol) and ZrCl₄ (2.031 g, 8.7 mmol) were dissolved in dry DMF (208 cm³). To this was added acetic acid (50 cm³). This mixture was left to stir for 1 h before being separated into 3 equal portions and added into

$3 \times 125 \text{ cm}^3$ Teflon-lined stainless steel autoclaves. These were incubated at $120 \text{ }^\circ\text{C}$ for 48 h, with a ramping rate of $1 \text{ }^\circ\text{C min}^{-1}$ and a cooling rate of $0.1 \text{ }^\circ\text{C min}^{-1}$. Once cooled to room temperature, the products were combined and collected via centrifugation and washed with DMF ($2 \times 200 \text{ cm}^3$), followed by leaving to stand in MeOH for 72 h, exchanging for fresh solvent every 24 h. Finally, the product was dried under high vacuum for 16 h, to give $[\text{Zr}_6\text{O}_4(\text{OH})_4(\text{imbdc}\cdot\text{HCl})_6]$ (2.193 g, 66% based on zirconium) as a white powder, (Found: C, 34.1; H, 3.7; N, 7.2; Cl, 3.4. Expected: C, 34.8; H, 2.0; N, 7.4; Cl, 9.3%); δ_{H} (400 MHz; $(\text{CD}_3)_2\text{SO}$ and D_3PO_4) 6.82 (s, 1 H), 6.86 (s, 1 H), 7.37 (s, 1 H), 7.47 (br. m, 2 H), 8.14 (s, 1 H); δ_{C} (400 MHz; $(\text{CD}_3)_2\text{SO}$ and D_3PO_4) 118.78, 123.02, 128.33, 129.87, 131.35, 131.84, 133.39, 134.21, 135.13, 165.86, 169.99. The powder pattern was fitted using TOPAS Academic version 4.1 as an $Fm\bar{3}m$ space group where $a = 20.7881(3) \text{ \AA}$ (Figure 6.9, Appendix 7.3).²

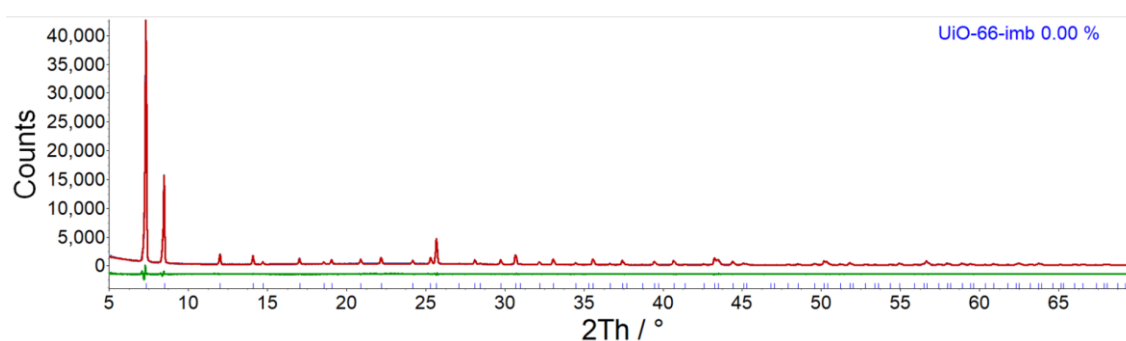
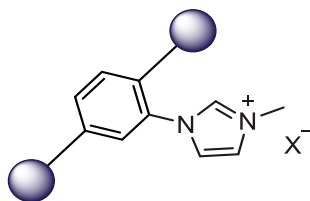


Figure 6.9. Pawley fit of UiO-66-imb showing the observed pattern (blue), the fit (red), and the difference (green).

6.5.5.2. Quaternisation



The cationic MOF was synthesised via postsynthetic modification of UiO-66-imb. UiO-66-imb (0.400 g, ~0.23 mmol) was added to a 10 cm³ microwave tube with dry MeCN (3 cm³) and MeI (1 cm³). The tube was heated to 120 °C in a microwave for 1 h, reaching a pressure of 6 bar, before drying under vacuum overnight to give [Zr₆O₄(OH)₄(**imbdc**)_{0.9}(**imbdc-Me**)_{5.1}]X_{5.1} (0.369 g) as a yellow powder, (Found: C, 28.5; H, 2.6; N, 1.2. Expected: C, 29.7; H, 2.0; N, 5.8%, assuming all X⁻ = I⁻); δ_{H} (400 MHz; (CD₃)₂SO and D₃PO₄) 3.14 (s, 2.6 H), 6.79 (m, 2 H), 7.40 (m, 3 H), 8.09 (m, 2 H); δ_{C} (400 MHz; D₂O and D₃PO₄) 35.45, 122.74, 123.47, 128.34, 129.90, 131.41, 131.88, 133.33, 134.27, 136.39, 165.91, 167.07; m/z (EI, (CD₃)₂SO and D₃PO₄) 247 (100%, M⁺), 233 (6%, M⁺ - CH₃). The powder pattern was fitted using TOPAS Academic version 4.1 as an *Fm* $\bar{3}$ *m* space group where $a = 20.813(1)$ Å (Figure 6.10, Appendix 7.3).²

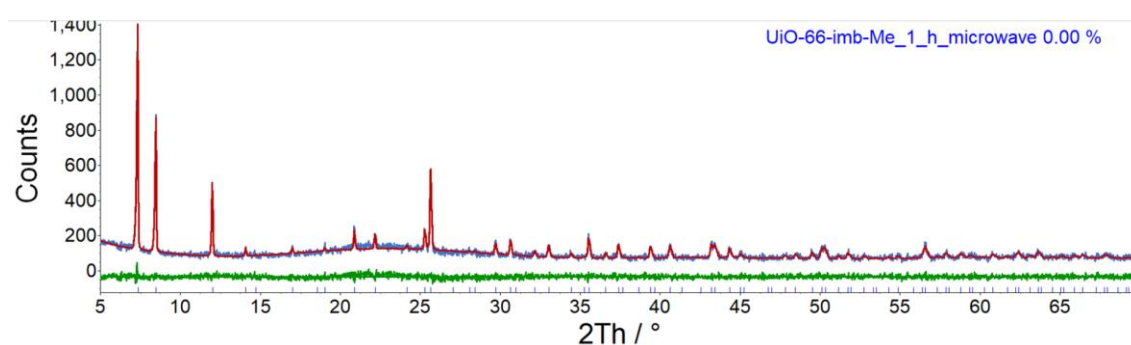
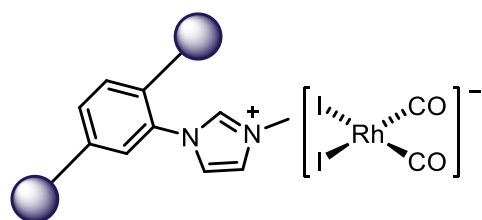
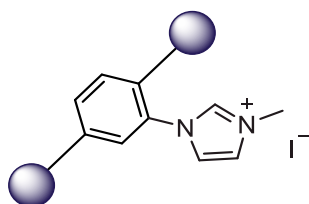


Figure 6.10. Pawley fit of the product of the reaction of UiO-66-imb with MeI after 1 hour in the microwave showing the observed pattern (blue), the fit (red), and the difference (green).

6.5.5.3. Reaction of UiO-66-imb-Me_{85%} with [Rh(CO)₂I]₂

Dry *n*-hexane (20 cm³) was added to a mixture of UiO-66-imb-Me_{85%} (63 mg) and [Rh(CO)₂I]₂ (46 mg, 0.08 mmol) under CO gas. The mixture was stirred at RT for 16 h. Solids were collected *via* centrifugation and washed with dry *n*-hexane (2 × 20 cm³) before drying under high vacuum for 1 h to give the product as a brown powder (38 mg), $\nu(\text{CO}) / \text{cm}^{-1}$ (ATR-IR) 2064 (s), 1994 (s). The product was stored at *ca.* 5 °C under CO.

6.5.6. UiO-66-imb-Me (attempted direct synthesis)



The MOF was synthesised according to a modified procedure from the literature.⁹ 1-(2,5-dicarboxyphenyl)-3-methyl-1*H*-imidazol-3-ium iodide (3.001 g, 8.0 mmol) and ZrCl₄ (1.866 g, 8.0 mmol) were dissolved in dry DMF (194 cm³). To this was added acetic acid (46 cm³). This mixture was left to stir for 1 h before being separated into 24 equal portions and added into glass vials. These were incubated at 80 °C for 48 h, with a ramping rate of 1 °C min⁻¹ and a cooling rate of 0.1 °C min⁻¹. Upon cooling to room temperature, no precipitate had formed, and so the solution was added into 3 × 125 cm³ Teflon-lined stainless steel autoclaves. These were incubated at 80 °C for 48 h, with a ramping rate of 1 °C min⁻¹ and a cooling rate of 0.1 °C min⁻¹. Once cooled to room temperature, the products were combined and collected *via* centrifugation and washed with DMF (2 × 150

cm³), followed by leaving to stand in MeOH for 72 h, exchanging for fresh solvent every 24 h. Finally, the product was dried under high vacuum for 16 h, to give the product (326 mg, 18% based on zirconium) as a white powder, δ_{H} (400 MHz; (CD₃)₂SO and D₃PO₄) 3.91 (s, 3 H), 7.74 (d, $J = 1.5$ Hz, 1 H), 7.88 (d, $J = 2.0$ Hz, 2 H), 8.11 (d, $J = 9.0$ Hz, 1 H), 8.24 (m, 2 H), 9.35 (s, 1 H). The powder pattern was fitted using TOPAS Academic version 4.1 as an $Fm\bar{3}m$ space group where $a = 20.776(7)$ Å (Figure 6.11, Appendix 7.3).²

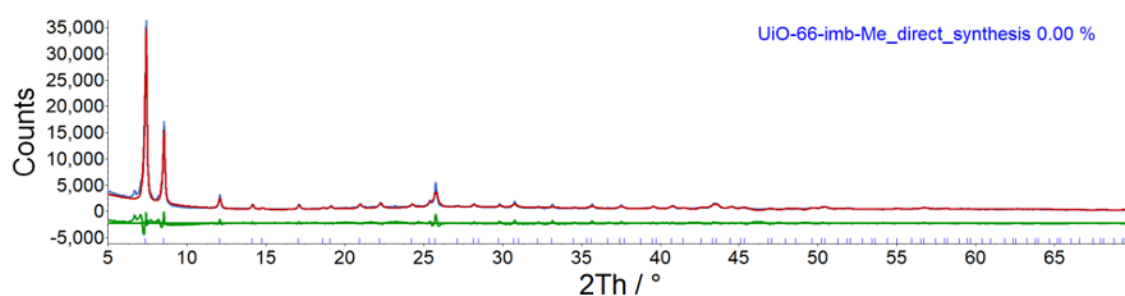
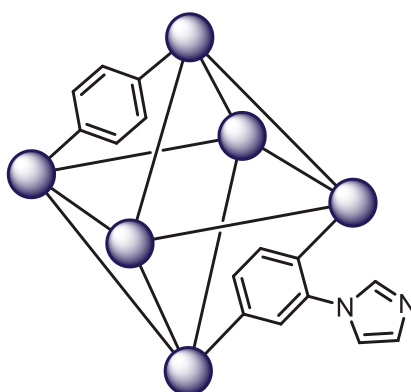


Figure 6.11. Pawley fit of UiO-66-imb-Me showing the observed pattern (blue), the fit (red), and the difference (green).

6.5.7. UiO-66-b/imb

6.5.7.1. Synthesis



The MOF was synthesised in an analogous manner to that described in Section 6.5.5.1. Briefly, ZrCl₄ (2.055 g, 8.8 mmol), terephthalic acid (1.205 g, 7.3 mmol),

2-(imidazol-1-yl)terephthalic acid (0.389 g, 1.7 mmol), acetic acid (50 cm³) and dry DMF (208 cm³) were added to 3 × 125 cm³ Teflon-lined stainless steel autoclaves. This mixture was incubated at 120 °C for 48 h, with a ramping rate of 1 °C min⁻¹ and a cooling rate of 0.1 °C min⁻¹. Once cooled to room temperature, the products were combined and collected via centrifugation and washed with DMF (2 × 200 cm³), and soaked in MeOH for 72 h, exchanging for fresh solvent every 24 h. Finally, the product was dried under high vacuum for 16 h, to give mixed-linker [Zr₆O₄(OH)₄(**bdc**)_{4.8}(**imbdc**)_{1.1}(**OAc**)_{0.1}] (2.477 g, 89% based on zirconium) as a white powder, (Found: C, 32.6; H, 2.6; N, 1.5. Expected: C, 35.3; H, 1.8; N, 1.8%); δ_H (400 MHz; D₂O and NaOD) 2.1 (s, 3 H), 7.03 (s, 1 H), 7.22 (s, 1 H), 7.45 (d, *J* = 8.0 Hz, 1 H), 7.71 (m, 2 H), 7.74 (s, 16 H), 7.80 (dd, *J* = 8.0, 1.5 Hz, 1 H). ¹H NMR analysis of the digested product (NaOD in D₂O) suggested a 4.3:1:0.1 ratio of **bdc** : **imbdc** : **OAc** in the final product. The powder pattern was fitted using TOPAS Academic version 4.1 as an *Fm* $\bar{3}$ *m* space group where *a* = 20.739(2) Å (Figure 6.12, Appendix 7.3).²

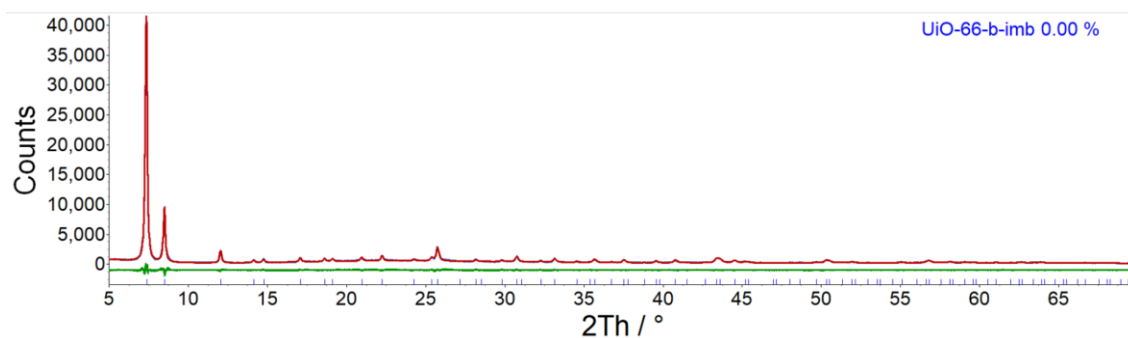
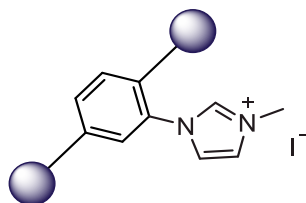


Figure 6.12. Pawley fit of UiO-66-b/imb showing the observed pattern (blue), the fit (red), and the difference (green).

6.5.7.2. Quaternisation



A sample of UiO-66-b/imb (200 mg) was added to a microwave reactor with dry MeCN (3 cm³) and MeI (1 cm³). This mixture was heated to 120 °C for one hour with stirring, reaching a pressure of *ca.* 6 bar. The product was collected by centrifugation and washed with MeOH (2 × 20 cm³) before drying under high vacuum for 16 h to give the product (186 mg) as an off-white powder, (Found: C, 28.5; H, 2.6; N, 1.2. Expected for [Zr₆O₄(OH)₄(bdc)_{4.8}(imbdc-Me)_{1.1}(OAc)_{0.1}]I_{1.1}: C, 33.1; H, 1.8; N, 1.6%); δ_{H} (400 MHz; (CD₃)₂SO and D₃PO₄) 3.84 (s, 2.9 H), 7.52 (s, 1 H), 7.60 (s, 1 H), 7.96 (s, 16 H), 8.00 (s, 1 H), 8.16 (m, 2 H), 8.97 (s, 1 H). ¹H NMR analysis of the digested product (D₂O and D₃PO₄) indicated near quantitative (97%) conversion of imidazole to *N*-methylimidazolium. The powder pattern was fitted using TOPAS Academic version 4.1 as an *Fm* $\bar{3}$ *m* space group where *a* = 20.750(1) Å (Figure 6.13, Appendix 7.3).²

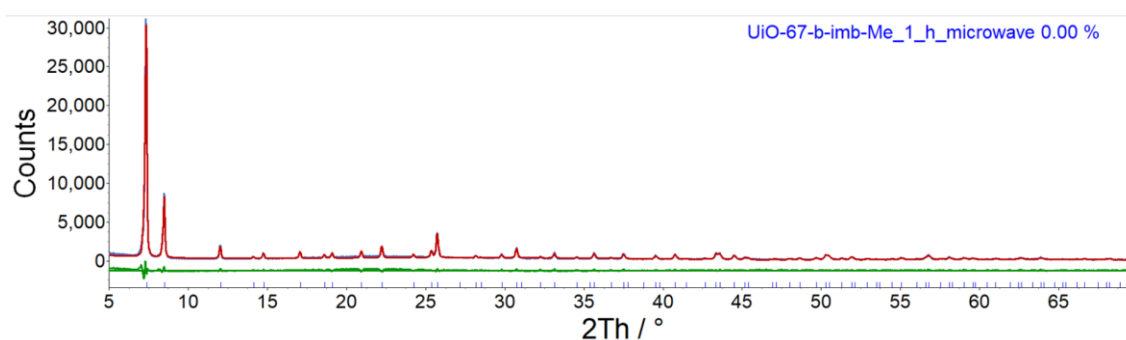
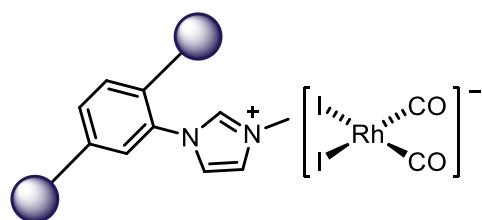


Figure 6.13. Pawley fit of the product of the reaction of UiO-66-b/imb with MeI after 1 hour in the microwave showing the observed pattern (blue), the fit (red), and the difference (green).

6.5.7.3. Reaction of UiO-66-b/imb-Me_{97%} with [Rh(CO)₂I]₂

Dry *n*-hexane (20 cm³) was added to a mixture of UiO-66-b/imb-Me_{97%} (150 mg) and [Rh(CO)₂I]₂ (27 mg, 0.04 mmol) under CO gas. The mixture was stirred at RT for 16 h. Solids were collected *via* centrifugation and washed with dry *n*-hexane (2 × 20 cm³) before drying under high vacuum for 1 h to give the product as a brown powder (145 mg), $\nu(\text{CO}) / \text{cm}^{-1}$ (KBr disc) 2060 (s), 1986 (s). The product was stored at *ca.* 5 °C under CO. The powder pattern was fitted using TOPAS Academic version 4.1 as an *Fm* $\bar{3}$ *m* space group where $a = 20.760(1) \text{ \AA}$ (Figure 6.14, Appendix 7.3).²

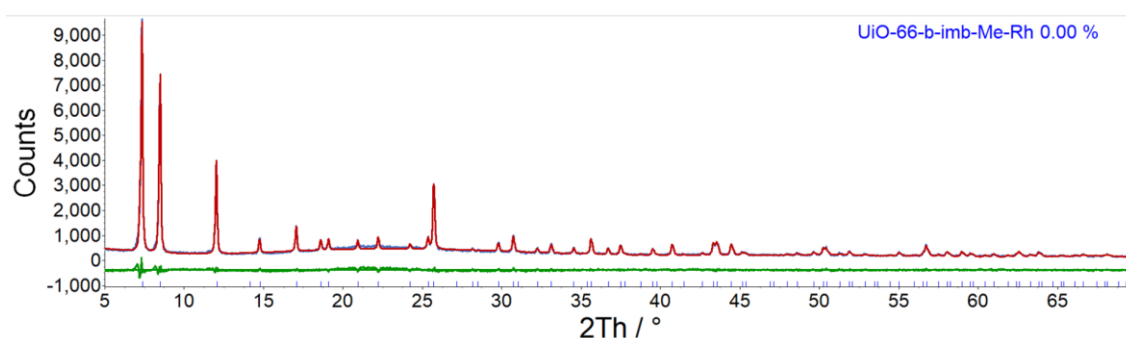


Figure 6.14. Pawley fit of the product of the reaction of UiO-66-b/imb-Me_{97%} with [Rh(CO)₂I]₂ showing the observed pattern (blue), the fit (red), and the difference (green).

6.5.7.4. Catalysis

Following the catalysis experiment using UiO-66-b/imb-Me_{97%} and [Rh(CO)₂I]₂ described in Section 6.8 the solid was recovered by centrifugation and powder X-ray diffraction analysis indicated retention of crystallinity. The powder pattern was fitted

using TOPAS Academic version 4.1 as an $Fm\bar{3}m$ space group where $a = 20.769(3)$ Å (Figure 6.15, Appendix 7.3).²

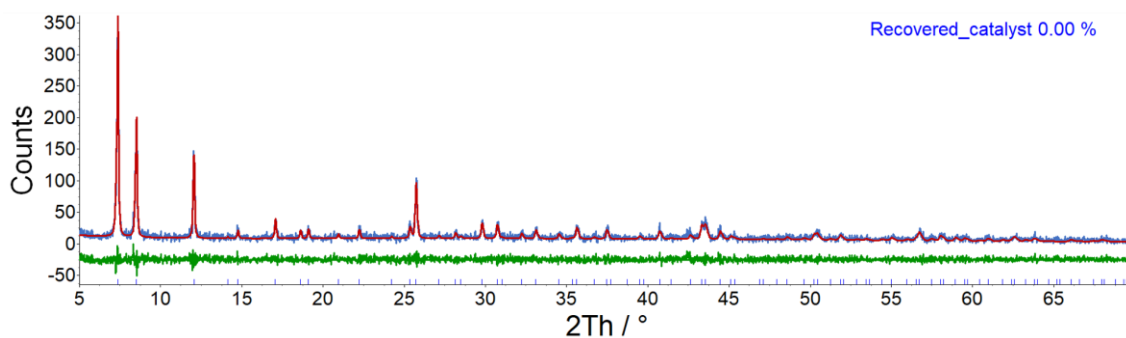
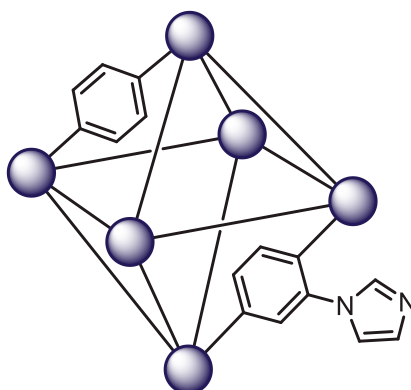


Figure 6.15. Pawley fit of the recovered product of the catalysis reaction showing the observed pattern (blue), the fit (red), and the difference (green).

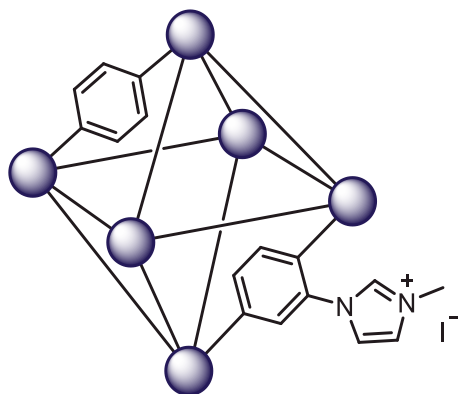
6.5.8. UiO-66-b/imb (attempted single crystal synthesis)



Single crystal synthesis was attempted according to a modified literature procedure.¹³ $ZrCl_4$ (304 mg, 1.3 mmol), terephthalic acid (181 mg, 1.1 mmol), 2-(imidazol-1-yl)terephthalic acid (58 mg, 0.2 mmol) and benzoic acid (38.5 mmol) were dissolved in dry DMF (10 cm³). The clear solution was added to a 25 cm³ Erlenmeyer flask which had been pre-treated with 2 M aq. KOH overnight. A loose cap was placed on the flask to allow evaporation of volatile by-products and the solution was heated without stirring at 130 °C for 48 h, during which colourless microscopic crystals were observed to form. After cooling to room temperature the remaining solvent was decanted

and the crystals washed with dry DMF ($5 \times 10 \text{ cm}^3$). The product was imaged via SEM and found to be unsuitable for single crystal X-ray diffraction analysis.

6.5.9. UiO-66-b/imb-Me (attempted single crystal synthesis)

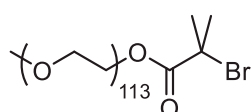


Single crystal synthesis was attempted according to a modified literature procedure.¹³ ZrCl_4 (303 mg, 1.3 mmol), terephthalic acid (181 mg, 1.1 mmol), 1-(2,5-dicarboxyphenyl)-3-methyl-1*H*-imidazol-3-ium iodide (83 mg, 0.2 mmol) and benzoic acid (38.5 mmol) were dissolved in dry DMF (10 cm^3). The clear solution was added to a 25 cm^3 Erlenmeyer flask which had been pre-treated with 2 M aq. KOH overnight. A loose cap was placed on the flask to allow evaporation of volatile by-products and the solution was heated without stirring at $130 \text{ }^\circ\text{C}$ for 48 h, during which colourless microscopic crystals were observed to form. After cooling to room temperature the remaining solvent was decanted and the crystals washed with dry DMF ($5 \times 10 \text{ cm}^3$). The product was imaged via SEM and found to be unsuitable for single crystal X-ray diffraction analysis.

6.6. Synthesis of dispersible microporous polymer nanoparticles

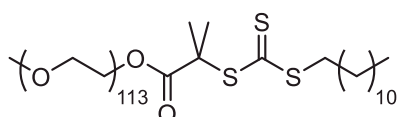
Syntheses in Sections 6.6.1-6.6.3 were performed by A. M. James.

6.6.1. Synthesis of PEG₁₁₃-Br



PEG₁₁₃-Br was prepared in a method similar to that reported previously.¹⁴ Poly(ethylene glycol) monomethyl ether (8 g, 1.6 mmol, 1 eq.) was dissolved in anhydrous toluene (100 cm³) in a two-neck round bottom flask. Triethylamine (0.32 cm³, 2.3 mmol, 1.4 eq.) was added and the solution was cooled to 0 °C. 2-bromoisobutyryl bromide (0.26 cm³, 2.1 mmol, 1.3 eq.) was added dropwise over the course of 1 h before being left to stir overnight at room temperature. The solvent was reduced before being precipitated into an excess of cold diethyl ether (200 mL). The crude product was dried under vacuum, dissolved in water before being extracted with CH₂Cl₂. The organic layers were collected, combined and dried over MgSO₄ before the solvent was removed under reduced pressure to afford the PEG₁₁₃-Br product, which was stored in a 5 °C fridge (87%), (Found: C, 53.8; H, 9.1. Expected C, 54.0; H, 9.0%).

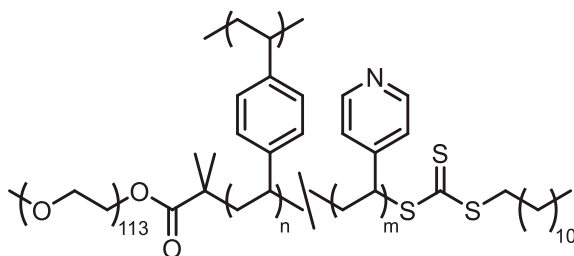
6.6.2. Synthesis of PEG-based macro-chain transfer agent (CTA)



The PEG-based macro-CTA was synthesised in an identical procedure to that previously reported.¹⁵ Dodecane thiol (0.60 cm³, 2.5 mmol, 1 eq.) was added to a stirred suspension

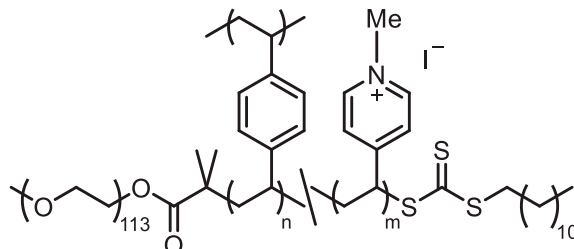
of K_3PO_4 (0.53 g, 2.5 mmol, 1 eq.) in acetone (50 mL) and stirred for 10 minutes. Carbon disulphide (0.36 cm³, 6 mmol, 2.5 eq.) was added to the suspension and left to stir for a further 10 minutes. PEG₁₁₃-Br (10 g, 2 mmol, 0.8 eq.) in acetone (30 cm³) was added to the suspension, which was left to stir overnight at room temperature. The solvent was removed by rotary evaporation precipitated into an excess of *n*-hexane twice and once into diethyl ether to further purify. The sample was dried *in vacuo* at 40 °C for 16 h to afford the RAFT macro-CTA (88%), (Found: C, 54.5; H, 9.1; S, 1.8. Expected: C, 54.5; H, 9.1; S, 1.8%).

6.6.3. Synthesis of PEG₁₁₃-*b*-DVB₃₀₀-*co*-VP₆₃ (1)



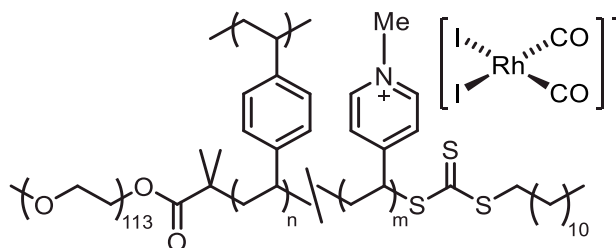
The PEG-based macro CTA (0.26 g, 0.05 mmol, 1 eq.) was added to a 2-necked round bottom flask and evacuated and back-filled with nitrogen 3 times. Water and ethanol in a 60:40 ratio along with 1,4-divinylbenzene (DVB) (1.70 cm³, 12 mmol, 240 eq.) and 4-vinylpyridine (VP) (1.32 cm³, 12 mmol, 240 eq.) were added to the flask to create a 1 % wt. solution. The solution was bubbled with nitrogen gas to remove any oxygen before heating to 70 °C. Polymerisation was initiated through the addition of potassium persulfate (KPS, 2.7 mg, 0.01 mmol, 0.2 eq.) and held at 70 °C for 24 h. The product was collected by centrifugation at 4500 rpm for 1 hour before being stirred with diethyl ether to remove any unreacted monomer. Finally, the white solid was isolated through vacuum filtration and dried *in vacuo* at 40 °C for 16 h (0.914 g, 30 %), (Found: C, 87.1; H, 7.7; N, 1.7. Expected: C, 86.7; H, 7.8; N, 1.7%).

6.6.4. *N*-methylation of **1** to give PEG₁₁₃-*b*-DVB₃₀₀-*co*-VP₁₃-*co*-[VP⁺I]₅₀ (**2**)



PEG₁₁₃-*b*-DVB₃₀₀-*co*-VP₆₃ (596 mg) was sonicated in a mixture of dry CHCl₃ (60 cm³) and MeI (6 cm³) for 30 minutes to suspend the material. This was then stirred at 75 °C under reflux for 72 h. The resulting yellow suspension was centrifuged at 4500 rpm for 1 h before decanting the supernatant and washing the solid in Et₂O (20 cm³ × 2). The product was dried under dynamic vacuum at 80 °C for 16 h to give **2** as a yellow powder (564 mg), (Found: C, 76.9; H, 6.9; N, 1.7; I, 10.5. Expected: C, 77.2; H, 7.1; N, 1.5; I 10.9%).

6.6.5. Reaction of **2** with [Rh(CO)₂I]₂ to give **3**



Dry CHCl₃ (40 cm³) was added to a mixture of **2** (487 mg) and [Rh(CO)₂I]₂ (100 mg, 0.17 mmol) under N₂ gas. The mixture was sonicated for 30 minutes to suspend the nanoparticles and then stirred at RT for 16 h. The solvent was removed *in vacuo* and the solid residue was stirred in dry *n*-hexane (50 cm³) for 30 minutes. The solid was collected by filtration and washed with dry *n*-hexane (25 cm³ × 2). The product was dried under high vacuum for 16 h and then stored at 4 °C under CO. **3** was synthesised as a brown

powder (440 mg) (Found: C, 59.0; H, 5.1; N, 1.9; I, 22.0; Rh, 4.5. Expected: C, 65.4; H, 5.9; N, 1.3; I 16.7; Rh, 6.2%); $\nu(\text{CO}) / \text{cm}^{-1}$ (KBr disc) 2059 (s), 1987 (s).

6.7. Kinetic measurements

Dry CH_2Cl_2 (3 cm^3) was added to a sample of the product of Section 6.6.5 ($\sim 10 \text{ mg}$) and the mixture was sonicated for 30 minutes. Varying amounts of MeI were added to a 2 cm^3 volumetric flask and this was made up to the mark with the suspension. The mixture was injected into a solution cell (CaF_2 windows, 0.5 mm path length) fitted with a thermostatted jacket (illustrated in Figure 6.16). A background spectrum was recorded using the appropriate solvent mixture and the reaction was monitored using Fourier transform infrared (FTIR) spectroscopy in the region $2200\text{-}1500 \text{ cm}^{-1}$.

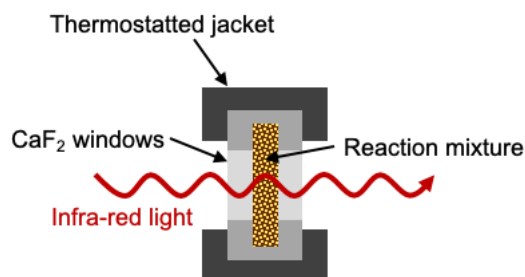


Figure 6.16. Schematic of kinetic cell.

Pseudo first-order rate constants, k_{obs} , were obtained by fitting exponential or double exponential decay curves to the experimental data using Origin software.

6.8. Catalytic reaction procedure

Methanol carbonylation reactions using supported or homogeneous *cis*-[Rh(CO)₂I₂]⁻ catalysts were monitored *in situ* by high-pressure IR spectroscopy using a cylindrical internal reflectance (CIR) cell comprising an autoclave (Parr) modified to accommodate a crystalline silicon CIR rod, as described previously (Figure 6.17).¹⁶ Spectra were recorded using a Perkin-Elmer Spectrum GX FTIR spectrometer fitted with an MCT detector. The cell was placed directly in the spectrometer sample compartment and aligned to maximize IR energy throughput using a tilt table. A background spectrum was recorded using the appropriate solvent mixture at 120 °C.

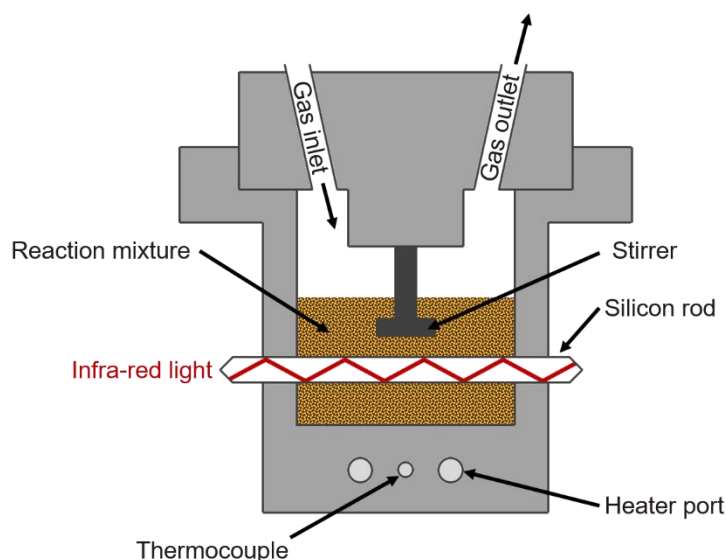


Figure 6.17. Schematic of HPIR cell.

For the dispersible polymer nanoparticle catalyst, one reaction was performed as follows; catalyst-supported material (**3**, 101.6 mg) was suspended in dry MeOH (5 cm³) via sonication (30 minutes). MeI (0.5 cm³) was added to a 5 cm³ volumetric flask which was made up to the mark with dry MeOH. The two mixtures were added to the cell, which was flushed five times with CO. It was subsequently pressurised with CO (10 bar) and

heated to 120 °C. Four scans were taken for each IR spectrum at ten minute intervals over the course of 12 hours in the region 2200-1500 cm⁻¹.

In all other procedures, dry CHCl₃ (5 cm³) was added to a quaternised support (100 mg) (either MOF UiO-66-b/imb-Me_{97%} or polymer **2**) and [Rh(CO)₂I]₂ (10 mg, 0.017 mmol) under CO gas to generate encapsulated *cis*-[Rh(CO)₂I]₂⁻ *in situ*. The mixture was sonicated for 30 minutes and stirred for 16 h at RT. Meanwhile, MeI (0.5 cm³) and dry MeOH (1 cm³) were added to a 5 cm³ volumetric flask which was made up to the mark with dry CHCl₃. This mixture of solvents and the previously prepared suspension were added to the cell. The cell was flushed 5 times with CO. It was subsequently pressurised with CO (10 bar) and heated to 120 °C. Four scans were taken for each IR spectrum at five minute intervals over the course of four hours in the region of 2200-1500 cm⁻¹.

For comparison an experiment was carried out under identical conditions but using *n*-Bu₄NI (13 mg, 0.035 mmol) in place of a quaternised support to generate homogeneous *cis*-[Rh(CO)₂I]₂⁻ from [Rh(CO)₂I]₂ *in situ*.

6.9. References

- 1 A. B. Pangborn, M. A. Giardello, R. H. Grubbs, R. K. Rosen and F. J. Timmers, *Organometallics*, 1996, **15**, 1518–1520.
- 2 A. A. Coelho, TOPAS Academic Version 4.1, see <http://www.topas-academic.net>.
- 3 B. R. Pauw, A. J. Smith, T. Snow, N. J. Terrill and A. F. Thünemann, *J. Appl. Crystallogr.*, 2017, **50**, 1800–1811.
- 4 J. Ilavsky and P. R. Jemian, *J. Appl. Crystallogr.*, 2009, **42**, 347–353.
- 5 J. S. Trent, *Macromolecules*, 1984, **17**, 2930–2931.
- 6 J. A. McCleverty, G. Wilkinson, L. G. Lipson, M. L. Maddox and H. D. Kaesz, *Inorg. Synth.*, 1966, **8**, 214–217.
- 7 A. Fulford, C. E. Hickey and P. M. Maitlis, *J. Organomet. Chem.*, 1990, **398**, 311–323.
- 8 T. Liu, D.-Q. Li, S.-Y. Wang, Y.-Z. Hu, X.-W. Dong, X.-Y. Liu and C.-M. Che, *Chem. Commun.*, 2014, **50**, 13261–13264.
- 9 J. Liang, R.-P. Chen, X.-Y. Wang, T.-T. Liu, X.-S. Wang, Y.-B. Huang and R. Cao, *Chem. Sci.*, 2017, **8**, 1570–1575.
- 10 J. Liang, Y.-Q. Xie, X.-S. Wang, Q. Wang, T.-T. Liu, Y.-B. Huang and R. Cao, *Chem. Commun.*, 2017, **54**, 342–345.
- 11 H. Fei and S. M. Cohen, *Chem. Commun.*, 2014, **50**, 4810.
- 12 L. Xu, Y. Luo, L. Sun, S. Pu, M. Fang, R. Yuan and H. Du, *Dalton Trans.*, 2016, **45**, 8614–8621.
- 13 S. Øien, D. Wragg, H. Reinsch, S. Svelle, S. Bordiga, C. Lamberti and K. P. Lillerud, *Cryst. Growth Des.*, 2014, **14**, 5370–5372.
- 14 J. Chen, M. Liu, H. Gong, Y. Huang and C. Chen, *J. Phys. Chem. B*, 2011, **115**, 14947–14955.

- 15 A. M. James, M. J. Derry, J. S. Train and R. Dawson, *Polym. Chem.*, 2019, **10**, 3879–3886.
- 16 W. R. Moser, J. E. Cnossen, A. W. Wang and S. A. Krouse, *J. Catal.*, 1985, **95**, 21–32.

Chapter 7 Appendices

7.2. Determination of TOF value for MOF-supported catalyst in CHCl_3

Table 7.3 gives key values for the determination of the rate of formation of methyl acetate, where ϵ is the measured extinction coefficient of methyl acetate in CHCl_3 in the cell.

Table 7.1. Key values for determination of rate of formation of methyl acetate.

$$\epsilon / \text{mol}^{-1} \text{ dm}^3 \quad 0.193$$

$$\text{Volume} / \text{dm}^3 \quad 0.01$$

$$\text{Gradient} / \text{h}^{-1} \quad 0.0045$$

The rate of formation of methyl acetate can be calculated as shown in Equation 7.1, and gives a value of $2.33 \times 10^{-4} \text{ mol h}^{-1}$.

$$\text{Rate of formation} = \text{Gradient} \div \frac{\epsilon}{\text{Volume}}$$

Equation 7.1.

As 10 mg of $[\text{Rh}(\text{CO})_2\text{I}]_2$ was used, this corresponded to 3.53×10^{-5} moles of rhodium in total.

To calculate the TOF, the rate of formation of methyl acetate was divided by the number of moles of rhodium in the system in total, to give a value of 6.60 h^{-1} .

7.3. Pawley phase fits

All patterns were fit as cubic $Fm\bar{3}m$ space groups with nine background terms, one zero-point term and five peak profile terms.

Indexing and Pawley refinements were carried out using TOPAS Academic version 4.1.¹

Indices of fit between the calculated and experimental diffraction patterns (R_{wp} and R_{wp}') are defined by Equation 7.2 and Equation 7.3 respectively.

$$R_{wp} = \sqrt{\frac{\sum[w(Y_{obs} - Y_{calc})^2]}{\sum[wY_{obs}^2]}}$$

Equation 7.2.

$$R_{wp}' = \sqrt{\frac{\sum[w(Y_{obs} - Y_{calc})^2]}{\sum[w(Y_{obs} - bkg)^2]}}$$

Equation 7.3.

Table 7.2. Data from Pawley phase fits of MOF materials.

Sample	$a / \text{Å}$	R_{wp}	R_{wp}'	Reflections
UiO-67-bpy	26.6062(4)	7.0	9.8	121
UiO-67-bp/ppy	26.890(2)	25.5	32.3	265
UiO-67-bp/ppy-Me _{51%}	26.880(3)	13.8	28.0	267
UiO-67-bp/ppy-Me _{61%}	26.931(4)	16.2	29.8	267
UiO-67-bp/ppy-Me _{73%}	26.890(25)	14.0	22.6	267
UiO-66-b/py	20.7364(4)	8.1	13.5	131
UiO-66-b/py-Me _{79%}	20.7548(7)	8.8	16.8	131
UiO-66	20.8054(5)	8.2	10.6	131
UiO-66-imb	20.7881(3)	7.7	13.3	131
UiO-66-imb-Me _{85%}	20.813(1)	10.4	39.7	131
UiO-66-imb-Me (direct synthesis)	20.776(7)	14.3	24.1	131
UiO-66-b/imb	20.739(2)	8.0	13.5	131
UiO-66-b/imb-Me _{97%}	20.750(1)	14.9	26.1	131
Rh@UiO-66-b/imb-Me _{97%}	20.760(1)	8.3	11.5	131
Rh@UiO-66-b/imb-Me _{97%} (post-catalysis)	20.769(3)	32.7	58.3	131

7.4. SAXS fitting

The X-ray scattering of homogeneous solid spheroids, represented by the scattering cross-section per unit sample volume, $\frac{d\Sigma}{d\Omega}(q)_n$, can be expressed as:

$$\frac{d\Sigma}{d\Omega}(q)_n = N_n S_{PY}(q)_n \int_0^{\infty} g_{Gauss}(R_n) |F(qR_n)|^2 dR_n$$

Equation 7.4.

Where N_n is the number of scatterers, $S_{PY}(q)_n$ is the hard-sphere interaction structure factor based on the Percus-Yevick approximation,² $g_{Gauss}(R_n)$ is their Gaussian size distribution function and $F(qR_n)$ is the particle form factor. Specifically, $g_{Gauss}(R_n)$ is expressed as:

$$g_{Gauss}(R_n) = \frac{1}{\sigma_{R_n} \sqrt{2\pi}} e^{-\frac{(R_n - \bar{R}_n)^2}{2\sigma_{R_n}^2}}$$

Equation 7.5.

Where \bar{R}_n is the mean radius of the particles and σ_{R_n} is the standard deviation of the size distribution. The particle form factor, $F(qR_n)$, is expressed as:

$$F(qR_n) = \frac{4}{3} \pi R_n^3 \Delta\xi \left(3 \frac{\sin(qR_n) - qR_n \cos(qR_n)}{(qR_n)^3} \right)$$

Equation 7.6.

Where $\Delta\xi$ is the X-ray scattering contrast.

Initial inspection of the background-subtracted SAXS pattern for each sample in indicated a complex morphology with two populations present, as in an analogous system.³ Hence, a two-population approximation could be used to fit the data satisfactorily:

$$I(q) = \frac{d\Sigma}{d\Omega}(q)_1 + \frac{d\Sigma}{d\Omega}(q)_2$$

Equation 7.7.

7.5. Decay graphs of IR absorption at 1987 cm^{-1} with double exponential curve fits during reaction of polymer-supported catalyst with MeI in CH_2Cl_2 (298 K)

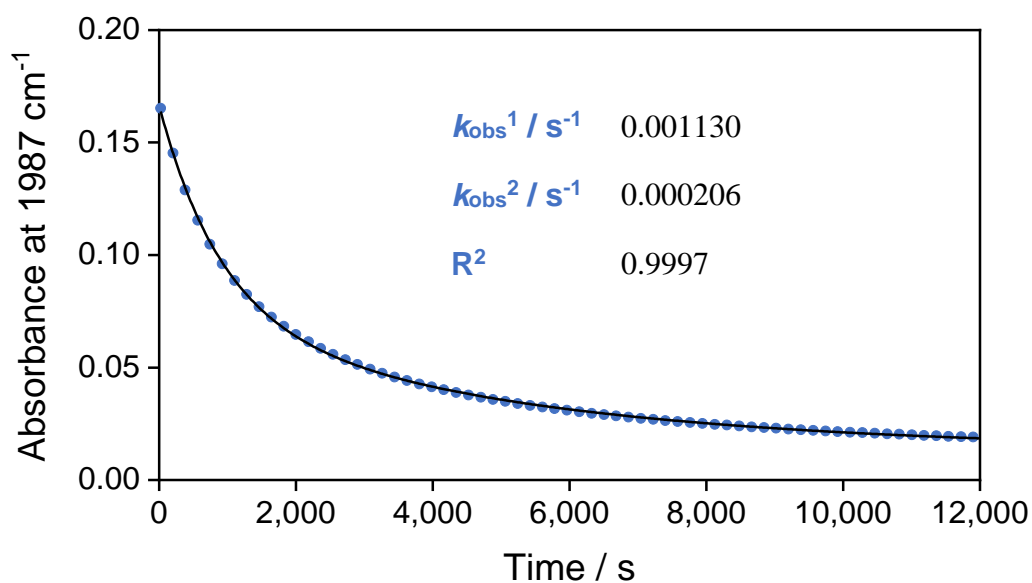


Figure 7.2. Decay of IR absorption at 1987 cm^{-1} with double exponential curve fit during reaction of **3** with 1 M MeI in CH_2Cl_2 (298 K).

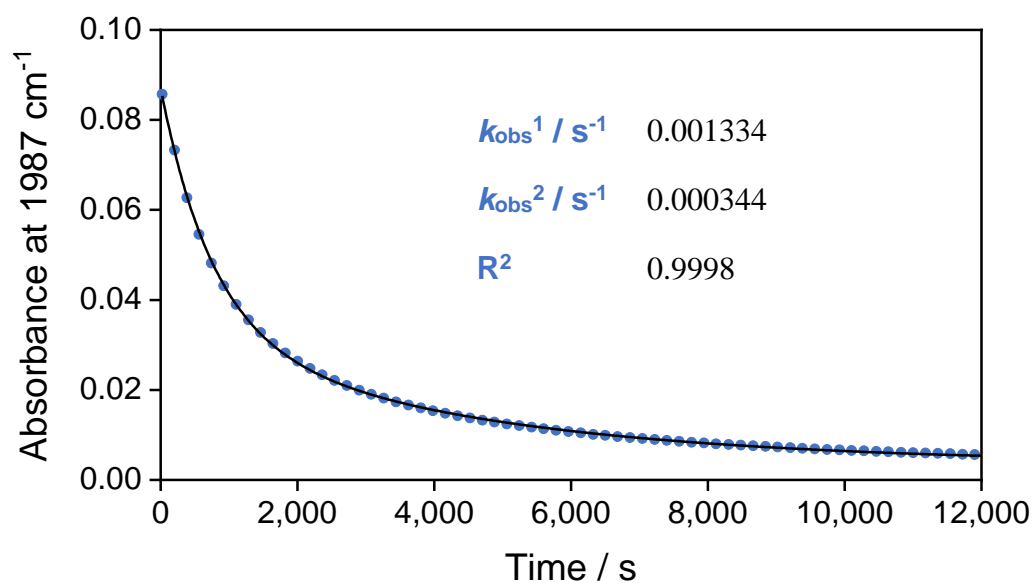


Figure 7.3. Decay of IR absorption at 1987 cm⁻¹ with double exponential curve fit during reaction of **3** with 2 M Mel in CH₂Cl₂ (298 K).

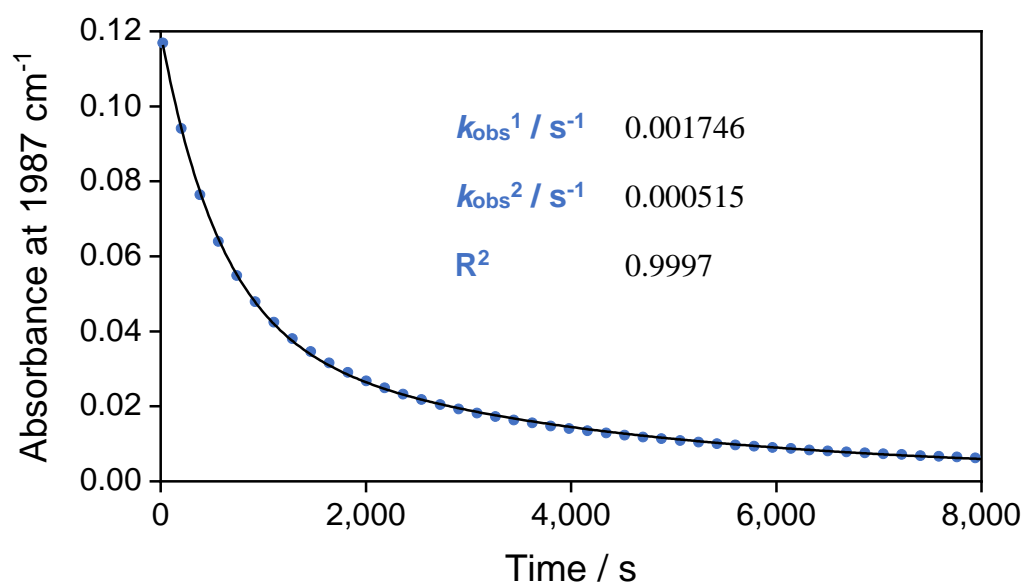


Figure 7.4. Decay of IR absorption at 1987 cm⁻¹ with double exponential curve fit during reaction of **3** with 4 M Mel in CH₂Cl₂ (298 K).

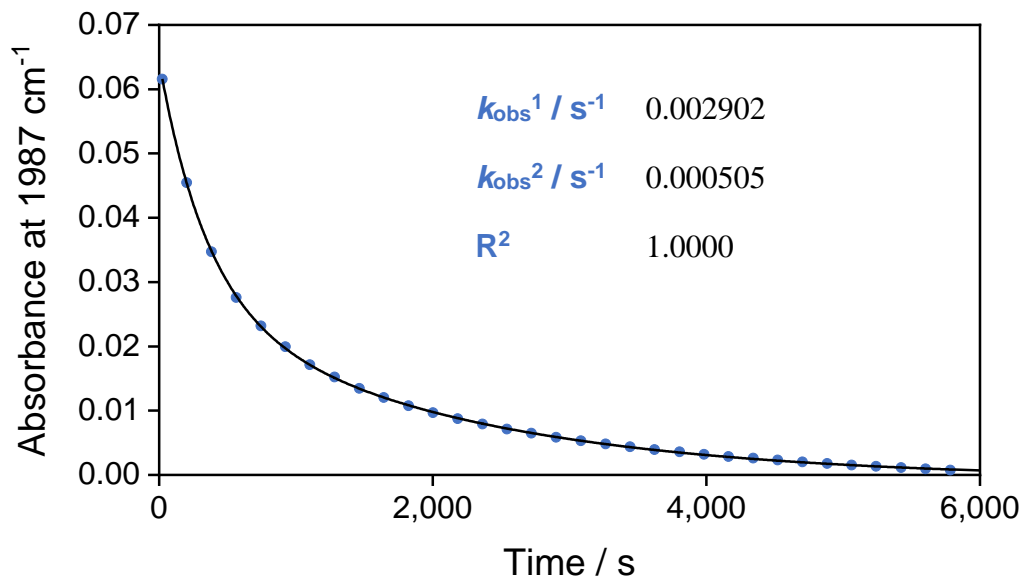


Figure 7.5. Decay of IR absorption at 1987 cm⁻¹ with double exponential curve fit during reaction of **3** with 6 M MeI in CH₂Cl₂ (298 K).

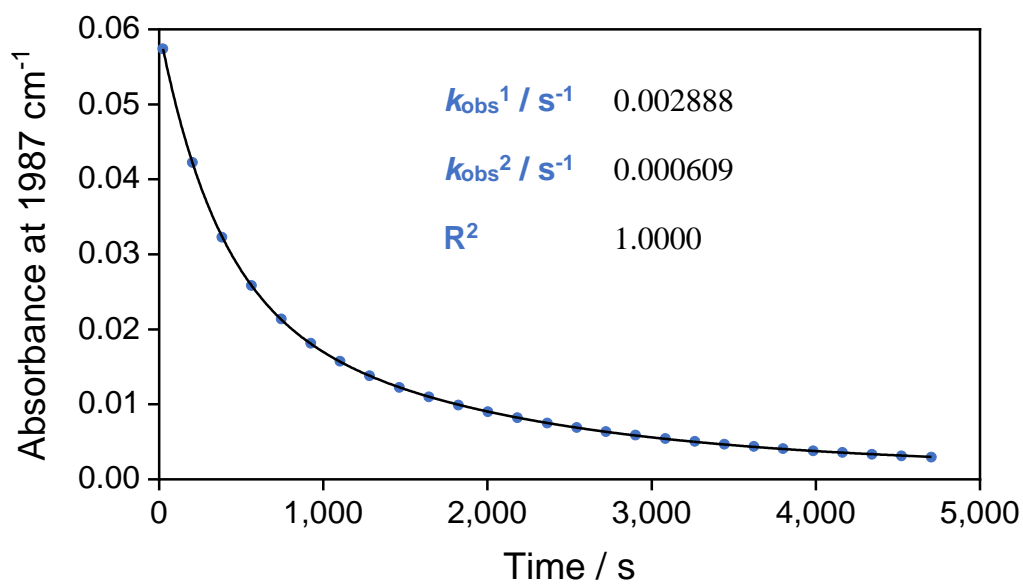


Figure 7.6. Decay of IR absorption at 1987 cm⁻¹ with double exponential curve fit during reaction of **3** with 8 M MeI in CH₂Cl₂ (298 K).

7.6. Determination of TOF value for polymer-supported catalyst in MeOH

Table 7.3 gives key values for the determination of the rate of formation of methyl acetate, where ϵ is the measured extinction coefficient of methyl acetate in MeOH in the cell.

Table 7.3. Key values for determination of rate of formation of methyl acetate.

$\epsilon / \text{mol}^{-1} \text{ dm}^3$	0.0652
Volume / dm^3	0.01
Gradient / h^{-1}	0.0112

The rate of formation of methyl acetate can be calculated as shown in Equation 7.1, and gives a value of $1.72 \times 10^{-3} \text{ mol h}^{-1}$.

To calculate the number of moles of rhodium in the system, the percentage rhodium by mass in the polymer was determined via ICP-MS as 4.48%. As 102 mg of polymer was used, this corresponds to 4.57 mg of rhodium, or 4.42×10^{-5} moles of rhodium in total.

To calculate the TOF, the rate of formation of methyl acetate was divided by the number of moles of rhodium in the system in total, to give a value of 38.91 h^{-1} .

7.7. Determination of TOF value for polymer-supported catalyst in CHCl_3

Table 7.3 gives key values for the determination of the rate of formation of methyl acetate, where ϵ is the measured extinction coefficient of methyl acetate in CHCl_3 in the cell.

Table 7.4. Key values for determination of rate of formation of methyl acetate.

$$\epsilon / \text{mol}^{-1} \text{ dm}^3 \quad 0.193$$

$$\text{Volume} / \text{dm}^3 \quad 0.01$$

$$\text{Gradient} / \text{h}^{-1} \quad 0.0077$$

The rate of formation of methyl acetate can be calculated as shown in Equation 7.1, and gives a value of $3.99 \times 10^{-4} \text{ mol h}^{-1}$.

As 10 mg of $[\text{Rh}(\text{CO})_2\text{I}]_2$ was used, this corresponded to 3.53×10^{-5} moles of rhodium in total.

To calculate the TOF, the rate of formation of methyl acetate was divided by the number of moles of rhodium in the system in total, to give a value of 11.30 h^{-1} .

7.8. References

- 1 A. A. Coelho, TOPAS Academic Version 4.1, see <http://www.topas-academic.net>.
- 2 C. J. David Kinning and E. L. Thomas, *Hard-Sphere Interactions between Spherical Domains in Diblock*, 1984, vol. 17.
- 3 A. M. James, M. J. Derry, J. S. Train and R. Dawson, *Polym. Chem.*, 2019, **10**, 3879–3886.